A fully-coupled coastal hydro-morphodynamical numerical solver

Giorgio Incelli

Thesis submitted to the University of Nottingham

for the degree of Doctor of Philosophy

July 2016

Abstract

This research work aims at using a fully-coupled hydro-morphodynamical numerical solver to study the beachface evolution at the storm time-scale.

The proposed model originates from that of Briganti et al. (2012a), who considered a system comprising the Nonlinear Shallow Water Equations and the Exner one (bed-load only). Suspended load, bed diffusion and infiltration are now included, following Zhu (2012) and Dodd et al. (2008) approaches.

The original version of the numerical scheme (TVD-MCC) is modified to deal with the aforementioned additional physics, while the infiltration computation is implemented at the end of each time step (see Dodd et al., 2008). A new treatment for the wet / dry front is adopted, following the previous work of Hubbard & Dodd (2002).

About model validation, enhanced results are obtained in both the fluvial dune and the dam break tests with respect to those of Briganti et al. (2012a). In the uniform bore test with bed-load the results confirm those of the previous version (see Zhu et al., 2012), while in the case with combined load they show an overall good agreement with the reference solution, even though the maximum run-up is underestimated. Single swash on fixed slope experiments are reproduced as well. In the impermeable case the results are improved on those of Briganti et al. (2011), while in the permeable one the overall performance is thought to be reasonable (better the uprush than the backwash).

Although the maximum predicted inundations are smaller than measured, hydrodynamic results compare quite well with field data for real single swash events, thus confirming that one-dimensional, depth-averaged description of the swash is reasonable. The final computed bed changes show the correct order of magnitude but are generally underestimated and the predicted pattern is not always observed in the data. The sensitivity analyses indicate that this discrepancy is probably due to the initial (unknown) distributions of pre-suspended sediment concentration and velocity.

The morphodynamic evolution of two beaches at the storm time-scale is studied. In the bed-load test, results compare very well with the reference ones from Dodd et al. (2008) and Sriariyawat (2009) and, in general, the sensitivity analyses for the permeable beach case confirm previous findings. In the combined load test, the Meyer-Peter and Müller formula is applied excluding the threshold for sediment movement. This assumption is not expected to have a significant impact on the morphodynamic evolution, in the limits of the chosen parameters and settings. Increased efficiency in the entrainment rate for suspended load is found to promote onshore transport, extending Pritchard & Hogg (2005) observation for single swash events to the case of multiple ones. Variations in the incoming wave period and height yield different final bed change profiles from the default one (three long-shore bars and generally deposition seaward and erosion landward), showing differences in the number of formed bars and in the morphodynamic pattern, with sometimes accretion in the upper beach.

Beside this, new seaward boundary conditions (REBCs) are derived. They do not alter flow and bed level patterns generated by nonlinear standing waves on mobile bed, do converge to the hydrodynamic conditions on virtually-fixed bed and perform reasonably well in the demanding morphodynamic bore test.

Acknowledgements

Firstly, I am extremely grateful to my supervisor Doctor Riccardo Briganti for giving me the opportunity of undertake this research project and for his continuous and dedicated support over the last three years. Secondly, I wish to thank my secondary supervisor Professor Nicholas Dodd for providing helpful suggestions and encouragement.

I would also like to thank all my colleagues from the Coastal Dynamics and Engineering Research Group for the nice working environment I experienced and those from C1 and the former C11 rooms for making the office a pleasant place.

I wish to acknowledge the important support I received from my family and friends during these three years. In particular, I would like to thank my grandparents, my parents and my precious wife, Barbara, who have helped me through tough times.

Throughout the course of this research work I was in receipt of a generous grant from the University of Nottingham to whom I am indebted.

Contents

List of Figures

List of Tables

Nomenclature

units of the variable or parameter are in [ ]; when multiple units are possible or in case of vector / matrix symbols, an asterisk is left between the brackets.

Symbols

Latin

a_0	constant term coefficient for cubic equation solution [*]
a_1	linear term coefficient for cubic equation solution [*]
a_2	quadratic term coefficient for cubic equation solution [*]
a_{inf}	Forchheimer linear coefficient [sm^{-1}]
A_{sed}	sediment mobility parameter for bed-load [s^2m^{-1}]
b	bed change from initial bathymetry [m]
b_{inf}	Forchheimer quadratic coefficient [s^2m^{-2}]
b^*	non-dimensional bed change from initial bathymetry [–]
c	depth-averaged suspended sediment volume concentration [m^3m^{-3}]
CN	global Courant Number [–]
d_{50}	median sediment grain diameter [m]
d_{65}	nominal sediment grain diameter [m]
D	depositional rate for suspended load [ms^{-1}]
D_{par}	discriminant for cubic equation solution [*]
$\mathbf{D}$	TVD-function vector [*]

$\mathbf{e}_k$	k-th right eigenvector [*]
E	erosional rate for suspended load [ms^{-1}]
f_c	friction coefficient [–]
$\mathbf{F}$	vector of fluxes [*]
g	acceleration due to gravity [ms^{-2}]
h	water depth [m]
h_{ini}	initial maximum or reference water depth [m]
h_{min}	minimum water depth parameter [m]
h_{rep}	representative scale for water depth [m]
h_{rsv}	initial still water depth inside idealised reservoir [m]
h^*	non-dimensional water depth [–]
H	wave or bore height [m]
H_{dune}	maximum dune height [m]
I	hydraulic gradient [–]
$\mathbf{J}$	Jacobian matrix [*]
$\widehat{\mathbf{J}}$	modified Jacobian matrix (Castro Diaz et al., 2008, approach) [*]
k_{inf}	hydraulic conductivity [ms^{-1}]
k_b	bed roughness [m]
k_{vk}	von Karman constant [–]
L	sinusoidal wavelength [m]
L_x	numerical domain extension [m]
m_e	parameter for erosional rate [ms^{-1}]
$m_{e,bw}$	parameter for erosional rate for backwash [ms^{-1}]
$m_{e,up}$	parameter for erosional rate for uprush [ms^{-1}]
m_e^*	non-dimensional parameter for erosional rate [–]
M	number of cells comprised in numerical domain [–]
N	chosen time step for V_{inf} computation [–]
p_b	bed porosity [–]
q_b	bed-load flux [m^{2}s^{-1}]

$\hat{q}_b$	bed-load flux with bed diffusion term dependent on z_b [m^2s^{-1}]
$\tilde{q}_b$	bed-load flux with bed diffusion term dependent on b [m^2s^{-1}]
q_w	constant water discharge per unit of width [$m^3s^{-1}m^{-1}$]
Q_{par}	Q parameter for cubic equation solution [*]
R_{ent}	ratio between uprush and backwash m_e values [–]
R_{par}	R parameter for cubic equation solution [*]
$\Re_k$	k-th Riemann Equation [ms^{-1}]
s_{rel}	relative density of sediment compared to water [–]
S_b	bed diffusion source term [ms^{-1}]
S_{bed}	component of bed diffusion source term [m^2s^{-1}]
S_f	friction source term [m^2s^{-2}]
S_g	geometric source term [m^2s^{-2}]
S_s	suspended sediment source term [ms^{-1}]
$\mathbf{S}$	vector of source terms (infiltration-related ones excluded) [*]
$\mathbf{S}_g$	geometric source term vector [*]
$\mathbf{S}_{inf}$	vector of infiltration-related source terms [*]
t	time [s]
t^*	non-dimensional time [–]
tol	relative error tolerance value [–]
T	sinusoidal wave period [s]
u	depth-averaged cross-shore horizontal velocity [ms^{-1}]
u_{crs}	critical horizontal velocity for suspended load [ms^{-1}]
u_{rep}	representative scale for horizontal velocity [ms^{-1}]
u^*	non-dimensional depth-averaged cross-shore horizontal velocity [–]
U	horizontal velocity [ms^{-1}]
U_0	free stream horizontal velocity [ms^{-1}]
U_f	friction velocity [ms^{-1}]
V_{inf}	cumulative infiltrated volume [m^3m^{-1}]
V_{shock}	shock speed [ms^{-1}]

w_{inf}	infiltration velocity [ms^{-1}]
w_s	effective settling velocity for suspended load [ms^{-1}]
$\mathbf{w}$	vector of primitive variables [*]
$\mathbf{W}$	vector of conserved variables [*]
x	cross-shore distance [m]
x_s	shoreline (or tip) position [m]
x^*	non-dimensional cross-shore distance [–]
X	auxiliary initial abscissa [m]
z_0	height at which $U = 0$ [m]
z_b	bed level [m]
z_b^*	non-dimensional bed level [–]
Z	non-dimensional parameter for momentum integral method [–]

Greek

α_k	k-th wave strength [m]
β_k	k-th wave strength for source terms [m^{2}s^{-1}]
γ_h	linearised time gradient for hydraulic head [ms^{-1}]
γ_ζ	linearised time gradient for infiltration depth [ms^{-1}]
δ	bottom boundary layer thickness [m]
δ_k	k-th parameter value for entropy correction [ms^{-1}]
Δx	spatial step size [m]
Δx_s	dimensional (absolute) error for shoreline (or tip) position [m]
Δt	temporal step size [s]
ϵ	generic relative or estimate of non-dimensional error [–]
ζ	infiltration depth [m]
η	water surface perturbation from initial water level [m]
θ	Shields parameter [–]
θ_{crb}	critical Shields parameter for bed-load [–]
θ_{crs}	critical Shields parameter for suspended load [–]

θ_k	k-th smoothness ratio [–]
λ_k	k-th eigenvalue (or eigenspeed) [ms^{-1}]
Λ	harmonic amplitude [m]
μ	μ coefficient for Riemann Equation solution [–]
ν_k	k-th local Courant Number [–]
ξ	bed porosity parameter [–]
ρ_s	sediment unit of mass (or density) [$\mathrm{kg\,m}^{-3}$]
ρ_w	water unit of mass (or density) [$\mathrm{kg\,m}^{-3}$]
σ	σ source term for Riemann Equation solution [m]
τ_b	bottom shear stress [Nm^{-2}]
τ_{crs}	critical bottom shear stress for suspended load [Nm^{-2}]
τ_{rep}	representative scale for bottom shear stress [Nm^{-2}]
ϕ	angle of repose of sediment [°]
Φ	generic flux limiter [–]
Ψ	Harten & Hyman entropy correction [ms^{-1}]
ω	ω coefficient for Riemann Equation solution [s]
Ω	auxiliary variable for Riemann Equation solution [$\mathrm{m}^{1/2}$]

Subscripts

A	at point A
B	at point B
C	at point C
eq	at equilibrium
i	related to the incoming wave
m	at generic cell
mb	Minmod (or Minbee) flux limiter
Lt	on the left side of a shock
P	at point P
r	related to the reflected wave

Rt	on the right side of a shock
sb	Superbee flux limiter
vl	van Leer flux limiter

Superscripts

cr	at corrector stage
n	at generic time step (or level)
pr	at predictor stage

Abbreviations

BBL	bottom boundary layer
BCs	boundary conditions
IS	instrument station
MCC	MacCormack
MOC	Method of Characteristics
MPM	Meyer-Peter and Müller
NSWEs	Nonlinear Shallow Water Equations
PIV	particle image velocimeter
REBCs	Riemann Equation Boundary Conditions
RMSE	root mean square error
TVD	Total-Variational-Diminishing
UA	ultrasonic altimeter
WAF	Weighted Average Flux

Chapter 1

Introduction

1.1 Motivation

Coastal regions are areas where the edge of the land is continuously remodelled by the action of oceans and seas. These areas are more and more a source of interest, for example because of economic development, as a number of different human activities take place beside the sea, from travel and recreational to commercial and industrial, just to cite a few.

Where people settle their houses or interests, there are engineering problems to be faced. For instance, the interaction between the land and the sea can result in a progressive erosion of the beaches, leading to the risk of settlements and damages to the maritime structures and the nearby buildings. On the other hand, sediment accumulation can severely affect the efficiency of harbours and other facilities.

In the light of this, it is apparent how useful and important is to achieve a deeper understanding of the physics involved in the evolution of the shape of the coasts and the possibility to predict their changes, at least in the short and medium terms. This knowledge would lend itself to guarantee a safer

enjoyment and a more sustainable exploitation of the nearshore areas.

1.2 Nearshore region and swash zone

Following Masselink & Hughes (2003) and Svendsen (2005) among others, it is possible to identify a number of physical processes which take place in the nearshore region, where the sea waves and currents propagate, evolve and dynamically interact with the bottom sediment, finally inducing changes of the beachface. In particular, this work focuses on wave action and three zones can be generally distinguished within the nearshore region (see Fig. 1.1), depending on wave transformation while approaching the shore.

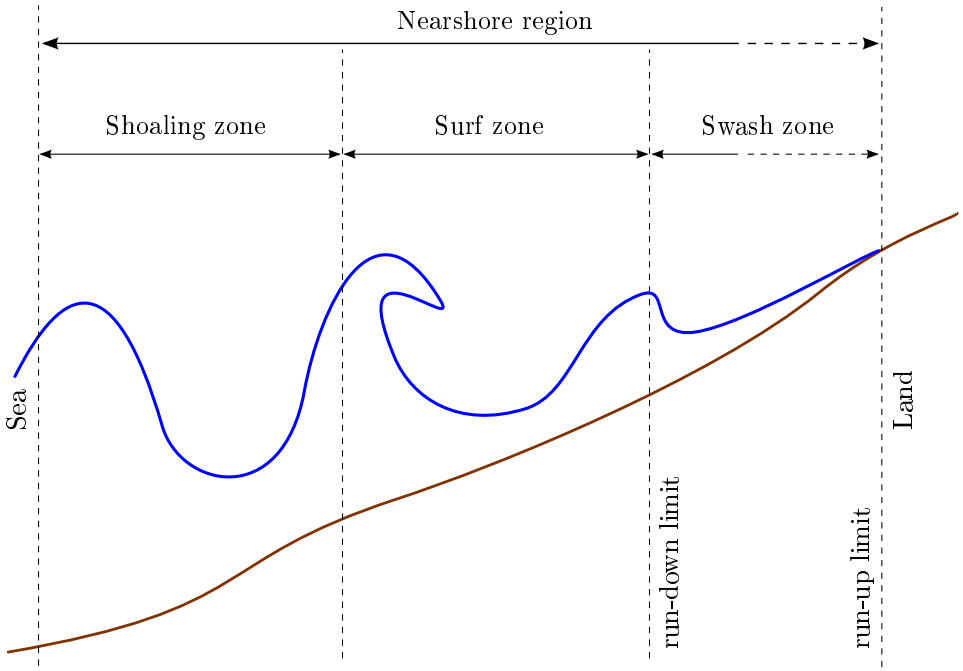

Figure 1.1: Sketch of the nearshore region and its basic partition zones.

Starting from offshore, firstly there is the shoaling zone, where the waves pointing landward begin to be affected by the reducing water depth and, as a consequence of energy conservation, their height tends to increase.

Secondly, waves generally break, signposting the surf zone, and continue to move shoreward. The breaking waves are also called bores, which are usually associated with noticeable sediment transport due to great turbulence and considerable energy dissipation.

Finally, waves impact on the foreshore, inundating and then receding from it, thus marking two time-dependent boundaries, namely the run-up and run-down limits respectively, which delimit the swash zone. This unsteady (swash) motion is therefore composed of two phases, the first with the water moving landward (run-up or uprush) and the second with it heading seaward (run-down or backwash). Throughout this oscillatory process the flow strongly interacts with the sediment, which can be mobilised as bed- and / or suspended load, yielding rapid changes of the beach profile therein.

1.3 Aim and objectives

The general aim of this work is to develop a numerical model to study the beachface evolution caused by a multiple swash event of a duration comparable with the typical time-scale of a storm (i.e. some hours, see § 2.4).

The above-mentioned aim is pursued through the following objectives:

- to improve the Briganti et al. (2012a) model, in order to make it suitable to represent the complexity of the swash zone and to reliably predict the beach change due to a multiple swash event;
- to assess the performance and robustness of the improved model against available analytical solutions and numerical results from literature;
- to reproduce experimental and observed single swash events in order to compare numerical results with laboratory and field measurements respectively;

- to simulate the evolution of an erodible beach under a series of regular (sinusoidal) waves for the time-scale of a storm.

Note that the complexity of the physics of the swash zone largely reduces the possibility of useful analytical solutions. This accentuates the need for numerical models which are able to approximate the natural phenomena with more and more reliability and accuracy.

1.4 Thesis outline

This introductory chapter provides the research motivation and background, while presenting the aim and objectives which are developed later.

Chapter 2 offers a review of some relevant works on the swash zone, with focus on swash zone morphodynamics (i.e. the beachface evolution).

Chapter 3 presents the governing equations used in the improved numerical model, which now includes suspended sediment transport, bed diffusion and infiltration as well.

Their implementation in the numerical scheme is then explained in Chapter 4, along with the description of the applied shoreline boundary conditions, which differ from those of Briganti et al. (2012a) and follow the original approach of Hubbard & Dodd (2002).

Several validation tests are described in Chapter 5, drawing attention to specific aspects of the present model performance. This preliminary assessment is necessary to enhance the confidence in a reasonable and realistic morphodynamic prediction by the model when benchmarks are unavailable.

An attempt at reproducing real single swash events is reported in Chapter 6, showing how challenging the simulation of field swash motions is.

Chapter 7 presents the evolution of two different beaches at the storm time-

scale, the first steeper than the second and modelling sediment transport as bed-load only (for consistent comparison with literature) or combined load (i.e. including both bed- and suspended load) respectively.

Beside this main work-stream, Chapter 8 describes the new absorbing-generating seaward boundary conditions for fully-coupled hydro-morphodynamical solvers derived and validated by Incelli et al. (2015a). Although these conditions cannot be applied to the previously considered tests, they are an interesting added value and represent a starting point for new advances in this important numerical topic.

Finally, Chapter 9 provides the conclusions of this work and suggests future developments which, in the light of this research experience, can lead to further improvements in the modelling of the swash zone morphodynamics.

Chapter 2

Literature review

2.1 Swash zone physical background

Following the description of the nearshore region given in § 1.2, the swash zone can be defined as '*that part of the beach alternately covered and exposed by uprush and backwash*' (Masselink & Puleo, 2006).

The natural swash process is inherently complicated due to the moving shoreward boundary or simply due to the fact that subsequent swash motions can interact and generate the catch-up and absorption, and collision occurrences during the uprush and backwash phases respectively (see Fig. 2.1 and Erikson et al., 2005; Caceres & Alsina, 2012).

Firstly there is the hydrodynamics, i.e. how water behaves in the swash zone. In general it is assumed that the swash motion is dominated by two distinct kind of forcing actions, namely incident bores and long waves (Elfrink & Baldock, 2002). Bores are generated by short waves (period between 1 and 30 s), while long ones (period greater than 30 s) are characterised by a low-frequency non-breaking profile. One of these two actions generally prevails, mainly depending on the specific surf and swash zone morphology (Butt

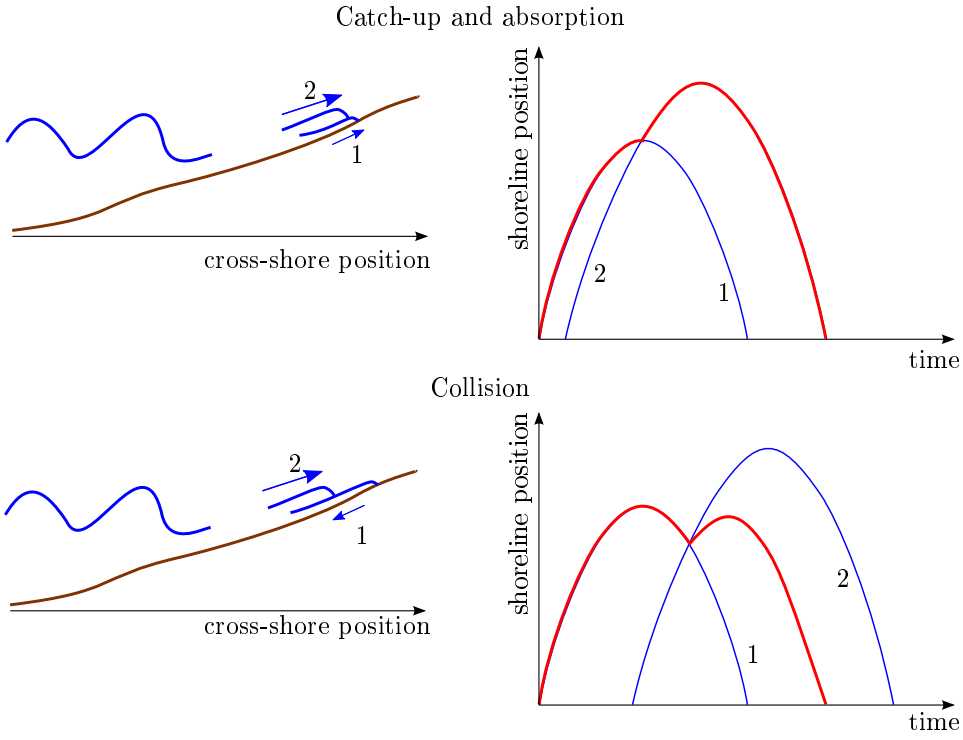

Figure 2.1: Sketch of the catch-up and absorption (top panels), and collision (bottom panels) interactions. In the left panels, the blue arrows indicate the wave directions and their length corresponds to the associated wave energy. In the right panels, the blue thin lines and the red thick ones indicate the shoreline evolution without interaction (i.e. if waves 1 and 2 occur separately) and with it respectively. This figure is modified from Fig. 1 of Erikson et al. (2005).

et al., 2005). Nonetheless, Baldock et al. (1997) found that the low-frequency component can be still significant even on steep beaches, where the process is usually bore-driven.

Bore-driven swash motion shares also analogies with other kinds of flow conditions and in particular Peregrine & Williams (2001) provided a solution for a single swash event which is identical to that of a dam break problem on a fixed slope beach (thus giving a useful benchmark for numerical models in later years, see § 2.3).

Secondly, it is necessary to understand how the flow and the sediment interact. For example in the case of a bore-driven single swash event, the maximum sediment transport is usually observed at the beginning and at the

end of the cycle, i.e. at the impact of the bore on the foreshore and when, after the flow reversal, the velocity peaks in the offshore direction (see Fig. 2.2).

In subsequent swash motions, the occurrence of a retrogressive bore, caused by the collision of the previous supercritical backwash flow with the following incoming bore, can enhance sediment mobilisation (Masselink & Puleo, 2006). Moreover, the interaction between short waves and between short and long ones can induce the generation and reflection of additional low-frequency motion, which is in turn able to transport sediment suspended within the swash zone seaward of it (see e.g. Brocchini & Baldock, 2008).

Furthermore, the amount of sediment mobilised during one of the two phases (run-up or run-down) is found typically to be two or three orders of magnitude greater than the net sediment transport (Hughes et al., 1997), this aspect requiring consequently particular modelling care. However, Masselink et al. (2009) demonstrated that the net sediment flux can be of the same order of those of uprush or backwash, being one of the latter two considerably smaller than the other. More recently, Puleo et al. (2014b) observed that both cases can actually coexist on the same beach.

Sediment transport is usually classified in reason of different transport modes, generally distinguishing between bed-load, i.e. the sediment maintains continuous (or nearly) contact with the bottom, and suspended load, i.e. the sediment is advected at the flow velocity and it is expressed through a concentration value (see e.g. van Rijn, 2007a,b). Note that the bed-load mode assumes an immediate feedback of the sediment fluxes on the bed level (i.e. the sediment is instantaneously removed from / deposited on the bottom, which changes accordingly), while the suspended load one requires time for sediment entrainment / settlement, introducing a lag mechanism which may promote onshore transport (see Pritchard & Hogg, 2005). Besides, bed-load

can reach the sheet flow conditions at high shear stress, i.e. the sediment moves as a dense transport layer of the thickness of several grain diameters (see e.g. Wilson, 1989; van der A et al., 2010). Fig. 2.2 illustrates a sketch of the different sediment transport processes which can take place during a single swash cycle.

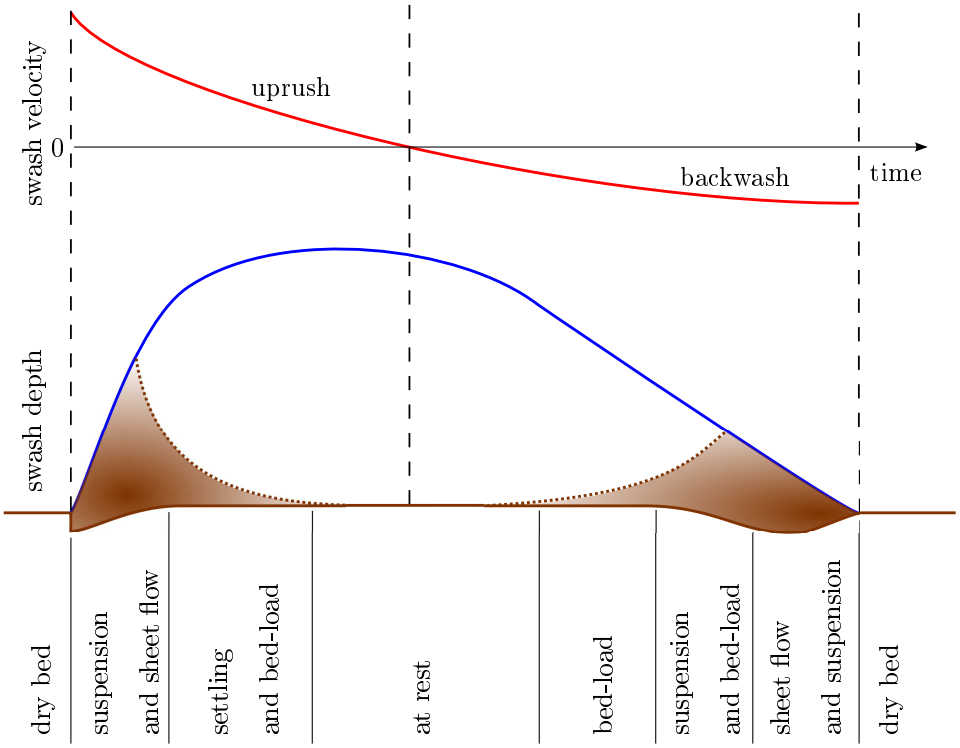

Figure 2.2: Sketch of the sediment transport processes during a swash cycle. Shaded areas indicate the presence of sediment transport, darker where more intense. This figure is modified from Fig. 5 of Masselink & Puleo (2006).

Some field measurements and investigations (Hughes et al., 1997; Masselink & Hughes, 1998) showed a strong relationship between the amount of sediment transport and the time-averaged (over uprush or backwash) velocity cubed, which is consistent with energetic-based formulae for bed-load and for sediment transport under sheet flow conditions. However, Masselink & Russell (2006) criticised these formulae for both bed- and suspended load transport modes because unable to predict deposition in the upper part of the beach, as field

observations showed the mean flow to be predominantly offshore-directed.

Additionally, Masselink & Hughes (1998) and Puleo et al. (2000) pointed out that the fundamental physical mechanism leading to sediment transport in each phase of the cycle is different. They correlated the uprush to the surface-generated turbulence due to the initial bore collapse on the foreshore, while the backwash to the bed-generated one, linked to the bottom boundary layer evolution. So this should be considered somehow in the modelling.

Moreover, the use of local fluid acceleration as a proxy for the bore turbulence was highlighted by Puleo et al. (2003), but then its importance was scaled down by Puleo et al. (2007), even though their findings were not conclusive. Recent valuable attempts to account for the bore turbulence in the swash zone modelling were made by Reniers et al. (2013) and Lanckriet & Puleo (2015). In particular, the former used a simplified turbulence model to examine sediment sorting processes, acknowledging that further study was warranted to enhance confidence in their approach. The latter developed a very interesting semianalytical model for sheet flow description in the swash zone. However, to estimate their bore turbulence term they used visual observations during the laboratory experiment and experiment-specific evidence, procedures which do not seem suitable for predictive simulations.

Very recently, thanks to improved instrumentations and consequent high-resolution field measurements (see Puleo et al., 2014a), sheet flow conditions were investigated in detail by Lanckriet et al. (2014), who provided a detailed study of concentration profiles useful for future modelling.

Finally, interactions between surface and subsurface flows, i.e. infiltration / exfiltration, may play a significant role in the evolution of coarse sediment beaches, enhancing shoreward accretion through increased swash asymmetry, as pointed out by Masselink & Li (2001).

To summarise, this overview gives a brief description of the two fundamental aspects involved in the swash zone processes, that is the hydrodynamic and the morphodynamic ones, and highlights how complex and still under discussion the related physics is.

2.2 Coastal hydro-morphodynamical solvers

In recent years a wide range of models was employed in hydro-morphodynamics, and in particular in the coastal environment, therefore this review is restricted to the latter research field.

The models are generally depth-averaged, this choice offering the best balance between result accuracy and computational cost (Brocchini & Dodd, 2008), and can consider one or both directions on the horizontal plane. Some solvers are averaged on wave groups, looking for further numerical efficiency and robustness (see e.g. Roelvink et al., 2009), while others allow a wave-by-wave analysis of the swash processes, dealing with the often strong swash-swash interactions on a smaller spatial scale for a more detailed simulation (see e.g. Dodd et al., 2008).

Additionally, depth-averaged models usually describe flow evolution through the Nonlinear Shallow Water Equations (hereinafter NSWEs, see e.g. Zhu et al., 2012) or Boussinesq-type ones (e.g. Kim, 2015). Hybrid models, which can consider both the NSWEs and the Boussinesq ones, were developed as well (see Xiao et al., 2010). The NSWEs are more appropriate landward of the inner surf zone, where nonlinearity dominates in shallow water conditions, while the latter account for the dispersion required further seaward (Brocchini & Dodd, 2008). Sometimes a diffusive term for the flow velocity is added to the NSWEs to simulate energy dissipation through horizontal eddies (see van Rooijen et al., 2012).

Another distinction can be made in reason of the modelled sediment transport, for example if this is considered as bed-load, suspended load or both, i.e. as combined load, (see e.g. Kobayashi & Johnson, 2001; Kelly & Dodd, 2010; Zhu & Dodd, 2015, respectively).

In addition to this, aiming at simulating the evolution of coarse sediment beaches, Dodd et al. (2008) included infiltration in their solver, while McCall et al. (2015) showed that their model is able to successfully predict the morphodynamic change of gravel beaches accounting for exfiltration and groundwater motion as well.

An important model feature is how the hydrodynamic and the morphodynamic parts of the problem are considered in the numerical implementation. If the two of them are solved simultaneously, the model is called fully-coupled, while if they are computed subsequently, the model is decoupled (or uncoupled). The first approach is to be preferred when the interaction between flow and sediment is strong and the bed evolves at the same time-scale of the flow (Kelly & Dodd, 2010). However fully-coupled solvers can present mathematical, and hence numerical, challenges when complicated sediment transport formulae are employed, for example if no exact or explicit expression of Jacobian matrix terms is available (see Castro Diaz et al., 2008, among others). The decoupled approach instead allows more flexibility about these formulae and the choice of different integration time steps for the hydrodynamic and the morphodynamic modules (see e.g. Reniers et al., 2004). More recently, Postacchini et al. (2012) developed a weakly-coupled approach, which uses an approximation for the morphodynamic eigenvalue (suitable for complex closures) within the hydro-morphodynamic eigenstructure, keeping separated the solution of the flow and bed update equations (with the same time step). However they needed to introduce a targeted filter when spurious numerical

oscillations occurred in their results.

As bores (or shocks) are expected to be frequent in swash zone processes (Brocchini & Dodd, 2008), the solvers can be finally distinguished between shock-fitting and shock-capturing ones. On one hand, the former are those models requiring an explicit treatment for shocks. For example, the solver of Kelly & Dodd (2010) belongs to this group and is based on the Method of Characteristics (henceforth MOC). Despite a considerable numerical cost and a complex implementation, MOC results are highly accurate to the point to be regarded as benchmark when analytical solutions are unavailable (Kelly & Dodd, 2009). On the other hand, the latter automatically deal with shock conditions (e.g., the model of Briganti et al., 2012a) and are generally simple to implement and computationally inexpensive. However, this second class is expected to be less accurate than the first one, as for instance the shock cannot be resolved as a sharp discontinuity but is represented by a steep transition (or gradient) over three or more cells (or mesh points). Additionally high-resolution schemes (i.e. accurate to the second order or more, see Hudson, 2001; Castro Diaz et al., 2008, among others) need appropriate filtering to avoid the occurrence of spurious numerical oscillations, sometimes complicating the numerical method though.

The above-mentioned features of the coastal hydro-morphodynamical solvers are summarised in Tab. 2.1 to provide a clearer and general view of the different possible options.

As mentioned in § 1.3, in this work the Total-Variational-Diminishing MacCormack (hereinafter TVD-MCC) model of Briganti et al. (2012a) is developed further to make it able to simulate the morphodynamic evolution of the beach-face at the storm time-scale. This model is depth-averaged, wave-resolving and shock-capturing, aiming at an accurate but computationally efficient descrip-

Solved Equations	
Spatial resolution	depth-resolving / depth-averaged (one- or two-dimensional horizontally)
Time resolution	wave-resolving / group-averaged
Flow Equations	NSWEs / Boussinesq-type / Hybrid
Sediment transport modes	bed-load (sheet flow) / suspended load / combined load
Subsurface flow	excluded / included
Numerical aspects	
Coupling	fully-coupled / uncoupled / weakly-coupled
Shock treatment	shock-fitting / shock-capturing

Table 2.1: Coastal hydro-morphodynamical solvers. Synoptic table of their relevant features. '/' separates alternative options.

tion of the swash processes. It adopts the NSWEs as the focus is on the swash zone (Brocchini & Dodd, 2008) and it is fully-coupled to account for the complex and quick interactions between flow and sediment in such a dynamic environment (see § 2.3 and Kelly & Dodd, 2010). The original model considered bed-load only, through the well-known Grass or Meyer-Peter and Müller (MPM henceforth) formulae. In this work the suspended load, a bed diffusion mechanism and the effects of infiltration (exfiltration and groundwater motion are neglected) are introduced with the purpose of successfully simulate morphodynamics on sandy (from fine to coarse grained) beaches.

2.3 Morphodynamic single swash event

The preliminary step before the simulation of a multiple swash event is necessarily the understanding of the morphodynamics which characterises a single

swash one.

Kelly (2009) and Kelly & Dodd (2010) analysed in detail the single swash event produced by the bore-collapse initial conditions of Shen & Meyer (1963) and Peregrine & Williams (2001), which are reproduced in Fig. 2.3.

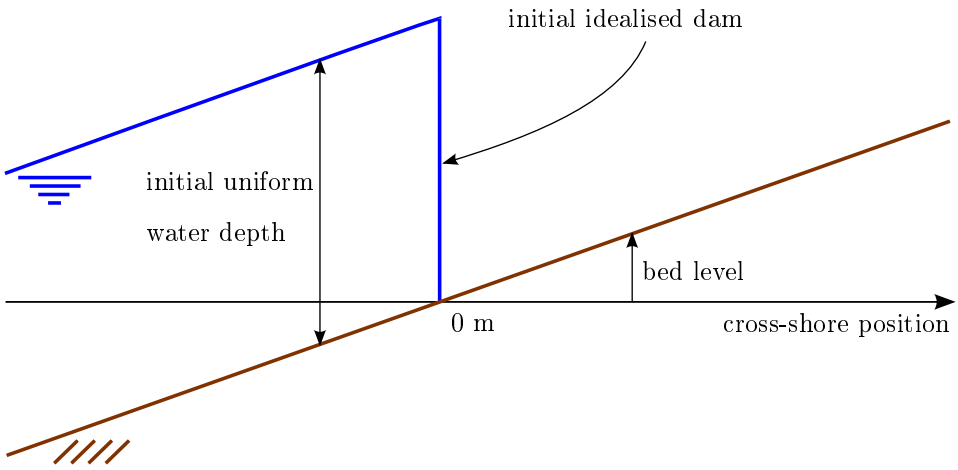

Figure 2.3: Peregrine & Williams (2001) single swash event. Sketch of initial conditions.

Additionally, Kelly & Dodd (2010) demonstrated that a full coupling is necessary for a correct morphodynamic prediction in the swash zone, regardless of other physical effects, like turbulence or infiltration. They showed a comparison of fully-coupled and decoupled simulations, the former displaying a smaller maximum run-up and considerably less final erosion of the beachface than the latter. More recently, Postacchini et al. (2012) achieved good results with their weakly-coupled approach, confirming that decoupled results significantly differ from fully- and weakly-coupled ones. Furthermore, Postacchini et al. (2014) showed that the uncoupled procedure is not suitable to predict the bed evolution where the largest bed change occurs during a bore-driven uprush.

Zhu et al. (2012) considered the impact of a uniform bore on an erodible beach, moving from the fixed bed case studied by Hibberd & Peregrine (1979).

The expected occurrence of the backwash bore was accompanied by the formation of a bed step in the bottom profile and the results were found to be consistent with some field data. The model from Briganti et al. (2012a) was tested against the MOC one of Zhu et al. (2012) and a remarkable agreement between the two was pointed out. This is of paramount importance for the present work because obtained despite a very different technique to deal with shocks was employed (see § 2.2).

Furthermore, the original model of Briganti et al. (2012a) was extended in Briganti et al. (2012b), where a new approach for bottom friction estimation was implemented, namely the momentum integral method for the description of the bottom boundary layer (hereinafter BBL). The numerical results were compared with laboratory measurements, showing a fairly accurate description of a single swash cycle.

Later, Zhu & Dodd (2013) used the Peregrine & Williams (2001) swash flow to study a range of different bed-load transport formulae in fully-coupled and uncoupled simulations, the former reducing net erosion compared with the latter. Moreover, the influence of bed shear stress was investigated and results showed that in certain cases deposition may occur in the mid and upper swash zone when bed shear stress is included.

All the above-mentioned works comprising fully-coupled solvers assumed bed-load as the only transport mode, by means of an Exner-type equation coupled with the NSWEs. About models with suspended load, firstly that of Kobayashi & Johnson (2001) can be cited; it is decoupled and includes sediment mobilisation because of wave breaking and bottom friction. Secondly, Pritchard & Hogg (2005) proposed a decoupled analytical description for suspended sediment transport driven by the Peregrine & Williams (2001) single swash event. This time the sediment entrainment is enforced by means of bot-

tom friction only. They found that settling lag can promote onshore sediment movement, in spite of the offshore bias of swash motion velocities (see e.g. Masselink & Russell, 2006), and pre-suspended sediment, i.e. that advected from the inner surf zone into the swash one, plays a key role in the possible prediction of net deposition on the beachface. These findings were confirmed by later works (Pritchard et al., 2008; Pritchard, 2009).

Very recently, Zhu & Dodd (2015) extended the MOC solver of Zhu & Dodd (2013) including also the suspended sediment transport. They considered the morphodynamic change of an initially plane erodible beach which undergoes a single swash event of the Peregrine & Williams (2001) type or driven by the impact of a solitary wave. The first test showed that coupling with suspended load yields minor effects on the flow evolution and that bed-load transport does not seem to be substantially affected by the other transport mode. Solitary wave simulations presented the formation of a backwash bore and of a corresponding bed step, substantially related to bed-load only, which is an interesting feature as it could have an influence on the subsequent beach profile evolution in the case of multiple swash events.

Finally, Zhu & Dodd (2015) employed the solitary wave test to provide a preliminary guidance for the estimation of the parameter which represents the entrainment efficiency for the suspended load. Albeit some limitations to their findings apply, this investigation is useful for calibration purposes.

2.4 Morphodynamic multiple swash event

The logical development beyond the simulation of a single swash event is the prediction of the bed changes yielded by a series of them. In particular, this work aims at studying the morphodynamic beach evolution at the storm timescale, which typically ranges from few to tens of hours (see e.g. Roelvink et al.,

2009). This duration scale is also referred to as mid-term in the following, because intermediate between the short-term one of a single swash event, of the order of seconds / one minute, and the long-term one of longer simulations, not considered in this work.

In literature there are examples of laboratory experiments, which reproduced the morphodynamic beach evolution (through suspended load only) due to a series of solitary waves (Young et al., 2010), random waves (Caceres & Alsina, 2012; Alsina et al., 2012) or bichromatic ones (van der Zanden et al., 2015) and could represent possible benchmarks for the numerical results. However, in these experiments the flow field measurements where bed change and sediment transport are small (necessary for the open boundary conditions in the modelling) were located in the surf zone, where the NSWEs are no longer appropriate. Moreover, measurements from instruments further onshore (i.e. in the swash zone) cannot be used as driving boundary conditions, because appropriate ones for fully-coupled hydro-morphodynamical solvers including suspended load have not been developed or because the observed time series are frequently incomplete (note that data interpolation could lead to a significant error accumulation in mid-term simulations). Therefore previous literature results which were obtained exclusively using NSWEs in mid-term morphodynamic simulations are considered hereafter.

Dodd et al. (2008) examined the evolution of perturbations on an erodible slope beach in the context of the study of the beach cusp formation process. Although this problem is inherently two-dimensional, a purely cross-shore, i.e. one-dimensional, case was also simulated and results were provided for the bed profile after a series of thousands of regular waves, considering or neglecting infiltration. In the same research field, Sriariyawat (2009) investigated further the one-dimensional mid-term evolution of the same permeable slope

beach, using an improved version of the model of Dodd et al. (2008). Influence of numerical settings and physical parameters was studied in detail through dedicated sensitivity analyses.

Note that both the above-mentioned works considered bed-load only. Hence, the present research firstly intends to reproduce their results using the improved version of the solver of Briganti et al. (2012a), in order to assess its performance. Secondly, the morphodynamic response of an initially plane slope beach is examined when combined load is considered. This points to the twofold aim of achieving a deeper understanding of the physical processes involved in a multiple swash event and of providing new reference results for future models to come.

Chapter 3

Governing equations

3.1 Introduction

In this chapter, the governing equations for the flow, bed and sediment evolution are illustrated. Firstly, for the hydrodynamics, the one-dimensional NSWEs are presented (see § 3.2). Two possible approaches for the inclusion of the bottom friction in the model are considered, namely one based on the Chézy approach while the other being the solution of the momentum integral equation for the BBL (see § 3.2.1).

Secondly, an Exner-type equation describes the bed-load transport by means of the well-known Grass or MPM formulae (see § 3.3). Note that the above-mentioned equations are included in the original model of Briganti et al. (2012a), while the BBL solver approach was used by Briganti et al. (2011) for the simulation of a bore-driven swash event on an impermeable fixed slope.

In this work, an extension of the original model to further physical aspects is proposed. In particular, suspended sediment transport, bed diffusion and infiltration are introduced and the mathematical formulation is modified accordingly (see § 3.4).

Finally, the complete system of conservation laws for combined load morphodynamics is summarised in § 3.5.

3.2 One-dimensional Nonlinear Shallow Water Equations

The NSWEs are derived from the Euler equations (i.e. no viscous effects) under the assumptions of negligible compressibility and no vorticity. Additionally long wave motion is assumed, which means that the water depth is very small in comparison with the spatial scale of the flow (or a wavelength). This allows to neglect the vertical accelerations of the fluid, which corresponds to considering a hydrostatic pressure distribution within the water column. A complete derivation of the NSWEs can be found for example in Toro (2001) or Zhu (2012), while the one-dimensional NSWEs are recalled below:

$$\frac{\partial h}{\partial t} + \frac{\partial hu}{\partial x} = 0 \text{ and} \tag{3.1}$$

$$\frac{\partial hu}{\partial t} + \frac{\partial}{\partial x}\left(hu^2 + \frac{1}{2}gh^2\right) = -gh\frac{\partial z_b}{\partial x}, \tag{3.2}$$

which represent the continuity and conservation of momentum equations in the order. In Eqs. (3.1) and (3.2) x and t are the independent variables (space and time respectively), while g is the gravitational acceleration. $h(x,t)$, $u(x,t)$ and $z_b(x,t)$ are the dependent variables, namely the water depth, the depth-averaged horizontal (water) velocity and the bed (or bottom) level in the order. Variables appearing in the NSWEs are illustrated in Fig. 3.1, which for example shows that the water surface level is simply given by the sum of the water depth and the bed level values, i.e. $h(x,t) + z_b(x,t)$. Recall that the NSWEs describe the flow evolution only, therefore the time dependence of z_b is modelled through an additional equation (see § 3.3).

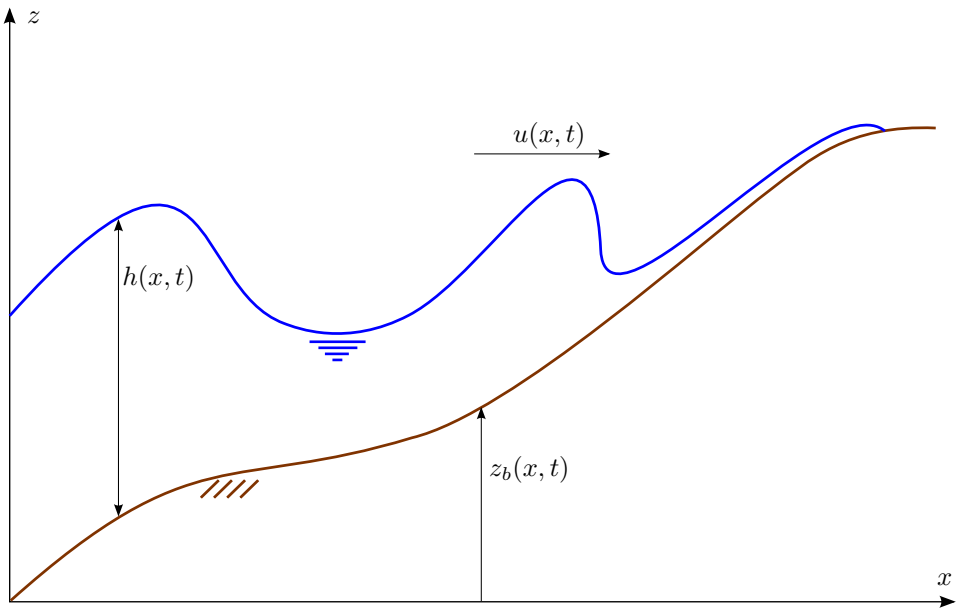

Figure 3.1: Sketch of the variables involved in a generic hydrodynamic swash event.

3.2.1 Bottom friction

Bottom friction can be straightforwardly added as a source term in Eq. (3.2), which becomes

$$\frac{\partial hu}{\partial t} + \frac{\partial}{\partial x}\left(hu^2 + \frac{1}{2}gh^2\right) = -gh\frac{\partial z_b}{\partial x} - \frac{\tau_b}{\rho_w}, \tag{3.3}$$

with τ_b and ρ_w indicating the shear stress at the bottom and the water density respectively.

Bottom friction can be expressed through the Chézy approach, which means

$$\frac{\tau_b}{\rho_w} = \frac{1}{2} f_c \, u|u|, \tag{3.4}$$

where f_c is the non-dimensional friction coefficient, which is usually estimated as a constant value in reason of the bed sediment grain size or, more broadly, of the bed roughness.

Another way to include the bottom friction is the momentum integral method for the BBL, following previous work of Briganti et al. (2011). This

solution allows a description of the evolution of the boundary layer thickness and therefore of the shear stress exchanged between the fluid and the bottom. As a consequence, the assumption of a constant friction coefficient, which characterises the Chézy approach, can be removed. The BBL solver computes the friction velocity U_f, which is related to τ_b by the relationship

$$\frac{|\tau_b|}{\rho_w} = U_f^2. \tag{3.5}$$

Details of the equations employed in the BBL solver are provided in Appendix A.

3.3 Exner equation for bed-load transport

Following Briganti et al. (2012a), bed-load transport is included in the model by means of an Exner-type equation, which is

$$\frac{\partial z_b}{\partial t} + \xi \frac{\partial q_b}{\partial x} = 0, \tag{3.6}$$

where ξ is the bed porosity parameter, defined as $\xi = 1/(1-p_b)$, with p_b being the bed porosity. q_b stands for the instantaneous bed-load transport (or bed-load flux), for which several formulations exist (see for example Zhu & Dodd, 2013, among many others).

In this work, two different formulae are considered. The first is the well-known Grass formula:

$$q_b = A_{sed}\, u^3, \tag{3.7}$$

with A_{sed} being the sediment mobility parameter.

The second is the MPM formula (see e.g. Fredsøe & Deigaard, 1992):

$$q_b = \begin{cases} 8.0\ \mathrm{sgn}\,(u)\ (\theta - \theta_{crb})^{3/2}\left[g(s_{rel}-1)d_{50}^3\right]^{1/2} & \text{if } \theta > \theta_{crb}, \\ 0 & \text{otherwise,} \end{cases} \tag{3.8}$$

where θ is the Shields parameter, i.e.

$$\theta = \frac{|\tau_b|}{\rho_w \, g(s_{rel} - 1)d_{50}} \tag{3.9}$$

and θ_{crb} the critical Shields parameter for the initiation of the sediment movement. d_{50} is the median sediment grain diameter and s_{rel} the relative density of sediment compared to water. $\mathrm{sgn}\,(u)$ is added to the original formula to account for the oscillating nature of the swash motion.

A number of reasons justifies the choice of these two alternative formulae. On one hand, the Grass formula is:

- simple and with straightforward exact derivatives;
- largely employed in previous literature, in both analytical solutions and numerical tests;
- therefore necessary for the validation of the present model.

On the other hand, the MPM formula is recognised to be more physically-based. It includes a threshold for the initiation of the sediment transport as well as an explicit dependence on the bottom shear stress and on the bed sediment characteristics. As a consequence, the latter is expected to lead to better results in simulations against measurements from laboratory experiments and field campaigns.

Besides, it is acknowledged the recent development of other bed-load transport formulae, as that presented by Reniers et al. (2013), which origins from the MPM one and includes some parameters related to the incident wave conditions, as the orbital near-bed excursion and the wave mean period.

3.4 Model development

Part of the scope of the present research is to introduce more physics into the original model of Briganti et al. (2012a). The following aspects are now included:

- *suspended sediment transport:* the transport of finer sediment can deviate from the bed-load mechanism and the contribution of the suspended load becomes increasingly important with smaller grain sizes;
- *bed diffusion:* the presence of a slope in the flow direction affects the sediment transport, which is expected to be enhanced / reduced if downslope / upslope directed (see Sriariyawat, 2009);
- *infiltration:* especially in coarser sand environments, the losses of water mass and momentum are expected to modify the swash hydrodynamics and consequently the resulting bed change.

3.4.1 Suspended sediment transport

The suspended sediment transport is considered through a new equation and a new dependent variable $c(x,t)$, i.e. the depth-averaged sediment volume concentration. The new equation, for the derivation of which the reader is referred to Zhu (2012), is

$$\frac{\partial hc}{\partial t} + \frac{\partial huc}{\partial x} = (E - D)\,, \tag{3.10}$$

with E and D being the erosional (or entrainment) and depositional rates respectively, defined as

$$E = m_e \left(\frac{|\tau_b| - \tau_{crs}}{\tau_{rep}} \right) \text{ and} \tag{3.11}$$

$$D = w_s c, \tag{3.12}$$

where m_e is the parameter for the erosional rate, τ_{crs} the critical (or threshold) shear stress for initiation of suspended load transport and τ_{rep} the representative scale value for the bottom shear stress. Note that the absolute value for τ_b in Eq. (3.11) is necessary as it can be positive or negative (see Eq. (3.4)), while τ_{crs} and τ_{rep} are positive by definition. In Eq. (3.12), w_s is the effective settling velocity for the suspended sediment (see Pritchard & Hogg, 2005).

To satisfy the sediment conservation, Eq. (3.6) needs to account for the net amount of suspended sediment eroded from / deposited on the bottom (pre-multiplied by ξ because of the bed porosity), as shown below:

$$\frac{\partial z_b}{\partial t} + \xi \frac{\partial q_b}{\partial x} = -\xi \left(E - D \right). \tag{3.13}$$

3.4.2 Bed diffusion

Following Dodd et al. (2008), the bed diffusion is included through an additional term which allows the sediment to move downslope when it is already mobilised, i.e. if $q_b \neq 0$. The modified instantaneous bed-load transport is

$$\hat{q}_b = q_b - \frac{1}{\tan \phi} |q_b| \frac{\partial z_b}{\partial x}, \tag{3.14}$$

where ϕ is the angle of repose of the sediment. Substituting Eq. (3.14) into Eq. (3.13), the latter becomes

$$\frac{\partial z_b}{\partial t} + \xi \frac{\partial \hat{q}_b}{\partial x} = -\xi \left(E - D \right). \tag{3.15}$$

Additionally, following Sriariyawat (2009) the bed diffusion term, i.e. the second one at right-hand side of Eq. (3.14), is treated as a source term (see also § 3.5) and therefore moved to the right-hand side of Eq. (3.15). Starting from

$$\frac{\partial z_b}{\partial t} + \xi \frac{\partial q_b}{\partial x} - \xi \frac{1}{\tan \phi} \frac{\partial \left(|q_b| \frac{\partial z_b}{\partial x} \right)}{\partial x} = -\xi \left(E - D \right), \tag{3.16}$$

where ϕ is assumed independent of x, the bed evolution equation now reads

$$\frac{\partial z_b}{\partial t} + \xi \frac{\partial q_b}{\partial x} = \xi \left(\frac{1}{\tan\phi} \frac{\partial \left(|q_b| \frac{\partial z_b}{\partial x} \right)}{\partial x} - (E - D) \right). \tag{3.17}$$

Note that the bed diffusion term in Eq. (3.14) differs from that used by Dodd et al. (2008) and Sriariyawat (2009), as they considered the bed change from the initial bathymetry instead of the bed level in the spatial derivative. Thus their formulation for the modified instantaneous bed-load transport is

$$\tilde{q}_b = q_b - \frac{1}{\tan\phi} |q_b| \frac{\partial b}{\partial x}, \tag{3.18}$$

where $b(x,t) = z_b(x,t) - z_b(x,0)$. They and other previous workers (see Falques et al., 1996; Garnier, 2006; Garnier et al., 2008, and references therein) focussed on the study of the evolution of two-dimensional bed patterns, i.e. beach cusps, long-shore / oblique / transverse bars and rip channels. They were predominantly interested in the development of these morphodynamic features in both the cross- and along-shore directions and in particular in the analysis of the deviation from the initial bed profile, which they assumed to be an equilibrium one. Therefore they removed the contribution of the initial bed level from the bed diffusion term.

In the present work it is acknowledged that considering z_b rather than b allows a more general formulation, which is more appropriate for example if no assumption is possible on the initial bathymetry, hence Eq. (3.14) is the preferred option. However, the simulations for the morphodynamic beach evolution at storm time-scale (see § 7) are performed using Eq. (3.18). This choice is justified by the assumption of the initial equilibrium profile, which is perturbed by the storm wave action, and by the required consistency with the previous works of Dodd et al. (2008) and Sriariyawat (2009), which are used for result comparison.

3.4.3 Infiltration

The effects of infiltration are included following the approach of Dodd et al. (2008). This considers only water percolating into the beach (i.e. no exfiltration) and a static water table, which means that no groundwater motion is modelled. Additionally, after each swash event the infiltration wedge is discarded, therefore water is not conserved. This approach aims at keeping the present model effective but simple, i.e. able to capture the main physical aspects while using a simplified description of the processes within the beach. It is acknowledged for example that Steenhauer et al. (2012b) recently developed a hydrodynamic only solver with a complex subsurface flow module (comprising infiltration, exfiltration, horizontal pore-air movement and horizontal groundwater flow) and achieved numerical predictions in good agreement with the laboratory experiments of Steenhauer et al. (2011). Their findings suggest for instance that the inclusion of exfiltration in the present model would require to be part of a more comprehensive and detailed subsurface flow description, which appears not straightforward because of the further challenges due to the morphodynamic problem (e.g. the time dependent bed level) and possibly an additional source of uncertainties in the result interpretation.

Dodd et al. (2008) approach is based on the Darcy resistance law, following the original work of Packwood (1983). The infiltration velocity w_{inf} (positive downward) is determined from the equation

$$w_{inf} = p_b \frac{\partial \zeta}{\partial t} = k_{inf} I = k_{inf} \left(1 + \frac{h}{\zeta} \right), \tag{3.19}$$

where ζ is the local infiltration depth, k_{inf} the hydraulic conductivity of the sediment and I the hydraulic gradient. In the last right-hand side of Eq. (3.19), I is expressed as a function of h and ζ, where h assumes the role of a local pressure head, which drives the infiltration process.

In the case of higher infiltration rates for a coarser sediment, the Darcy flow

regime is no longer appropriate and should be replaced by the Forchheimer one (see Burcharth & Andersen, 1995, among others), which allows the hydraulic gradient to be expressed by

$$I = a_{inf} w_{inf} + b_{inf} w_{inf}^2, \tag{3.20}$$

where a_{inf} and b_{inf} are the linear and quadratic Forchheimer coefficients respectively. It is acknowledged that in Eq. (3.20) an absolute value should appear in the quadratic term, i.e. it should be $b_{inf} w_{inf} |w_{inf}|$, and that an inertia term should be added because of the unsteady flow (see Burcharth & Andersen, 1995). However the former is removed as infiltration only is modelled in the present study, while the latter is neglected following Steenhauer et al. (2012b) approach, which proved to lead to good numerical results against laboratory measurements. Following Steenhauer et al. (2012a), Eq. (3.20) can be rearranged to obtain w_{inf} as a function of I. Hence, keeping $I = (1 + h/\zeta)$ and considering the Forchheimer law instead of the Darcy one, the analogous of Eq. (3.19) is

$$w_{inf} = p_b \frac{\partial \zeta}{\partial t} = \frac{1}{2 b_{inf}} \left(\sqrt{a_{inf}^2 + 4 \left(1 + \frac{h}{\zeta} \right) b_{inf}} - a_{inf} \right). \tag{3.21}$$

Because of the expression of I, both Eqs. (3.19) and (3.21) are singular at the beginning of the infiltration process, as initially $\zeta = 0$. A possible way to overcome this singularity in the first integration step is provided in Appendix B, following Dodd et al. (2008) for Eq. (3.19), while a new approximation is derived for Eq. (3.21).

In the present model, infiltration is assumed to produce no alteration on the bottom friction description and on the sediment transport formulae. Its effects are explicitly taken into account as losses of water mass and momentum, thus influencing the sediment transport through the hydrodynamics and causing additional settling of suspended sediment (see § 3.5).

3.5 Combined load system of conservation laws

After the introduction of the additional physical aspects, it is worth restating all the equations solved by the present model. They constitute a system of conservation laws with source terms, which are

$$\frac{\partial h}{\partial t} + \frac{\partial hu}{\partial x} = -w_{inf}, \tag{3.22}$$

$$\frac{\partial hu}{\partial t} + \frac{\partial}{\partial x}\left(hu^2 + \frac{1}{2}gh^2\right) = S_g + S_f - u\,w_{inf}, \tag{3.23}$$

$$\frac{\partial z_b}{\partial t} + \xi\frac{\partial q_b}{\partial x} = \xi\,(S_b - S_s) + \xi\,c\,w_{inf}, \tag{3.24}$$

$$\frac{\partial hc}{\partial t} + \frac{\partial huc}{\partial x} = S_s - c\,w_{inf}. \tag{3.25}$$

The meaning of the new symbols at right-hand sides is provided below:

$$S_g = -gh\frac{\partial z_b}{\partial x}, \tag{3.26}$$

$$S_f = -\frac{\tau_b}{\rho_w}, \tag{3.27}$$

$$S_b = \frac{1}{\tan\phi}\frac{\partial\left(|q_b|\frac{\partial z_b}{\partial x}\right)}{\partial x}, \tag{3.28}$$

$$S_s = E - D. \tag{3.29}$$

Eqs. (3.26)–(3.29) are the geometric, friction, bed diffusion and suspended sediment source terms in the order. Besides, at right-hand sides of Eqs. (3.22)–(3.25) there are four additional source terms which stem from the inclusion of infiltration in the model, which explicitly depend on w_{inf}.

Finally, Eqs. (3.22)–(3.25) are also referred to as the combined load system, as it considers both bed- and suspended load, consistently with the previous work of Zhu (2012) and Zhu & Dodd (2015). A sketch of the variables involved in a generic morphodynamic swash event is provided in Fig. 3.2 for convenience.

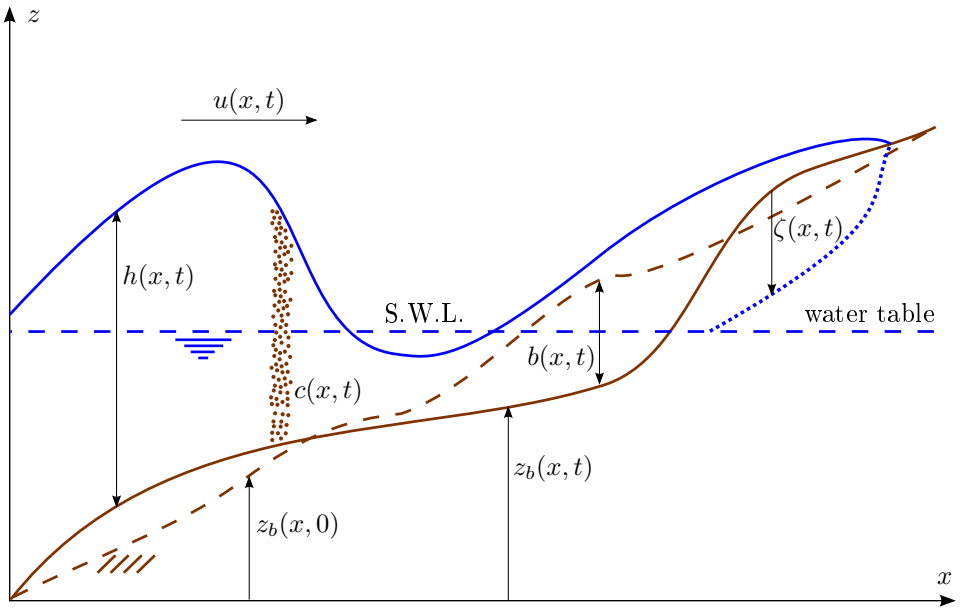

Figure 3.2: Sketch of the variables involved in a generic morphodynamic swash event.

Chapter 4

Numerical solver

4.1 Introduction

Before proceeding to the numerical solver details, it is convenient rewriting Eqs. (3.22)–(3.25) in the following more compact (vectorial) form:

$$\frac{\partial \mathbf{W}}{\partial t} + \frac{\partial \mathbf{F}(\mathbf{W})}{\partial x} = \mathbf{S} + \mathbf{S}_{inf}, \tag{4.1}$$

where

$$\mathbf{W} = \left[h, hu, z_b, hc\right]^T, \tag{4.2}$$

$$\mathbf{F} = \left[hu, \frac{(hu)^2}{h} + \frac{1}{2}gh^2, \xi q_b, \frac{(hu)\,(hc)}{h}\right]^T, \tag{4.3}$$

$$\mathbf{S} = \left[0, S_g + S_f, \xi\left(S_b - S_s\right), S_s\right]^T, \tag{4.4}$$

$$\mathbf{S}_{inf} = \left[-w_{inf}, -u\,w_{inf}, \xi\,c\,w_{inf}, -c\,w_{inf}\right]^T, \tag{4.5}$$

which are the vectors of conserved variables (unknowns), of fluxes, of source terms and of infiltration-related source terms in the order.

The choice of splitting into two different vectors the infiltration-related source terms and the non-infiltration-related ones, i.e. $\mathbf{S}_{inf}$ and $\mathbf{S}$ respectively, is justified by the different adopted solving procedures. The non-infiltration-

related source terms are solved with the left-hand side part of System (4.1) through the fully-coupled TVD-MCC scheme. Then the effects of infiltration are computed separately at the end of each time step, following the approach of Dodd et al. (2008).

This approach proved to be far more robust than that of including $\mathbf{S}_{inf}$ inside the TVD-MCC scheme. Actually, some attempts at a simultaneous solution of the whole System (4.1) were carried out but the model often crashed or returned non-physical results. For example it sometimes happened that a cell with initial very shallow water became dry after the predictor step, leading to the computation of spurious negative water depth values in the following corrector one (see § 4.2 for the definition of the predictor and corrector stages). Additionally, it is noted that the infiltration process is faster at the beginning and then slows down increasingly with time because of the growing infiltration depth. Therefore numerical problems are somehow to be expected when the swash lens is thinner and in particular in the vicinity of the shoreline during the run-up phase. In the light of these points, the separated computation of the infiltration effects is implemented in the present model.

In this chapter, the TVD-MCC scheme of Briganti et al. (2012a) is recalled in § 4.2 for convenience, then the development of the numerical aspects is discussed in § 4.3.

4.2 TVD-MCC from Briganti et al. (2012a)

The TVD-MCC scheme consists of three steps:

$$\mathbf{W}_m^{pr} = \mathbf{W}_m^n - \frac{\Delta t}{\Delta x}\left(\mathbf{F}_{m+1}^n - \mathbf{F}_m^n\right) + \Delta t\,\mathbf{S}_{m+1/2}^n, \tag{4.6}$$

$$\mathbf{W}_m^{cr} = \mathbf{W}_m^n - \frac{\Delta t}{\Delta x}\left(\mathbf{F}_m^{pr} - \mathbf{F}_{m-1}^{pr}\right) + \Delta t\,\mathbf{S}_{m-1/2}^{pr}, \tag{4.7}$$

$$\mathbf{W}_m^{n+1} = \frac{1}{2}(\mathbf{W}_m^{pr} + \mathbf{W}_m^{cr}) + \left(\mathbf{D}_{m+1/2}^n - \mathbf{D}_{m-1/2}^n\right), \tag{4.8}$$

where $\mathbf{D}$ is the TVD-function vector. n and m identify the values at the generic time step n at a certain cell m, while pr and cr indicate the predictor and the corrector stages in the order. Δt and Δx are the time and spatial steps respectively.

The numerical domain of length L_x is divided in M cells of equal width Δx, so that $L_x = M\Delta x$. Values of the variables are considered stored at cell centres, i.e. at $x = (m-1/2)\Delta x$ with $m \in [1, \ldots, M]$, where piecewise constant states for the unknowns are assumed.

Note that the TVD-MCC is a hybrid scheme, as the original MCC is a finite difference scheme while the TVD-function needs the knowledge of quantities at numerical cell interfaces (as a typical finite volume solver). Thus, it is more convenient to refer to a finite volume domain division in cells assuming their centres coincident with the nodes in the finite difference framework.

Neither suspended sediment transport nor bed diffusion are modelled. Therefore, the geometric and friction source terms, i.e. S_g and S_f, are approximated in Eqs. (4.6) and (4.7) as

$$S_{g,m+1/2} = -\frac{g}{2\Delta x}\left(h_m + h_{m+1}\right)\left(z_{b,m+1} - z_{b,m}\right) \text{ and} \tag{4.9}$$

$$S_{f,m+1/2} = -\frac{1}{2}\frac{\left(\tau_{b,m} + \tau_{b,m+1}\right)}{\rho_w} = -\frac{\tau_{b,m+1/2}}{\rho_w}. \tag{4.10}$$

The adopted TVD-function $\mathbf{D}$ is

$$\mathbf{D}^n_{m+1/2} = \frac{\Delta t}{2\Delta x}\sum_{k=1}^{3}\left[\left(\bar{\alpha}_k\bar{\Psi}\left(\bar{\lambda}_k\right) - \bar{\beta}_k\,\mathrm{sgn}\left(\bar{\lambda}_k\right)\right)\left(1 - |\bar{\nu}_k|\right)\left(1 - \bar{\Phi}_{mb}\left(\bar{\theta}_k\right)\right)\bar{\mathbf{e}}_k\right]^n. \tag{4.11}$$

Note that in Eq. (4.11) $k = 1, 2, 3$ as a three equation system (NSWEs plus the Exner equation) is used in Briganti et al. (2012a).

In Eq. (4.11) the overbar indicates values at the cell interface $m + 1/2$, where Roe averages are considered (see Briganti et al., 2012a). $\bar{\lambda}_k$ is k-th

eigenvalue and $\bar{\mathbf{e}}_k$ the corresponding right eigenvector of the Jacobian matrix $\widehat{\mathbf{J}}(\mathbf{W})$ of System (4.1), when expressed in the quasi-linear form proposed by Castro Diaz et al. (2008). As first step, System (4.1) is linearised (recall that $\mathbf{S}_{inf}$ is excluded):

$$\frac{\partial \mathbf{W}}{\partial t} + \mathbf{J}(\mathbf{W})\frac{\partial \mathbf{W}}{\partial x} = \mathbf{S}, \tag{4.12}$$

with the Jacobian being the matrix defined by

$$\mathbf{J}(\mathbf{W}) = \frac{\partial \mathbf{F}(\mathbf{W})}{\partial \mathbf{W}} = \begin{bmatrix} 0 & 1 & 0 \\ gh - \frac{(hu)^2}{h^2} & 2\frac{(hu)}{h} & 0 \\ \xi\frac{\partial q_b}{\partial h} & \xi\frac{\partial q_b}{\partial (hu)} & 0 \end{bmatrix}, \tag{4.13}$$

which is apparently singular. This is to be avoided because it could lead to numerical problems (see e.g. Hudson, 2001). Hence the geometric source term is subtracted from both sides of Eq. (4.12), obtaining

$$\frac{\partial \mathbf{W}}{\partial t} + \widehat{\mathbf{J}}(\mathbf{W})\frac{\partial \mathbf{W}}{\partial x} = \mathbf{S} - \mathbf{S}_g, \tag{4.14}$$

where $\widehat{\mathbf{J}}$ is the modified Jacobian, which reads

$$\widehat{\mathbf{J}} = \begin{bmatrix} 0 & 1 & 0 \\ gh - \frac{(hu)^2}{h^2} & 2\frac{(hu)}{h} & gh \\ \xi\frac{\partial q_b}{\partial h} & \xi\frac{\partial q_b}{\partial (hu)} & 0 \end{bmatrix}, \tag{4.15}$$

and $\mathbf{S}_g$ is the vectorial form of the geometric source term, i.e.

$$\mathbf{S}_g = \begin{bmatrix} 0 \\ -gh\frac{\partial z_b}{\partial x} \\ 0 \end{bmatrix}. \tag{4.16}$$

$\bar{\alpha}_k$ is the k-th wave strength, defined by

$$\sum_{k=1}^{3} (\bar{\alpha}_k \bar{\mathbf{e}}_k)^n = \Delta \mathbf{W}^n_{m+1/2}, \text{ with } \Delta \mathbf{W}^n_{m+1/2} = \mathbf{W}^n_{m+1} - \mathbf{W}^n_m, \tag{4.17}$$

and expressed by

$$\bar{\alpha}_k = \frac{\Delta h\left(\bar{\lambda}_j\bar{\lambda}_l - \bar{u}^2 + g\bar{h}\right) + \Delta(hu)\left(2\bar{u} - \bar{\lambda}_j - \bar{\lambda}_l\right) + \Delta z_b\, g\bar{h}}{\left(\bar{\lambda}_k - \bar{\lambda}_j\right)\left(\bar{\lambda}_k - \bar{\lambda}_l\right)}, \tag{4.18}$$

where $j \neq k \neq l$.

$\bar{\beta}_k$ is the k-th wave strength for the source term, determined by

$$\frac{1}{\Delta x}\sum_{k=1}^{3}\left(\bar{\beta}_k\bar{\mathbf{e}}_k\right)^n = \mathbf{S}^n_{*,m+1/2}, \tag{4.19}$$

where the $*$ in $\mathbf{S}^n_{*,m+1/2}$ stands for the choice of which source term to be treated. In Briganti et al. (2012a) the choice is

$$\mathbf{S}^n_{*,m+1/2} = \begin{bmatrix} 0 \\ -S^n_{g,m+1/2} \\ 0 \end{bmatrix}, \tag{4.20}$$

leading to

$$\bar{\beta}_k = \frac{g\bar{h}\Delta z_b\left(2\bar{u} - \bar{\lambda}_j - \bar{\lambda}_l\right)}{\left(\bar{\lambda}_k - \bar{\lambda}_j\right)\left(\bar{\lambda}_k - \bar{\lambda}_l\right)}, \tag{4.21}$$

where $j \neq k \neq l$[1].

Moreover, $\bar{\Psi}\left(\bar{\lambda}_k\right)$ is the entropy correction to $\bar{\lambda}_k$, which is defined as (see Harten & Hyman, 1983; Kermani & Plett, 2001)

$$\bar{\Psi}\left(\bar{\lambda}_k\right) = \begin{cases} |\bar{\lambda}_k| & \text{if } |\bar{\lambda}_k| \geq \delta_k, \\ \delta_k & \text{if } |\bar{\lambda}_k| < \delta_k, \end{cases} \tag{4.22}$$

where δ_k is a non-negative number given by the relationship

$$\delta_k = \max\left(0, \bar{\lambda}_k - \lambda_{k,m}, \lambda_{k,m+1} - \bar{\lambda}_k\right). \tag{4.23}$$

Finally, $\bar{\nu}_k = \bar{\lambda}_k(\Delta t/\Delta x)$ is the local Courant Number and $\bar{\Phi}(\bar{\theta}_k)$ is the flux limiter. In Briganti et al. (2012a) the Minmod (or Minbee) flux limiter is

[1]There appears to be a misprint in Briganti et al. (2012a), in which the equivalent of Eq. (4.21) reports $\bar{z_b}\Delta h$ instead of $\bar{h}\Delta z_b$

employed:

$$\bar{\Phi}_{mb}(\bar{\theta}_k) = \max\left(0, \min\left(\bar{\theta}_k, 1\right)\right), \tag{4.24}$$

with $\bar{\theta}_k$ being a smoothness ratio defined by

$$\bar{\theta}_k = \frac{\dot{\bar{\alpha}}_k}{\bar{\alpha}_k}, \tag{4.25}$$

where $\dot{\bar{\alpha}}_k$ is evaluated at $\dot{m} = m + 1/2 - \mathrm{sgn}\left(\bar{\lambda}_k\right)$.

4.3 Model development

The original numerical solver of Briganti et al. (2012a) represents the starting point of this work. From the implementation viewpoint, the Fortran code is largely reworked, optimised in terms of coding (e.g. the use of modules is introduced), precision (i.e. double precision is adopted) and performance (i.e. reduced computational time is achieved, also through a more efficient subroutine structure).

From the numerical standpoint, because of the additional physical aspects introduced in § 3.4, the model is modified to include the suspended sediment transport equation and the bed diffusion source term. Therefore, the TVD-MCC scheme is applied to all four equations of the combined load System (4.1), $\mathbf{S}_{inf}$ excluded, and the TVD-function $\mathbf{D}$ changed accordingly. Details are provided in § 4.3.1.

Additionally, the model now accounts for the infiltration effects, following Dodd et al. (2008), through the approach described in § 4.3.2.

Besides, boundary conditions (hereinafter BCs) are considered. In swash zone simulations, there are two different external boundaries. On the seaward side, it is required to consistently treat the open boundary which confines the numerical domain, while, on the landward direction, a specific approach for the moving shoreline, i.e. the wet / dry front, is needed.

The chosen location of the seaward boundary is often a matter of computational cost and area of interest, but can be also limited by the applicability of the equations (e.g. validity of the shallow water assumption) and by possible lack of knowledge, for example missing information for evolving bed level and / or sediment concentration therein.

New absorbing-generating seaward BCs for fully-coupled hydro-morphodynamical numerical solvers, the Riemann Equation BCs or REBCs, are derived for the frictionless bed-load only system (see Incelli et al., 2015a). They are presented in detail in § 8, along with the corresponding validation tests. However Incelli et al. (2015a) demonstrated that the REBCs cannot cope with strong morphodynamic bores. Furthermore, they are for the frictionless case only and do not include bed diffusion. These observations prevent from using them in the tests from previous literature which are presented in §§ 5 and 7. As the seaward BCs are often test-specific, they are indicated together with each test settings later.

The original shoreline boundary approach from Briganti et al. (2012a) was found not to be sediment conservative (see later § 4.3.3). However, the results published in Briganti et al. (2012a), and also in Briganti et al. (2012b), involve short simulations only, like single swash events, where this issue has substantially no effect on the solutions. Aiming at employing the model for simulations at the storm time-scale, different shoreline BCs are adopted in this work. They follow the approach of Hubbard & Dodd (2002), which was used by Dodd et al. (2008) and Sriariyawat (2009) in the study of beach cusp formation, i.e. in mid-term morphodynamical simulations (see § 4.3.3 for more details).

Finally, with reference to the computational domain described in § 4.2, note that in this work the seaward boundary is always located at the left edge of

the domain and the corresponding conditions are applied to an external cell, cell 0, to the left of the first inner one, cell 1. Besides, the domain length is usually designed in order to keep the wet / dry front within it, so that the rightmost cell, cell M, is never wet. However, if water is present at the right edge of the domain, the right BCs are applied to another external cell, cell $M+1$, located to the right of cell M.

4.3.1 Combined load TVD-MCC

The TVD-MCC scheme, i.e. Eqs. (4.6)–(4.8), is applied to System (4.1), $\mathbf{S}_{inf}$ excluded. In Eqs. (4.6) and (4.7) the bed diffusion and suspended sediment source terms, i.e. S_b and S_s, are approximated as follows:

$$S_{b,m+1/2} = \frac{(S_{bed,m+1} - S_{bed,m})}{\Delta x} \text{ and} \tag{4.26}$$

$$S_{s,m+1/2} = E_{m+1/2} - D_{m+1/2}, \tag{4.27}$$

with

$$S_{bed,m} = \frac{|q_{b,m}|}{\tan\phi} \frac{z_{b,m+1} - z_{b,m-1}}{2\Delta x}, \tag{4.28}$$

$$E_{m+1/2} = m_e \left(\frac{|\tau_{b,m+1/2}| - \tau_{crs}}{\tau_{rep}} \right), \tag{4.29}$$

$$D_{m+1/2} = w_s \frac{c_m + c_{m+1}}{2}. \tag{4.30}$$

Note that $\tau_{b,m+1/2}$ is defined in Eq. (4.10).

The new TVD-function $\mathbf{D}$ for four equations is

$$\mathbf{D}^n_{m+1/2} = \frac{\Delta t}{2\Delta x} \sum_{k=1}^{4} \left[\left(\bar{\alpha}_k \bar{\Psi}\left(\bar{\lambda}_k\right) - \bar{\beta}_k \operatorname{sgn}\left(\bar{\lambda}_k\right) \right) \left(1 - |\bar{\nu}_k|\right) \left(1 - \bar{\Phi}\left(\bar{\theta}_k\right)\right) \bar{\mathbf{e}}_k \right]^n, \tag{4.31}$$

where now $k = 1, 2, 3, 4$.

The new Jacobian, again following Castro Diaz et al. (2008) approach and accounting for the suspended sediment transport, is

$$\widehat{\mathbf{J}} = \begin{bmatrix} 0 & 1 & 0 & 0 \\ gh - \frac{(hu)^2}{h^2} & 2\frac{(hu)}{h} & gh & 0 \\ \xi\frac{\partial q_b}{\partial h} & \xi\frac{\partial q_b}{\partial (hu)} & 0 & 0 \\ -\frac{(hu)(hc)}{h^2} & \frac{(hc)}{h} & 0 & \frac{(hu)}{h} \end{bmatrix}, \tag{4.32}$$

where the partial derivatives of q_b are required. Their expressions depend on the chosen bed-load transport formula and on the adopted bottom friction approach. While those for the Grass formula and for the MPM one using the Chézy approach are analytical (see e.g. Briganti et al., 2012a), those for the MPM formula with the BBL solver are not, as τ_b is no more an explicit function of the conserved variables. Direct numerical computation of these derivatives was initially implemented through a first order scheme. For example, the partial derivative of q_b with respect to h was approximated as

$$\left.\frac{\partial q_b}{\partial h}\right|_{m+1/2} \simeq \frac{q_{b,m+1} - q_{b,m}}{h_{m+1} - h_m}. \tag{4.33}$$

However this approach was found to cause an excess of noise in the results, hence a different procedure is adopted. The τ_b value provided by the BBL solver is used to calculate a local instantaneous friction coefficient, i.e.

$$f_c = \frac{2\,|\tau_b|}{\rho_w\, u^2}, \tag{4.34}$$

which is then substituted in the derivatives of Eq. (3.8), the same for the Chézy approach and recalled below for convenience:

$$\frac{\partial q_b}{\partial h} = -12.0\; f_c \frac{u|u|}{h}\; \left[\frac{d_{50}\,(\theta - \theta_{crb})}{g(s_{rel} - 1)}\right]^{1/2} \text{ and} \tag{4.35}$$

$$\frac{\partial q_b}{\partial hu} = 12.0\; f_c \frac{|u|}{h}\; \left[\frac{d_{50}\,(\theta - \theta_{crb})}{g(s_{rel} - 1)}\right]^{1/2}, \tag{4.36}$$

both for $\theta > \theta_{crb}$.

The eigenvalues of the new Jacobian, i.e. Eq. (4.32), are the same of $\widehat{\mathbf{J}}$ in Eq. (4.14), plus $\lambda_4 = u$. The corresponding right eigenvectors are

$$\mathbf{e}_k = \begin{bmatrix} 1 \\ \lambda_k \\ \frac{(\lambda_k - u)^2}{gh} - 1 \\ c \end{bmatrix} \tag{4.37}$$

for $k = 1, 2, 3$ and

$$\mathbf{e}_4 = \begin{bmatrix} 0 \\ 0 \\ 0 \\ 1 \end{bmatrix}. \tag{4.38}$$

Again Roe averages are used at cell interfaces $m + 1/2$ and we define the missing one for concentration as

$$\bar{c} = \frac{c_m\sqrt{h_m} + c_{m+1}\sqrt{h_{m+1}}}{\sqrt{h_m} + \sqrt{h_{m+1}}}. \tag{4.39}$$

Because of the new eigenstructure, the k-th wave strength is

$$\bar{\alpha}_k = \frac{\Delta h\left(\bar{\lambda}_j\bar{\lambda}_l - \bar{u}^2 + g\bar{h}\right) + \Delta(hu)\left(2\bar{u} - \bar{\lambda}_j - \bar{\lambda}_l\right) + \Delta z_b\, g\bar{h}}{\left(\bar{\lambda}_k - \bar{\lambda}_j\right)\left(\bar{\lambda}_k - \bar{\lambda}_l\right)}, \tag{4.40}$$

with $j \neq k \neq l$ for $k = 1, 2, 3$, while

$$\bar{\alpha}_4 = \Delta h(-\bar{c}) + \Delta(hc). \tag{4.41}$$

About the wave strengths for the source terms, firstly it is adopted a different approach from that of Briganti et al. (2012a). It is decided not to consider the geometric source term in the computation of $\bar{\beta}_k$ because it is already included in $\widehat{\mathbf{J}}(\mathbf{W})$, as apparent in Eq. (4.15). In other words, with reference to the NSWEs-Exner equation system considered in Briganti et al. (2012a), in Eq. (4.19) there should be the friction source term only instead of the geometric

one:

$$\mathbf{S}^n_{*,m+1/2} = \begin{bmatrix} 0 \\ S^n_{f,m+1/2} \\ 0 \end{bmatrix} \tag{4.42}$$

and therefore

$$\bar{\beta}_k = \Delta x \frac{\bar{S}_f \left(2\bar{u} - \bar{\lambda}_j - \bar{\lambda}_l\right)}{\left(\bar{\lambda}_k - \bar{\lambda}_j\right)\left(\bar{\lambda}_k - \bar{\lambda}_l\right)}, \tag{4.43}$$

where $j \neq k \neq l$ for $k = 1, 2, 3$.

Secondly, the source terms related to bed diffusion and suspended sediment transport are included as well. As a consequence, the new $\bar{\beta}_k$ are given by

$$\bar{\beta}_k = \Delta x \frac{\bar{S}_f \left(2\bar{u} - \bar{\lambda}_j - \bar{\lambda}_l\right) + \xi \left(\bar{S}_b - \bar{S}_s\right) g\bar{h}}{\left(\bar{\lambda}_k - \bar{\lambda}_j\right)\left(\bar{\lambda}_k - \bar{\lambda}_l\right)}, \tag{4.44}$$

where $j \neq k \neq l$ for $k = 1, 2, 3$, while

$$\bar{\beta}_4 = \Delta x \bar{S}_s. \tag{4.45}$$

Finally, apart from Minmod defined by Eq. (4.24), the following two further flux limiters are considered in this research:

$$\bar{\Phi}_{sb}\left(\bar{\theta}_k\right) = \max\left(0, \min\left(2\bar{\theta}_k, 1\right), \min\left(\bar{\theta}_k, 2\right)\right) \text{ and} \tag{4.46}$$

$$\bar{\Phi}_{vl}\left(\bar{\theta}_k\right) = \frac{|\bar{\theta}_k| + \bar{\theta}_k}{1 + |\bar{\theta}_k|}, \tag{4.47}$$

which are Superbee and van Leer flux limiters respectively (Toro, 1999).

The flux limiter is an automatic tool to detect areas where the solution is smooth, so that the second order accuracy of the scheme is retained, and areas where there are discontinuities, i.e. shocks, so that diffusion is added by reverting the scheme to a first order upwind one, hence avoiding the occurrence of spurious oscillations (see Hudson, 2001, among many others). Sweby (1984) proved that the three above-mentioned flux limiters satisfy the TVD property. These differ in the amount of diffusion they allow near discontinuities, therefore it is interesting to investigate if and how this may affect the numerical results.

4.3.2 Infiltration computation

As anticipated in § 4.1, infiltration effects, expressed by Eq. (4.5), are considered in the model following the approach proposed by Dodd et al. (2008).

After dependent variables have been updated at each time level, Eq. (3.19) or Eq. (3.21) is solved to calculate the new infiltration velocity w_{inf}, in the case of the Darcy or the Forchheimer laws respectively.

Computation is performed only if at that specific cell location the bed level is higher then the water table and if there is actually surface water therein, i.e. the bed is wet.

As both Eqs. (3.19) and (3.21) are singular at the first integration, suitable approximate solutions are reported in Appendix B, under the assumption of linear variation in time of h and ζ during this first integration. For subsequent time steps, the ordinary differential equation in ζ is solved by means of a Runge-Kutta 4^{th} order explicit scheme. Note that, in theory, the pressure head h reduces as the infiltration depth ζ increases, but this correction is neglected during the integration, following Dodd et al. (2008).

Once w_{inf} value has been updated, the water mass and momentum losses are subtracted from the hydrodynamic variables before the next simultaneous solution. When the suspended sediment transport is considered, the infiltration causes additional deposition, which is quantified equal to $\xi\, c\, w_{inf} \Delta t$.

A simple test was designed to investigate if the infiltration implementation could affect the conservation of an initial quiescent flow state. This test considered a uniform water depth over a permeable uniform bed. The results (not shown) confirm that no spurious oscillation is generated in the water surface level and velocity profiles during the infiltration process.

4.3.3 Shoreline BCs

The shoreline BCs involve the treatment of the wet / dry front, which is a characterising feature of swash zone simulations.

Briganti et al. (2012a) proposed a simple shoreline treatment which consists of a wetting-dry-cell algorithm and uses a ghost cell landward of the last wet one (see Fig. 4.1).

It is well-known that artificial wetting of the bed alters the wave structure at the shoreline, generating an additional bore at the front in place of the theoretically expected contact discontinuity (see Toro, 2001; Brocchini & Baldock, 2008). However, this procedure allows numerical schemes to perform well (see e.g. Sriariyawat, 2009) and it is straightforward to be implemented.

Briganti et al. (2012a) treatment includes the definition of a minimum water depth parameter (h_{min}), which has to be close to zero. With reference to Fig. 4.1, when the water surface level at cell $m-1$ exceeds the bed one at cell m, i.e. $z_{b,m-1} + h_{m-1} > z_{b,m}$, at the beginning of the new time step the first dry cell (i.e. cell m) is primed with $h = h_{min}$. At the next dry cell $m+1$ the ghost cell is introduced with $h_{m+1} = h_{min}$, $u_{m+1} = 0$ ms^{-1} and $z_{b,m+1} = z_{b,m}$. Consequently, when the predictor step, i.e. Eq. (4.6), is applied to cell m, it is obtained that $\mathbf{W}_m^{pr} = \mathbf{W}_m^n$. On the other hand, when it is $z_{b,m-1} + h_{m-1} < z_{b,m}$ and the flow is still advancing rightward, no new cell is flooded. As it is possible that $u_{m-1} \neq 0$ ms^{-1}, this can cause non-zero fluxes at the shoreline boundary. This issue, while negligible in short simulations, is deemed to be unacceptable for mid-term ones.

Therefore a different shoreline boundary treatment is adopted in this work and is based on that of Hubbard & Dodd (2002). It consists of a wetting / drying algorithm and a zero-flux condition at the wet / dry front.

The shoreline is again identified on the basis of the minimum water depth

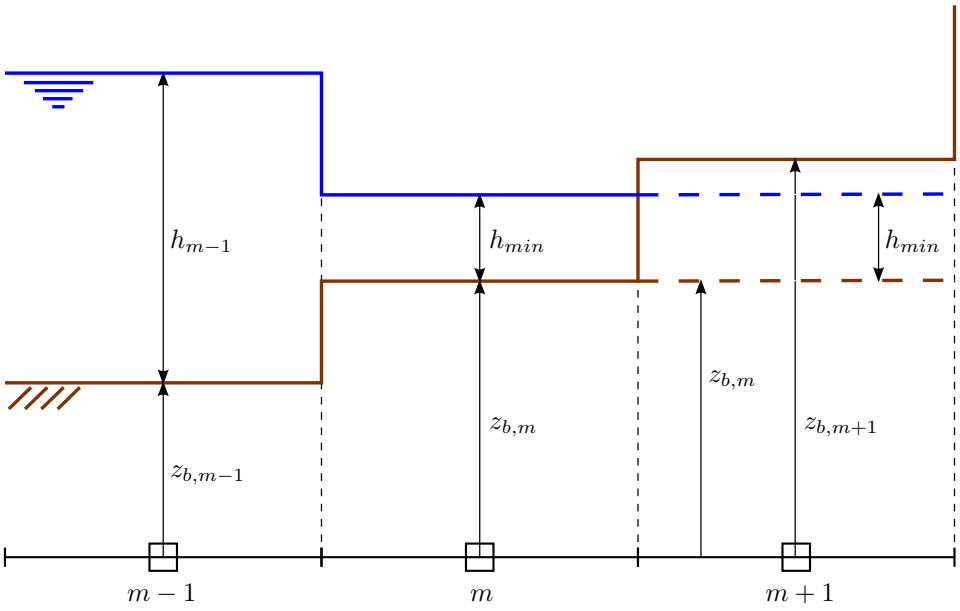

Figure 4.1: Shoreline BCs (from Fig. 2 at page 864 of Briganti et al., 2012a). Sketch of the previous treatment.

parameter h_{min}. At the beginning of each integration, the wetting procedure is operated. Starting from the seaward boundary, the last wet cell is identified as that where $h_m \geq h_{min}$, while $h_{m+1} < h_{min}$, i.e. $m+1$ is assumed to be the first dry cell. The latter is flooded with $h_{m+1} = h_{min}$ and u_{m+1} is set to 0 ms^{-1}, only if $h_m + z_{b,m} - z_{b,m+1} \geq h_{min}$. This restriction becomes less important as a smaller h_{min} is adopted, plays a minor role when bores are considered, because of their steep fronts, and helps to prevent possible non-physical oscillations at the shoreline, for example avoiding that water surface at the flooded cell is higher than that at the next wet one. When suspended sediment transport is included in the simulation, $c_{m+1} = 0$ $\mathrm{m}^3\mathrm{m}^{-3}$.

At the end of the integration, after dependent variables have been updated and infiltration effects, if present, applied, the drying procedure is performed. Where the water depth is below h_{min}, the water depth and momentum are reset to zero. In the case of suspended sediment transport, the suspended load

at a dried cell is assumed instantaneously deposited, increasing the bed level therein. Besides, note that this drying procedure overcomes the issue about the non-receding shoreline in the backwash phase when the bottom friction is modelled through the Chézy approach (for a detailed analysis see Antuono et al., 2012).

The zero-flux condition at wet / dry front is ensured resetting to zero the momentum at the last wet cell every time step. Additionally, to ensure conservation, no TVD-function $\mathbf{D}$ is computed at wet / dry interface (i.e. at $m + 1/2$), otherwise it should count for the dry cell as well, where no modification of variables is apparently acceptable.

Note that Dodd et al. (2008) considered a secondary threshold (an order of magnitude bigger than h_{min}), below which water is not dynamically active, i.e. velocity is reset to zero. This threshold is not used here, following the same choice of Sriariyawat (2009), except when results of the present model are compared with those of Dodd et al. (2008) to retain consistency (see § 7.2.1).

The TVD-MCC scheme is able to preserve the quiescent flow state when there are only wet / wet boundaries, e.g. in river flow simulations (see Hudson, 2001). When a wet / dry boundary is present, the numerical discretization and the approach with the minimum water depth parameter may cause spurious oscillations therein, due to the fact that the actual shoreline position is necessarily forced to fit into the cell grid. Therefore a fictitious bed level is considered at the first dry cell $m + 1$ (see Fig. 4.2), equal to $z_{b,m} + h_m$, in order to perfectly balance the momentum equation, i.e. Eq. (3.3), when the predictor step is applied at cell m.

A simple test involving still water in front of a slope beach was carried out and the results (not shown) confirm that the present treatment for the shoreline BCs is able to preserve the quiescent flow state (see also § 5.4.1).

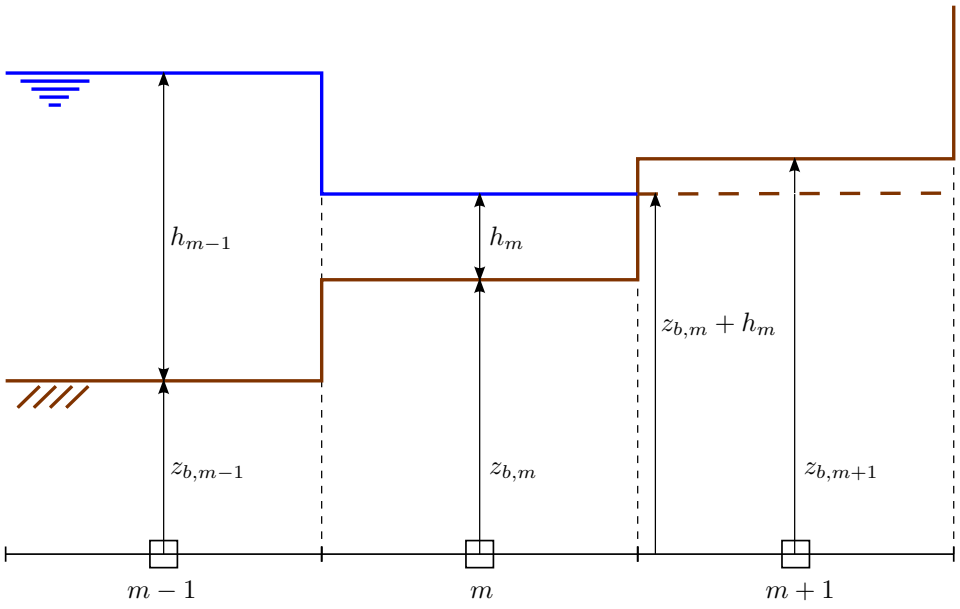

Figure 4.2: Shoreline BCs. Sketch of the present treatment.

Chapter 5

Validation tests

5.1 Introduction

As described in §§ 3 and 4, the model is modified substantially with respect to the original one of Briganti et al. (2012a), e.g. in the numerical implementation. Therefore this chapter examines the performance of the improved version against several validation tests, which generally consider simplified equations in comparison with the complete combined load System (4.1). These simplifying assumptions sometimes allow a quasi-analytical solution to be derived, which is a very good benchmark for the computed results. When exact solutions are not available, the model results can be compared with other numerical ones obtained through different solvers. What is more, such a validation approach allows to focus on specific aspects of the hydro-morphodynamical problem and to analyse the model behaviour and response to particular stress cases. Because of the different assumptions, a simplified version of the model is usually required to ensure a meaningful comparison and details are provided for each case in a summarising table on purpose.

This chapter is divided in four sections, one for each validation test con-

sidered. The tests are listed below, together with a brief description and highlighting the reason why they are useful for this research:

- *Fluvial dune test:* the model results are compared with the quasi-analytical solution developed by Hudson & Sweby (2003) for a submerged dune in a fluvial environment; the purpose of this test is to check the behaviour of the model in the case of a test of very long duration, paying particular attention to smearing and diffusive effects.

- *Dam break test:* the model results are compared with the Ritter solution (virtually-fixed bed case) and the Riemann wave solution (mobile bed case), following Kelly & Dodd (2009) and Briganti et al. (2012a); the aim of this test is to evaluate the performance with a fast evolving flow and in presence of a wet / dry front.

- *Uniform bore test:* the model results for the impact of a uniform bore on an erodible slope beach are compared with those obtained with the original one of Briganti et al. (2012a) for the case with bed-load only (see Zhu et al., 2012); then, aiming at a validation for the newly-implemented suspended sediment transport, a case with combined load is presented and results compared with the MOC ones from Zhu (2012). The purpose of this test is to assess the performance in the simulation of a single swash event with both bed- and combined load.

- *Single swash test on fixed slope:* University of Aberdeen laboratory experiments for a single swash event on both impermeable and permeable fixed slopes are reproduced (see Kikkert et al., 2012, 2013, respectively). For the impermeable slope case, the aim is to show how results compare with those obtained with the Weighted Averaged Flux (hereinafter WAF) method by Briganti et al. (2011), using the BBL solver. Beside

this, the permeable slope case help to assess if the adopted simplified approach for the infiltration modelling is able to return the correct order of magnitude of the percolated water and a realistic swash motion, at least on a fixed bed.

Finally, to facilitate comparisons with literature results, some of them are presented in non-dimensional form. Therefore, the following set of non-dimensional variables, which have analogous meanings to the corresponding dimensional ones, is defined:

$$x^* = \frac{x}{h_{rep}}, \tag{5.1}$$

$$t^* = t\sqrt{\frac{g}{h_{rep}}}, \tag{5.2}$$

$$h^* = \frac{h}{h_{rep}}, \tag{5.3}$$

$$u^* = \frac{u}{\sqrt{gh_{rep}}}, \tag{5.4}$$

$$z_b^* = \frac{z_b}{h_{rep}}, \tag{5.5}$$

$$b^* = \frac{b}{h_{rep}}, \tag{5.6}$$

where h_{rep} is the representative scale length for the water depth. This is taken equal to 1 m as it is the common value for all the tests where it is considered, following the previous researchers' choice.

5.2 Fluvial dune test

The fluvial dune test allows to assess the model performance in the case of a slowly varying bed subject to a steady flow for a long duration. The reader is referred to Hudson & Sweby (2003) for details about the developed quasi-analytical solution. Fig. 5.1 shows the initial conditions and the variables involved in this test.

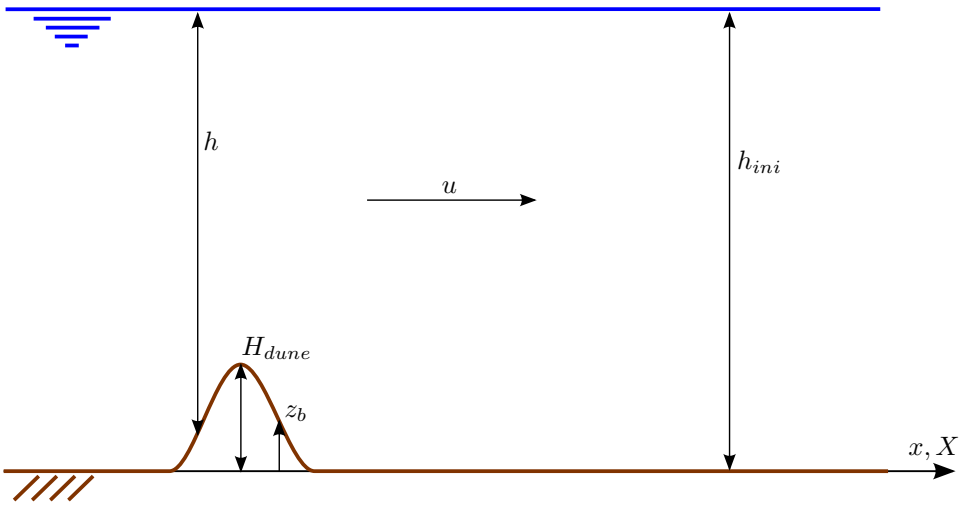

Figure 5.1: Fluvial dune test. Sketch of initial conditions and involved variables.

The initial bed profile $z_b(x = X, t = 0 \text{ s})$ is given by

$$z_b(X,0) = \begin{cases} H_{dune} \ \sin^2\left(\frac{\pi(X-300)}{200}\right) & \text{if } 300 \leq X \leq 500 \text{ m}, \\ 0 & \text{otherwise}, \end{cases} \tag{5.7}$$

where $X \equiv x$ is an auxiliary initial abscissa with origin at the left boundary, while $H_{dune} = 1.0$ m is the maximum height of the dune. The initial water depth is $h(X,0) = h_{ini} - z_b(X,0)$, with $h_{ini} = 10.0$ m. The initial velocity conditions are obtained imposing a constant water discharge (per unit of width), i.e. $q_w = 10 \text{ m}^3\text{s}^{-1}\text{m}^{-1}$, throughout the domain, the length of which is $L_x = 1,000$ m.

This test uses basic free flow BCs, which read

$$\mathbf{W}_0^n = \mathbf{W}_1^n \text{ and} \tag{5.8}$$

$$\mathbf{W}_{M+1}^n = \mathbf{W}_M^n \tag{5.9}$$

at the upstream (left) and downstream (right) boundaries respectively.

All the test settings are chosen equal to those in Kelly & Dodd (2009) and Briganti et al. (2012a) to allow a meaningful comparison. In particular, the solved problem is frictionless and the Grass formula, i.e. Eq. (3.7), is applied with $A_{sed} = 0.001$ s^{2}m^{-1}, consistent with the hypothesis of weak interaction between flow and sediment. No suspended load, bed diffusion or infiltration are considered. The bed porosity p_b is 0.40.

In this test $\Delta x = 4.0$ m and the imposed global Courant Number $CN = 0.80$. Minmod is applied (as in Briganti et al., 2012a) and simulations using Superbee and van Leer are carried out as well. Recall that the flux limiter limiter definitions are given in Eqs. (4.24), (4.46) and (4.47) in the order. A summary of this test assumptions, BCs, physical parameters and numerical settings is provided in Tab. 5.1.

The approximate quasi-analytical solution indicates that the bed profile at a certain time t is equally given by Eq. (5.7) but now $x \neq X$, $t \neq 0$ s and x is computed as follows:

$$x(X,t) = X + \xi\, 3A_{sed}\, q_w^3\, t \times \\ \times \begin{cases} \left(h_{ini} - H_{dune}\, \sin^2\left(\frac{\pi(X-300)}{200}\right)\right)^{-4} & \text{if } 300 \leq X \leq 500 \text{ m}, \\ h_{ini}^{-4} & \text{otherwise.} \end{cases} \tag{5.10}$$

According to Hudson (2001), this solution is valid only until $t \approx 238,079$ s, when the dune breaks (or breakpoint).

Assumptions and BCs	
Friction	not included
Sediment transport	bed-load only (Grass)
Bed diffusion	not included
Infiltration	not included
Upstream BCs	free flow
Downstream BCs	free flow
Physical parameters and numerical settings	
Sediment mobility parameter (A_{sed})	0.001 s^{2}m^{-1}
Bed porosity (p_b)	0.40
Domain length (L_x)	$1,000$ m
Spatial step size (Δx)	4.0 m
Courant Number (CN)	0.80
Duration of the simulations	$250,000$ s

Table 5.1: Fluvial dune. Assumptions, BCs, physical parameters and numerical settings.

Fig. 5.2 shows the numerical results, using Minmod, Superbee and van Leer, compared with the quasi-analytical solution at the breakpoint time. Using Minmod the overall agreement is good, even though the top of the dune is now lowered and smeared showing no more the instability displayed in Fig. 3 at page 865 of Briganti et al. (2012a). Due to the simplified assumptions for this test, it can be stated that the difference in the results is a consequence of the adopted new approach for the wave strengths for the source terms (i.e. $\bar{\beta}_k$). In fact, as the geometric source term is no longer considered in them, in contrast with Eq. (4.21), and being the problem frictionless, herein simply $\bar{\beta}_k = 0$ for $k = 1, 2, 3$.

Using Superbee instead of Minmod, it is apparent that the agreement improves noticeably, both at the top and at the toe of the dune at lee side. This

is consistent with the former being less diffusive than the latter (Toro, 1999). Note also that the results with Superbee exhibit a lag in the toe location, in opposition to what showed by those with Minmod. Adopting van Leer, results show an intermediate level of smearing of the top of the dune between those obtained applying the other two. Moreover, the toe of the dune at lee side appears to be the closest to the quasi-analytical solution.

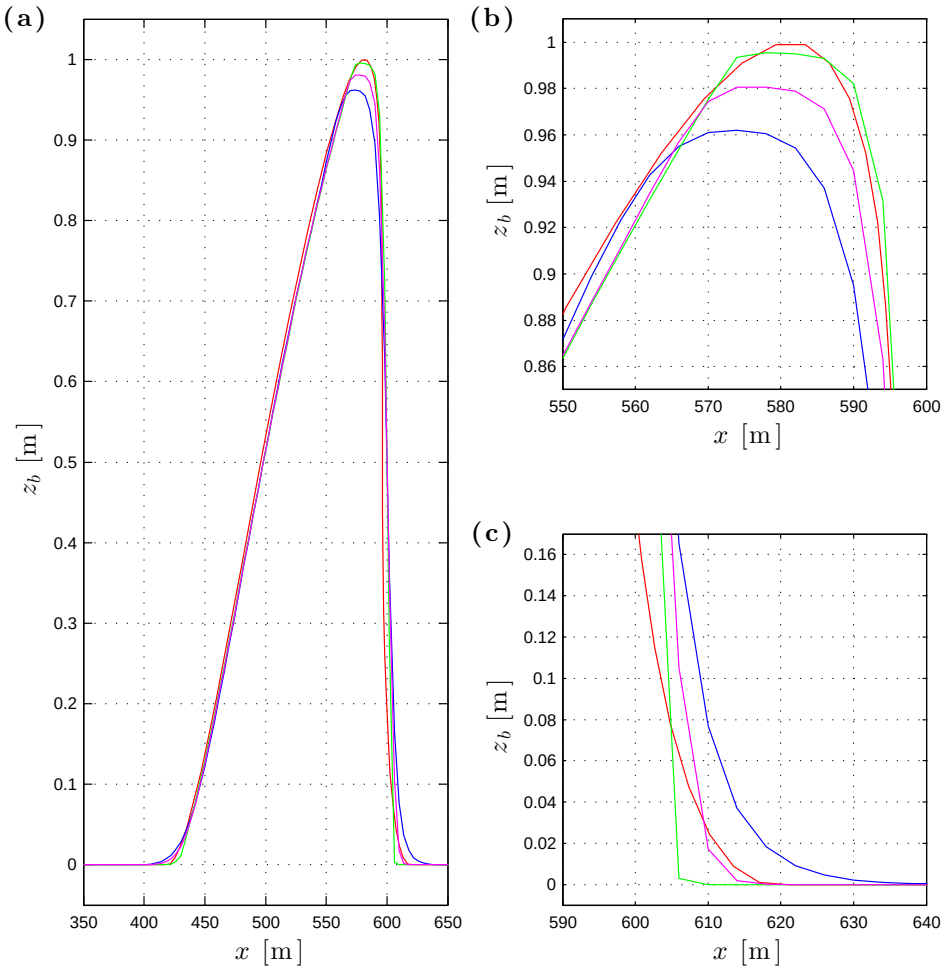

Figure 5.2: Fluvial dune. Dune profile at the breakpoint time. Reference solution and model results with different flux limiters. (a): final dune whole profile. (b): detail of the top of the final dune. (c): detail of the toe of the final dune at lee side. Solid lines: quasi-analytical solution (red); model results with Minmod (blue), Superbee (green) and van Leer (magenta) respectively.

5.2.1 Concluding remarks

To summarise, all three considered flux limiters yield results in good agreement with the quasi-analytical solution derived by Hudson & Sweby (2003). In particular, results with Superbee present a very accurate profile of the top of the dune at breakpoint time while those with van Leer display the best matching for the toe at lee side.

This seems to indicate that Minmod would be less accurate in longer simulations because exceedingly diffusive. It is acknowledged that this test is demanding because of its noticeable duration, however note that other aspects are less challenging from the hydro-morphodynamical viewpoint (e.g. the steady flow and the relatively high water depth compared with the bed changes). Additionally, aiming at minimising the occurrence of spurious oscillations, Hudson (2001) suggested Minmod to be generally the most robust and accurate flux limiter.

As a consequence, all three limiters are considered in the initial stage of the study of the mid-term beach evolution in § 7 in order to check their possible influence on the morphodynamic change.

5.3 Dam break test

The dam break test gives the possibility to assess how the model reacts to rapidly evolving flows in presence of a wet / dry front. Fig. 5.3 shows the initial conditions and the variables involved in this test, along with the generic evolution profiles for the water depth and the bed level when a mobile bed is considered.

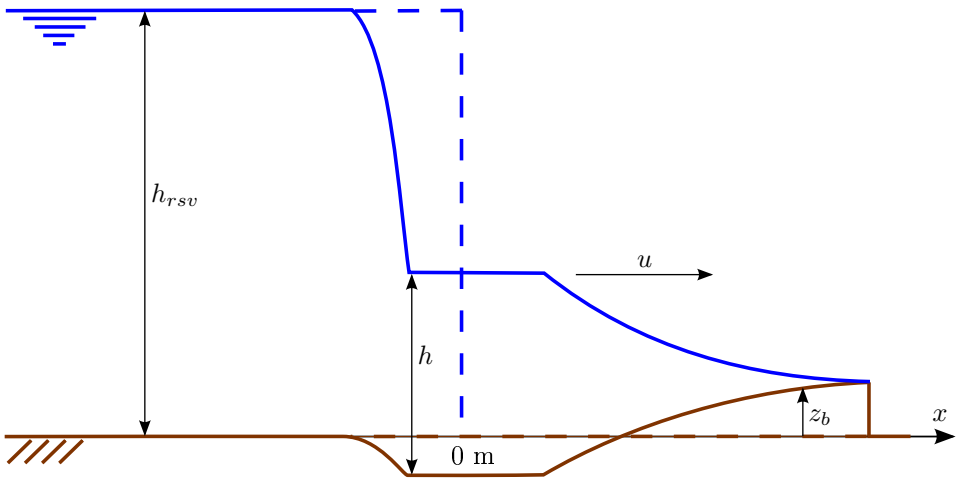

Figure 5.3: Dam break test. Sketch of initial conditions, involved variables and generic evolution profiles for the water depth (h) and the bed level (z_b) in the case of a mobile bed. Dashed lines: initial conditions for h and z_b. Solid lines: generic evolution profiles for h and z_b (mobile bed case).

The dam is modelled as an idealised discontinuity, located at $x = 0$ m, which separates two different regions where constant states for the dependent variables are assumed. On the left there is a reservoir, with initial water depth $h(x < 0 \text{ m}, 0) = h_{rsv} = 1$ m and velocity $u(x < 0 \text{ m}, 0) = 0$ ms^{-1}, while on the right there is no water, i.e. $h(x > 0 \text{ m}, 0) = 0$ m and consequently $u(x > 0 \text{ m}, 0) = 0$ ms^{-1}. The initial bed profile is $z_b(x, 0) = 0$ m. Finally, the domain length is $L_x = 60$ m.

This test uses the basic free flow conditions at the upstream boundary,

which are defined by Eq. (5.8). It is noted that they are dummy ones as the domain is long enough not to let any perturbation reach the upstream boundary within the duration of the simulation. The downstream BCs are the shoreline ones presented in § 4.3.3.

Most of this test settings are chosen equal to those in Briganti et al. (2012a). In particular, the solved problem is frictionless and the Grass formula is applied. Two different cases are considered: the first is a virtually-fixed bed one with $A_{sed} = 10^{-8}$ s^{2}m^{-1} and $p_b = 0$, i.e. a solid bed, while the second is a mobile bed one with $A_{sed} = 0.004$ s^{2}m^{-1} and $p_b = 0.4$. Note that Briganti et al. (2012a) considered $p_b = 0.40$ also for the virtually-fixed bed case, therefore a different benchmark for the results was used there (see later § 5.3.1). No suspended load, bed diffusion or infiltration are included.

In this test $\Delta x = 0.01$ m and $CN = 0.50$. The minimum water depth parameters (h_{min}) are 10^{-5} m for the virtually-fixed bed case and 10^{-4} m for the mobile bed one, following Briganti et al. (2012a), who chose these values because they were the minimum ones still preserving their model stability. Additionally, Minmod is firstly applied and additional simulations with Superbee and van Leer are carried out as well.

Finally, results are presented in non-dimensional form to facilitate comparison with those in Briganti et al. (2012a). Note that the water depth value used as scaling coincides with the reservoir initial one, i.e $h_{rep} = h_{rsv} = 1$ m.

Results for the virtually-fixed and mobile bed cases are presented separately in §§ 5.3.1 and 5.3.2 respectively, while final remarks are drawn in § 5.3.3.

5.3.1 Dam break on virtually-fixed bed

A summary of the present case assumptions, BCs, physical parameters and numerical settings is given in Tab. 5.2.

Assumptions and BCs	
Friction	not included
Sediment transport	virtually only (Grass)
Bed diffusion	not included
Infiltration	not included
Upstream BCs	free flow
Downstream BCs	shoreline
Physical parameters and numerical settings	
Sediment mobility parameter (A_{sed})	10^{-8} s^2m^{-1}
Bed porosity (p_b)	0
Domain length (L_x)	60 m
Spatial step size (Δx)	0.01 m
Courant Number (CN)	0.50
Minimum water depth parameter (h_{min})	10^{-5} / 10^{-6} m
Duration of the simulations	6 s

Table 5.2: Dam break on virtually-fixed bed. Assumptions, BCs, physical parameters and numerical settings. '/' separates alternative values used in the different simulations.

The Ritter solution for rigid (i.e. solid) bed is the analytical benchmark for the virtually-fixed bed case with $p_b = 0$ and it is recalled in Appendix C. As the virtually-fixed case was performed by Briganti et al. (2012a) with $p_b = 0.40$, they used as reference the results obtained through the MOC solver of Kelly & Dodd (2009) with the same bed porosity. However, because of the very small A_{sed} and of the reduced duration of the simulation, differences between the MOC results with $p_b = 0.4$ and the Ritter solution are expected, and actually are, negligible within the level of accuracy herein considered. Hence, the present model performance is directly compared with that reported by Briganti et al. (2012a).

In Fig. 5.4 the model results cannot be distinguished from the analytical solution, except in the vicinity of the wet / dry front (or tip), improving the performance of the original model. Additionally, the present model is stable for one order of magnitude smaller h_{min}/h_{rep} value, i.e. 10^{-6}, which corresponds to $h_{min} = 10^{-6}$ m. The latter appears to represent a standard edge value in fixed bed simulations (see Briganti & Dodd, 2009). The results with the reduced h_{min}/h_{rep} value are provided in Fig. 5.5, showing further enhanced compliance with the Ritter solution compared to that in Fig. 5.4. The mismatch in the tip location is reduced but still important, especially at higher times. The use of Superbee or van Leer has no substantial effect on the results (not reported) or deteriorates them, for example by introducing instabilities in the vicinity of the tip.

Tab. 5.3 shows a quantification of the error in the tip location for the dam break on virtually-fixed bed case, because of the apparent mismatches in wet / dry front location in previous Figs. 5.4 and 5.5. In particular, the non-dimensional (relative) error for the tip position is defined as

$$\epsilon_s(t) = \frac{\Delta x_s(t)}{x_{s,sol}(t)} \times 100, \tag{5.11}$$

where the dimensional (absolute) error $\Delta x_s(t)$ is

$$\Delta x_s(t) = x_{s,num}(t) - x_{s,sol}(t), \tag{5.12}$$

being $x_{s,num}(t)$ and $x_{s,sol}(t)$ the positions of the wet / dry front for the model results and for the reference solution (i.e. the Ritter one) respectively at the specified time t. Values reported in Tab. 5.3 confirm that the tip in the present solver results lags behind that in the reference solution, although the delays at different times is overall greatly reduced with respect to the analogous ones in Tab. I at page 870 of Briganti et al. (2012a). In particular, ϵ_s slightly decreases in absolute value with time for both simulations and is roughly reduced by one third when h_{min}/h_{rep} passes from 10^{-5} to 10^{-6}.

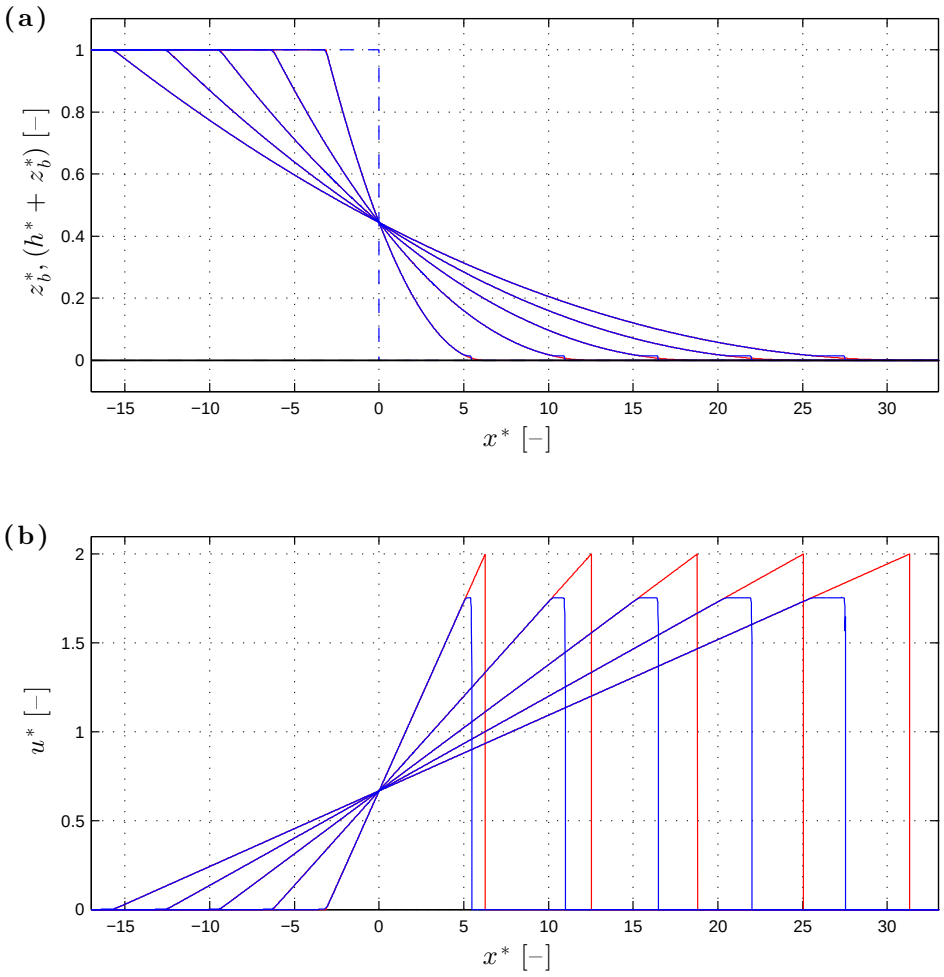

Figure 5.4: Dam break on virtually-fixed bed. Reference solution and model results with $h_{min}/h_{rep} = 10^{-5}$. (a): non-dimensional surface level ($h^* + z_b^*$) and bed level (z_b^*) profiles at $t = 1, 2, 3, 4, 5$ s. Blue and black dashed lines: initial conditions. Solid lines: Ritter solution (red); model results (blue); fixed bed (black). (b): non-dimensional velocity (u^*) profiles at $t = 1, 2, 3, 4, 5$ s. Solid lines: Ritter solution (red); model results (blue).

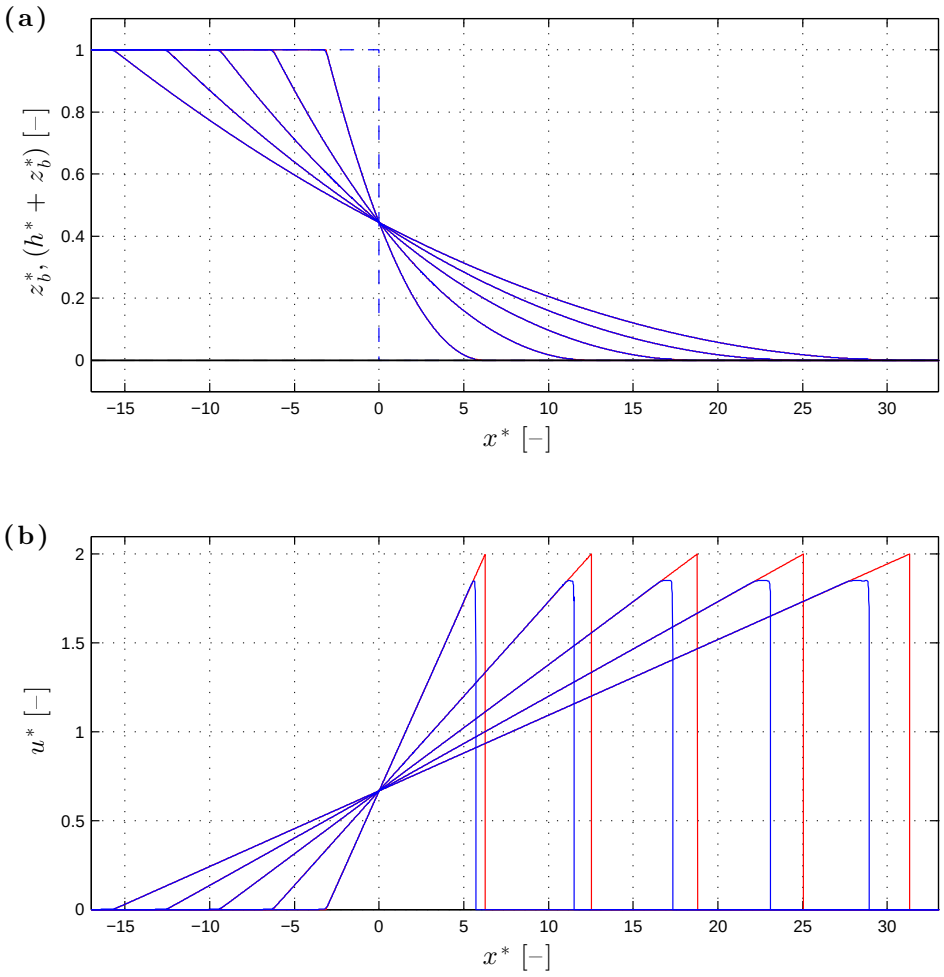

Figure 5.5: Dam break on virtually-fixed bed. Reference solution and model results with $h_{min}/h_{rep} = 10^{-6}$. (a): non-dimensional surface level ($h^* + z_b^*$) and bed level (z_b^*) profiles at $t = 1, 2, 3, 4, 5$ s. Blue and black dashed lines: initial conditions. Solid lines: Ritter solution (red); model results (blue); fixed bed (black). (b): non-dimensional velocity (u^*) profiles at $t = 1, 2, 3, 4, 5$ s. Solid lines: Ritter solution (red); model results (blue).

Error in wet / dry front location				
	Dam break on virtually-fixed bed			
	$h_{min}/h_{rep} = 10^{-5}$		$h_{min}/h_{rep} = 10^{-6}$	
t [s]	ϵ_s [%]	Δx_s [m]	ϵ_s [%]	Δx_s [m]
1	−12.47	−0.780	−8.63	−0.540
2	−12.22	−1.530	−8.06	−1.010
3	−12.19	−2.290	−7.72	−1.450
4	−12.14	−3.040	−7.71	−1.930
5	−12.10	−3.790	−7.60	−2.380

Table 5.3: Dam break on virtually-fixed bed. Error in wet / dry front location.

The improved results of Fig. 5.5 on those of Fig. 5.4 suggest that the delay in the tip location prediction could be related to the adopted treatment of the wet / dry front, and in particular to the choice of the h_{min} value (the smaller the better). However the above-mentioned treatment proved to be robust and takes into account additional constrains required by the morphodynamical problem (see § 4.3.3). With respect to other hydro-morphodynamical solvers, the MOC solution of Kelly & Dodd (2009) shows an excellent agreement with the Ritter one, including in the prediction of the tip location as well. The high accuracy of MOC solvers is well-known (see § 2.2), however they find a limited application to engineering problems because of their usual high computational cost and demanding implementation (see e.g. Briganti & Dodd, 2009).

5.3.2 Dam break on mobile bed

A summary of this case assumptions, BCs, physical parameters and numerical settings is provided in Tab. 5.4.

The reference solution for the mobile bed case is given by a Riemann wave

Assumptions and BCs	
Friction	not included
Sediment transport	bed-load only (Grass)
Bed diffusion	not included
Infiltration	not included
Upstream BCs	free flow
Downstream BCs	shoreline
Physical parameters and numerical settings	
Sediment mobility parameter (A_{sed})	0.004 s^2m^{-1}
Bed porosity (p_b)	0.40
Domain length (L_x)	60 m
Spatial step size (Δx)	0.01 m
Courant Number (CN)	0.50
Minimum water depth parameter (h_{min})	10^{-4} m
Duration of the simulations	6 s

Table 5.4: Dam break on mobile bed. Assumptions, BCs, physical parameters and numerical settings.

solver (see Kelly & Dodd, 2009), which is briefly presented in Appendix C.

In Fig. 5.6 a very good agreement between the Riemann wave solution and the model results is displayed, especially with reference to the rarefaction fans, improving under this aspect previous results presented in Briganti et al. (2012a). Nonetheless, a closer inspection reveals mismatches in the tip location. In particular, while in Briganti et al. (2012a) the numerical tip location lags behind that of the Riemann wave solution, with a reducing delay in time, in the present model results the tip precedes the reference solution, more distinctly for higher times.

Figs. 5.7 and 5.8 show results using Superbee and van Leer respectively. The description of the rarefaction fans remains very good in both simulations.

About the tip location issue, the results with Superbee seem to achieve a better matching with the reference solution, while those with van Leer do not exhibit substantial differences from those using Minmod.

The previous analysis is confirmed in Tab. 5.5, which shows the errors in tip position for the dam break on mobile bed case. Note that in Eqs. (5.11) and (5.12) the $x_{s,sol}(t)$ values are now those of the Riemann wave solution. In contrast to what showed for the virtually-fixed bed case, the present model results return a tip position which is leading the corresponding reference solution one, apart from $\epsilon_s(t = 1 \text{ s})$ with Superbee. Additionally, the non-dimensional error is reduced of at least an order of magnitude with respect to virtually-fixed bed simulations. Results with Minmod and van Leer show similar dimensional errors while those with Superbee are a further order of magnitude smaller.

With reference to the analogous values reported in Tab. I at page 870 of Briganti et al. (2012a), the numerical model prediction for the tip location is now no more behind the Riemann wave solution one. The non-dimensional error does not decrease significantly in absolute value when time increases (while it does in the aforementioned table, from 6.72% at $t = 1$ s to 0.08% at $t = 5$ s) but remains quite stable around low values, depending on the applied flux limiter (around 1.45%, 0.15% and 1.12% for Minmod, Superbee and van Leer respectively). Finally, note that, while in Briganti et al. (2012a) the dimensional error trend indicates that the numerical tip is catching up with the reference solution, in the present model results the tip keeps accumulating delay, although small.

5.3.3 Concluding remarks

In both the virtually-fixed and the mobile bed cases the results are overall improved with respect to the original ones of Briganti et al. (2012a).

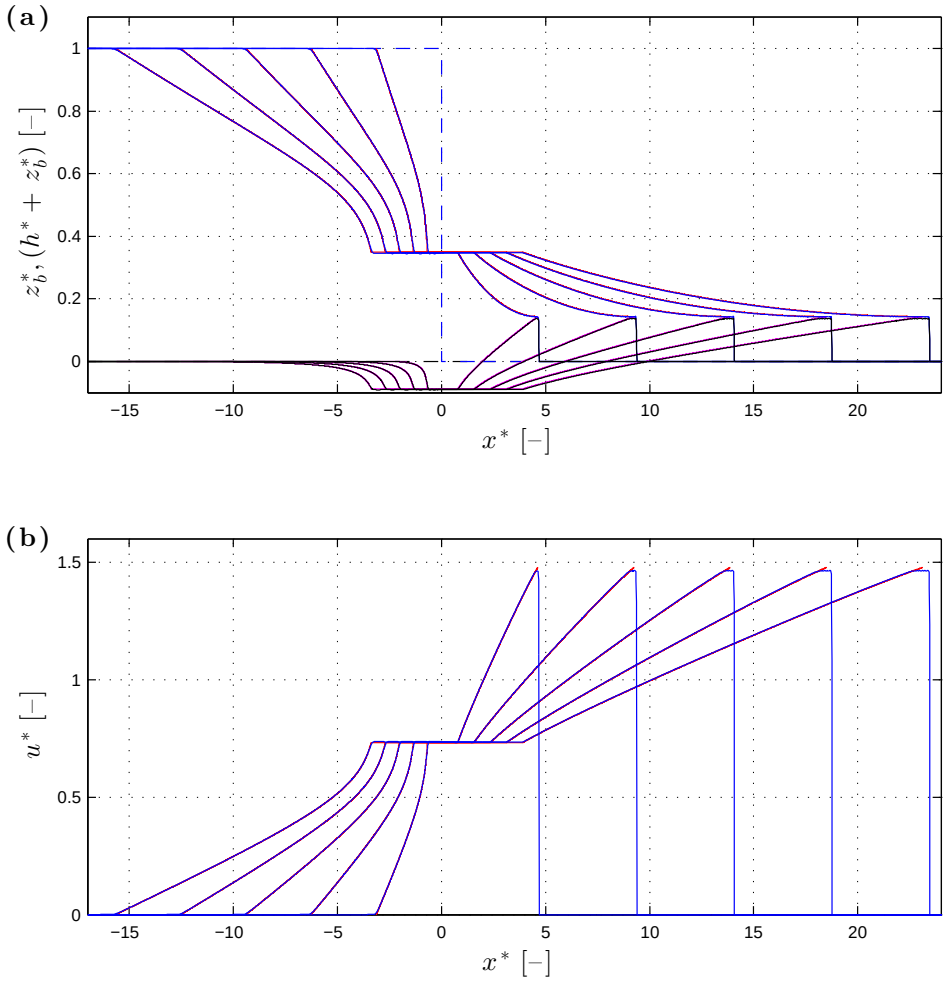

Figure 5.6: Dam break on mobile bed. Reference solution and model results with Minmod applied and $h_{min}/h_{rep} = 10^{-4}$. (a): non-dimensional surface level ($h^* + z_b^*$) and bed level (z_b^*) profiles at $t = 1, 2, 3, 4, 5$ s. Blue and black dashed lines: initial conditions. Solid lines: Riemann wave solution (red and magenta); model results (blue and black). (b): non-dimensional velocity (u^*) profiles at $t = 1, 2, 3, 4, 5$ s. Solid lines: Riemann wave solution (red); model results (blue).

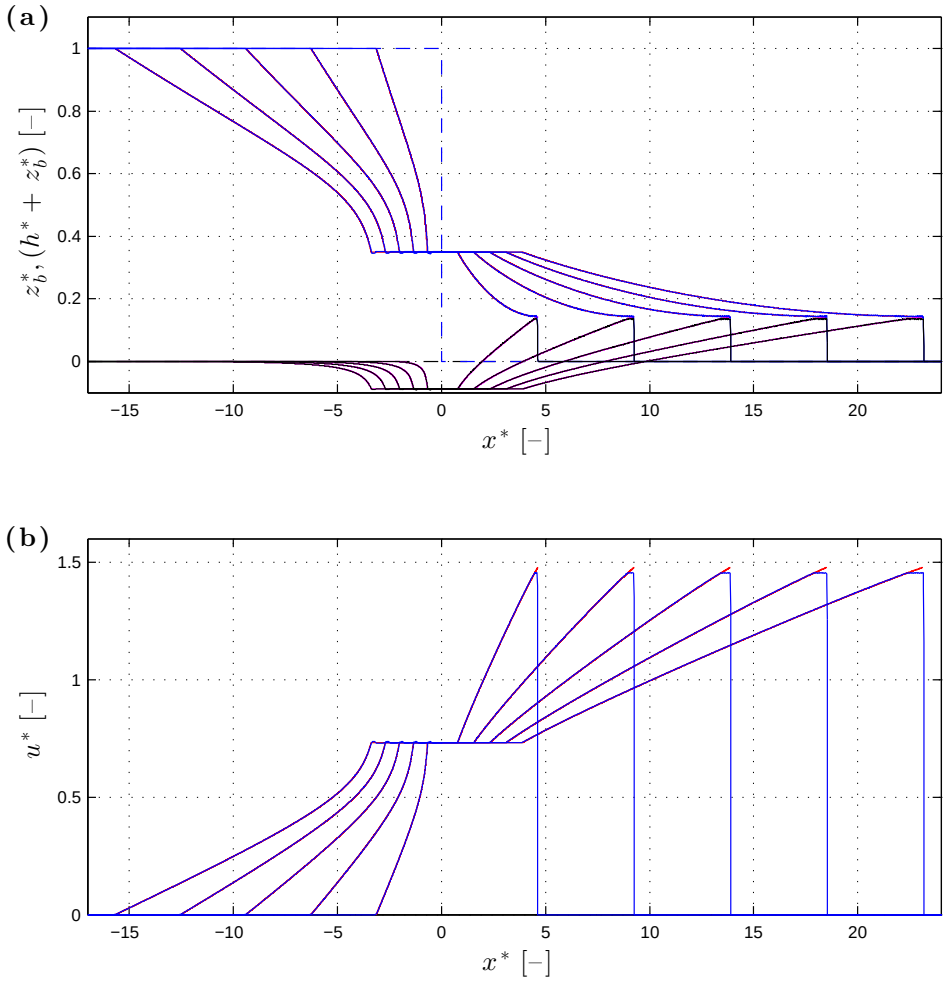

Figure 5.7: Dam break on mobile bed. Reference solution and model results with Superbee applied and $h_{min}/h_{rep} = 10^{-4}$. (a): non-dimensional surface level ($h^* + z_b^*$) and bed level (z_b^*) profiles at $t = 1, 2, 3, 4, 5$ s. Blue and black dashed lines: initial conditions. Solid lines: Riemann wave solution (red and magenta); model results (blue and black). (b): non-dimensional velocity (u^*) profiles at $t = 1, 2, 3, 4, 5$ s. Solid lines: Riemann wave solution (red); model results (blue).

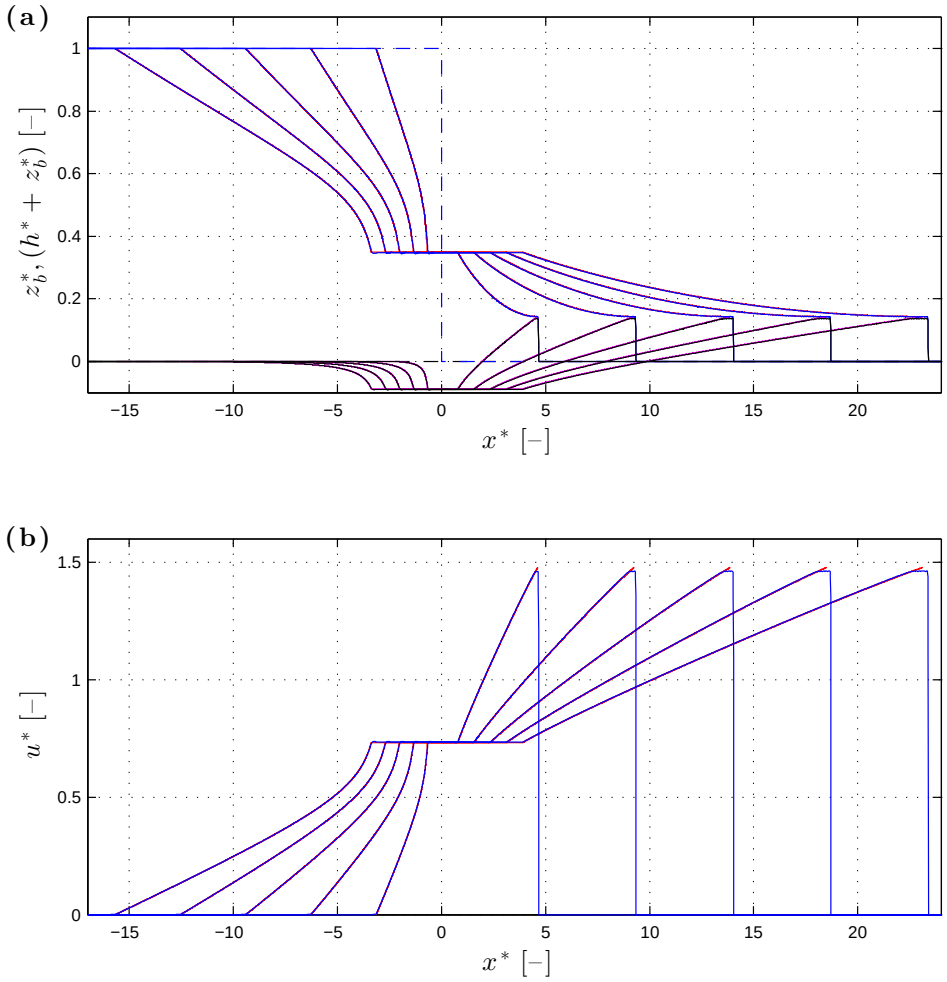

Figure 5.8: Dam break on mobile bed. Reference solution and model results with van Leer applied and $h_{min}/h_{rep} = 10^{-4}$. (a): non-dimensional surface level ($h^* + z_b^*$) and bed level (z_b^*) profiles at $t = 1, 2, 3, 4, 5$ s. Blue and black dashed lines: initial conditions. Solid lines: Riemann wave solution (red and magenta); model results (blue and black). (b): non-dimensional velocity (u^*) profiles at $t = 1, 2, 3, 4, 5$ s. Solid lines: Riemann wave solution (red); model results (blue).

Error in wet / dry front location						
	Dam break on mobile bed. $h_{min}/h_{rep} = 10^{-4}$.					
	Minmod		*Superbee*		*van Leer*	
t [s]	ϵ_s [%]	Δx_s [m]	ϵ_s [%]	Δx_s [m]	ϵ_s [%]	Δx_s [m]
1	1.50	0.069	−0.02	−0.001	1.07	0.049
2	1.44	0.134	0.15	0.014	1.12	0.104
3	1.43	0.198	0.20	0.028	1.14	0.158
4	1.42	0.262	0.17	0.032	1.15	0.212
5	1.46	0.337	0.20	0.047	1.15	0.267

Table 5.5: Dam break on mobile bed. Error in wet / dry front location.

In the virtually-fixed bed case, the present model shows enhanced stability, allowing an order of magnitude smaller h_{min} to be set, while Minmod proves to be more robust and reliable than the other two.

In the mobile bed case, the results display very good compliance with the Riemann wave solution and the analysis of the non-dimensional error in the tip location shows that Superbee returns the best performance in terms of tip location, although Minmod and van Leer limit error values within the 1.00%–1.50% range.

5.4 Uniform bore test

This test studies the impact of a uniform bore on an erodible slope beach and allows to assess the model performance in the case of a single swash event. The original problem with the fixed beach was addressed by Hibberd & Peregrine (1979), while the mobile bed one was analysed by Zhu et al. (2012) considering bed-load only, then extended to combined load by Zhu (2012). Fig. 5.9 shows the initial conditions and the variables involved in this test.

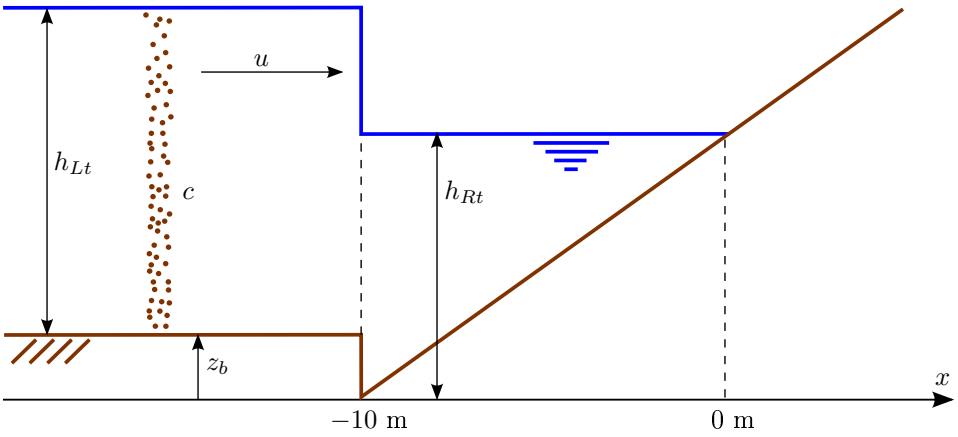

Figure 5.9: Uniform bore test. Sketch of initial conditions and involved variables.

In particular, $h_{Lt} = 1.6$ m, $h_{Rt} = 1$ m and the initial slope of the beach is 0.1. At $t = 0$ s, $x < -10$ m is a constant (left) region where the velocity u and the bed level z_b are computed imposing the morphodynamic shock conditions (see Zhu, 2012), which are reported for convenience in Appendix D. The remaining right side values required in the above-mentioned shock conditions are $u_{Rt} = 0$ ms^{-1} and $z_{b,Rt} = 0$ m, which is the initial bed level at the toe of the slope, i.e. $z_b(x = -10\text{ m}, t = 0\text{ s})$. Water is initially motionless in the slope region, i.e. $x \geq -10$ m, and the initial shoreline is located at $x = 0$ m. Finally, the domain length is $L_x = 130$ m, with the upstream (seaward) boundary located at $x = -100$ m.

The basic free flow conditions at the upstream boundary have no effect on the solution, as that is set far enough from the beach not to let any perturbation reach it within the duration of the simulation. The downstream BCs are the shoreline ones presented in § 4.3.3.

The settings are chosen equal to those in Zhu et al. (2012) and in Zhu (2012) for the bed- and combined load cases respectively. In particular, the solved problem is frictionless and no bed diffusion or infiltration are considered. In the

bed-load only case, the Grass formula is employed with $A_{sed} = 0.004$ s^2m^{-1} and $p_b = 0.40$. In the combined load case, the bed-load transport is again modelled through the Grass formula but this time with $A_{sed} = 6.118 \times 10^{-4}$ s^2m^{-1}, while p_b is confirmed 0.40. For the suspended sediment transport, the erosional rate E, defined by Eq (3.11), is rewritten under the assumption of the Chézy approach (see Pritchard & Hogg, 2005) as

$$E = m_e \left(\frac{u^2 - u_{crs}^2}{u_{rep}^2} \right), \tag{5.13}$$

with $m_e = 1.879 \times 10^{-3}$ ms^{-1}, $u_{crs} = 0$ ms^{-1} and $u_{rep} = \sqrt{gh_{rep}}$ ms^{-1}. In the deposition rate D, given by Eq (3.12), $w_s = 3.132 \times 10^{-2}$ ms^{-1}.

Note that when suspended sediment transport is considered, additional initial conditions for c have to be set. As $u(x \geq -10 \text{ m}, t = 0 \text{ s}) = 0$ ms^{-1}, it is assumed $c(x \geq -10 \text{ m}, t = 0 \text{ s}) = 0$ m^3m^{-3}. In the constant left region, the non-zero velocity u_{Lt} (from the morphodynamic shock conditions) allows a pre-suspended sediment concentration, or c_{Lt}, which is a finite value and could be zero. To retain consistency with Zhu (2012), $c_{Lt} = 1.76 \times 10^{-2}$ m^3m^{-3}, which equals the equilibrium concentration, or c_{eq}, which is obtained imposing $E - D = 0$, as detailed below:

$$m_e \frac{u^2}{u_{rep}^2} - w_s c_{eq} = 0 \Rightarrow c_{eq} = \frac{m_e}{w_s} \frac{u^2}{u_{rep}^2}. \tag{5.14}$$

About the numerical settings, $\Delta x = 0.01$ m (except for one simulation, see § 5.4.2) and $CN = 0.45$. Reference value for h_{min} is 0.003 m for the bed-load only case (see Zhu et al., 2012) while no previous value is available for the combined load case. Simulations are carried out for several h_{min} values, spanning a range between 10^{-5} m and 0.001 m, and using the different flux limiters. For both brevity and convenience, only a selection of significant results is reported herein.

Finally, some results are presented in non-dimensional form to facilitate

comparison with those in Zhu et al. (2012) and Zhu (2012), using as scaling the initial water depth value on the right (landward) side of the bore front, i.e. $h_{rep} = h_{Rt} = 1$ m.

Results for the bed- and combined load cases are examined separately in §§ 5.4.1 and 5.4.2 respectively, while final remarks are proposed in § 5.4.3.

5.4.1 Bed-load uniform bore

A summary of this case assumptions, BCs, physical parameters and numerical settings is given in Tab. 5.6.

Assumptions and BCs	
Friction	not included
Sediment transport	bed-load only (Grass)
Bed diffusion	not included
Infiltration	not included
Upstream BCs	free flow
Downstream BCs	shoreline
Physical parameters and numerical settings	
Sediment mobility parameter (A_{sed})	0.004 s^2m^{-1}
Bed porosity (p_b)	0.40
Domain length (L_x)	130 m
Spatial step size (Δx)	0.01 m
Courant Number (CN)	0.45
Minimum water depth parameter (h_{min})	10^{-4} m
Duration of the simulations	24 s

Table 5.6: Bed-load uniform bore. Assumptions, BCs, physical parameters and numerical settings.

In Figs. 5.10 and 5.11 the present model results are shown together with

those obtained using the original one (courtesy of Dr R. Briganti), so that the two different versions are compared. Note that, while for the latter the best agreement with the MOC solution (see Zhu et al., 2012) was achieved for $h_{min} = 0.003$ m, the former requires a smaller value, namely $h_{min} = 10^{-4}$ m. This discrepancy can be justified by the different shoreline treatment and approach for $\bar{\beta}_k$ adopted in the two models. Some spurious, but very small and non-increasing in time, oscillations are produced by the original model at the initial shoreline before of the bore arrival therein, due to the previous wet / dry boundary treatment. These oscillations are indicated by the vertical red line at $x^* = 0$ in panel (b) of Fig. 5.10, while no analogous line is obtained for the other results. Additionally, in Fig. 5.10 the present model returns almost identical contours for the non-dimensional water depth and velocity with any of the considered flux limiters.

Results highlight their sensitivity to the applied flux limiter in Fig. 5.11. In particular, the final bed changes for the original and the present models, both using Minmod, show some amount of noise, which is exacerbated when Superbee or van Leer are employed. This is more apparent in panel (b) of Fig. 5.11, where profiles for the non-dimensional bed change b^* at the time of bed step formation are plotted. Note that in the MOC solution this bed step is represented by a local sharp discontinuity in the bed profile (see Zhu et al., 2012), while the TVD-MCC, as expected for a shock-capturing scheme, smears it to some degree. In particular, the present model returns a higher bed-step than the original one, which is also reduced in width in the simulations with Superbee and van Leer.

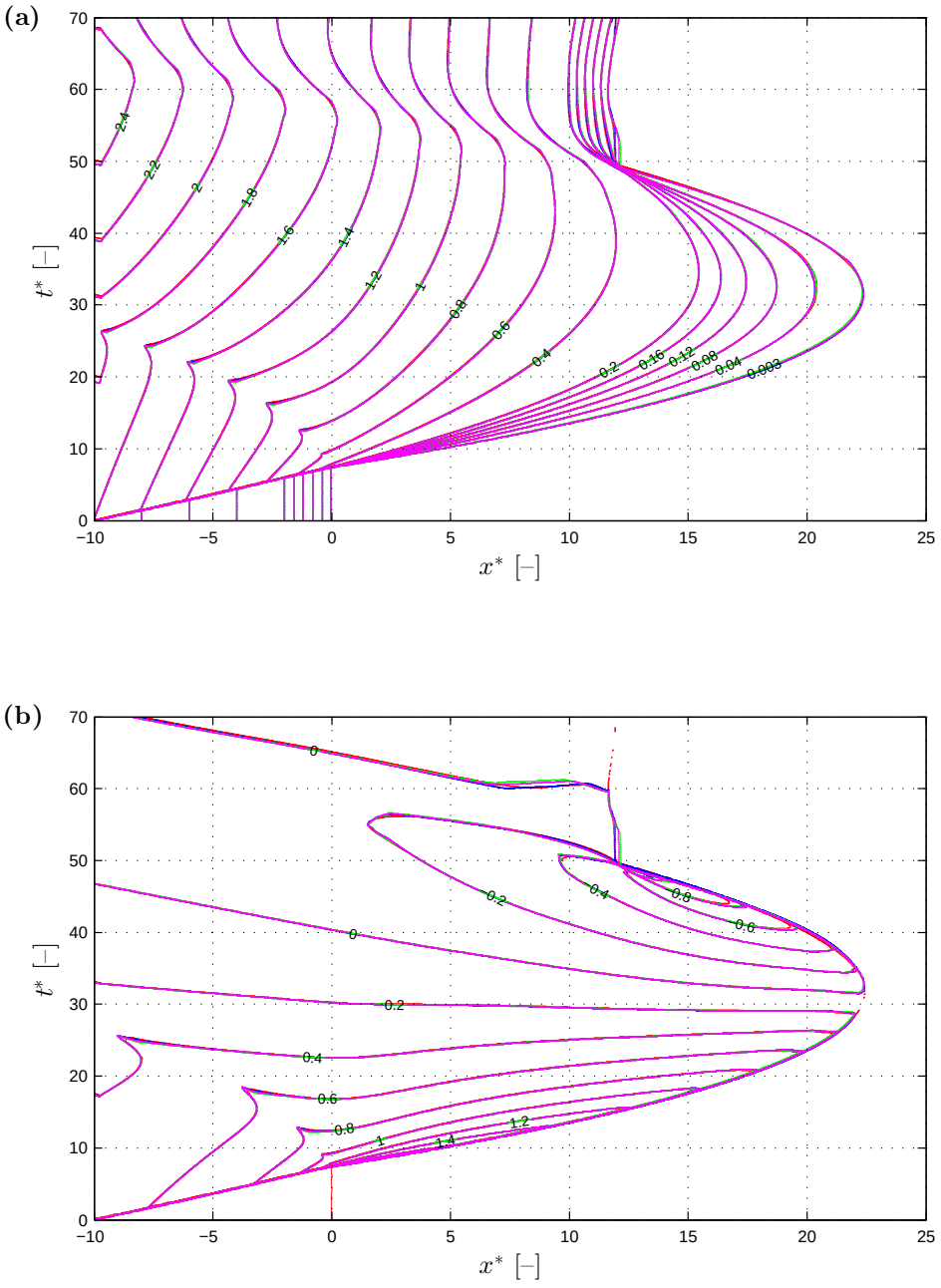

Figure 5.10: Bed-load uniform bore. Reference results and present model ones with different flux limiters. (a) and (b): comparison of contours for non-dimensional water depth (h^*) and velocity (u^*) respectively. Solid lines: previous model results with $h_{min} = 0.003$ m (red); present model results with $h_{min} = 10^{-4}$ m and Minmod (blue), Superbee (green) and van Leer (magenta) applied respectively.

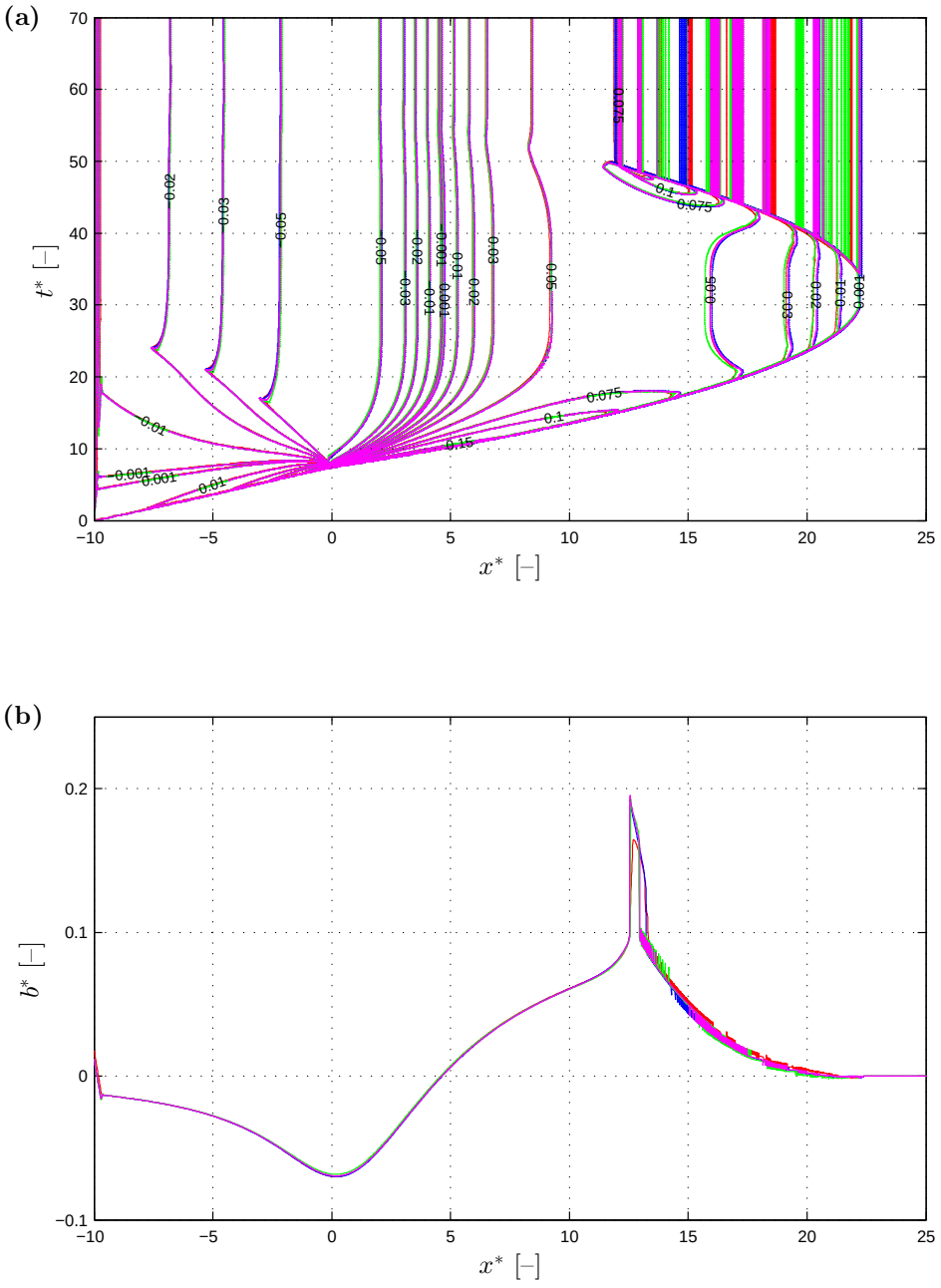

Figure 5.11: Bed-load uniform bore. Reference results and present model ones with different flux limiters. (a): comparison of contours for non-dimensional bed change (b^*); (b) b^* profiles at the time of bed-step formation ($t^* = 48.4$). Solid lines: previous model results with $h_{min} = 0.003$ m (red); present model results with $h_{min} = 10^{-4}$ m and Minmod (blue), Superbee (green) and van Leer (magenta) applied respectively.

5.4.2 Combined load uniform bore

A summary of this case assumptions, BCs, physical parameters and numerical settings is provided in Tab. 5.7.

Assumptions and BCs	
Friction	not included
Sediment transport	combined load (Grass)
Bed diffusion	not included
Infiltration	not included
Upstream BCs	free flow
Downstream BCs	shoreline
Physical parameters and numerical settings	
Sediment mobility parameter (A_{sed})	6.118×10^{-4} s^{2}m^{-1}
Bed porosity (p_b)	0.40
Erosional rate parameter (m_e)	1.879×10^{-3} ms^{-1}
Critical velocity for suspended load (u_{crs})	0 ms^{-1}
Representative scale for velocity (u_{rep})	$\sqrt{gh_{rep}}$ ms^{-1}
Representative scale for water depth (h_{rep})	1 m
Effective settling velocity (w_s)	3.132×10^{-2} ms^{-1}
Domain length (L_x)	130 m
Spatial step size (Δx)	0.01 / 0.001 m
Courant Number (CN)	0.45
Minimum water depth parameter (h_{min})	10^{-4} / 10^{-5} m
Duration of the simulations	16 s

Table 5.7: Combined load uniform bore. Assumptions, BCs, physical parameters and numerical settings. '/' separates alternative values used in the different simulations.

Figs. 5.12, 5.13 and 5.14 show comparison of the MOC reference solution (courtesy of Dr F. Zhu, from Zhu, 2012) with the results of the present model,

the latter using Minmod (sensitivity to the applied flux limiter is discussed later) and two different numerical settings. In the first simulation $\Delta x = 0.01$ m, consistent with the reference solution, and $h_{min} = 10^{-4}$ m, value which leads to good results in the previous bed-load only case. In the second one reduced values for both of them are considered, namely $\Delta x = 0.001$ m and $h_{min} = 10^{-5}$ m.

Comparing the contours in Figs. 5.12 and 5.13 for the MOC solution and the first simulation results, a reduced maximum inundation (of roughly 3) is noted in the latter (see panel (a) of Fig. 5.12), which consequently confines from the landward side any other variable evolution. The overall agreement is good and also the final bed change profile in Fig. 5.14 is well represented, with the final bed step reduced of around 0.05, consistent with previous results for the bed-load only case.

Figs. 5.12, 5.13 and 5.14 show also the results for the second simulation, which display an increased maximum run-up extension, closer to the reference solution one than that of the first simulation, and a general better compliance with the MOC solution. In particular in Fig. 5.14 some additional noise is evident with respect to the results of the first simulation, however the bed step shows excellent phasing with the reference solution, even though being slightly higher of around 0.01.

Figs. 5.15, 5.16 and 5.17 show the sensitivity of the present model results to the applied flux limiter, keeping $\Delta x = 0.01$ m and $h_{min} = 10^{-4}$ m (for justification of this choice, see later § 5.4.3). No noticeable differences can be seen, apart from some different levels of noise in the final bed change profiles (see Fig. 5.16 panel (a) and Fig. 5.17), more significant when van Leer and especially Superbee are applied.

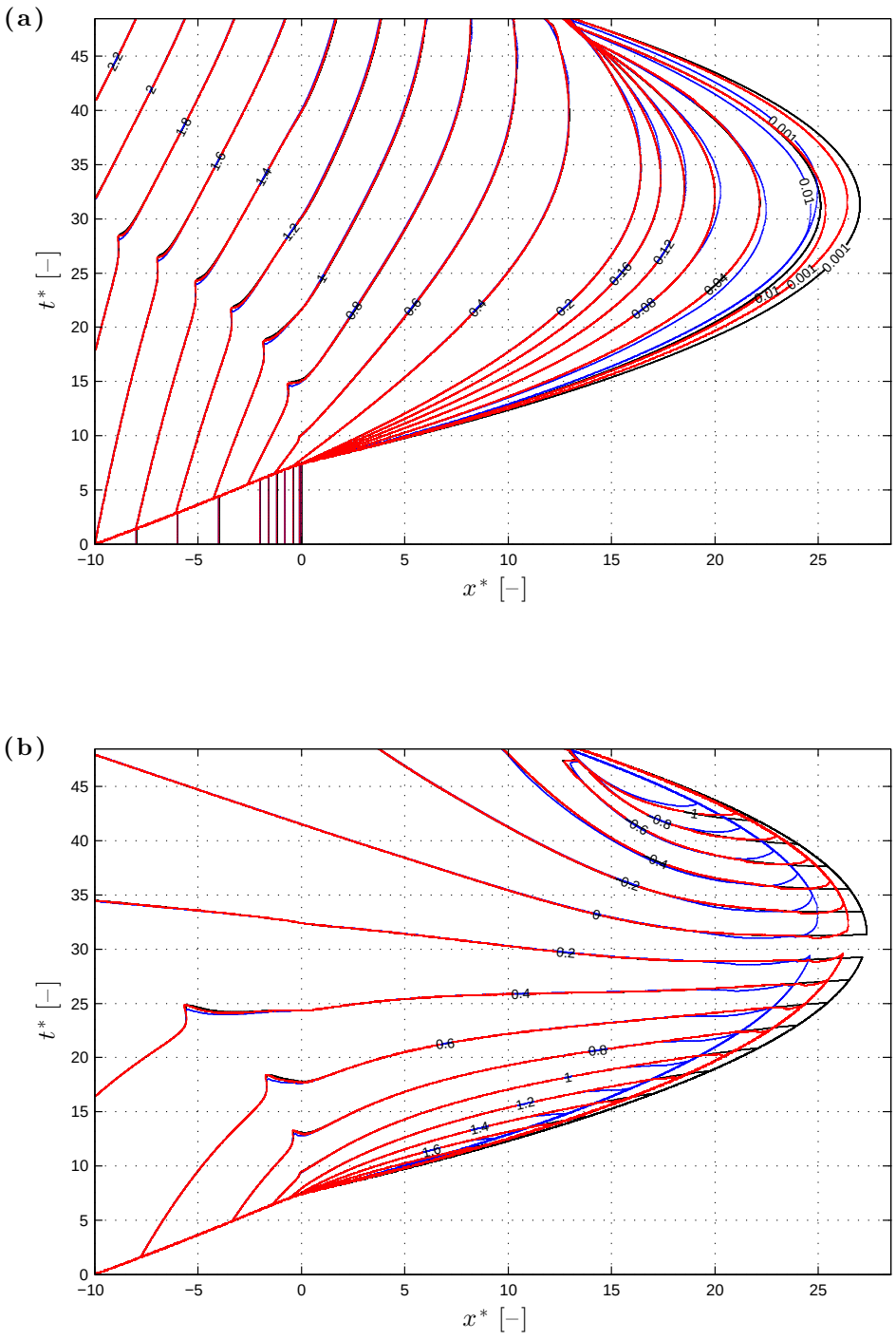

Figure 5.12: Combined load uniform bore. Reference solution and model results with Minmod applied. (a) and (b): comparison of contours for non-dimensional water depth (h^*) and velocity (u^*) respectively. Solid lines: MOC (reference) solution (black); model results with $\Delta x = 0.01$ m and $h_{min} = 10^{-4}$ m (blue); model results with $\Delta x = 0.001$ m and $h_{min} = 10^{-5}$ m (red).

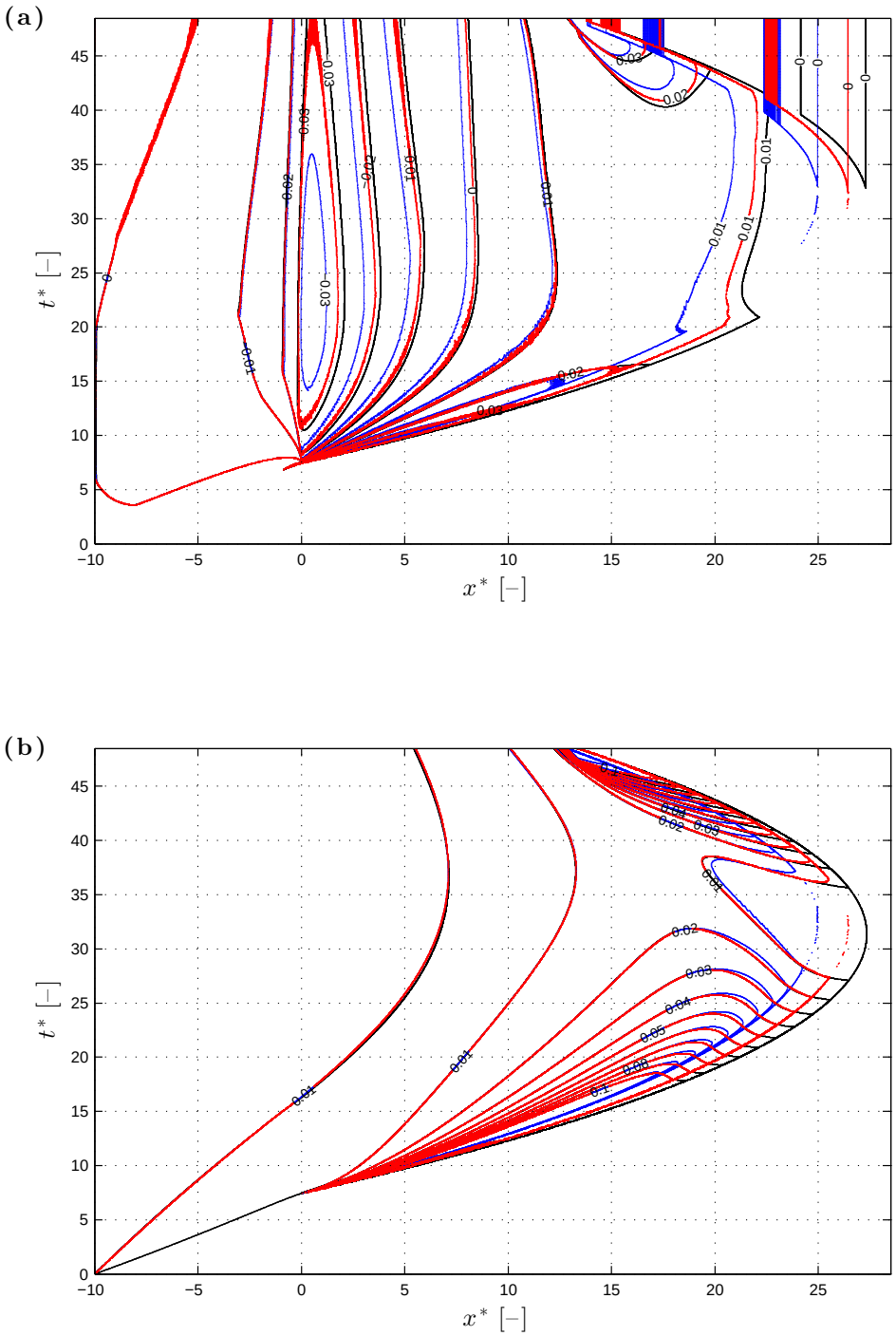

Figure 5.13: Combined load uniform bore. Reference solution and model results with Minmod applied. (a) and (b): comparison of contours for non-dimensional bed change (b^*) and suspended sediment concentration (c) respectively. Solid lines: MOC (reference) solution (black); model results with $\Delta x = 0.01$ m and $h_{min} = 10^{-4}$ m (blue); model results with $\Delta x = 0.001$ m and $h_{min} = 10^{-5}$ m (red).

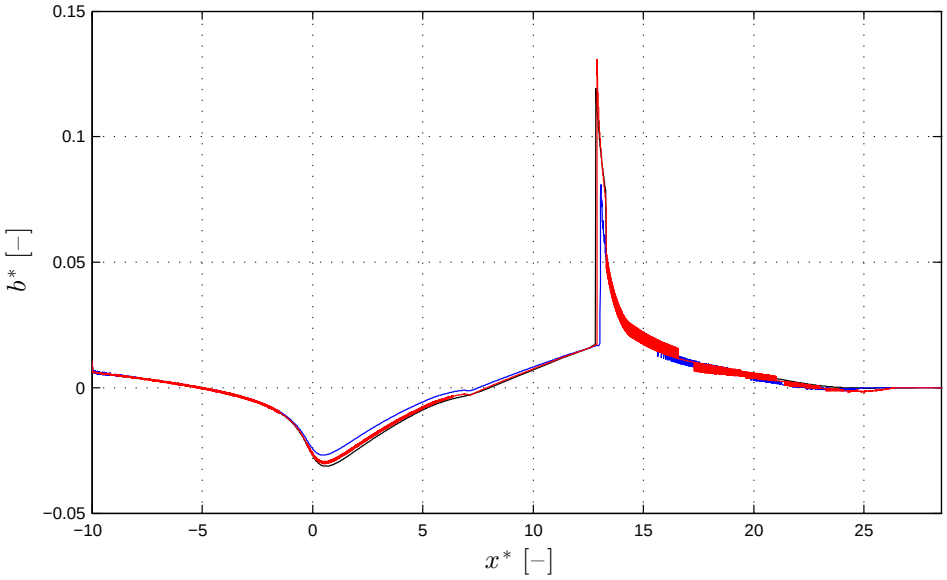

Figure 5.14: Combined load uniform bore. Reference solution and model results with Minmod applied. Comparison of non-dimensional final bed change (b^*) profiles. Solid lines: MOC (reference) solution (black); model results with $\Delta x = 0.01$ m and $h_{min} = 10^{-4}$ m (blue); model results with $\Delta x = 0.001$ m and $h_{min} = 10^{-5}$ m (red).

5.4.3 Concluding remarks

For the bed-load uniform bore case, the present model results confirm a very good compliance with the original version ones (and in turn with the corresponding MOC solution shown in Zhu et al., 2012), although h_{min} requires to be reduced to 10^{-4} m.

For the combined load uniform bore case, the results of two simulations using different numerical settings are showed. In the first simulation the model results display overall good agreement with the MOC solution, while with the second one (employing reduced Δx and h_{min}) they adhere more closely to it. However, it is worth noting that this improved performance is achieved at an increased computational cost. While the first simulation took roughly 8 minutes to run, the second one lasted around 12 hours, using the same standard PC (Processor: Intel (R) Core (TM) i3-2120 CPU 3.30GHz; RAM: 4GB). Such

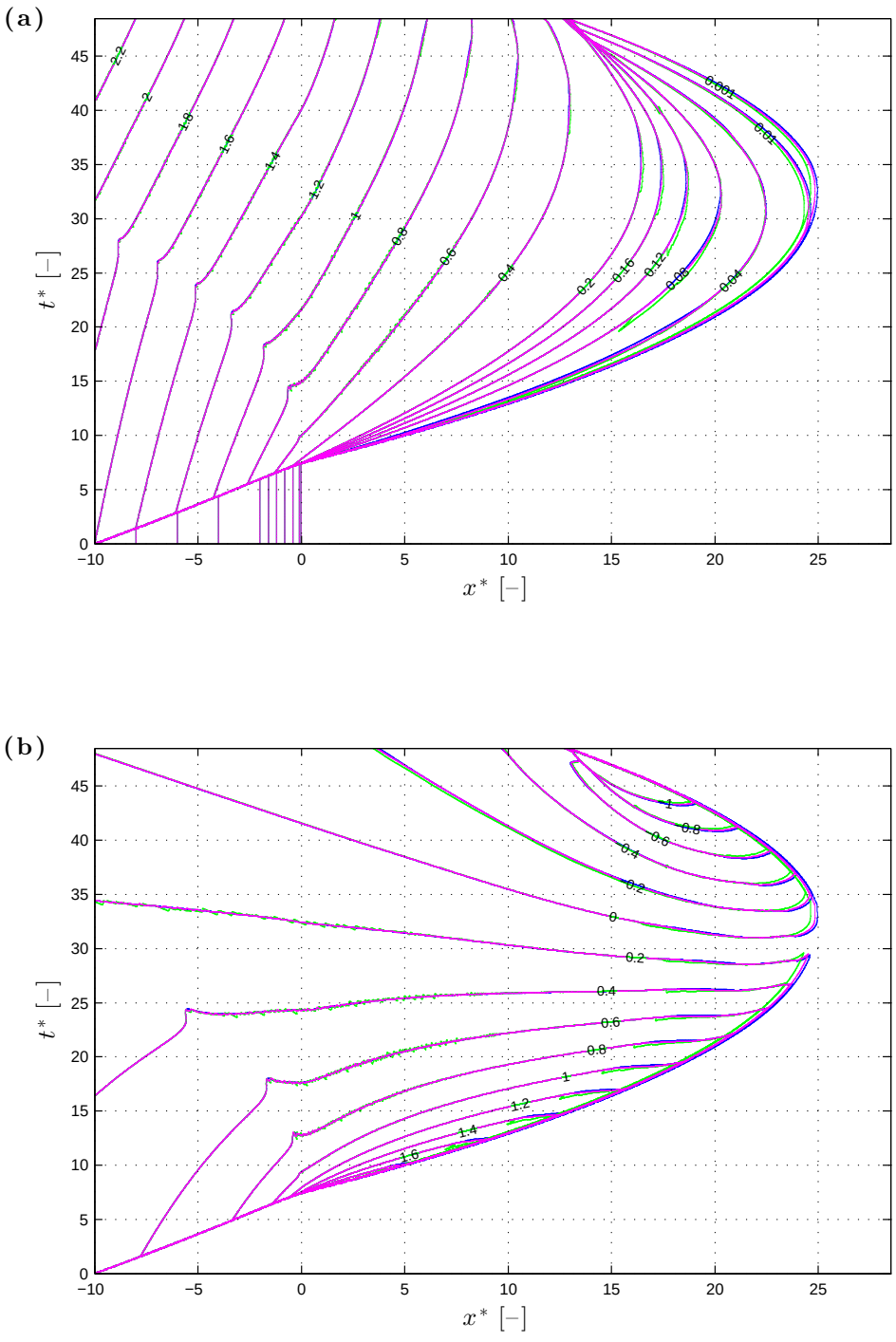

Figure 5.15: Combined load uniform bore. Model results with different flux limiters. (a) and (b): comparison of contours for non-dimensional water depth (h^*) and velocity (u^*) respectively. Solid lines: model results using Minmod (blue), Superbee (green) or van Leer (magenta) respectively.

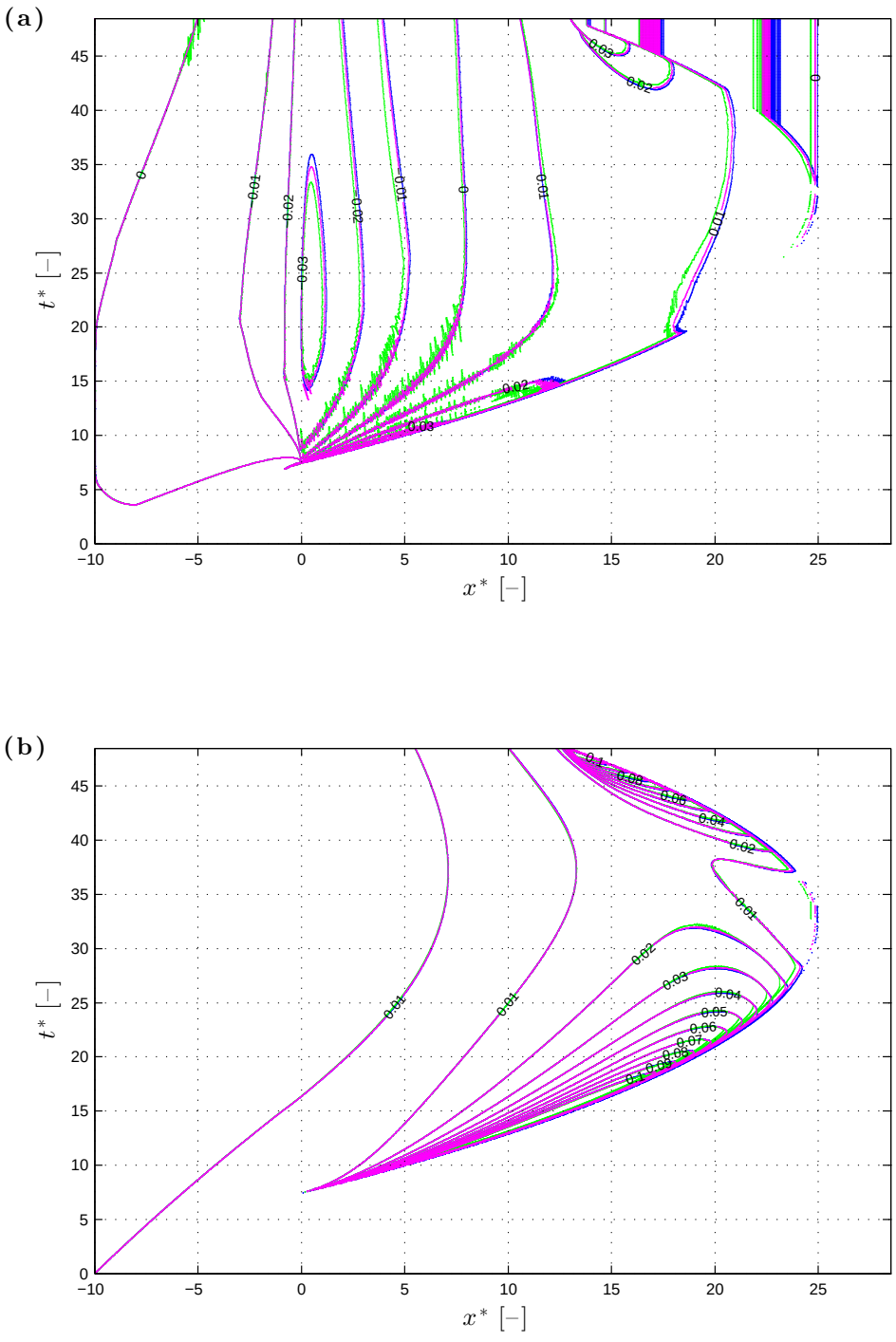

Figure 5.16: Combined load uniform bore. Model results with different flux limiters. (a) and (b): comparison of contours for non-dimensional bed change (b^*) and suspended sediment concentration (c) respectively. Solid lines: model results using Minmod (blue), Superbee (green) or van Leer (magenta) respectively.

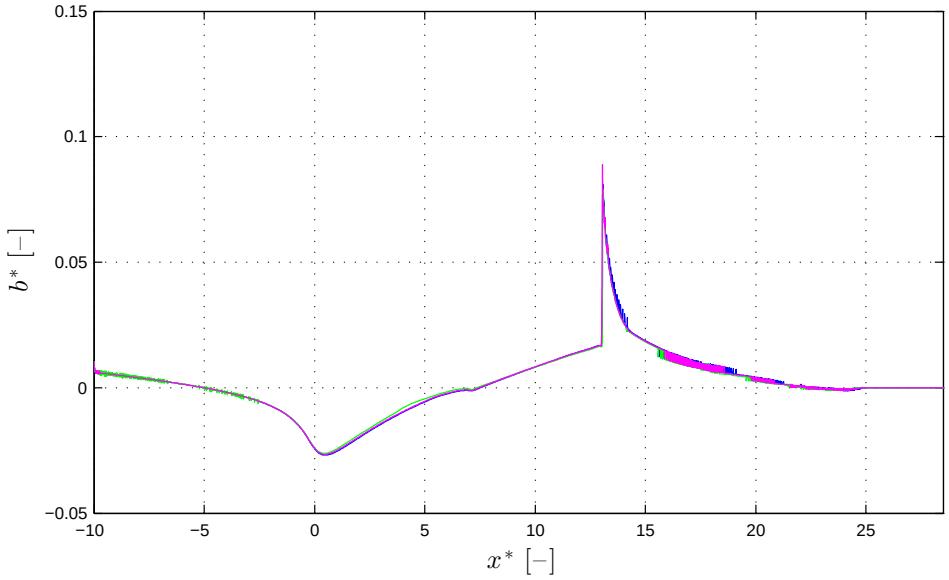

Figure 5.17: Combined load uniform bore. Model results with different flux limiters. Comparison of final non-dimensional bed change (b^*) profiles. Solid lines: model results using Minmod (blue), Superbee (green) or van Leer (magenta) respectively.

a long time, despite the enhanced results, is deemed to be unacceptable in the view of a future engineering use of the present model, which aims at being accurate but flexible and computationally inexpensive at the same time.

Because of previous good results in the dam break on mobile bed case (see § 5.3.2) and in the bed-load uniform bore one (see § 5.4.1), $h_{min} = 10^{-4}$ m is assumed to represent a reasonable (lower) limit value for the simulations. Additionally, note that at such a small depth other physical aspects (e.g. capillarity), which are not included here, are expected to play an increasing important role in the fluid dynamics.

In both considered bed- and combined load cases, results do not show an overall noticeable sensitivity to the applied flux limiters. If Superbee and van Leer describe shocks more sharply, as expected as less diffusive than Minmod, however they return increased numerical noise, especially in the bed change profiles. As numerical noise is generally to be avoided, and sometimes the first

step towards the development of instabilities and computational errors, results for the uniform bore test suggest to use Minmod rather than the other two for morphodynamic simulations in the swash zone.

5.5 Single swash test on fixed slope

The single swash test on fixed slope is designed to reproduce the laboratory experiments carried out at the swash facility of the University of Aberdeen (U.K.) between September 2007 and July 2008. In particular, two cases with the same coarse sand sediment are examined, the first being on an impermeable slope, while the second on a permeable but fixed beach. For comprehensive details on the facility and experimental conditions, the reader is referred to Kikkert et al. (2012) and Kikkert et al. (2013) respectively.

This test purpose is twofold. Firstly, to understand how the model compares with the WAF one of Briganti et al. (2011) for the impermeable beach case, both models employing the BBL solver (see Appendix A). Secondly, to check that the implemented simplified approach for infiltration modelling is able to provide a reasonably accurate estimate of percolated water and, more generally, a good swash description in the permeable slope case. Fig. 5.18 shows a sketch of the above-mentioned swash facility, along with the initial conditions and the variables involved in the simulations.

With reference to Fig. 5.18 and in the order from left to right, the experimental rig consists of an external fixed wall, a reservoir, a metal gate, an impermeable fixed flat-bottomed region, a slope beach and a weir, which in the permeable beach case keeps the initial water table inside the slope at the chosen level. $h_{rsv} = 0.600$ m is the initial still water depth inside the reservoir, i.e. before the gate, while after the gate the maximum initial still water depth is $h_{ini} = 0.062$ m, which coincides with the initial water level inside the per-

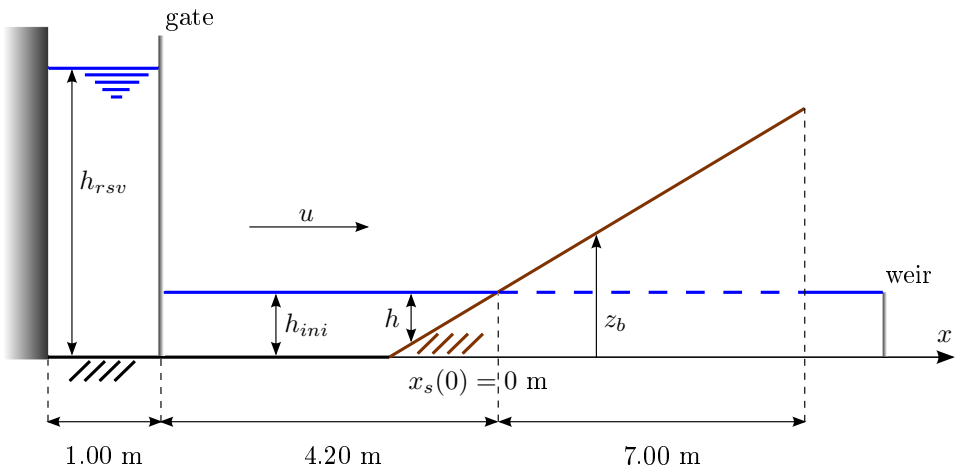

Figure 5.18: Single swash test on fixed slope. Sketch of the experimental rig, with initial conditions and involved variables (not to be scaled). Dashed blue line for the water table inside the slope and the weir are valid for permeable beach case only. Black and brown are used to indicate the steel flat bottom and the (coated with or cemented) sediment slope respectively.

meable beach. Note that $z_b(x,t) = z_b(x,0)$, as the bed is fixed. The reservoir is 1.00 m long, the gate 4.20 m far from the initial shoreline position and the slope measures 7.00 m in length, enough for no water overtopping its higher edge in any experiment. The shoreline position, $x_s(t)$, is initially located at $x = 0$ m. Finally, the domain length is $L_x = 12$ m.

This test uses basic fully reflective conditions at the upstream boundary, which are

$$h_0^n = h_1^n, \tag{5.15}$$

$$u_0^n = -u_1^n, \tag{5.16}$$

$$z_{b,0}^n = z_{b,1}^n, \tag{5.17}$$

while the downstream BCs are the shoreline ones (see § 4.3.3).

The settings are chosen equal to those in Briganti et al. (2011), then infiltration parameters are taken for the permeable case from Kikkert & Steenhauer (2008) and Steenhauer et al. (2011). The considered experiments are those for

the coarse sand with $d_{50} = 1.3 \times 10^{-3}$ m and $d_{65} = 1.5 \times 10^{-3}$ m, these being the median and nominal grain diameters respectively. The model is equipped with the BBL solver, with bed roughness k_b equal to $2\,d_{65} = 0.003$ m, following the calibration presented by Briganti et al. (2011).

As previously done for the dam break test on rigid bed (see § 5.3.1), the immobile bed is modelled as a virtually-fixed one through the Grass formula with $A_{sed} = 10^{-8}$ s^{2}m^{-1}. $p_b = 0$ and 0.30 in the impermeable and permeable cases respectively. No suspended load or bed diffusion are considered. For the permeable slope case, both the Darcy and the Forchheimer resistance laws are employed (see § 3.4.3), with the following parameters: $k_{inf} = 0.013$ ms^{-1} from Kikkert & Steenhauer (2008), while $a_{inf} = 81.2$ sm^{-1} and $b_{inf} = 3,587$ s^{2}m^{-2} from Steenhauer et al. (2011).

In this test $\Delta x = 0.01$ m, $CN = 0.80$ and $h_{min} = 0.001$ m for consistency with Briganti et al. (2011). Simulations with each one of the three flux limiters are carried out.

Results for the impermeable and permeable fixed slope cases are presented in §§ 5.5.1 and 5.5.2 respectively, while final remarks are drawn in § 5.5.3.

5.5.1 Single swash on impermeable fixed slope

A summary of this case assumptions, BCs, physical parameters and numerical settings is given in Tab. 5.8.

Fig. 5.19 shows comparison of the time series of the measured and the predicted shoreline positions, while Fig. 5.20 presents comparison between h and u time series at three selected particle image velocimeter (or PIV) locations, which are $x = 0.072$, 1.559 and 2.365 m for PIV2, PIV4 and PIV5 in the order. Note that only results using Minmod are displayed, as those with the other two do not show any significant difference or improvement.

Assumptions and BCs	
Friction	BBL solver
Sediment transport	virtually only (Grass)
Bed diffusion	not included
Infiltration	not included
Upstream BCs	reflective
Downstream BCs	shoreline
Physical parameters and numerical settings	
Median sediment grain diameter (d_{50})	1.3×10^{-3} m
Bed roughness (k_b)	0.003 m
Sediment mobility parameter (A_{sed})	10^{-8} s^{2}m^{-1}
Bed porosity (p_b)	0
Domain length (L_x)	12 m
Spatial step size (Δx)	0.01 m
Courant Number (CN)	0.80
Minimum water depth parameter (h_{min})	0.001 m
Duration of the simulations	11 s

Table 5.8: Single swash on impermeable fixed slope. Assumptions, BCs, physical parameters and numerical settings.

With reference to Fig. 5.19, the model results confirm those obtained through the WAF method (see Fig. 3, panel (a), at page 465 of Briganti et al., 2011), showing an overall good phasing with the measured data, slightly over-estimated maximum run-up and increasing lag for the numerical tip in the backwash (dashed line). The numerical prediction for $h = 0.005$ m, which is consistent with measurement resolution, is improved in comparison with the WAF results.

This is also confirmed in Fig. 5.20, where the model results return a better

compliance with data throughout the water depth and velocity time series (especially in the late swash) than that reported in Fig. 7 at page 467 of Briganti et al. (2011). This enhanced performance may be partly explained with the different modelled numerical domain. While Briganti et al. (2011) chose to limit their simulation at PIV1 location, i.e. $x = -1.802$ m, where input time series for h and u from PIV1 measurements were used as BCs, the numerical domain is here extended to the whole rig, thus simulating the initial dam break event and the subsequent reflected wave from the left external fixed wall as well.

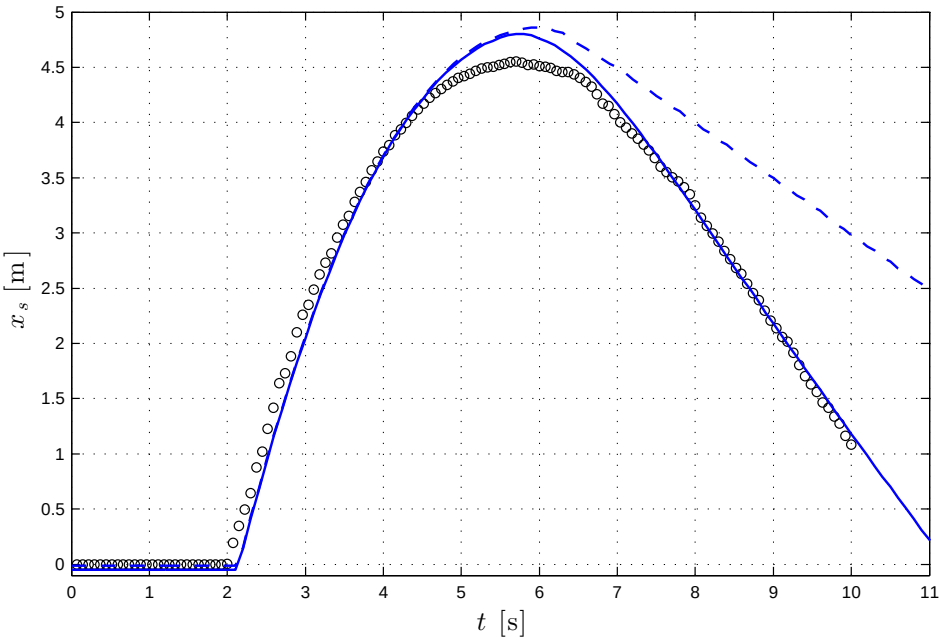

Figure 5.19: Single swash on impermeable fixed slope. Comparison of measured and predicted shoreline position time series. Black circles: measured shoreline (resolution at $h = 0.005$ m). Solid blue line: predicted shoreline position tracking the water depth consistent with the measurements ($h = 0.005$ m). Dashed blue line: predicted shoreline position tracking the numerical wet / dry front ($h = 0.001$ m).

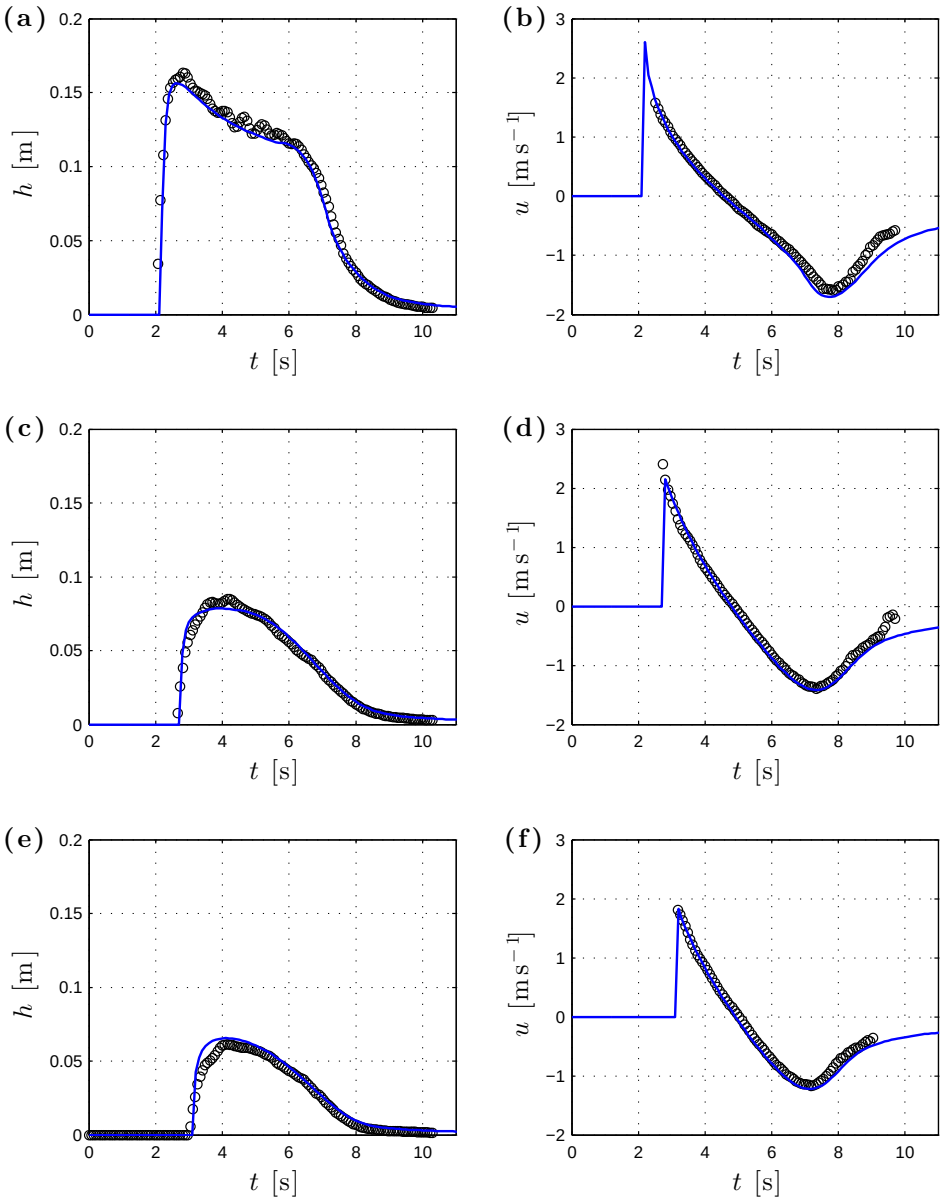

Figure 5.20: Single swash on impermeable fixed slope. Comparison of measured and predicted water depth (h) and velocity (u) time series at PIV2 (top row, (a) and (b)), PIV4 (mid row, (c) and (d)) and PIV5 (bottom row, (e) and (f)) locations. Black circles: measured data. Solid blue line: predicted h (left column) and u (right column) time series at selected PIV location.

5.5.2 Single swash on permeable fixed slope

A summary of this case assumptions, BCs, physical parameters and numerical settings is provided in Tab. 5.9.

Assumptions and BCs	
Friction	BBL solver
Sediment transport	virtually only (Grass)
Bed diffusion	not included
Infiltration	Darcy / Forchheimer law
Upstream BCs	reflective
Downstream BCs	shoreline
Physical parameters and numerical settings	
Median sediment grain diameter (d_{50})	1.3×10^{-3} m
Bed roughness (k_b)	0.003 m
Sediment mobility parameter (A_{sed})	10^{-8} s^{2}m^{-1}
Bed porosity (p_b)	0.30
Darcy hydraulic conductivity (k_{inf})	0.013 ms^{-1}
Forchheimer linear coefficient (a_{inf})	81.2 sm^{-1}
Forchheimer quadratic coefficient (b_{inf})	$3,587$ s^{2}m^{-2}
Domain length (L_x)	12 m
Spatial step size (Δx)	0.01 m
Courant Number (CN)	0.80
Minimum water depth parameter (h_{min})	0.001 m
Duration of the simulations	11 s

Table 5.9: Single swash on permeable fixed slope. Assumptions, BCs, physical parameters and numerical settings.

Fig. 5.21 shows comparison of the time series of the measured and the predicted shoreline positions, while Fig. 5.22 presents comparison between h

and u time series at PIV2, PIV4 and PIV5. Results using both resistance laws are plotted and, as previously for the impermeable case, only the simulation with Minmod is reported, because the other two do not yield any significant difference in the results.

With reference to Fig. 5.21, while during the uprush the swash tip is well simulated, especially with the Forchheimer law, the backwash is anticipated due to the excess of percolated water. The difference between the shoreline position predictions in the two simulations reduces after $t = 7$ s, when infiltration stops because of the completely filled void space available inside the permeable beach (recall that no groundwater motion is modelled).

In Fig. 5.22 the water depth evolution shows initially good compliance with measurements, then deteriorates with time. About velocity time series, the overall agreement is reasonably good, again weakening in the backwash phase. Appreciable difference between the two simulations can be seen only in the upper swash zone (see panels (e) and (f)).

With both the Darcy and the Forchheimer resistance laws, simulated infiltration exceeds the measured one. Fig. 5.23 shows the time stacks for the cumulative infiltrated volume per unit of width (V_{inf}) for the two simulations. This is computed at a generic cell m and until the chosen time step N as

$$V_{inf,m}^{N} = \sum_{n=1}^{N} w_{inf,m}^{n} \, \Delta t \, \Delta x. \tag{5.18}$$

Results highlight that the use of the Darcy law returns more final percolated water than that of the Forchheimer one. Note that in the lower swash zone, i.e. for roughly $x < 1.8$ m, the final contours in both panels match strictly, because in that part of the beach the void space between the water table and the slope top surface is relatively small and completely filled in both simulations. Additionally, the contour spacing in the time axis direction, and also in the space axis direction for $x > 2$ m, is wider in the simulation with

the Forchheimer law than in that with the Darcy one, consistently with the former being more dissipative than the latter (i.e. in the former the quadratic coefficient accounts for further resistance to infiltration) and thus delaying the infiltration process.

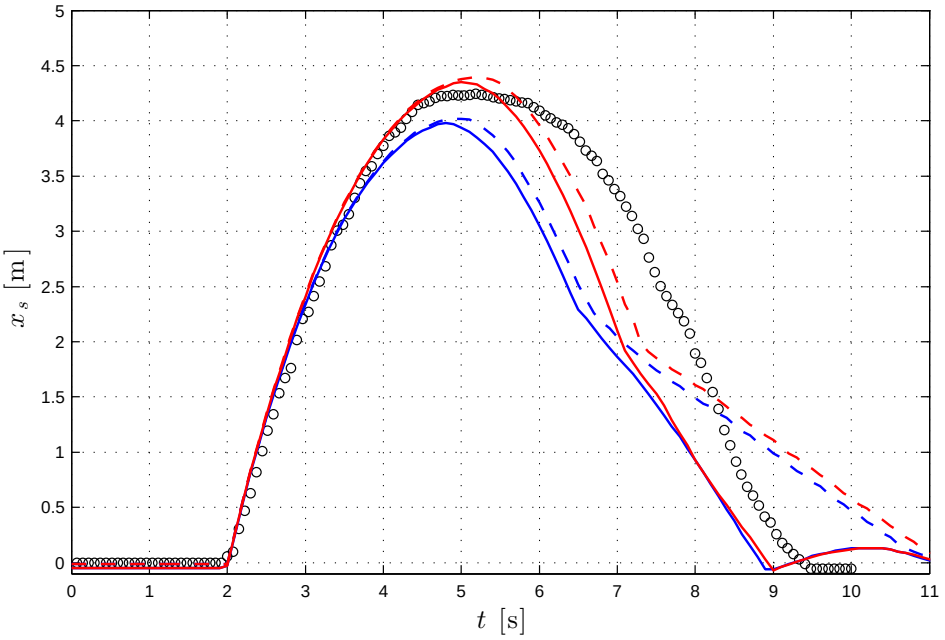

Figure 5.21: Single swash on permeable fixed slope. Comparison of measured and predicted shoreline position time series. Black circles: measured shoreline (resolution at $h = 0.005$ m). Solid lines: predicted shoreline positions tracking the water depth consistent with the measurements ($h = 0.005$ m). Dashed lines: predicted shoreline positions tracking the numerical wet / dry front ($h = 0.001$ m). Blue lines: simulation with the Darcy law. Red lines: simulation with the Forchheimer law.

5.5.3 Concluding remarks

Single swash events on impermeable and permeable fixed slopes are presented for the same sediment, i.e. a coarse sand. Note that Briganti et al. (2011) and Steenhauer et al. (2012b) carried out some numerical simulations (for the two cases respectively) considering also a coarser sediment, i.e. gravel, but no finer bed material. Additionally, very recently Pintado-Patiño et al. (2015)

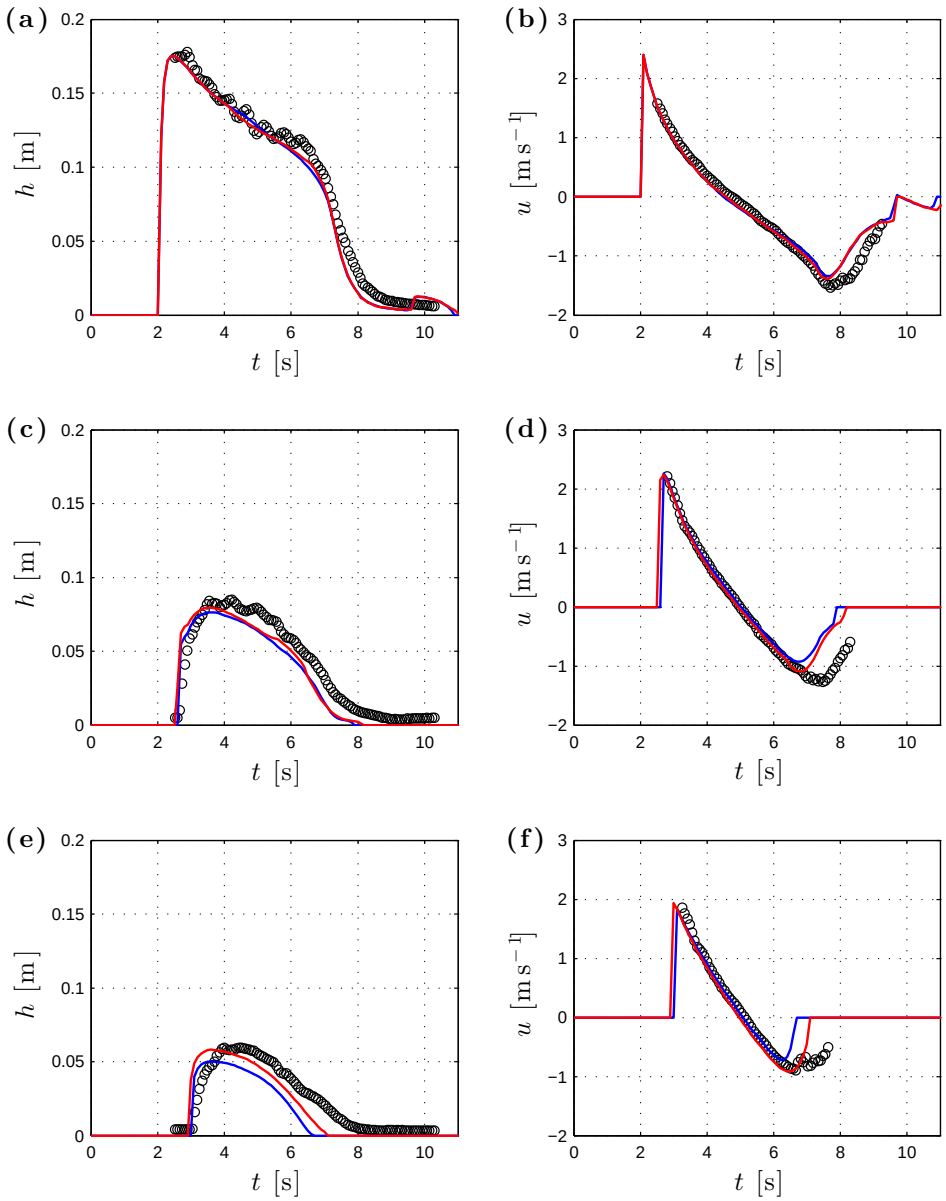

Figure 5.22: Single swash on permeable fixed slope. Comparison of measured and predicted water depth (h) and velocity (u) time series at PIV2 (top row, (a) and (b)), PIV4 (mid row, (c) and (d)) and PIV5 (bottom row, (e) and (f)) locations, using both the Darcy and the Forchheimer resistance laws. Black circles: measured data. Solid lines: predicted h and u time series at selected PIV locations. Blue lines: simulation with the Darcy law. Red lines: simulation with the Forchheimer law.

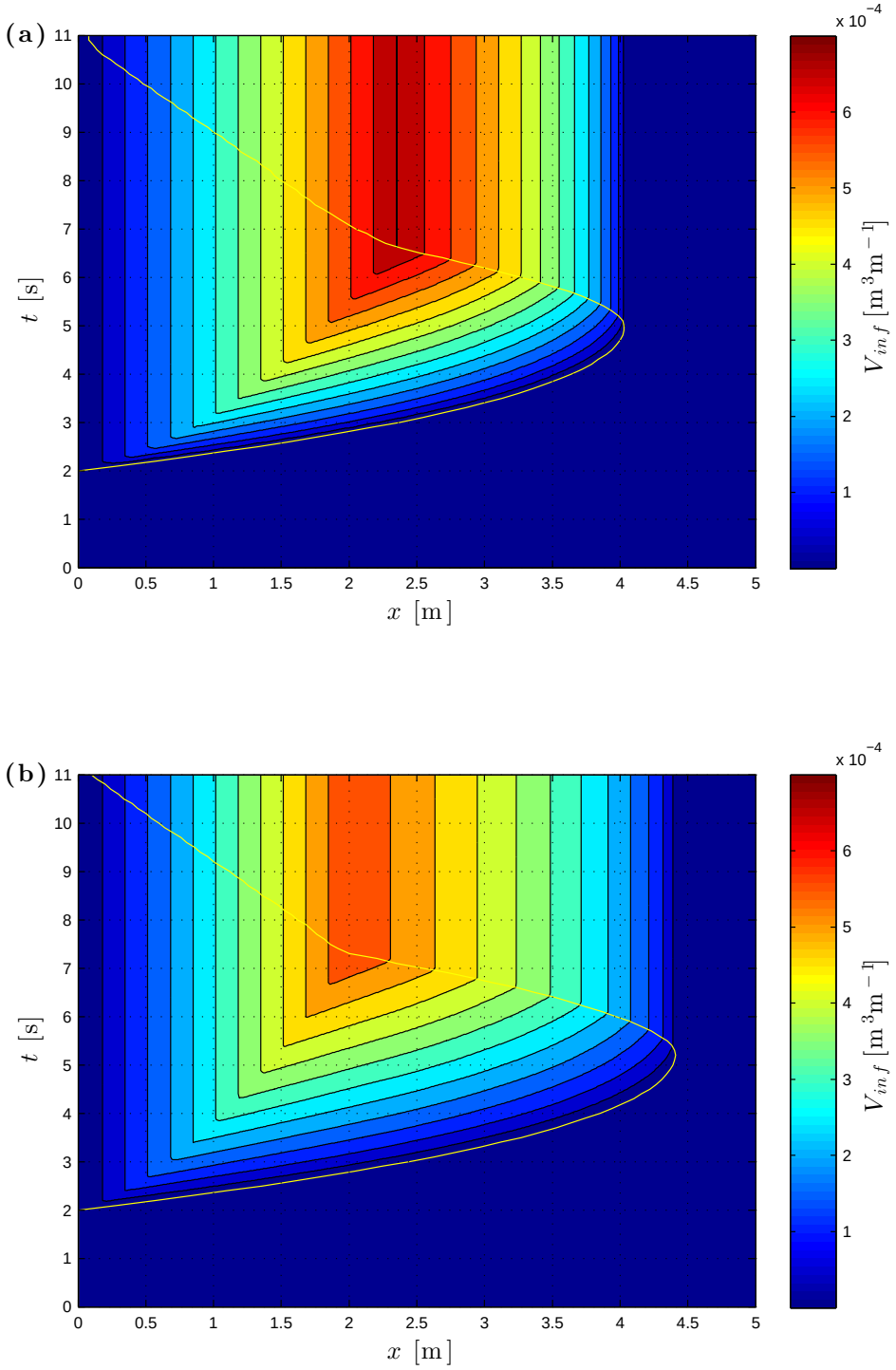

Figure 5.23: Single swash on permeable fixed slope. Time stacks for cumulative infiltrated volume (V_{inf}) using the Darcy and the Forchheimer laws. (a) and (b): results using the Darcy and the Forchheimer laws respectively, with contour lines plotted every 5×10^{-5} m^{3}m^{-1}. A solid yellow line is added to track the numerical wet / dry front in each simulation.

used a complex hydrodynamic only model (which solves the Volume-Averaged Reynolds-Averaged Navier-Stokes equations, with a Volume of Fluid tracking scheme and a k-ϵ turbulence closure, and includes both infiltration and exfiltration) to successfully reproduce both cases, but for the gravel experiment only. Gravel beaches are not examined in this work as only bed-load transport is realistic for them, thus excluding the suspended sediment transport implemented in the model, and because effects of exfiltration and groundwater motion are expected to be more significant (see Steenhauer et al., 2011; Pintado-Patiño et al., 2015).

With reference to the impermeable fixed slope case, the results show overall enhanced compliance with measurements compared to previous ones of Briganti et al. (2011). The extension of the numerical domain to the whole rig, simulating the complete dam break event, seems to play a role in this, especially in the backwash phase of the simulation.

In the permeable fixed slope case, results using both the Darcy and the Forchheimer resistance laws show a good agreement with measurements in the uprush, better with the Forchheimer one, while performance deteriorates during the backwash phase, because of an excess of predicted infiltration. Around 45% and 43% of the water entering the region landward of the initial shoreline, i.e. $x = 0$ m, infiltrate during the whole swash event with the Darcy and the Forchheimer laws respectively, while the corresponding measurement indicates a water loss of around 33% (Kikkert et al., 2013). By the time of the maximum run-up, analogous percentages decrease to around 35% and 32% respectively but remain higher than the experimental evidence, which shows a 20% of percolated water (Steenhauer et al., 2011).

The results confirm Packwood (1983) findings, i.e. the influence of infiltration is minimal in the uprush but more significant in the backwash phase.

However, most of the percolated water is lost by the time of the maximum run-up. The measurements quantify this loss around 60% of the final infiltrated volume, while in the simulations this percentage rises at 78% and 75% with the Darcy and the Forchheimer laws respectively.

Additionally, it is noted that the sensitivity of the results to the particular resistance law does not seem marked, even though the Forchheimer one allows a better performance, consistently with being more appropriate for the considered coarse sand (see Burcharth & Andersen, 1995).

Finally, recall that some processes, e.g. pore-air entrapment and groundwater motion, are not included in the current simulations, aiming at keeping the present approach effective but simple (see also § 3.4.3). These processes were found to have some relevance in the experiments (see Steenhauer et al., 2011), even though they could be partially related to rig-scale effects. Additionally, Steenhauer et al. (2012b) obtained numerical predictions in good agreement with these experiments by means of a hydrodynamic only solver with a complex subsurface flow model (comprising infiltration, exfiltration, horizontal pore-air movement and horizontal groundwater flow). Hence, given the adopted simplified approach for the infiltration prediction, it can be stated that the present model provides a reasonable description of a single swash event on a permeable fixed slope.

Chapter 6

Numerical modelling of field-scale single swash events

6.1 Introduction

This chapter presents a study with the purpose of reproducing observed single swash events from both the hydro- and morphodynamic viewpoints. So far there have been only few attempts to reproduce real swash motions, generally because of their random and three-dimensional character, with related difficulties in accurate wave condition prescription, and of their intermittent and shallow water aspects, which represent a challenge for measurements. Nonetheless, as beach levels primarily vary in the offshore direction, and as wave refraction tends to change wave directions into shore-normal approaching the swash zone, it is reasonable to suppose that a one-dimensional description can be appropriate for some beaches in some circumstances.

Such an approach was used by van Rooijen et al. (2012) to simulate two high tides happened at Le Truc Vert beach on the Atlantic French coast in the early spring of 2008, for which field measurements are available (Blenkinsopp

et al., 2011). Their model consists of the one-dimensional NSWEs, including a diffusion term related to energy dissipation through horizontal eddies and accounting for turbulence due to breaking, plus bed change and suspended load equations, comprising near bed turbulence effects. Additionally, they used measured water levels in about 1 to 1.5 m depth of water (in the surf zone) to drive swash motions at the beachface. Although discrepancies between results and measurements are sometimes substantial, their results are promising in both hydrodynamics and bed change predictions.

In this chapter a similar study is undertaken, but this time focussed on the swash zone only and for single swash events, as operationally defined by Blenkinsopp et al. (2011). This aims at assessing how accurate simulation results for the hydro-morphodynamics can be, provided the level of detail of the measurements from a comprehensive field campaign. Part of this chapter is included in the manuscript Incelli et al. (2015b), currently accepted for publication.

The field campaign and the selected events are briefly described in § 6.2. The modelling approach is outlined in § 6.3, where the adopted assumptions, the required (boundary and initial) conditions and the (physical and numerical) settings are reported. Simulation results are presented in § 6.4 and then compared with data in § 6.5. Sensitivity analyses are illustrated in § 6.6. Finally, findings are discussed in § 6.7 and summarised in § 6.8.

6.2 Field campaign and selected events

6.2.1 Experiment site and instrumentation

The used data-set was specifically collected to enable the analysis of swash hydrodynamics and sediment transport at the time-scale of individual waves and was obtained at Le Truc Vert beach over a spring to spring tidal cycle from 19$^{\text{th}}$ March to 4$^{\text{th}}$ April 2008 as part of the ECORS project (Senechal & Ardhuin, 2008). Le Truc Vert is a long west-facing sandy beach on the Atlantic coast of France. The beach is relatively steep with a typical gradient of around 1:15 and median sediment grain size of approximately 4.0×10^{-4} m. The reader is referred to Blenkinsopp et al. (2011) for further details about the experiment site.

A total of 89 sensors were installed on the beachface (see Fig. 6.1 for an overall visualization), a complete description of which was provided by Masselink et al. (2009), while only instrumentation of interest for this study is presented below.

In particular, three arrays of 15 ultrasonic altimeters (hereinafter UA) were deployed along three, 26.6 m long and 1.9 m alongshore-spaced cross-shore lines on a scaffold frame. They provided surface level (i.e. $h + z_b$) data for both wet and dry regions of the beach with space resolution of 1.9 m (i.e. the UA cross-shore spacing) at intra-wave time resolution (sample frequency of 4 Hz), and their working principles were described by Turner et al. (2008).

The considered data were obtained over the morning high tide on 26$^{\text{th}}$ March, which is thought to provide suitable quasi-one-dimensional swash events, as values recorded by each of the three cross-shore lines of UA are almost identical (see also Blenkinsopp et al., 2011). Therefore, only data from the central line are used in the present study and the 15 UAs are indicated in

Figure 6.1: Instrument deployment at Le Truc Vert beach during the March-April 2008 field measurement campaign. This picture is courtesy of Dr C. Blenkinsopp and originally taken by Prof I. Turner.

Fig. 6.2 with progressive numbers in the landward direction (from UA01 to UA15).

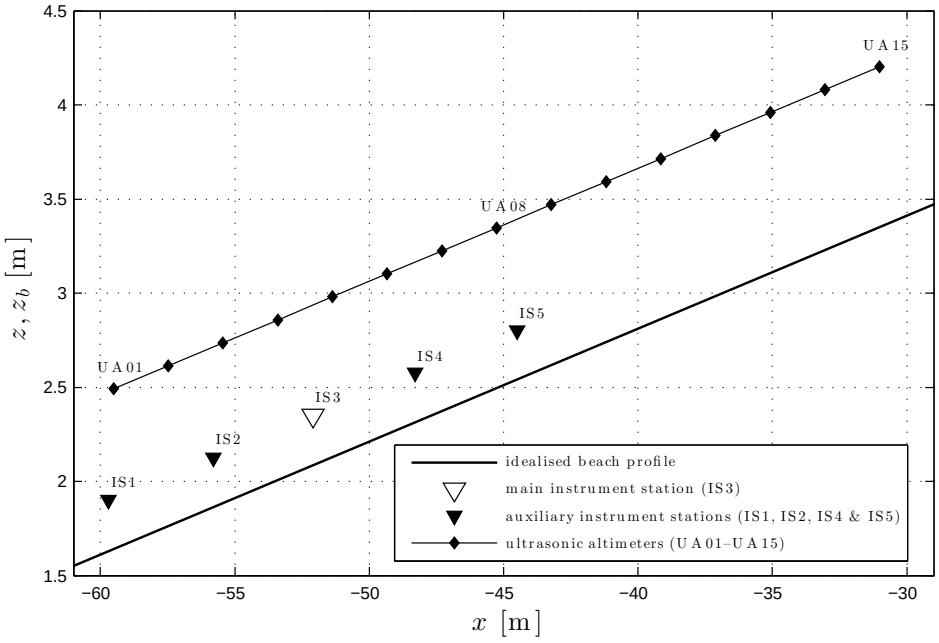

Figure 6.2: Schematic showing the instrument locations during 26$^{\text{th}}$ March, 2008.

Flow velocities were measured at five instrument stations (henceforth IS) located at 3.8 m intervals along the centre of the scaffold frame. They are numbered from IS1 ($x = -59.7$ m) to IS5 ($x = -44.5$ m) in Fig. 6.2. The main IS (i.e. IS3) was installed in the mid high tide swash zone ($x = -52.1$ m) and equipped with four electromagnetic current meters which are able to measure cross-shore flow velocity at elevations 0.03 m, 0.06 m, 0.10 m and 0.14 m above the local bed, while the other four (auxiliary) ones were each equipped with a single electromagnetic current meter deployed 0.06 m above the bed. Note that during the 26$^{\text{th}}$ March tide, the current meters at auxiliary IS1 and IS5 were not working and thus they are not considered in this study.

6.2.2 Selected events

Three events, referred to with a numbering system that reflects the original number considered, are denoted Event 1, 3 and 5, and selected from the data for the aforementioned tide.

They are all single swash events — although sometimes comprising more than one wave / bore — of a reasonable duration (20–30 s), and are firstly selected because of the different kind of final bed change profile they produced. Event 1 generated variable accretion in most of the swash zone; Event 3 caused significant erosion in the lower swash zone but accretion in the upper part; Event 5 produced an erosional profile, especially in the lower swash zone.

Secondly, these events are chosen because complete (or nearly complete) time series for water depth and velocity are available at UA03 / IS2 locations ($x = -55.7$ m / $x = -55.8$ m respectively), which are almost coincident (see Fig. 6.2). These time series are needed as input at the seaward boundary for the numerical simulations. Note that, typically, complete velocity time series are not available.

The initial time for each event is defined such that the initial shoreline position is at UA06 location ($x = -49.9$ m), where water depth is therefore set to zero, following the approach to detect a dried bed described by Blenkinsopp et al. (2011). This choice of relating the initial time to the shoreline location at UA06 is somewhat arbitrary but for both Events 3 and 5 it identifies a time at which velocity time series exist after a sequence of unrecorded values. The same approach is retained for consistency for Event 1 as well.

The duration of each event is limited to a few seconds after the shoreline has retreated seaward of its initial position, in order to be confident that the beachface has returned to a dry state. This allows a consistent comparison between initial and final bed profiles and therefore the computation of the measured final bed change profile.

6.3 Numerical modelling

The employed numerical model is the combined load TVD-MCC solver presented in § 4.3.1. It uses the BBL solver (see Appendix A) for bottom friction calculation and considers bed diffusion (with the formulation with z_b, i.e. Eq. (3.14)), combined load (using the MPM formula for bed-load description) and infiltration (with the Darcy resistance law). The modelling approach is presented in § 6.3.1, which explains the applied boundary and initial conditions, while estimates of the physical parameters and specifications of the numerical settings are examined in § 6.3.2.

6.3.1 Modelling approach

As mentioned in §§ 6.1 and 6.2.1, the actual swash events, including the beach itself, show alongshore variation, but measurements at adjacent alongshore

UA locations confirm a predominant cross-shore character (Blenkinsopp et al., 2011). This observation gives reasonable confidence in the use of the present one-dimensional model, provided that some loss of accuracy in the computed results compared to the field data is acknowledged.

Boundary conditions

The driving seaward boundary is located at UA03 position (see § 6.2.2), where the boundary time series for h and u are available. Note that for modelling purposes the measured velocity values therein (0.06 m above the bed) are interpreted as depth-averaged ones. The prototype scale measurements of Briganti et al. (2011) provide justification for this in the uprush while in the backwash there is some evidence that this could lead to an overestimate of the depth-averaged value. Further comments on this point are provided in § 6.5.

Sometimes, especially when water depth becomes small and a previous significant backwash meets the subsequent uprush, the water velocity time series are incomplete in the later stages of the events. When required, gaps in the time series are filled with values obtained through a piecewise cubic interpolation from adjacent values.

Note also that because single swash events only are considered, the accumulated effects of interpolations are assumed small. Example time series (h and u for Event 1) are shown in Fig. 6.3. Note that hereafter in this chapter only the symbol u is used to refer interchangeably to depth-averaged and (measured) instantaneous values, only distinguishing between these quantities as necessary.

No corresponding information for z_b and c is available at the seaward boundary. Two different approaches were tested, the first not to update bed level and depth-averaged concentration at the driving boundary, and the second to

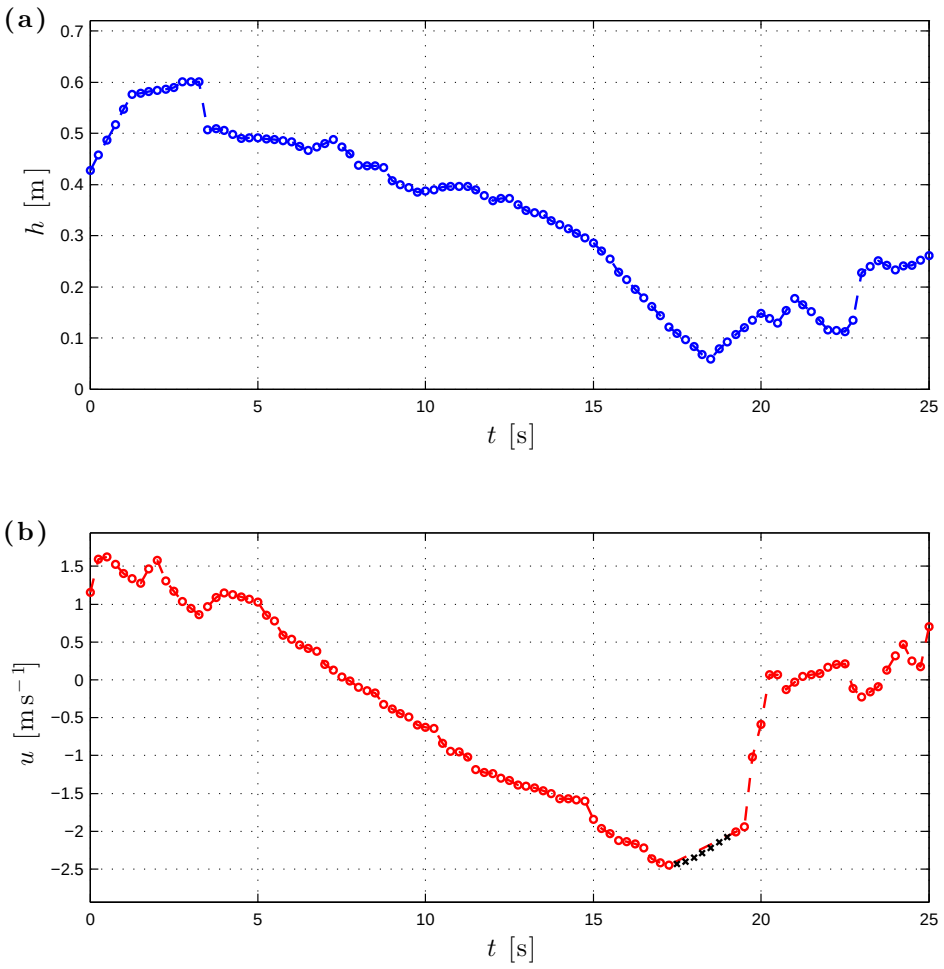

Figure 6.3: Event 1. Data boundary time series. (a): water depth (h). (b): water velocity (u), with black crosses indicating interpolated values.

extrapolate them from the nearest internal point at each time step. Both these approaches led to very similar predictions for bed changes at a distance > 1 m landward of the driving boundary (not shown). Therefore the first of these is used in the simulations.

Note that the driving signals therefore, in theory, include both incoming and reflected components, contrary to the driving signals used by van Rooijen et al. (2012). Recall, however, that in this study the seaward boundary is located at the base of the swash zone, where disentangling these two com-

ponents from field data is more difficult. Additionally, the uprush / backwash of the considered events is expected to primarily consist of shoreward / seaward propagating component, exclusively so if the flow is supercritical. Lastly, because the spatial dimension and (especially) the time durations are considerably reduced, it may be expected that this approach leads to fewer discrepancies because there is no accumulation.

At the other boundary, i.e. the shoreline one, the BCs are those for the wet / dry front treatment presented in § 4.3.3.

Initial conditions

UAs provided values for the surface level, which coincides to the bed level for the initially dry part of the beach and to the water surface for the initially wet one. For the latter, water depths are then computed by subtracting the bed levels recovered from the previous time when the bed was exposed at these locations. At numerical grid points between UA locations, linear interpolation is used to estimate z_b and h.

Initial velocities are not available at all locations, so a spatial distribution is constructed by linear interpolation between the initial value at the seaward boundary and that estimated at the initial shoreline. The latter is calculated by evaluating the time interval for the shoreline position, initially at UA06 location, to reach the first UA further landward (UA07). Note that measurements for velocity at the IS3 location are also not available at the initial time.

Because no reliable or cross-shore measurements of c are available, a zero depth-averaged initial concentration is imposed everywhere. The sensitivity to this assumption is examined in § 6.6.2.

Because of lack of knowledge, the initial BBL thickness is set to zero (no

BBL present), which then rapidly develops as solution progresses.

Measurements concerning the water table within the beach also are not available. It is therefore assumed that the water table is equal to the bed level at the initial shoreline, i.e. at UA06 location. The sensitivity to this assumption is considered in § 6.6.2.

6.3.2 Physical parameters and numerical settings

The physical parameters and numerical settings used in the simulation of the three events are presented below and summarised in Tab. 6.1.

The bed porosity is $p_b = 0.35$, the relative sediment density compared to salted water $s_{rel} = 2.580$ (sediment density $\rho_s = 2,650$ kgm^{-3}, salted water density $\rho_w = 1,027$ kgm^{-3}) and the median sediment diameter $d_{50} = 4.0 \times 10^{-4}$ m (Blenkinsopp et al., 2011). The critical Shields parameter for bed-load is $\theta_{crb} \approx 0.036$, following van Rijn (2007a). As the beach sediment is a medium grain size sand, the angle of repose of sediment $\phi = 33°$ is assumed.

The effective settling velocity $w_s = 0.05$ ms^{-1} is imposed (Blenkinsopp et al., 2011), while the critical friction velocity for suspended load is $U_{f,crs} = \sqrt{\tau_{crs}/\rho_w} \approx 0.025$ ms^{-1} (van Rijn, 1984).

It is more difficult to estimate the parameter for the erosional rate m_e and the representative bed shear stress value τ_{rep}. Zhu & Dodd (2015) made an attempt to find a relationship between erosional and depositional rates for given net onshore flux of sediment entrained in the uprush only of a solitary wave swash event. Although it is difficult to understand to what extent those results can be applied to this field case, they suggest a reasonable range of values for the non-dimensional parameter $m_e^* = m_e / \left(\sqrt{gh_{rep}}(1 - p_b)\right)$, being the representative water depth $h_{rep} = 1$ m. Therefore $m_e = 0.002$ ms^{-1} is chosen, which corresponds to $m_e^* = 0.001$. An analysis on this assumption is

Physical parameters and numerical settings	
Median sediment grain diameter (d_{50})	4.0×10^{-4} m
Bed roughness (k_b)	0.001 m
Bed porosity (p_b)	0.35
Angle of repose of sediment (ϕ)	33°
Salted water density (ρ_w)	$1,027$ kgm^{-3}
Relative density of sediment (s_{rel})	2.580
The critical Shields parameter for bed-load (θ_{crb})	0.036
Erosional rate parameter (m_e)	0.002 ms^{-1}
Critical friction velocity for suspended load ($U_{f,crs}$)	0.025 ms^{-1}
Representative scale for velocity (u_{rep})	$\sqrt{gh_{rep}}$ ms^{-1}
Representative scale for water depth (h_{rep})	1.00 m
Friction coefficient for τ_{rep} estimate (f_c)	0.01
Effective settling velocity (w_s)	0.05 ms^{-1}
Darcy hydraulic conductivity (k_{inf})	0.001 ms^{-1}
Domain length (L_x)	25 m
Spatial step size (Δx)	0.01 m
Courant Number (CN)	0.50
Minimum water depth parameter (h_{min})	0.001 m
Duration of the simulation	25 / 25 / 33 s

Table 6.1: All events. Physical parameters and numerical settings used in the simulations. '/' separates alternative values for the three simulated events.

provided in § 6.6.1.

Additionally, $\tau_{rep} = \rho_w f_c/2\ u_{rep}^2$ is taken, with $u_{rep} = \sqrt{gh_{rep}}$ and $f_c = 0.01$, the latter being justified by a preliminary analysis, reported for convenience in Appendix E.

In the BBL solver an estimate of the bed roughness k_b is needed. Its value

is usually related to the sediment grain size at various percentiles (see van Rijn, 1982, among others). Following previous work of van Rooijen et al. (2012), it is assumed that $k_b = 2.5\, d_{50} = 0.001$ m.

To simulate infiltration, a hydraulic conductivity of the sediment k_{inf} of 0.001 ms^{-1} is employed, following the guidance for a medium sand proposed by Packwood & Peregrine (1980).

Finally, $L_x = 25$ m, $\Delta x = 0.01$ m, $CN = 0.50$ and $h_{min} = 0.001$ m are used. The latter value appears to be a reasonable one as it agrees with the measured level vertical resolution.

6.4 Simulation results

In this section, results for each event are presented, including a brief description of the hydro-morphodynamics and a quantification of the infiltration.

6.4.1 Event 1

Fig. 6.4 shows the time stacks for the dependent variables for Event 1. The hydrodynamics presents a large event generated by a single bore. The water retreats slowly as a thin film in the backwash, due to the effect of friction. Bed change contours display some deposition in the upper swash with significant erosion in the lower swash zone. The suspended sediment concentration increases rapidly in the uprush phase, drops at flow reversal and peaks again in late backwash, consistently with the development of the BBL.

Fig. 6.5 presents the time stack for V_{inf}, defined by Eq. (5.18). The final volume of percolated water is 0.418 $\mathrm{m}^3\mathrm{m}^{-1}$, which corresponds to approximately the 15.7% of the total volume that enters the region landward of the initial shoreline during the whole event.

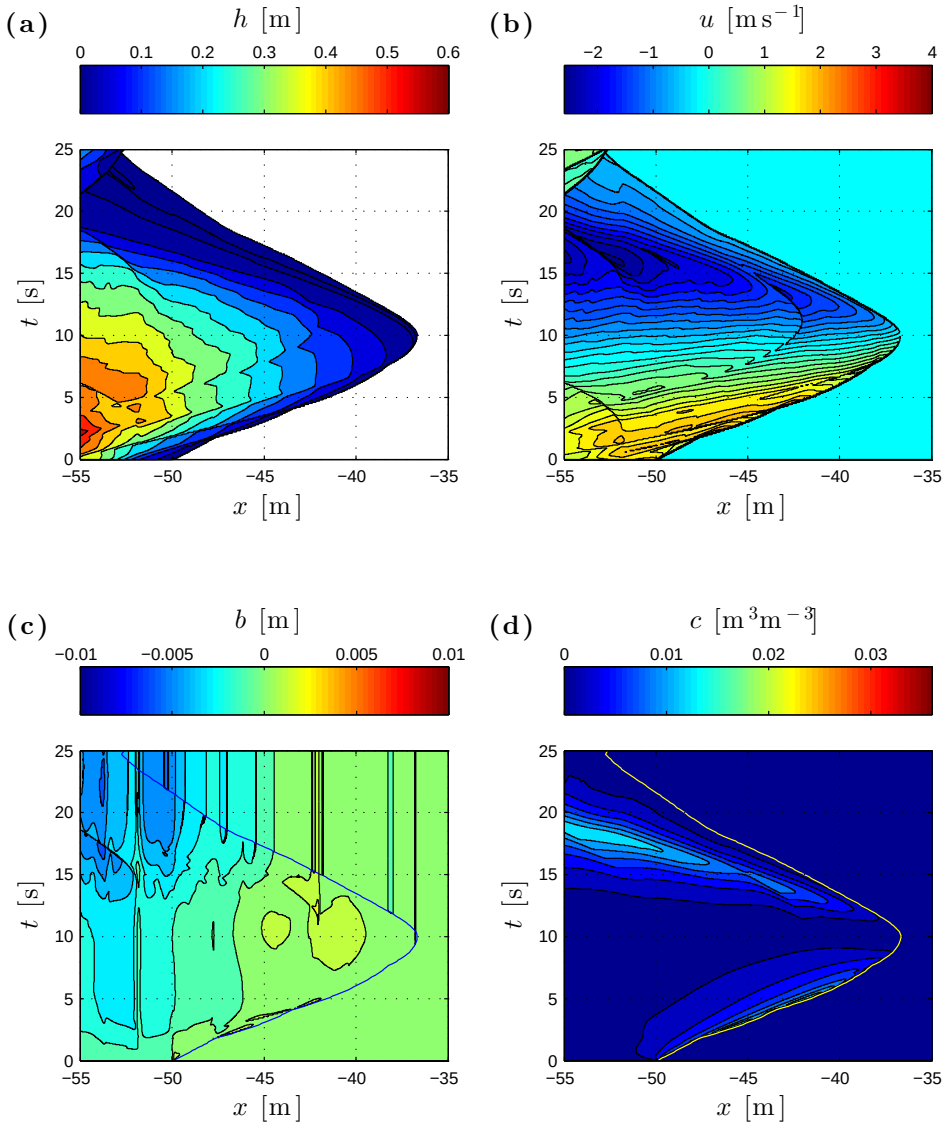

Figure 6.4: Event 1. Time stacks. (a): water depth (h), with contour lines for $h = 0.001$, 0.005, 0.01 and 0.05 m and then plotted with a 0.05 m interval. (b): velocity (u), with contour lines every 0.2 ms^{-1}. (c): bed change (b), with contour lines every 0.001 m. (d): suspended sediment concentration (c), with contour lines every 0.002 $\mathrm{m}^3\mathrm{m}^{-3}$. A line tracking the numerical shoreline is added for convenience in (c) and (d) in blue and yellow respectively.

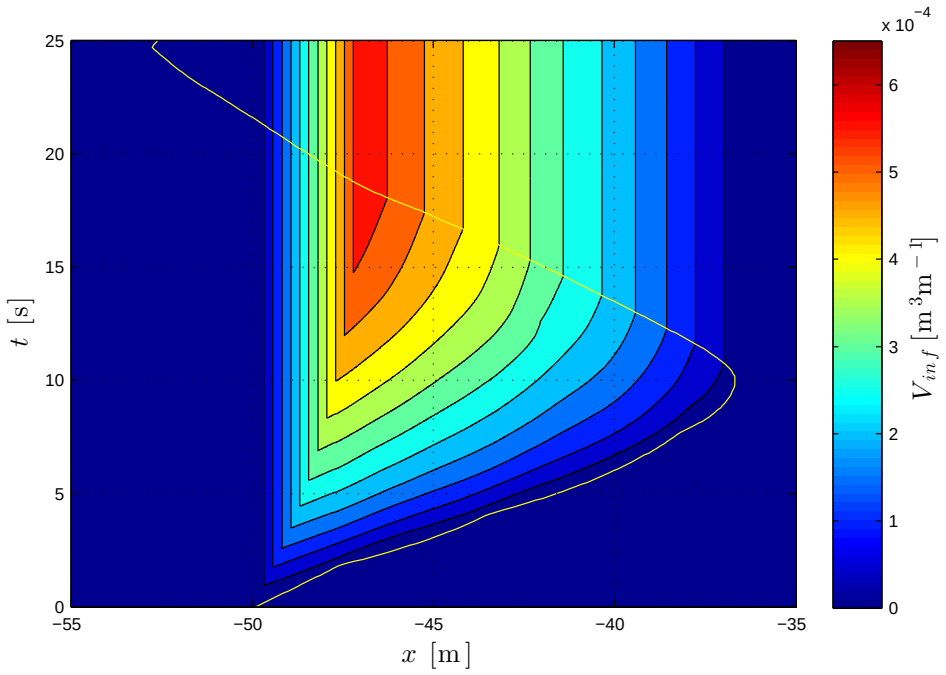

Figure 6.5: Event 1. Time stack for cumulative infiltrated volume (V_{inf}), with contour lines plotted every 5×10^{-5} m^{3}m^{-1}. A yellow line tracking the numerical shoreline is added for convenience.

6.4.2 Event 3

Fig. 6.6 shows the time stacks for the dependent variables for Event 3. The swash event is produced by two subsequent bores. The second one reaches its maximum run-up while water from the first one has already started receding. Significant deposition in the upper swash and noticeable erosion in the lower swash zone are highlighted by the bed change contours. The suspended sediment concentration rises quickly in the uprush phase, reaching values greater than twice the maximum ones in Event 1, indicating that Event 3 is much more energetic than the previous one. The evolution of c then follows the same behaviour as for Event 1.

The equivalent plot for V_{inf} is shown in Fig. 6.7 and it is qualitatively similar to that for Event 1. The final volume of percolated water is 0.427 m^{3}m^{-1} (16.9% of the water entering the region landward of the initial shoreline).

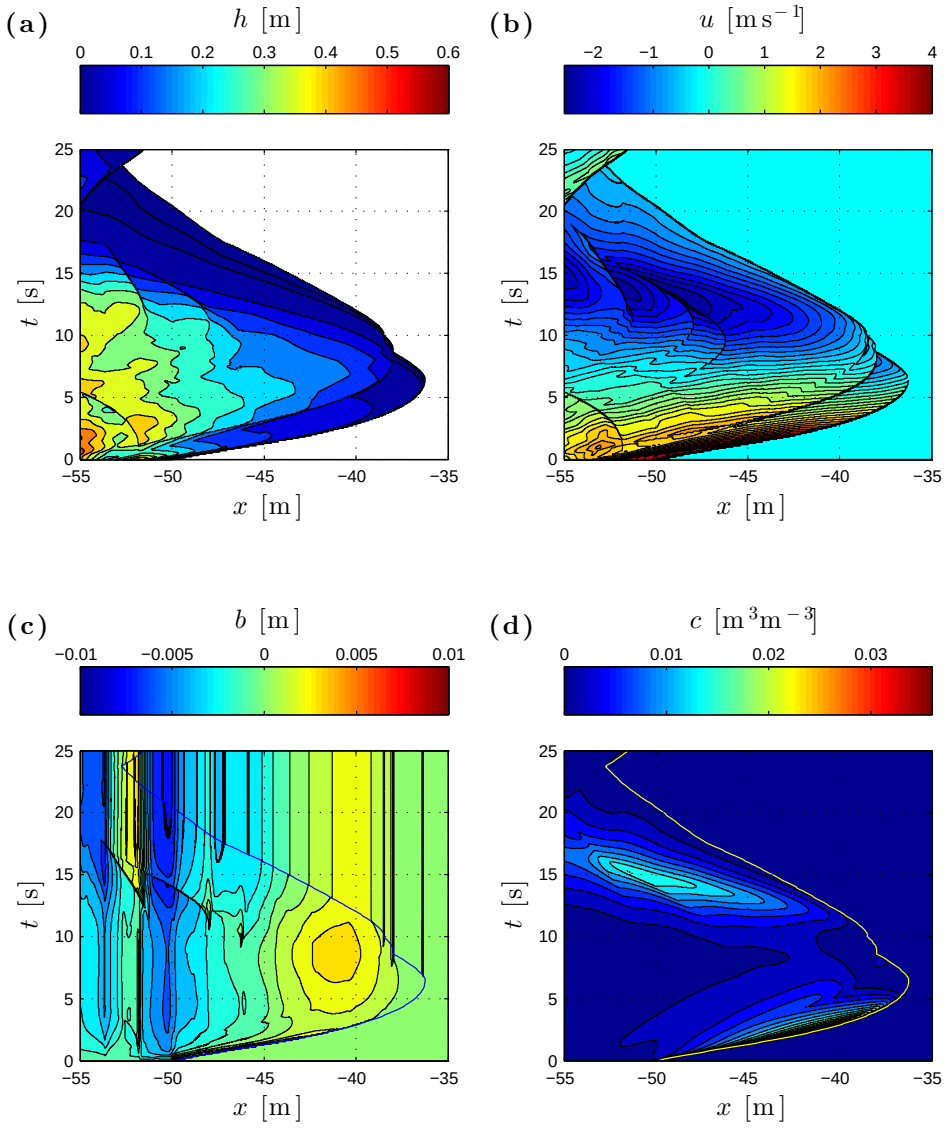

Figure 6.6: Event 3. Time stacks. (a): water depth (h), with contour lines for $h = 0.001$, 0.005, 0.01 and 0.05 m and then plotted with a 0.05 m interval. (b): velocity (u), with contour lines every 0.2 ms^{-1}. (c): bed change (b), with contour lines every 0.001 m. (d): suspended sediment concentration (c), with contour lines every 0.002 $\mathrm{m}^3\mathrm{m}^{-3}$. A line tracking the numerical shoreline is added for convenience in (c) and (d) in blue and yellow respectively.

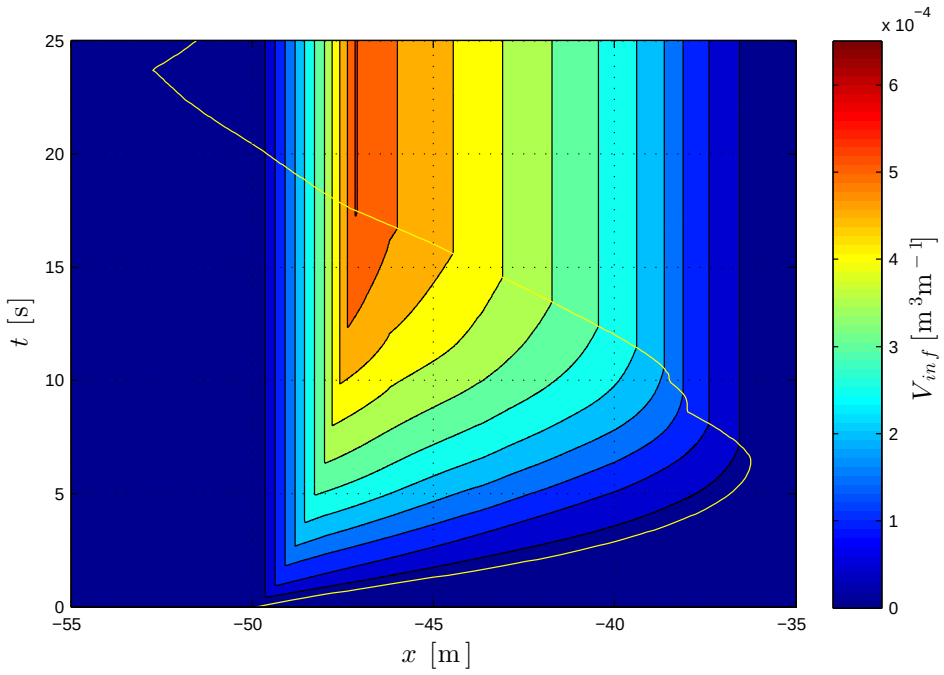

Figure 6.7: Event 3. Time stack for cumulative infiltrated volume (V_{inf}), with contour lines plotted every 5×10^{-5} m^3m^{-1}. A yellow line tracking the numerical shoreline is added for convenience.

6.4.3 Event 5

Three consecutive bores, the first of them smaller than the following two, are included in Event 5 (see Fig. 6.8). Little accretion is observed in the upper swash while erosion is predicted in the lower swash zone. The first bore produces no significant amount of suspended sediment transport. Then the suspended load increases during uprush and backwash phases of the other waves and hits its maximum concentration in the last uprush phase.

Fig. 6.9 shows once more the infiltration process, with the three bores apparent. The final volume of percolated water is 0.329 m^3m^{-1} (16.6% of the water entering the region landward of the initial shoreline). This relatively small amount of water, compared to 0.418 m^3m^{-1} and 0.427 m^3m^{-1} of the two previous events, could be caused by the smaller maximum run-up in this event, which means reduced time and pore space available for infiltration.

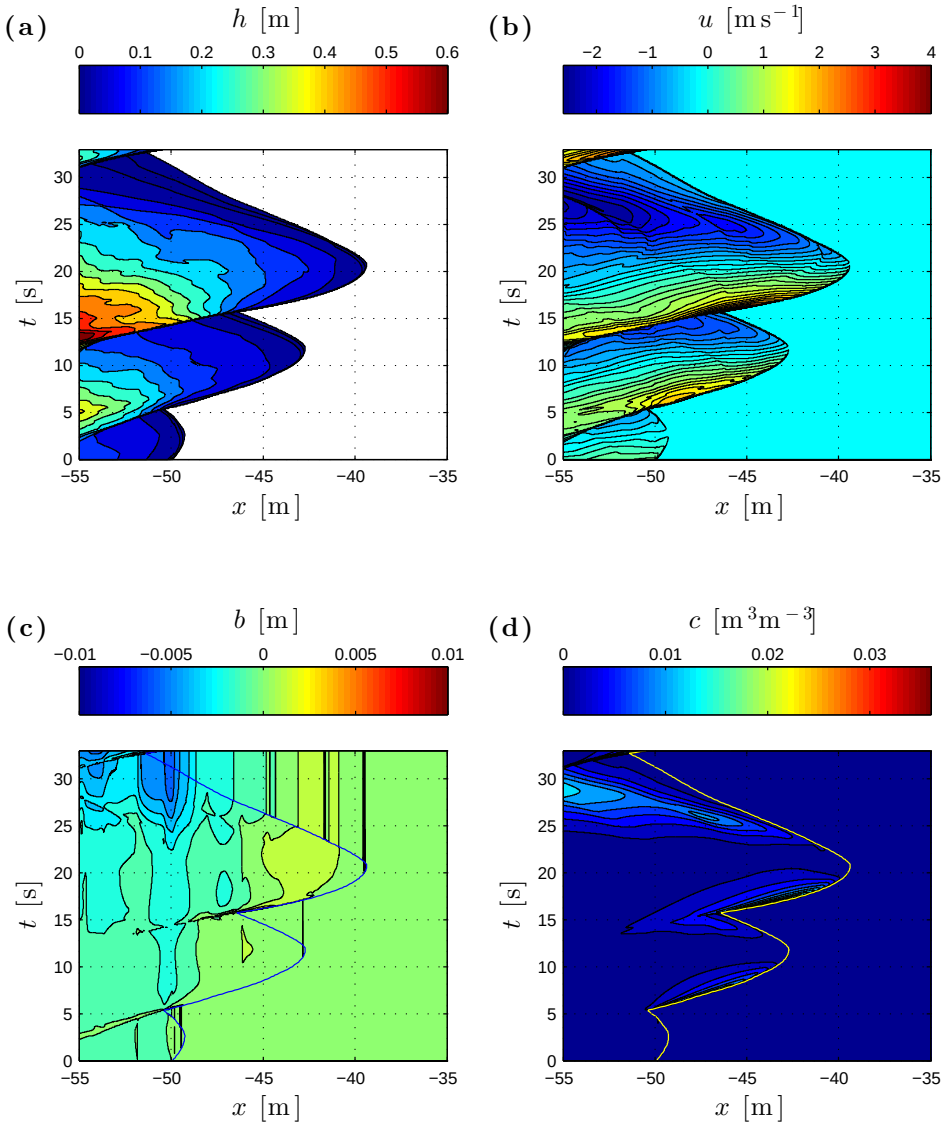

Figure 6.8: Event 5. Time stacks. (a): water depth (h), with contour lines for $h = 0.001$, 0.005, 0.01 and 0.05 m and then plotted with a 0.05 m interval. (b): velocity (u), with contour lines every 0.2 ms^{-1}. (c): bed change (b), with contour lines every 0.001 m. (d): suspended sediment concentration (c), with contour lines every 0.002 $\mathrm{m}^3\mathrm{m}^{-3}$. A line tracking the numerical shoreline is added for convenience in (c) and (d) in blue and yellow respectively.

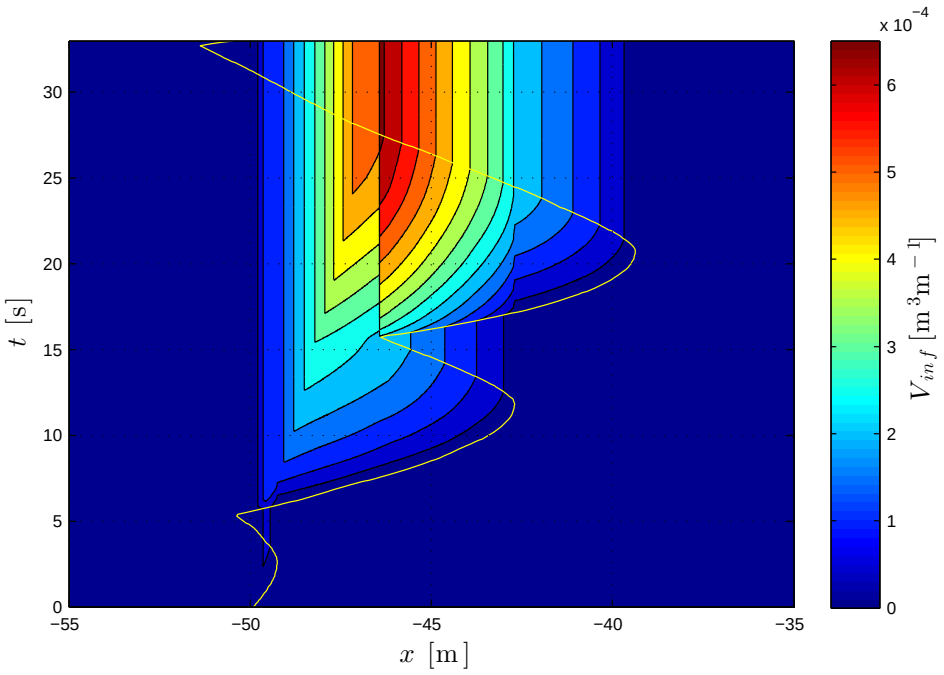

Figure 6.9: Event 5. Time stack for cumulative infiltrated volume (V_{inf}), with contour lines plotted every 5×10^{-5} $\mathrm{m^3m^{-1}}$. A yellow line tracking the numerical shoreline is added for convenience.

6.5 Comparison with data

In this section, comparisons between data and numerical results are shown in terms of surface level and velocity time series, and of final bed change profiles.

Figs. 6.10, 6.11 and 6.12 show comparisons between the measured surface levels and the computed ones for Events 1, 3 and 5 respectively. The numerical results compare quite well with the data in all three events, notwithstanding all the uncertainties mentioned in § 6.3.1. All simulated events exhibit smaller maximum run-ups, in particular Event 3. The missing water depth between the measured and the computed maximum levels is never more than 0.06 m and generally around 0.03 m. For Events 1 and 5, some lag in the uprush phases can be observed starting from lower UA locations and increasing slightly landward. This lag can be noticed in the backwash phases of both events as well, but to a smaller extent. Note, however, that the reduced water in the upper swash

zone results in the numerical signal leading the measured one in the backwash. On the other hand, nearly no lag can be seen for Event 3 in the uprush.

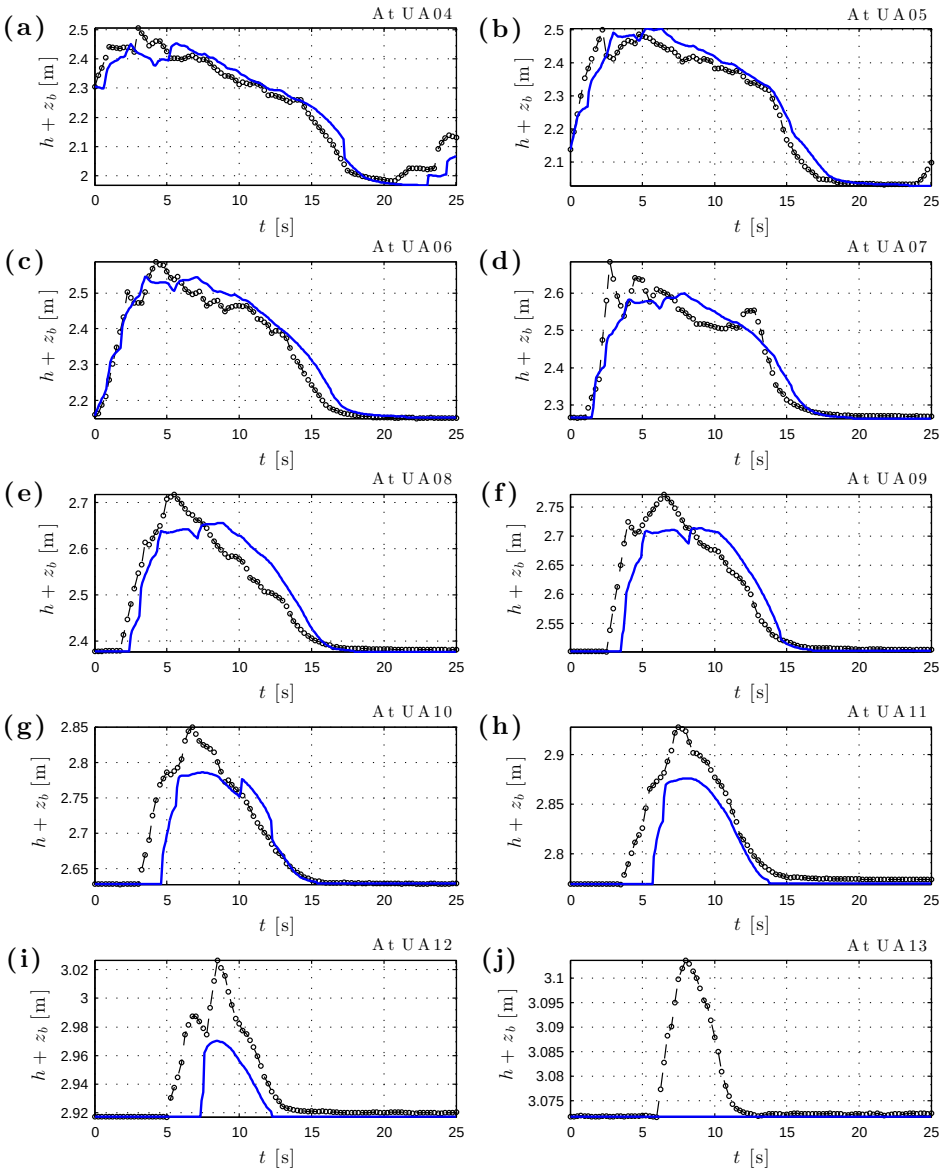

Figure 6.10: Event 1. Comparison of surface level ($h + z_b$) time series at UA locations. Dashed black line with circles: data. Solid blue line: computed results.

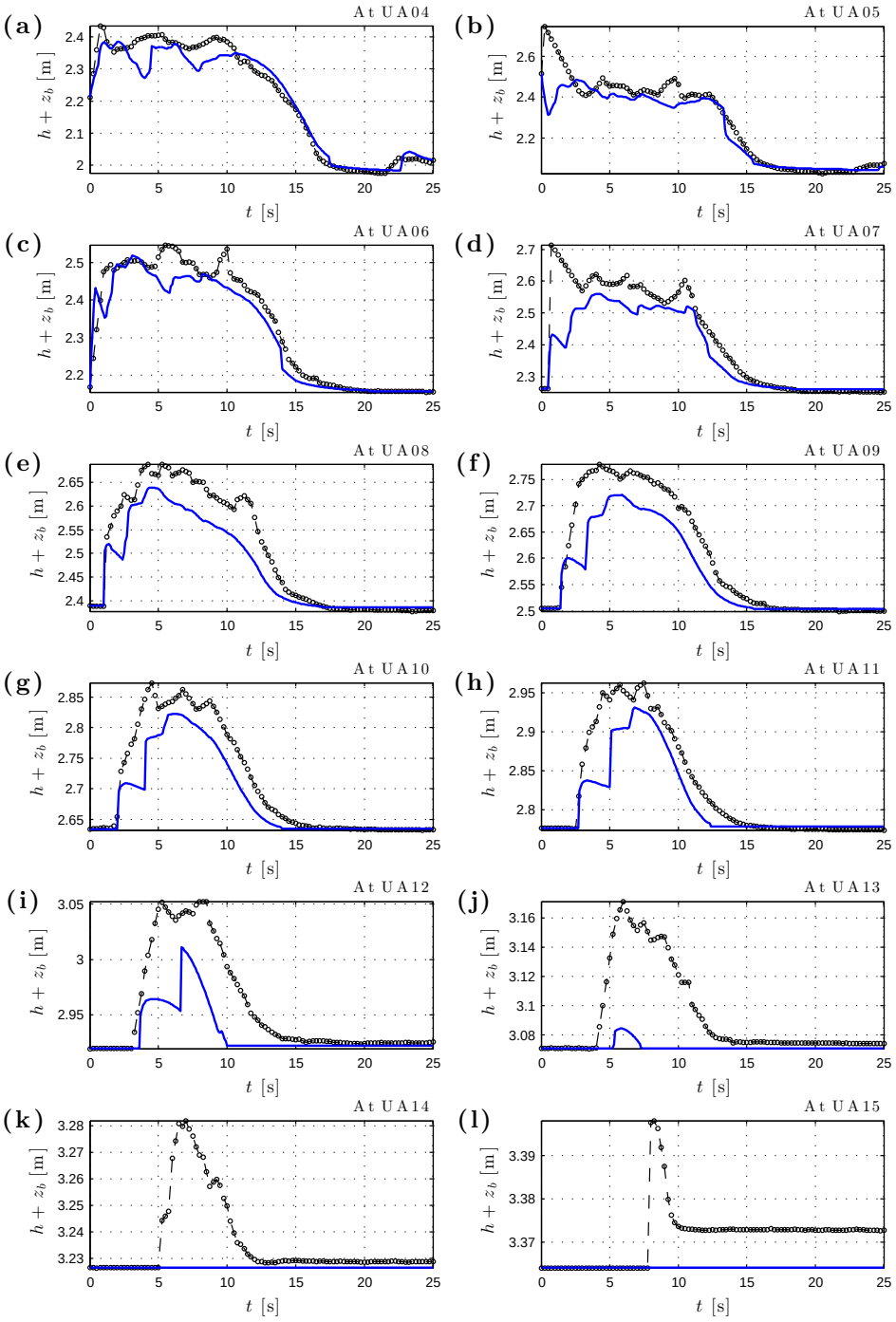

Figure 6.11: Event 3. Comparison of surface level ($h + z_b$) time series at UA locations. Dashed black line with circles: data. Solid blue line: computed results.

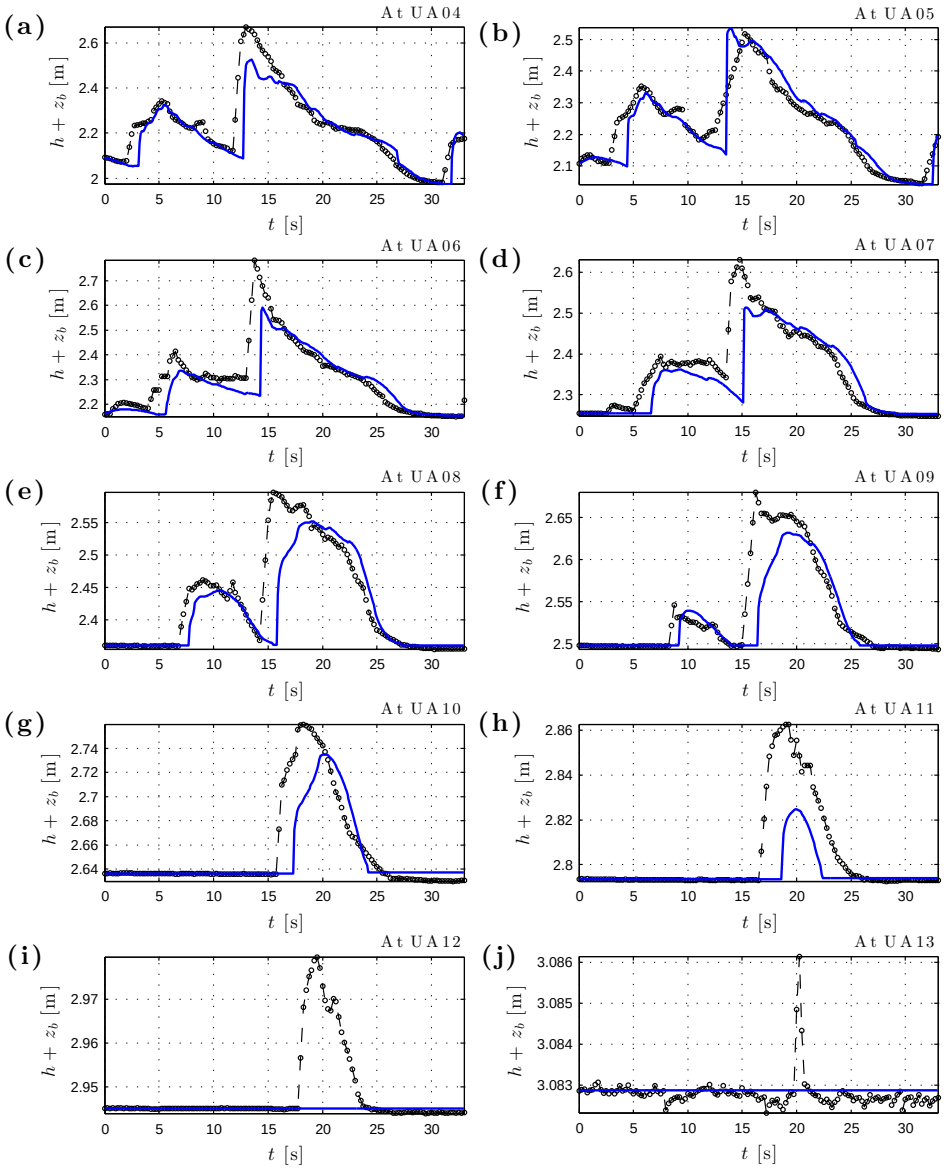

Figure 6.12: Event 5. Comparison of surface level ($h + z_b$) time series at UA locations. Dashed black line with circles: data. Solid blue line: computed results.

When IS3 remains submerged for a long enough time to let velocity data be recorded by the current meters, it is possible to compare predicted velocities with measured ones (see Fig. 6.13). The measured velocities at different elevations overall show similar values for most of the time series and are in general good agreement with the computed ones.

This indicates that the use of raw velocities (0.06 m above the bed, at IS2; see § 6.3.1) as depth-averaged driving boundary values nonetheless enables the numerical model to capture the hydrodynamics reasonably well. Additionally Fig. 6.13 shows that, indeed, for most of the swash cycle depth-averaged velocities represent well values measured over the water column.

To display the morphodynamic effects of the simulated swash events, final profiles of measured and computed bed changes are shown in Fig. 6.14 landward of the initial shoreline location. Considering this region ensures that all measured changes are due to the considered event only (recall that in the initially wet part of the domain, z_b values are recovered from previous time when the bed was exposed, therefore more uncertainty is related to them).

In Event 1 the computed deposition is much smaller than that measured, and some erosion is apparent in the lower swash zone. In Event 3 the numerical results seem to reproduce the overall morphodynamic pattern (i.e. erosion in the lower swash zone, deposition in the upper one), although the amount of bed change is reduced. In particular, the reduced maximum run-up confines the accretion such that it is more seaward than that measured in the field, which progressively increases landward. In Event 5 the generally erosive event (the three bores) is only reproduced in a bulk sense, with far more erosion occurring in the field measurements.

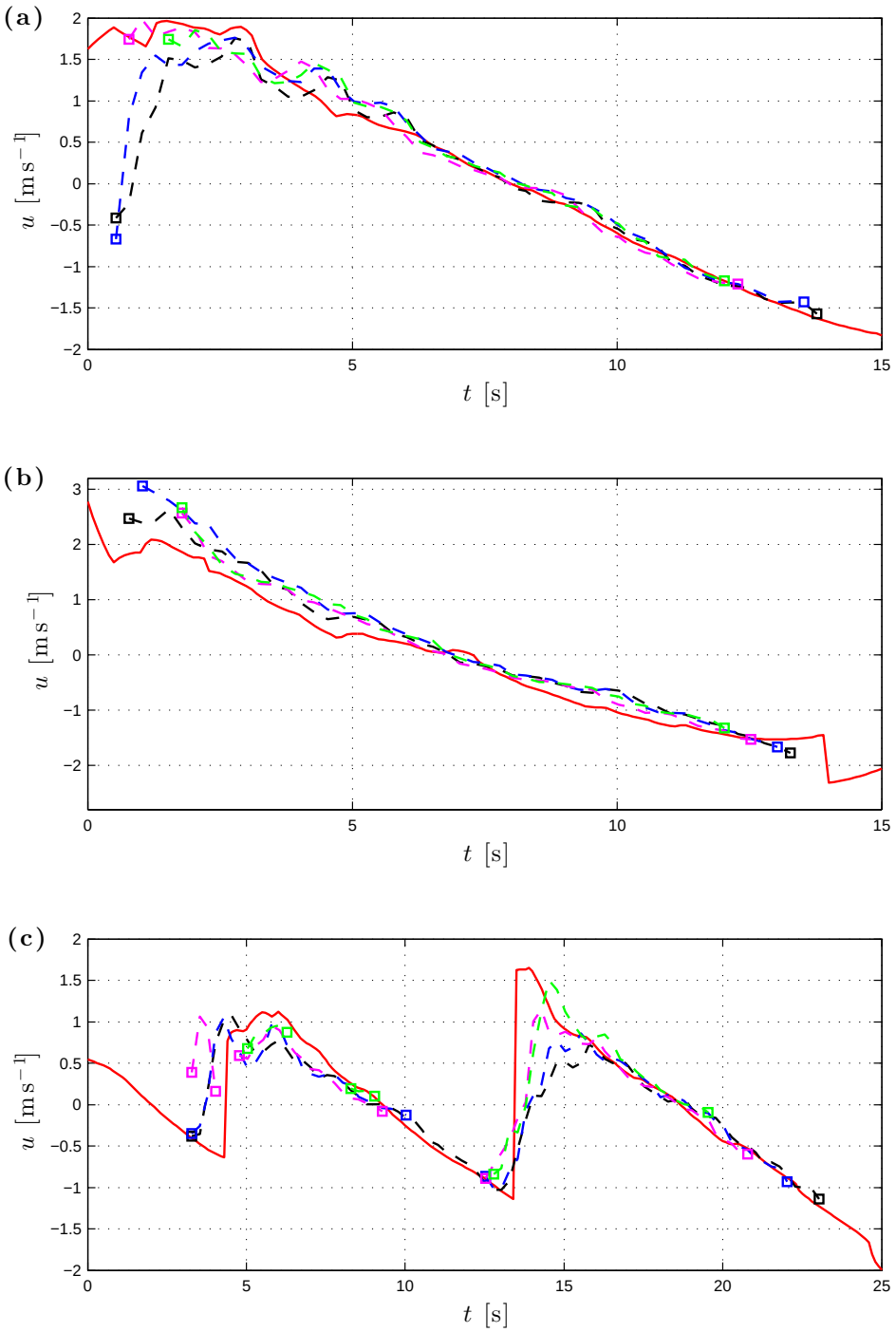

Figure 6.13: All events. Comparison of velocity (u) time series at IS3 location. (a): Event 1. (b): Event 3. (c): Event 5. Dashed lines: data at elevations of 0.03 m (black), 0.06 m (blue), 0.10 m (magenta) and 0.14 m (green) above the bed level. Empty squares, coloured according to the dashed lines, indicate first and last values of interval(s) of the measured time series with recorded values. Solid red line: computed results (depth-averaged values).

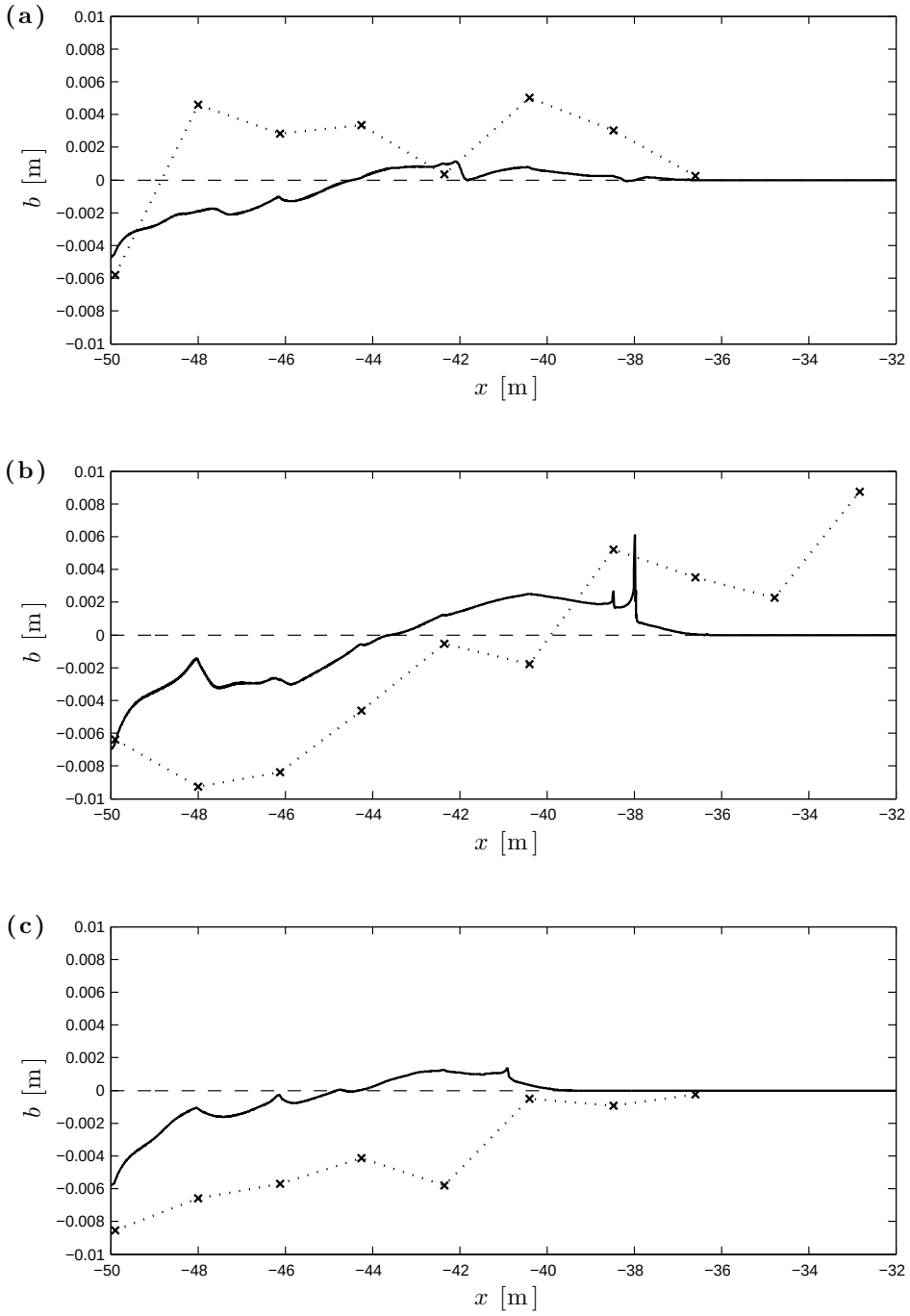

Figure 6.14: All events. Comparison of final bed change (b) profiles. (a): Event 1. (b): Event 3. (c): Event 5. Dotted black line with crosses: data at UA locations. Dashed black line: no change line. Solid black line: computed results.

6.6 Sensitivity analyses

As mentioned, some elements of the modelling have little or no site data to provide estimates of initial conditions (u, c) or of parameter values (m_e, k_{inf}). Other variables (h, z_b) and parameters (d_{50}, p_b, ϕ, k_b, w_s) are considered reasonably well estimated.

About BCs, it could be argued that those for z_b and c are inadequately defined, but a limited region of influence of them (within 1 m landward of the open boundary) was found in preliminary testing, at least for durations of the simulation of the order of the present ones (see § 6.3.1).

From the numerical viewpoint, there could be an influence of the particular applied flux limiter (Minmod), even though, according to previous results presented in § 5, the effects are not expected to be substantial, due to the reduced durations of the simulations. The sensitivity of results to other numerical settings, as Δx or h_{min}, is not considered, as the adopted values are thought to be already at their reasonable limits, provided the level of accuracy of the measurements.

Sensitivity analyses are focussed on Event 3, as this is the most energetic one (see Fig. 6.6) and yielded significant bed changes (see mid panel of Fig. 6.14) over most of the swash region for both data and simulation. Results for Event 3 shown in Fig. 6.11 and in panel (b) of Fig. 6.14, along with the corresponding chosen parameters and settings, are referred to as default ones in the following.

6.6.1 Sensitivity to physical parameters

The parameter for the erosional rate m_e is the least well determined of all parameters and it is originally set equal to 0.002 ms^{-1}. Fig. 6.15 shows results obtained halving or doubling the m_e value (0.001 and 0.004 ms^{-1} respectively).

It can be seen that the overall pattern of erosion / deposition is unchanged. This is consistent with Zhu & Dodd (2015), who also noted that this parameter affects primarily the amount of erosion / deposition (per unit time) rather than the pattern, unless the flow is significantly affected by the bed change. These values of m_e span a range of m_e^* values between 5×10^{-4} and 0.002 (see Fig. 16 at page 130 of Zhu & Dodd, 2015). The largest value corresponds to the uprush movement of around 60 kgm^{-1} of sand in their investigation, which is consistent with field observations (see Blenkinsopp et al., 2011).

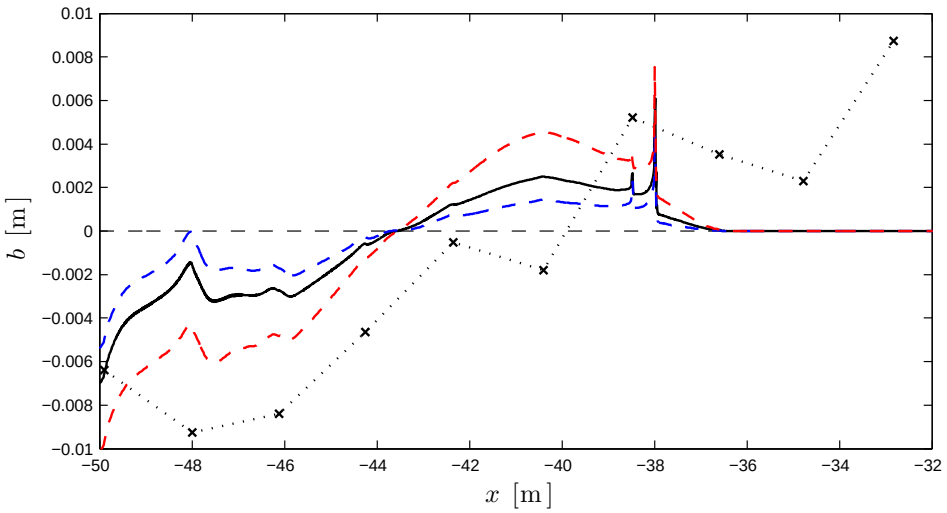

Figure 6.15: Event 3. Sensitivity of final bed change (b) profile to m_e. Results with different m_e values. Dotted black line with crosses: data at UA locations. Dashed black line: no change line. Solid black line: computed results with $m_e = 0.002$ ms^{-1} (default). Dashed blue line: computed results with $m_e = 0.001$ ms^{-1}. Dashed red line: computed results with $m_e = 0.004$ ms^{-1}.

Additionally, the possibility of different m_e values for the uprush and the backwash phases is considered, which are indicated in the following as $m_{e,up}$ and $m_{e,bw}$ respectively, and their ratio is defined as $R_{ent} = m_{e,up}/m_{e,bw}$.

Fig. 6.16 shows results obtained with $m_{e,up} = 0.004$ ms^{-1} and different R_{ent} values (note that $R_{ent} = 1$ means $m_{e,up} = m_{e,bw}$). The results exhibit an apparent sensitivity to R_{ent}, with increased / reduced erosion in the lower and mid swash zone for lower / higher R_{ent} value, consistent to the fact of

enhancing / diminishing erosion efficiency in the backwash compared to that in the uprush.

Fig. 6.17 displays final profiles for the bed change for two different $m_{e,up}$ values (i.e. 0.004 ms^{-1} and 0.008 ms^{-1}) and for three different R_{ent} ones. A maybe interesting feature is that there is a common point around which profiles for a given R_{ent} rotate. It appears to roughly signpost the transition from the erosional area to the depositional one and shifts seaward when a bigger R_{ent} value is adopted.

However, the adoption of different parameter values for the two phases is not ideal in terms of best modelling practice. The present research approach aims at minimising the deterministic interferences by the modeller on the results, i.e. using event-specific knowledge to tune the model for a best fitting, not least because the uncertainties in the data could undermine meaningful conclusions. Therefore, previous results are presented as part of the work undertaken and mainly because they confirm that the use of different m_e values for uprush and backwash affects primarily the amount of bed change rather than the morphodynamic pattern.

Less uncertain is the hydraulic conductivity k_{inf}, however accurate estimates of it could be an issue for a field site. Thus, in Fig. 6.18 default results are compared with those for an impermeable beach. Both erosion and deposition increase in the lower and upper swash zone respectively, however the difference is not substantial from the morphodynamic viewpoint. Some improvements are observed in the hydrodynamics in terms of extended maximum run-up (not shown), which allows deposition to occur further landward.

Note that the chosen default value for k_{inf} leads to substantially uniform infiltrated volume percentages (between 15% and 17%) of the water entering the region landward of the initial shoreline. These, for a sandy beach with

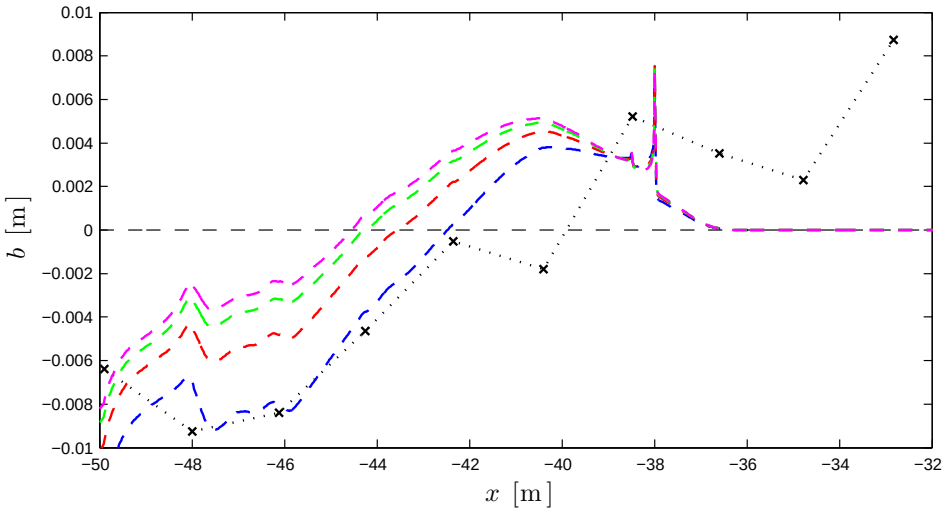

Figure 6.16: Event 3. Sensitivity of final bed change (b) profile to m_e. Results with $m_{e,up}$ fixed at 0.004 ms^{-1} and different R_{ent} values. Dotted black line with crosses: data at UA locations. Dashed black line: no change line. Other dashed lines: computed results with $R_{ent} = 1/2$ (blue), $R_{ent} = 1$ (red), $R_{ent} = 2$ (green) and $R_{ent} = 4$ (magenta) respectively.

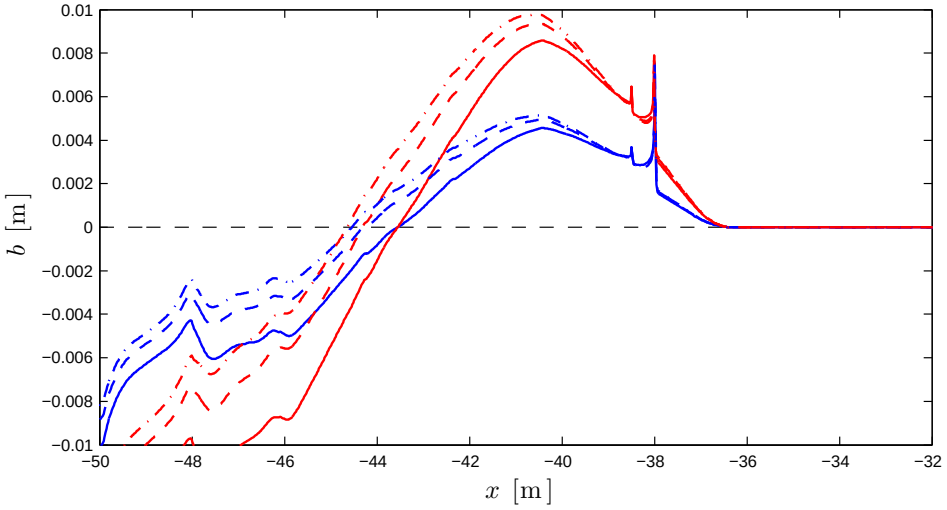

Figure 6.17: Event 3. Sensitivity of final bed change (b) profile to m_e. Results for two different $m_{e,up}$ values and three different R_{ent} ones. Dashed black line: no change line. Solid lines: $R_{ent} = 1$. Other dashed lines: $R_{ent} = 2$. Dot-dash lines: $R_{ent} = 4$. Blue lines: computed results with $m_{e,up} = 0.004$ ms^{-1}. Red lines: computed results with $m_{e,up} = 0.008$ ms^{-1}.

$d_{50} = 4.0 \times 10^{-4}$ m, seem consistent with that value (33%) measured by Kikkert et al. (2013) in a flume for a coarser sand ($d_{50} = 1.3 \times 10^{-3}$ m).

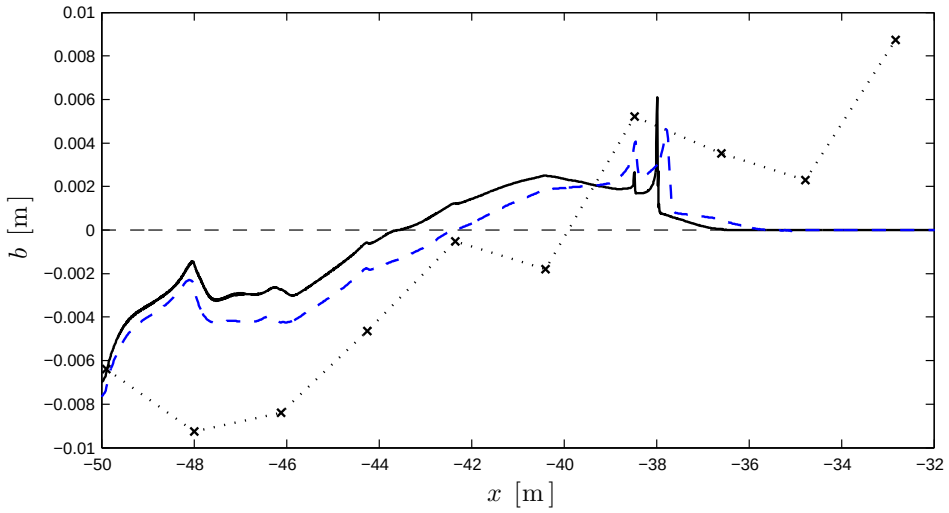

Figure 6.18: Event 3. Sensitivity of final bed change (b) profile to infiltration. Dotted black line with crosses: data at UA locations. Dashed black line: no change line. Solid black line: computed results for permeable beach with $k_{inf} = 0.001$ ms^{-1} (default). Dashed blue line: computed results for impermeable beach.

Finally, other values for the bed roughness k_b around the default one ($k_b = 0.001$ m) are used, but differences between the time series of the predicted surface levels are found to be negligible (see Fig. 6.19). Additionally, Fig. 6.20 shows that the overall morphodynamic pattern remains unchanged, confirming a reduced sensitivity to the bed roughness.

6.6.2 Sensitivity to initial conditions

The reconstruction procedure to obtain the initial velocity profile is described in § 6.3.1. To account for the related uncertainties, a markedly different but still physically plausible initial velocity profile is obtained as follows. Instead of estimating a non-zero velocity at the initial shoreline, its value is set to zero there. Then intermediate values between the seaward boundary and the

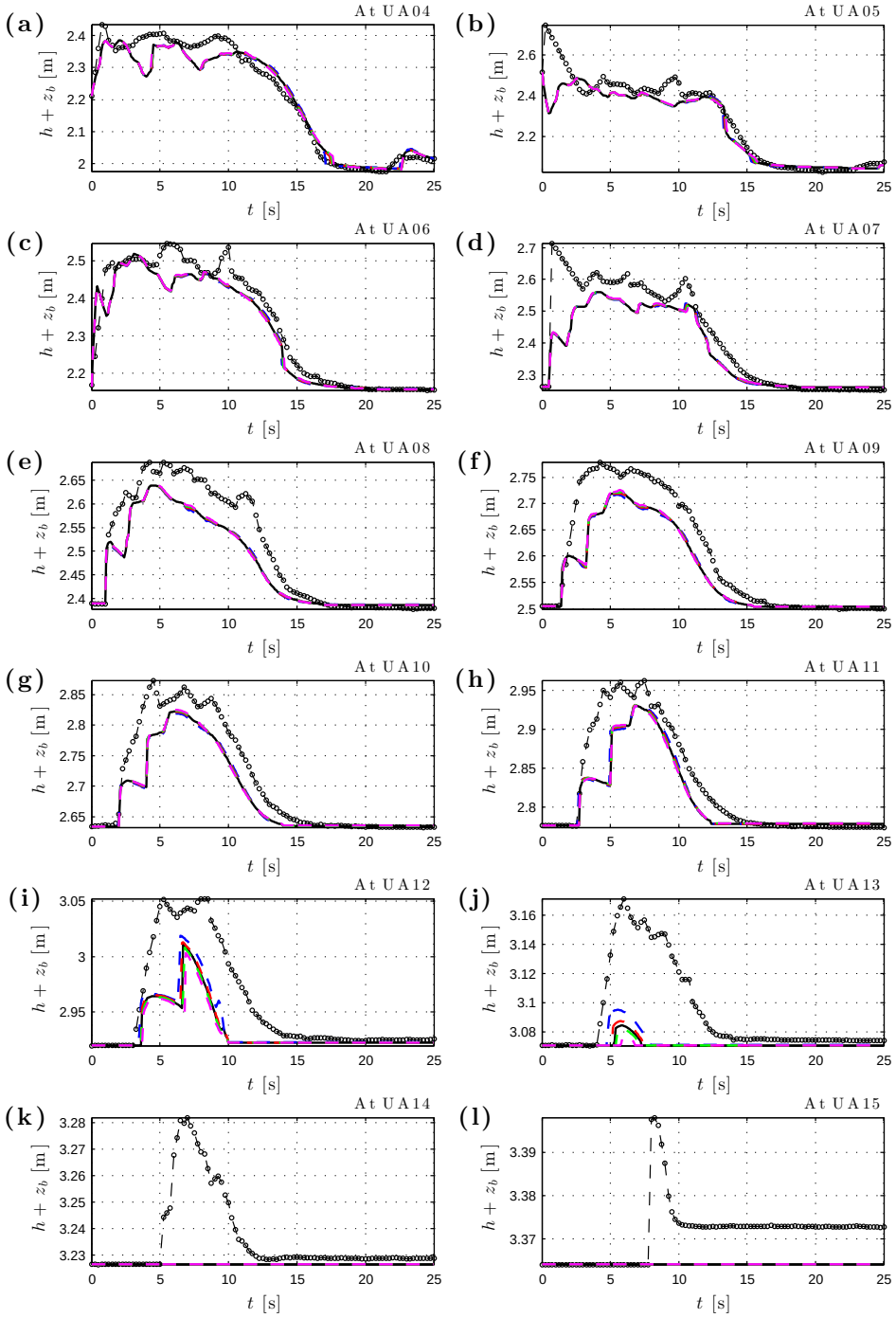

Figure 6.19: Event 3. Sensitivity of surface level ($h + z_b$) time series at UA locations to k_b. Dashed black line with circles: data. Solid black line: computed results with $k_b = 0.001$ m (default). Dashed lines: computed results with $k_b = 4 \times 10^{-4}$ m (blue), $k_b = 8 \times 10^{-4}$ m (red), $k_b = 1.2 \times 10^{-3}$ m (green) and $k_b = 1.6 \times 10^{-3}$ m (magenta) respectively.

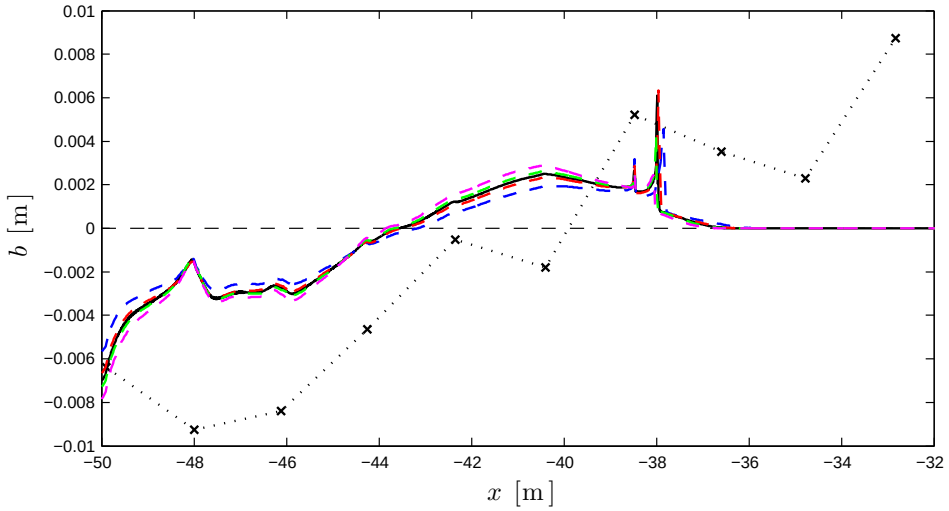

Figure 6.20: Event 3. Sensitivity of final bed change (b) profile to k_b. Dotted black line with crosses: data at UA locations. Dashed black line: no change line. Solid black line: computed results with $k_b = 10^{-3}$ m (default). Other dashed lines: computed results with $k_b = 4 \times 10^{-4}$ m (blue), $k_b = 8 \times 10^{-4}$ m (red), $k_b = 1.2 \times 10^{-3}$ m (green) and $k_b = 1.6 \times 10^{-3}$ m (magenta) respectively.

initial shoreline are again calculated by linear interpolation between these two extremes. Results for these new initial conditions are shown in Fig. 6.21. The final bed change profile loses nearly completely the depositional area in the upper swash zone, while the erosional one is substantially reduced. The influence is therefore marked.

In the same figure the effect of assuming an initial equilibrium concentration profile, i.e. $c(x,0) = c_{eq}(x)$, is illustrated. This corresponds to a steady state profile where entrainment balances erosion in Eq. (3.29):

$$m_e \left(\frac{|\tau_b| - \tau_{crs}}{\tau_{rep}} \right) - w_s c_{eq} = 0 \Rightarrow c_{eq} = \frac{m_e}{w_s} \left(\frac{f_c/2\, u^2 - U_{f,crs}^2}{f_c/2\, u_{rep}^2} \right). \tag{6.1}$$

The presence of the pre-suspended sediment removes all the erosion from the final bed profile throughout the swash zone in Fig. 6.21. The effects of the new initial conditions significantly weaken in the upper swash zone, where the new bed change profile tends to the default one.

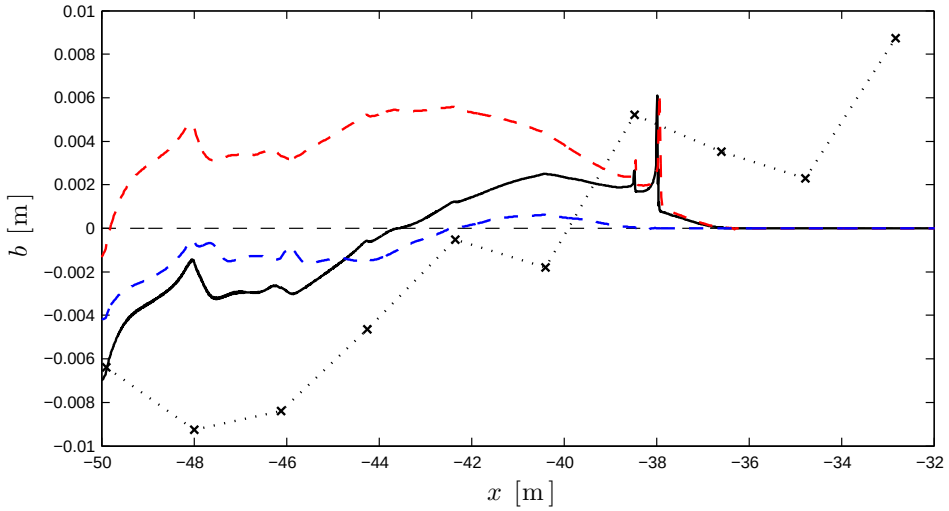

Figure 6.21: Event 3. Sensitivity of final bed change (b) profile to initial velocity and suspended sediment concentration profiles. Dotted black line with crosses: data at UA locations. Dashed black line: no change line. Solid black line: computed results with increasing landward initial velocity profile and $c(x,0) = 0$ m^{3}m^{-3} (default). Dashed blue line: computed results with decreasing landward initial velocity profile and $c(x,0) = 0$ m^{3}m^{-3}. Dashed red line: computed results with increasing landward initial velocity profile and $c(x,0) = c_{eq}(x)$.

Finally, the water table is assumed coincident to the bed level at the initial shoreline, i.e. at UA06 location (see § 6.3.1). A different case where the initial water table is set equal to the bed level at the seaward boundary, i.e. at a lower level, is presented and the results reported in Fig. 6.22. The final bed change is nearly unchanged from the default one in the lower and mid swash zone, while the deposition in the upper swash zone is shifted seaward because of the reduced run-up extent (not shown).

This behaviour is partly expected because with a lower water table the infiltration process starts further seaward and lasts for a longer time than in the default simulation, worsening the maximum run-up prediction. However, note that no information is available for the initial infiltration depth in the initially wet region, this being an additional source of uncertainty.

About simulations with a higher water table, the adopted approach for

modelling infiltration does not consider exfiltration or groundwater motion, therefore simulating a higher water table corresponds to an increased portion of the beach where infiltration does not occur, i.e. a bigger part of the beach being as impermeable. Therefore, setting a very high water table coincides to considering a whole impermeable beach and the results for this case are already presented in Fig. 6.18.

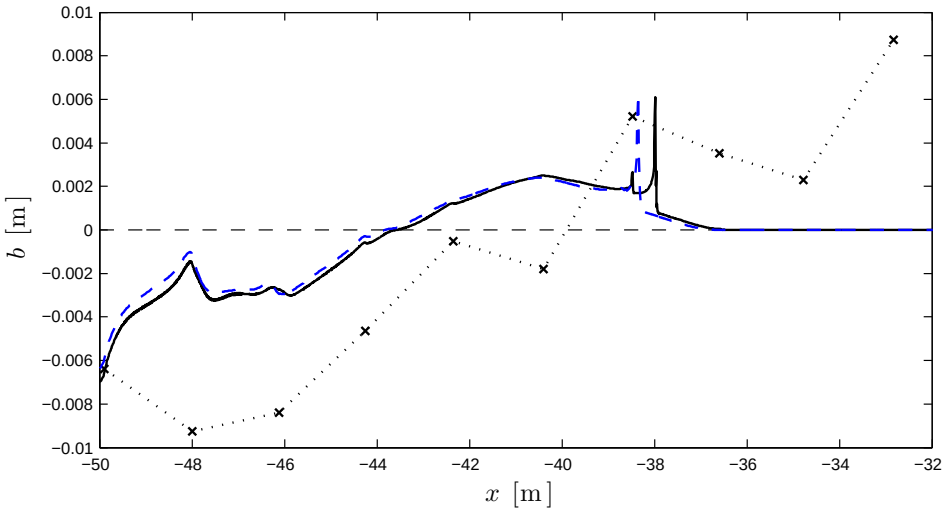

Figure 6.22: Event 3. Sensitivity of final bed change (b) profile to water table. Dotted black line with crosses: data at UA locations. Dashed black line: no change line. Solid black line: computed results for water table equal to the bed one at initial shoreline position, i.e. at UA06 location (default). Dashed blue line: computed results for water table equal to the bed one at seaward boundary position, i.e. at UA03 location.

6.6.3 Sensitivity to the applied flux limiter

A sensitivity analysis of the hydro-morphodynamic results to the particular flux limiter is carried out, which are shown in Figs. 6.23 and 6.24. As anticipated in § 6.6, the computed results show no appreciable sensitivity to the applied flux limiter, confirming that this choice has little importance in simulations of relatively short duration (see also 5.4).

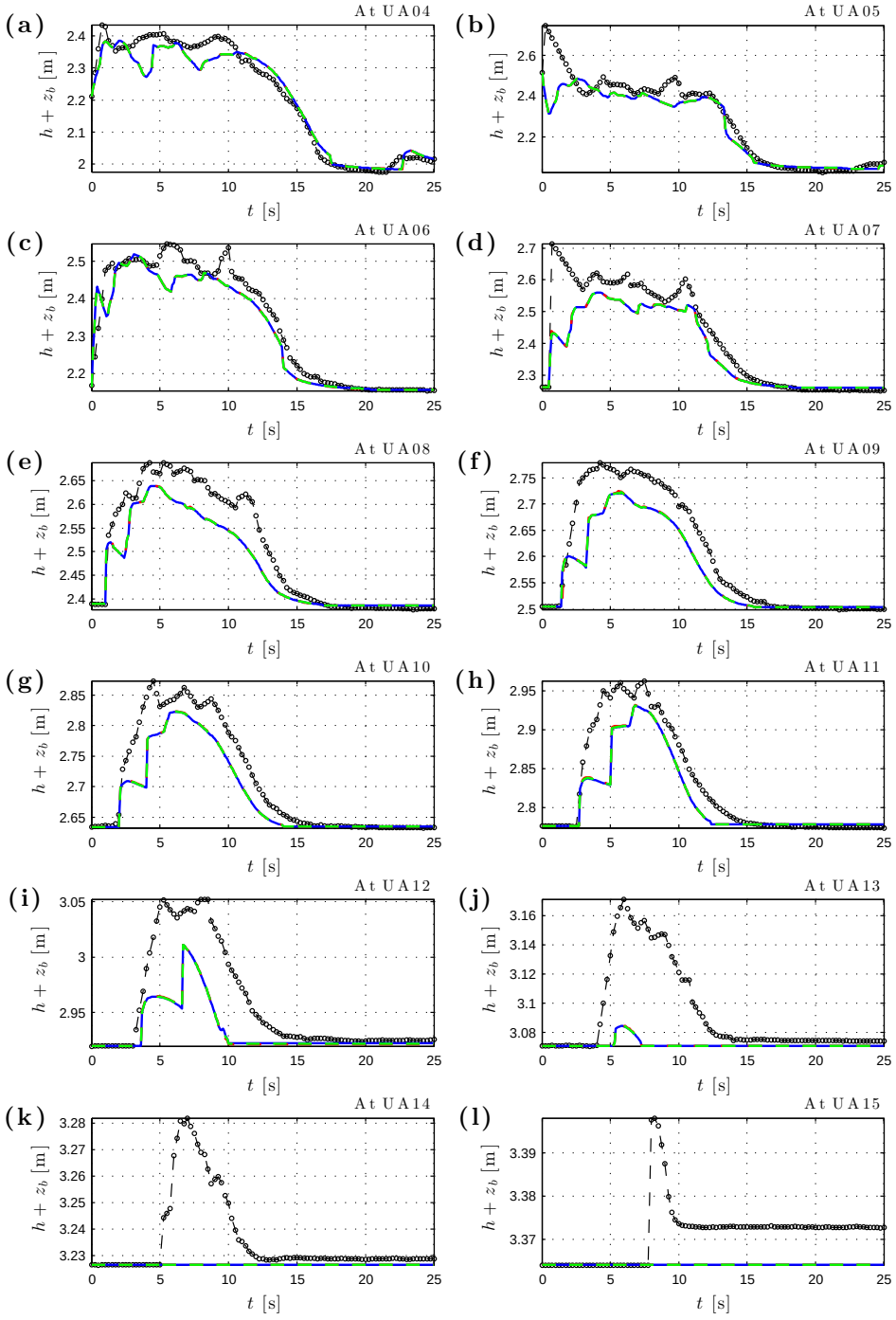

Figure 6.23: Event 3. Sensitivity of surface level ($h+z_b$) time series at UA locations to applied flux limiter. Dashed black line with circles: data. Solid blue line: computed results with Minmod (default). Dashed lines: computed results with Superbee (red) and van Leer (green) respectively.

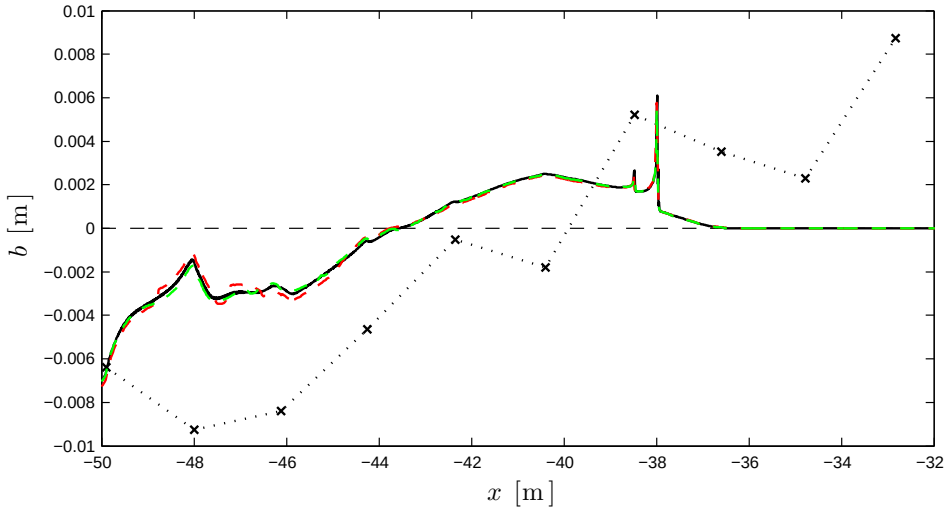

Figure 6.24: Event 3. Sensitivity of final bed change (b) profile to applied flux limiter. Dotted black line with crosses: data at UA locations. Dashed black line: no change line. Solid black line: computed results with Minmod (default). Other dashed lines: computed results with Superbee (red) and van Leer (green) respectively.

6.7 Discussion

The present study reveals that there is an underestimation of wave run-up and flow depths in the upper swash zone. This was also noted by van Rooijen et al. (2012), who used similar hydrodynamic equations but with the addition of a diffusion term. However, they neglected infiltration in their study. In this work, although infiltration exclusion yields water depths in the upper swash zone and run-up predictions (not shown) which are closer to the measured ones, Fig. 6.18 shows that the final bed change for the impermeable case is little different from that with infiltration included and still significantly different from that recorded for Event 3. On the other hand, increased infiltration due to an assumed lower water table does not improve the morphodynamic prediction (see Fig. 6.22). So, sensitivity to infiltration appears to be not large enough to account for most of the discrepancies on this sandy beach.

Event 3 was very depositional in the upper swash zone (see panel (l)

Fig. 6.11), and is not well captured by the model, particularly in the upper beach. This may suggest a large suspended load entrained at the tip of the advancing shoreline, which is not re-entrained in the backwash (see Pritchard & Hogg, 2005). This might also point to entrainment by flow turbulence (not included in this study) as being an important factor, considering that Event 3 contains two bores. In neither Event 1 (depositional) nor Event 5 (erosional) the bed change is particularly well reproduced (see Fig. 6.14). Considering all the events, it is predicted in general less bed change than that observed in data. Furthermore, the predicted pattern is consistent: erosion in the lower swash and deposition in the upper, even though in differing proportions.

With respect to the sensitivity analyses (§ 6.6), all the simulations substantially confirm a reduced run-up prediction and most of them (excluded those to initial conditions) show an overall similar shape of the final bed change profile for Event 3, with erosion seaward and deposition landward.

The entrainment of sediment as suspended load is governed by m_e, alterations in which primarily affect the magnitude of bed change only (see Fig. 6.15). This holds also when different m_e values for the uprush and the backwash phases are considered (see Figs. 6.16 and 6.17), so it is concluded that this parameter is not the main reason for the discrepancies.

The estimate of the bed roughness k_b or the particular flux limiter choice are found to affect the resulting bed change negligibly (see Figs. 6.20 and 6.24 respectively).

Sensitivity to initial velocity profile is notable (see Fig. 6.21). While the computed velocity values appear to well reproduce the real ones (see Fig. 6.13), it is acknowledged that the adopted procedure to estimate velocity at the initial shoreline location, i.e. reconstruction of the tip velocity from UA data, could lead to some loss in accuracy.

The assumed initial concentration profile has a considerable effect on the net bed change (see Fig. 6.21). This and the concentration time series at the seaward boundary are unknown. If concentration inaccuracies are to account for observed discrepancies, they can only do so with a spatially varying profile, perhaps with regions of very high concentrations (primarily due to turbulence) near the tip and much lower values seaward of this. On the other hand, as mentioned in § 6.3.1, concentration values at the open boundary are likely to affect results at most in the lower swash zone.

As recalled above, the effect of sediment entrainment / mobilisation by turbulence is not included in the model. It could be said that this was considered to some degree by van Rooijen et al. (2012), who included an acceleration term in their Nielsen (2002) bed-load transport expression, aiming at an enhanced bed shear stress for strongly accelerated flows, e.g. at a bore front. In measured time series, some bore fronts were recorded, and others not (see Fig. 6.3 and 6.13), so it is not clear how much effect including an acceleration term would have had on model predictions.

No sensitivity of results to bed-load transport, using only the standard MPM formula, is examined in the present study. However, Kelly & Dodd (2010) noted that the pattern of bed change, including the inundation limit, is affected by bed-load transport (see also Zhu & Dodd, 2015). It therefore could be interesting to show effects of varying proportion of bed- and suspended load, with the former affecting the erosion / deposition pattern and the latter primarily the magnitudes (see above).

In the light of this last point, an analysis is proposed to show how much of the final bed change is due to bed-load and how much to suspended load. However, note that some characteristics of the TVD-MCC scheme (e.g. the predictor-corrector procedure and the complex TVD-function) and, in prin-

ciple, the nonlinearity of the solved problem prevent from completely distinguishing between the two transport modes. Essentially, bed change with both modes included is not equal, in general, to the sum of bed change with bed-load only plus that with suspended load only.

Nevertheless, two additional simulations for each event are performed, the first with bed-load only (setting $m_e = 0$ ms^{-1}) and the second with suspended load only (setting $q_b = 0$ m^{2}s^{-1}). The results for these additional simulations are presented in Fig. 6.25. Bed-load transport tends to produce mainly net erosion in the lower swash zone, with some local regions of deposition, with diminishing effect in the upper beach. Suspended sediment transport mainly causes deposition in the upper swash zone, consistent with the existence of settling lag (see Pritchard & Hogg, 2005), and erosion in the lower part (most evident for Event 3, as expected because it is the largest of the three). Fig. 6.25 shows the sum of the bed changes of the aforementioned bed- and suspended load only simulations for each event, which are indeed close to the combined load results. Although consistent with Zhu & Dodd (2015) findings, this conclusion cannot generally be drawn *a priori*.

Lastly, it should also be remembered that, although UA data reveal very little alongshore difference between measurements, differences in velocities and, indeed, water and bed levels exist, and hence contribute to the discrepancies observed. It is difficult to quantify how large these can be, but it is noted that both the present study and that of van Rooijen et al. (2012) show generally good modelling in hydrodynamics.

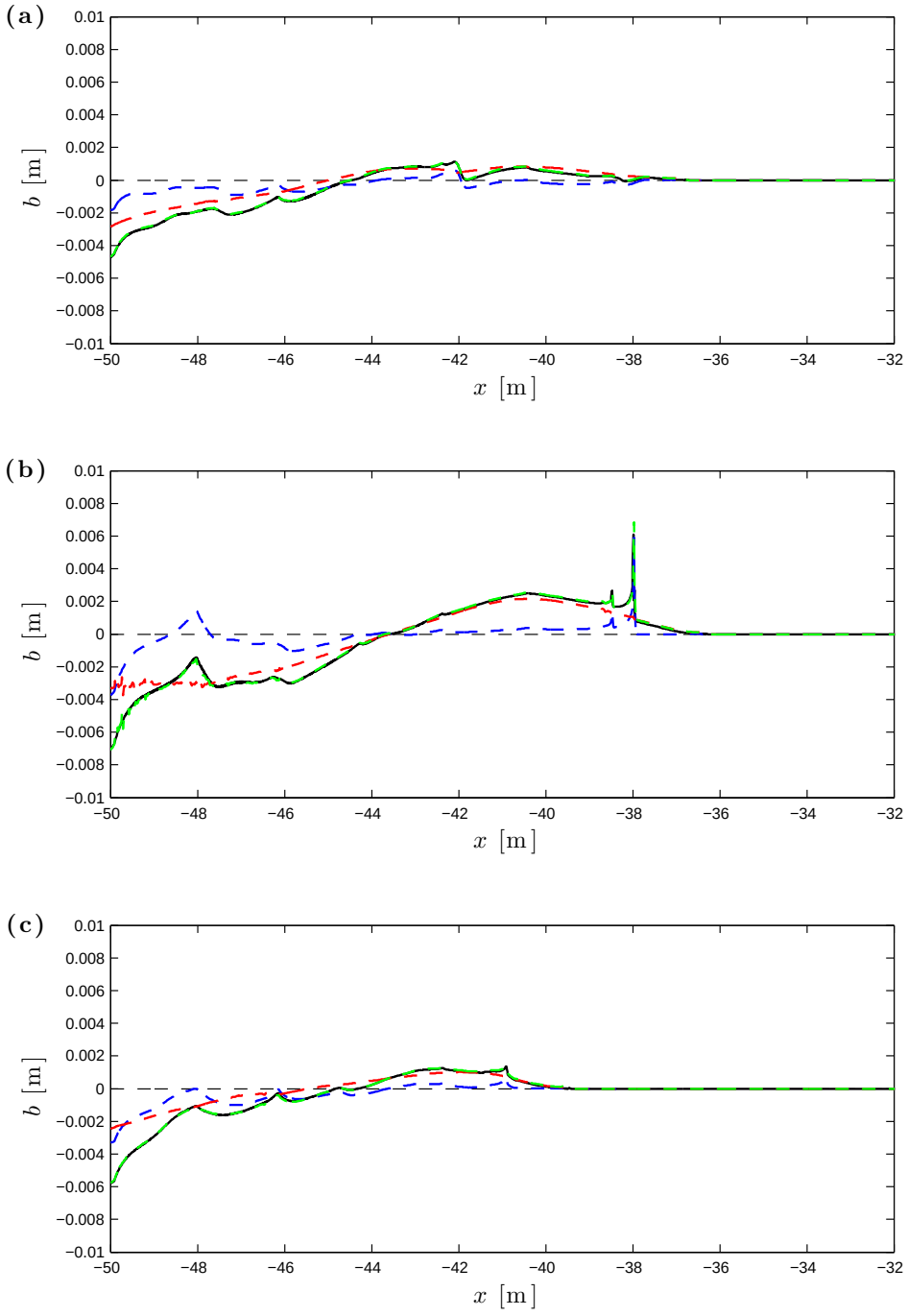

Figure 6.25: All events. Comparison of final bed change (b) profiles considering different sediment transport modes. (a): Event 1. (b): Event 3. (c): Event 5. Dashed black line: no change line. Solid black line: computed results with combined load. Other dashed lines: computed results with bed-load only (blue), with suspended load only (red) and cumulative ones for bed-load only and suspended load only simulations (green) respectively.

6.8 Concluding remarks

To summarise, the results for all the events compare quite well with field data in terms of hydrodynamics. This confirms that one-dimensional, depth-averaged description of the swash is reasonable for modelling hydrodynamics on this beach, and, more broadly, in other cases. It is noted, however, that the maximum inundation is smaller than that measured in all the simulations, the reason for this not being straightforward. This issue is in common with previous work of van Rooijen et al. (2012), notwithstanding they used a different model (in both governing equations and numerical implementation) and a different modelling approach with respect to that adopted in this study, for example in the chosen seaward boundary conditions. They tentatively hypothesised that the mismatch could be due to two-dimensional effects.

The final predicted bed changes show the correct order of magnitude but are generally underestimated, in terms of both deposition and erosion, and the predicted pattern — in the absence of pre-suspended sediment, generally erosion further offshore and deposition onshore — is not always observed in the data. Additionally, the reduced run-up prediction plays an important role on the computed bed change profile as the former apparently confines the latter more seaward of that measured in the field.

The sensitivity analyses on Event 3 reveal that the water table level, k_b and the flux limiters have no appreciable influence on the morphodynamics, while the bed change profile is affected by infiltration (weakly), m_e (significantly), initial velocity and concentration profiles (largely). Therefore discrepancies in the morphodynamic prediction by the model are thought not to be due to inaccurate estimation of physical parameters, but more probably due to initial (unknown) distributions of pre-suspended sediment concentration and velocity.

Chapter 7

Morphodynamic beach evolution at storm time-scale

7.1 Introduction

This chapter examines the morphodynamic beach evolution at the storm time-scale, aiming at understanding more about the processes involved. So far, the model performance has been assessed through some validation tests (see § 5) and real swash morphodynamics has been reproduced (see § 6), obtaining promising results provided the uncertainties in the available data, both driving and for comparison.

As mentioned in § 2.4, it is difficult to find benchmark results for mid-term simulations. Cross-shore evolution of a initial plane beach which undergoes the action of a train of sinusoidal waves was presented by Dodd et al. (2008) for both the impermeable and the permeable cases. Then, the latter case was examined further through sensitivity analyses by Sriariyawat (2009), who employed an improved version of the original model used by Dodd et al. (2008). Their models include bottom friction, through the Chézy approach, bed diffu-

sion and infiltration (for the permeable case), while the sediment transport is considered as bed-load only, using the Grass formula.

Hence, the present model results are firstly compared with benchmark ones from Dodd et al. (2008) and Sriariyawat (2009) in § 7.2.1 and § 7.2.2 respectively, considering bed-load only.

Secondly, the results for a combined load test are reported in § 7.3, using the MPM formula for the description of the bed-load transport. However, errors at the tip of the swash lens sometimes occurred and appeared to be related to the threshold for sediment movement included in the latter formula. Following Zhu & Dodd (2015), this threshold is neglected and a comparison of results with and without it is reported in § 7.3.1, along with additional results obtained including or excluding the analogous threshold in the entrainment rate for the suspended sediment transport. The sensitivity analyses to physical parameters and to variation of the incoming wave characteristics are then examined in §§ 7.3.2 and 7.3.3 respectively.

Recall that the initial bathymetry is assumed to be an equilibrium one in all the mid-term simulations in this chapter, therefore the bed diffusion is modelled considering b instead of the z_b in the spatial derivative, i.e. using Eq. (3.18) instead of Eq. (3.14).

Finally, overall conclusions are presented in § 7.4.

7.2 Mid-term beach evolution test with bed-load

The problem geometry and the physical parameters are set as those imposed by Dodd et al. (2008) and by Sriariyawat (2009) for the impermeable and the permeable cases respectively to allow consistent comparisons. Fig. 7.1 shows the initial conditions for this test.

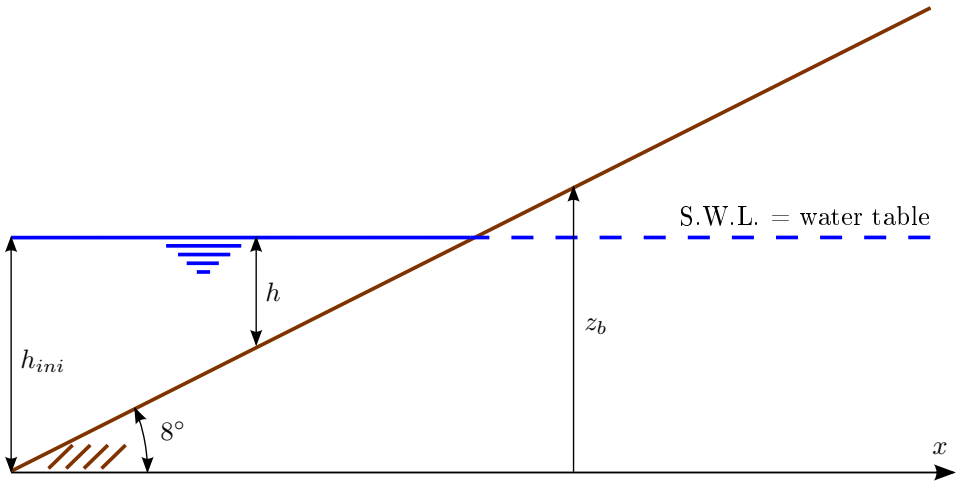

Figure 7.1: Mid-term beach evolution test with bed-load. Sketch of initial conditions. Dashed blue line for the water table inside the slope is valid for the permeable beach case only.

In particular, the still water depth at the seaward boundary is $h_{ini} = 1$ m and the initial slope of the beach is $\tan 8° \approx 0.14$. The domain length is $L_x = 12$ m and the upstream (seaward) boundary, coinciding with the toe of the slope, is located at $x = 0$ m. The incoming signal is a series of sinusoidal waves with period $T = 5$ s and height $H = 0.25$ m. The whole test duration is set to $20,000$ s, which means $4,000$ periods of the incoming wave.

This test uses the hydrodynamic BCs of Kobayashi et al. (1987) for h and u at the seaward boundary, where the bed level is updated setting it equal to that at the first inner cell at each time step, following the extrapolation approach proposed by Dodd et al. (2008). The downstream BCs are the shoreline ones

presented in § 4.3.3. However, note that for the impermeable case only, a secondary threshold ($= 10 \times h_{min}$) is also added (see § 7.2.1), below which water is no longer dynamically active, again following Dodd et al. (2008). The permeable reference case provided by Sriariyawat (2009) does not consider this secondary threshold, therefore the adopted shoreline BCs are back to those described in § 4.3.3.

Then, the physical parameters are set as follows: $f_c = 0.05$, $A_{sed} = 0.004$ s^2m^{-1}, $p_b = 0.40$ and $\phi = 32°$. In the permeable case, $k_{inf} = 0.01$ ms^{-1} and the water table is set at the initial still water surface level (see Fig. 7.1).

In this test $\Delta x = 0.05$ m and $CN = 0.80$. The applied flux limiter is Minmod, while the values for the minimum water depth parameter are different between impermeable and permeable cases, being $h_{min} = 0.002$ m and $h_{min} = 0.001$ m respectively for consistency with benchmark ones.

7.2.1 Mid-term impermeable beach evolution with bed-load

A summary of this case assumptions, BCs, physical parameters and numerical settings is given in Tab. 7.1.

The present model results cannot match the reference ones for the impermeable case if the secondary threshold is excluded. However these are the only ones available in previous literature for an impermeable beach.

Fig. 7.2 shows the evolution of the bed change profiles and the final change in the beachface, confirming the development of a long-shore bar roughly between $x = 1.5$ m and 3 m in the lower part of the beach and the erosive action in the upper one (compare with Fig. 5 at page 154 of Dodd et al., 2008).

Fig. 7.3 displays a direct comparison of the reference beach profiles at different times with the corresponding ones produced by the present model (the

Assumptions and BCs	
Friction	Chézy approach
Sediment transport	bed-load only (Grass)
Bed diffusion	included (formulation with b)
Infiltration	not included
Upstream BCs	Kobayashi et al. (1987) and extrapolation
Downstream BCs	shoreline (added 2^{nd} threshold)
Physical parameters and numerical settings	
Friction coefficient (f_c)	0.05
Sediment mobility parameter (A_{sed})	0.004 s^2m^{-1}
Bed porosity (p_b)	0.40
Angle of repose of sediment (ϕ)	32°
Domain length (L_x)	12 m
Spatial step size (Δx)	0.05 m
Courant Number (CN)	0.80
Minimum water depth parameter (h_{min})	0.002 m
Secondary water depth threshold	0.02 m
Duration of the simulation	20,000 s

Table 7.1: Mid-term impermeable beach evolution with bed-load. Assumptions, BCs, physical parameters and numerical settings.

latter kindly provided by Dr A. Sriariyawat), showing a remarkable agreement throughout the test duration.

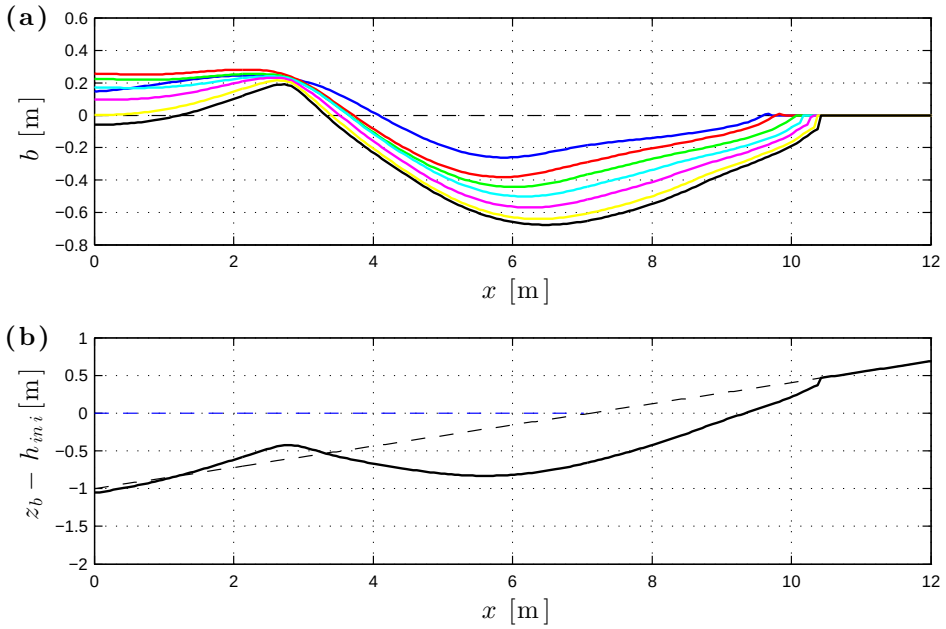

Figure 7.2: Mid-term impermeable beach evolution with bed-load. (a): bed change (b) profiles at different times. Dashed black line: no change line ($t = 0$ s). Solid lines: results at $t = 1,000$ s (blue), $t = 3,000$ s (red), $t = 5,000$ s (green), $t = 7,000$ s (cyan), $t = 10,000$ s (magenta), $t = 15,000$ s (yellow) and $t = 20,000$ s (black). (b): final beach profile after $20,000$ s. Dashed black line: initial beach profile. Dashed blue line: initial water surface profile. Solid black line: model results.

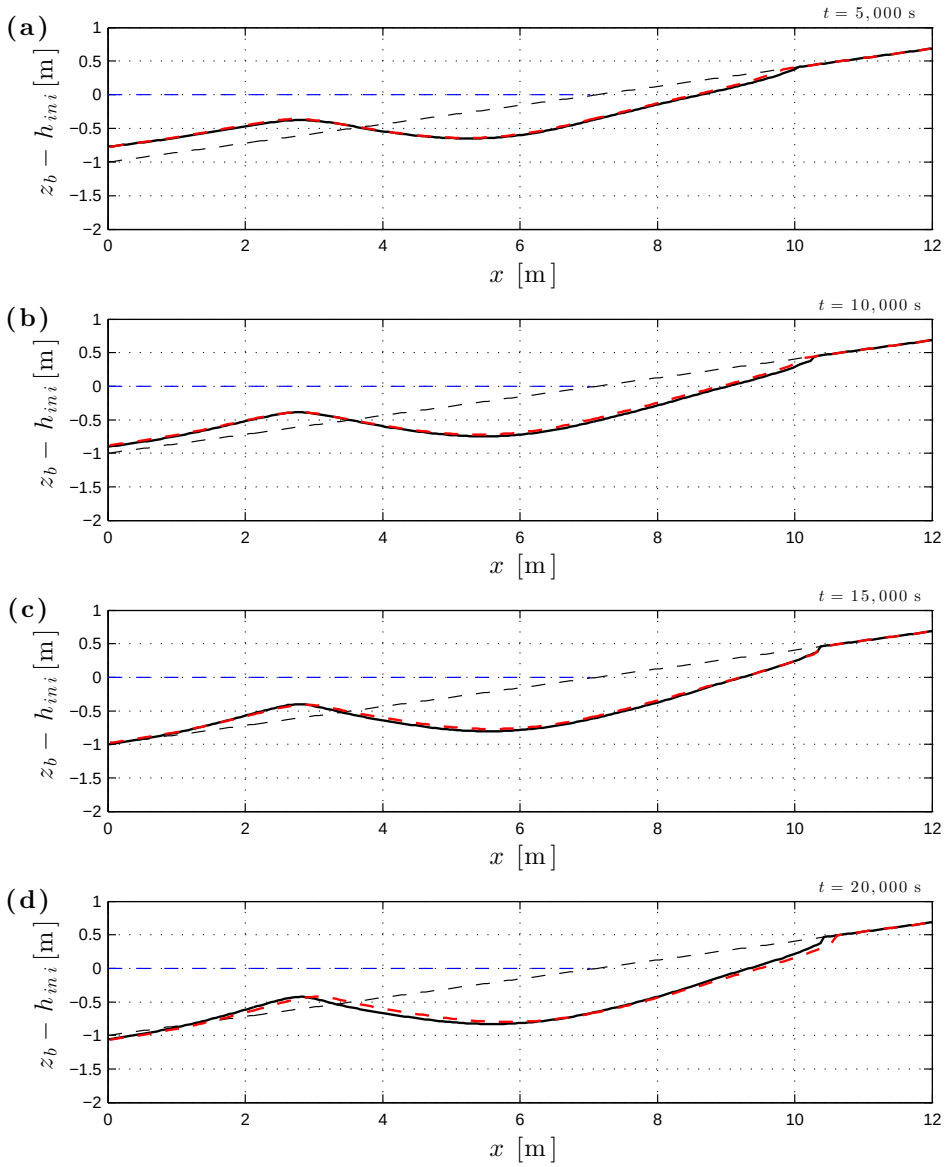

Figure 7.3: Mid-term impermeable beach evolution with bed-load. Reference results and present model ones. Comparison of beach profiles ($z_b - h_{ini}$) at different times. (a): $t = 5,000$ s; (b): $t = 10,000$ s; (c): $t = 15,000$ s; (d): $t = 20,000$ s. Dashed black line: initial beach profile. Dashed blue line: initial water surface profile. Solid black line: reference results. Dashed red line: present model results.

7.2.2 Mid-term permeable beach evolution with bed-load

A summary of this case assumptions, BCs, physical parameters and numerical settings is provided in Tab. 7.2.

Assumptions and BCs	
Friction	Chézy approach
Sediment transport	bed-load only (Grass)
Bed diffusion	included (formulation with b)
Infiltration	Darcy law
Upstream BCs	Kobayashi et al. (1987) and extrapolation
Downstream BCs	shoreline
Physical parameters and numerical settings	
Friction coefficient (f_c)	0.05
Sediment mobility parameter (A_{sed})	0.004 s^2m^{-1}
Bed porosity (p_b)	0.40
Angle of repose of sediment (ϕ)	32°
Darcy hydraulic conductivity (k_{inf})	0.01 ms^{-1}
Domain length (L_x)	12 m
Spatial step size (Δx)	0.05 m
Courant Number (CN)	0.80
Minimum water depth parameter (h_{min})	0.001 m
Duration of the simulation	20,000 s

Table 7.2: Mid-term permeable beach evolution with bed-load. Assumptions, BCs, physical parameters and numerical settings.

Fig. 7.4 shows the evolution of the bed change profiles and the final change in the beachface, confirming the dynamics presented in Fig. 5.2 at page 101 of Sriariyawat (2009). In comparison with the impermeable case (see Fig. 7.2),

the long-shore bar in the lower beach now extends until the seaward boundary at the end of the simulation, while a swash berm initially develops around $x = 9$ m (absent in the impermeable case) but then is eroded, leaving a final erosional profile in the mid and upper beach.

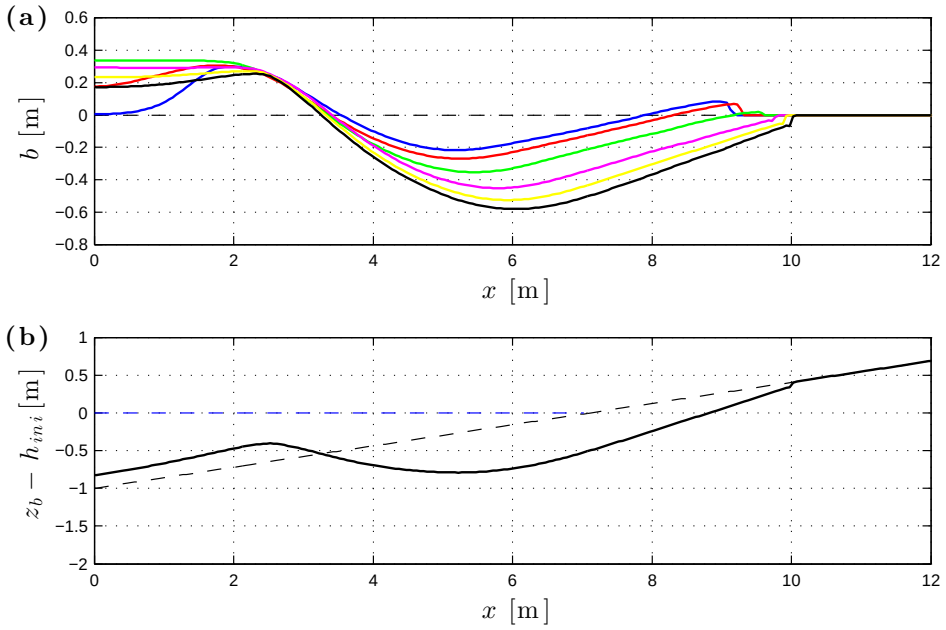

Figure 7.4: Mid-term permeable beach evolution with bed-load. (a): bed change (b) profiles at different times. Dashed black line: no change line ($t = 0$ s). Solid lines: results at $t = 1,000$ s (blue), $t = 2,000$ s (red), $t = 5,000$ s (green), $t = 10,000$ s (magenta), $t = 15,000$ s (yellow) and $t = 20,000$ s (black). (b): final beach profile after 20,000 s. Dashed black line: initial beach profile. Dashed blue line: initial water surface profile. Solid black line: model results.

Hereafter in this section, the results obtained with the settings shown in Tab. 7.2 are referred to as default ones for this permeable beach case and the same sensitivity analyses proposed by Sriariyawat (2009) are reproduced, pointing out when discrepancies emerge. Additional simulations obtained varying the applied flux limiter and the resistance law for the infiltration modelling are considered as well.

Sentivity to numerical settings

An important numerical parameter, which affects both the shoreline BCs and the model stability, is h_{min}. The sensitivity of the results to this parameter are presented in Fig. 7.5. As noted by Sriariyawat (2009), they consistently converge for decreasing minimum depth value and do not vary significantly for $h_{min} \leq 0.001$ m, which is thus used in all other simulations.

As the present test duration is relatively long, it is worth assessing the result sensitivity to a change in the applied flux limiter, as suggested in § 5.2. Fig. 7.6 shows the sensitivity of bed change profiles when Minmod, Superbee or van Leer are applied. With respect to the results with the other two limiters, those obtained with Superbee (see panel (b)) show a wider initial swash berm and a smaller final erosion around $x = 6$ m and at the seaward boundary. However, the final bed change after $20,000$ s does not exhibit significant differences among the three simulations.

In the light of this substantial agreement, for consistency with previous works (i.e. Dodd et al., 2008; Sriariyawat, 2009) and considering that Superbee and van Leer show increased numerical noise in the uniform bore test (see § 5.4), Minmod is retained in this study of the mid-term beach evolution.

Sentivity to physical parameters

In this section, the sensitivity analyses to f_c, k_{inf} and A_{sed} are presented, following Sriariyawat (2009). Additionally, a comparison of results obtained using the Darcy law and the Forchheimer one is displayed, assuming that the infiltration-related parameters for the coarse sand experiment on permeable fixed slope (see § 5.5.2) can be used.

Fig. 7.7 shows the result sensitivity to different friction coefficient values in the range 0.005–0.1. An increased f_c value yields a final erosive profile which

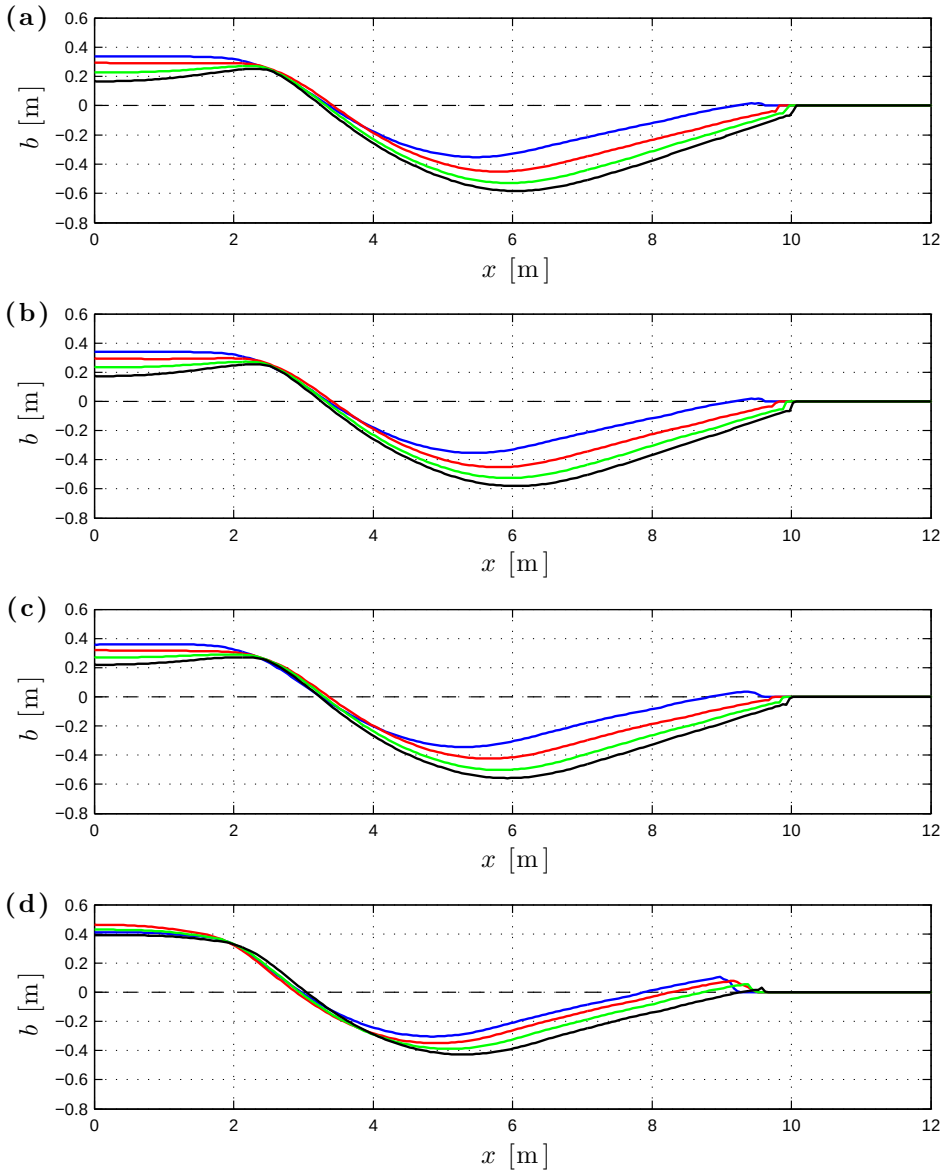

Figure 7.5: Mid-term permeable beach evolution with bed-load. Sensitivity of bed change (b) profiles to h_{min}. (a): $h_{min} = 5 \times 10^{-4}$ m. (b): $h_{min} = 0.001$ m (default). (c): $h_{min} = 0.002$ m. (d): $h_{min} = 0.005$ m. Dashed black line: no change line ($t = 0$ s). Solid lines: results at $t = 5,000$ s (blue), $t = 10,000$ s (red), $t = 15,000$ s (green) and $t = 20,000$ s (black).

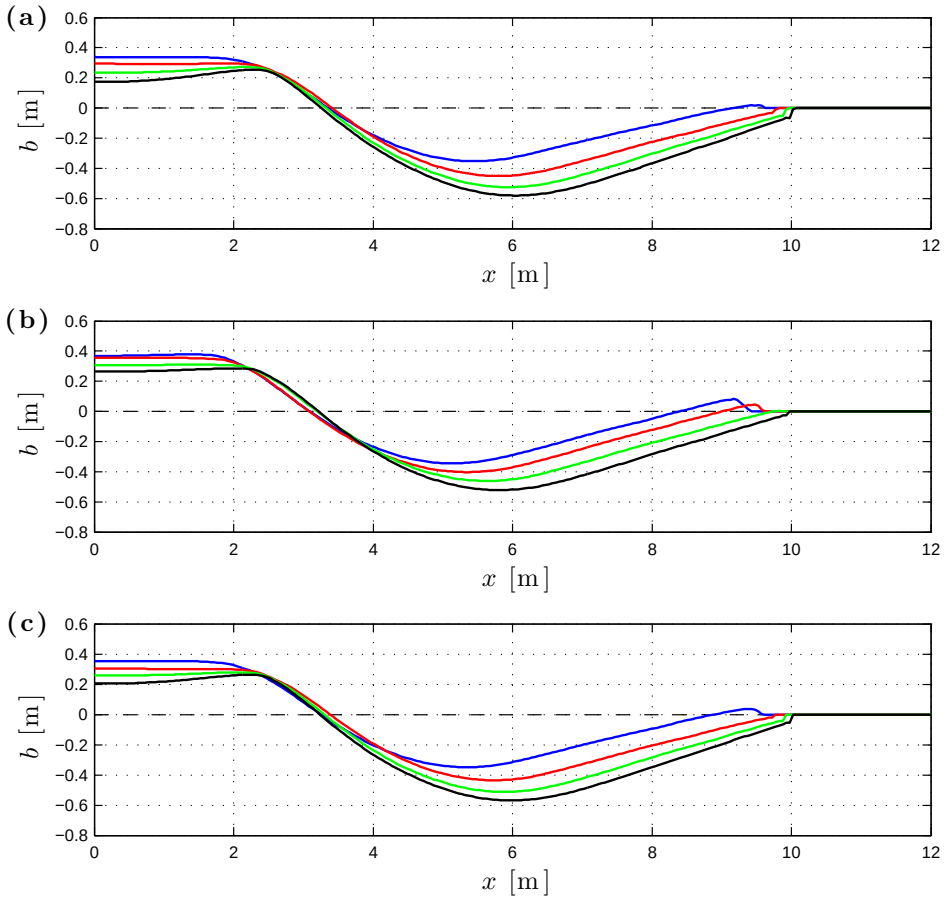

Figure 7.6: Mid-term permeable beach evolution with bed-load. Sensitivity of bed change (b) profiles to applied flux limiter. (a): Minmod (default). (b): Superbee. (c): van Leer. Dashed black line: no change line ($t = 0$ s). Solid lines: results at $t = 5,000$ s (blue), $t = 10,000$ s (red), $t = 15,000$ s (green) and $t = 20,000$ s (black).

is shifted seaward, consistent with an enhanced dissipation of the incoming wave action, as observed by Sriariyawat (2009). Note that the latter found a depositional final profile for $f_c = 0.005$, which was not clearly understood and partly justified by pointing out that the initial formation of a swash berm in the upper swash zone might have affected the whole morphodynamic evolution. However, this unique behaviour is not captured in panel (a) of Fig. 7.7 and the present results seem more in keeping with the trend shown using higher friction values.

Fig. 7.8 shows the result sensitivity to the hydraulic conductivity, employing the Darcy law. The simulation for the reduced k_{inf} value (i.e. $k_{inf} = 0.001$ ms^{-1}, see panel (a)) shows enhanced erosion with respect to the default one throughout the swash zone, consistent with more water being available in the backwash and, more generally, in the upper beach. However the evolution does not exhibit a continuously advancing erosion of the beachface as in Sriariyawat (2009). This different behaviour may be due to the implementation of the wetting restriction in the shoreline BCs (see § 4.3.3), which was not considered by Sriariyawat (2009). The simulation with the increased k_{inf} value is in very good agreement with that shown by Sriariyawat (2009), with the accrued infiltration leading to the formation of a relatively high swash berm and a nearly-fixed bed change profile since from $t = 5,000$ s. This morphological response, i.e. increased deposition in the upper beach caused by enhanced swash asymmetry, was for example pointed out by Masselink & Li (2001) in their study on the effects of infiltration in the swash zone.

However, higher infiltration rates may require to change from the Darcy law to the Forchheimer one. Therefore, two further simulations are carried out using the two different resistance laws and imposing the infiltration-related parameters of the coarse sand experiment on permeable fixed slope (see § 5.5.2).

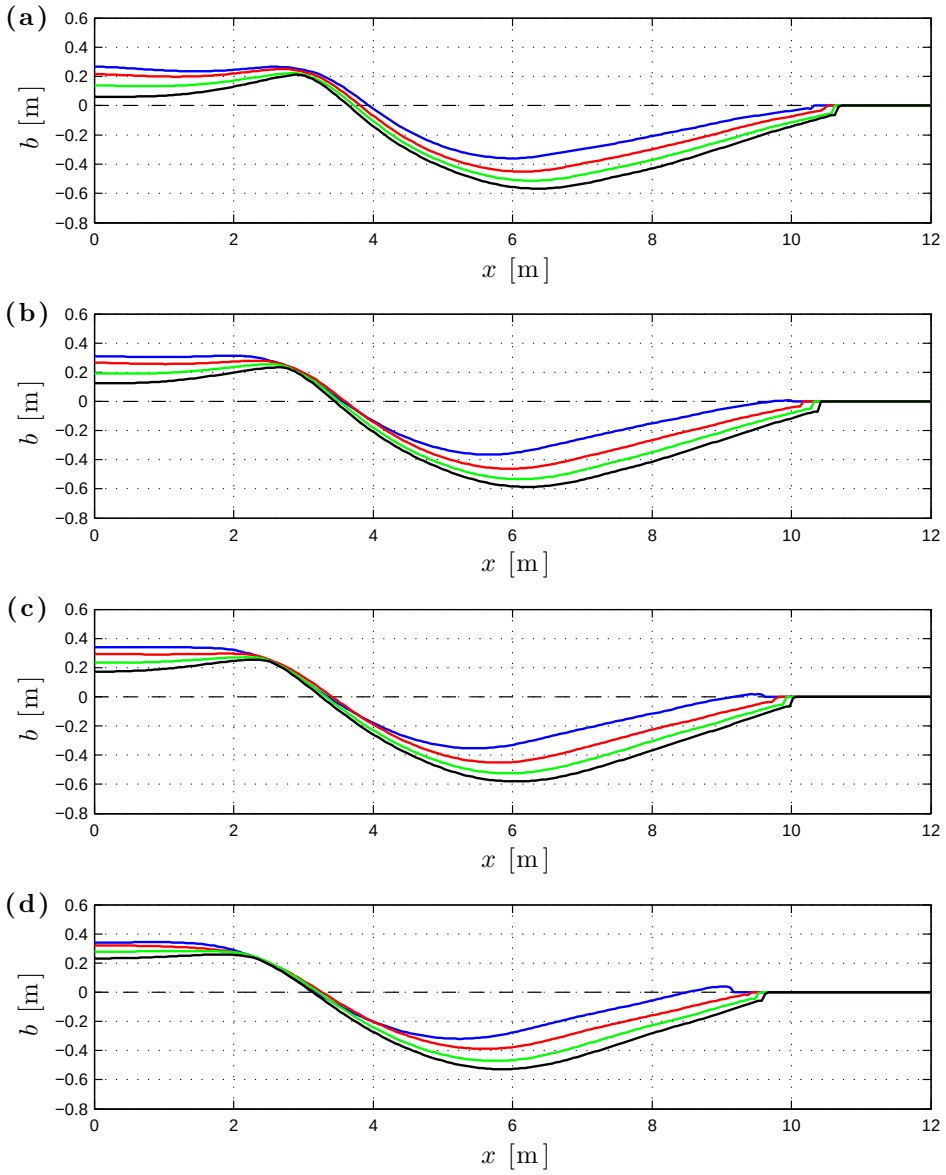

Figure 7.7: Mid-term permeable beach evolution with bed-load. Sensitivity of bed change (b) profiles to f_c. (a): $f_c = 0.005$. (b): $f_c = 0.02$. (c): $f_c = 0.05$ (default). (d): $f_c = 0.1$. Dashed black line: no change line ($t = 0$ s). Solid lines: results at $t = 5,000$ s (blue), $t = 10,000$ s (red), $t = 15,000$ s (green) and $t = 20,000$ s (black).

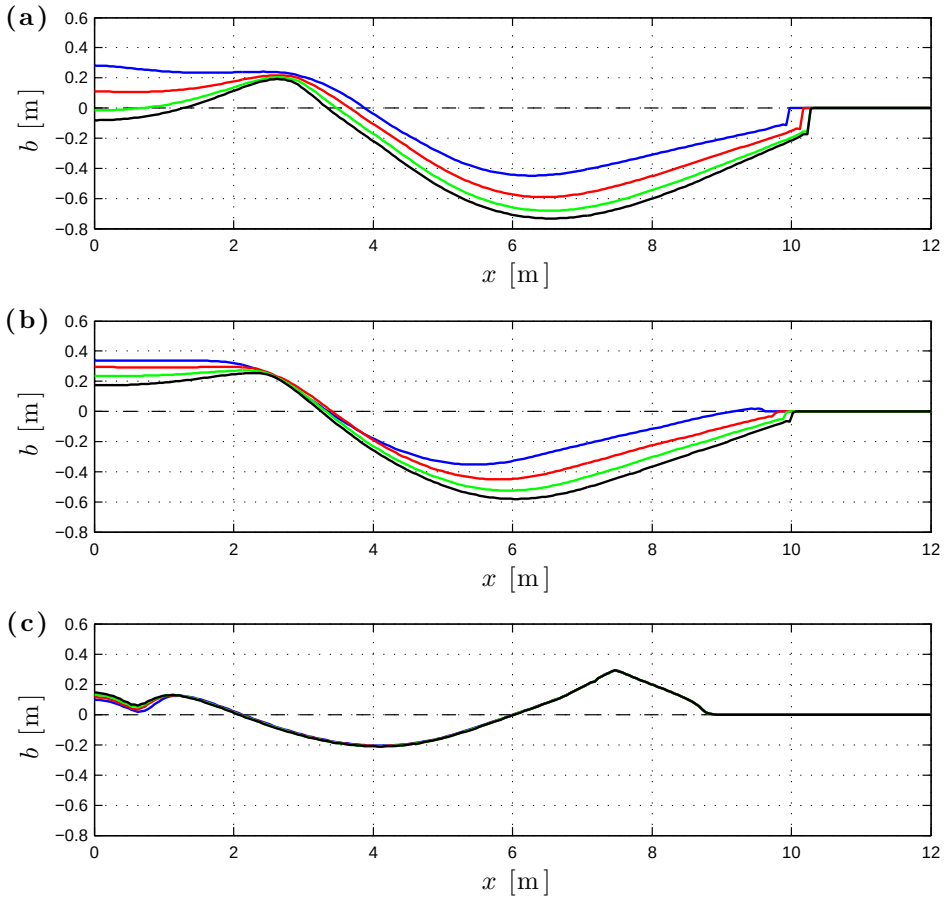

Figure 7.8: Mid-term permeable beach evolution with bed-load. Sensitivity of bed change (b) profiles to k_{inf}. (a): $k_{inf} = 0.001$ ms^{-1}. (b): $k_{inf} = 0.01$ ms^{-1} (default). (c): $k_{inf} = 0.04$ ms^{-1}. Dashed black line: no change line ($t = 0$ s). Solid lines: results at $t = 5,000$ s (blue), $t = 10,000$ s (red), $t = 15,000$ s (green) and $t = 20,000$ s (black).

The results, displayed in Fig. 7.9, present a substantially erosive final beach profile with the Darcy law (although intermediate profiles show the presence of a swash berm in the upper swash zone) and even more erosion with the Forchheimer one, which is consistent with the expected reduction in the infiltration rate. Notwithstanding the simplifications included in the present model (e.g. exfiltration and groundwater motion are neglected), these results suggest that, when permeability is high, additional modelling care is required in the choice of the appropriate approach for infiltration.

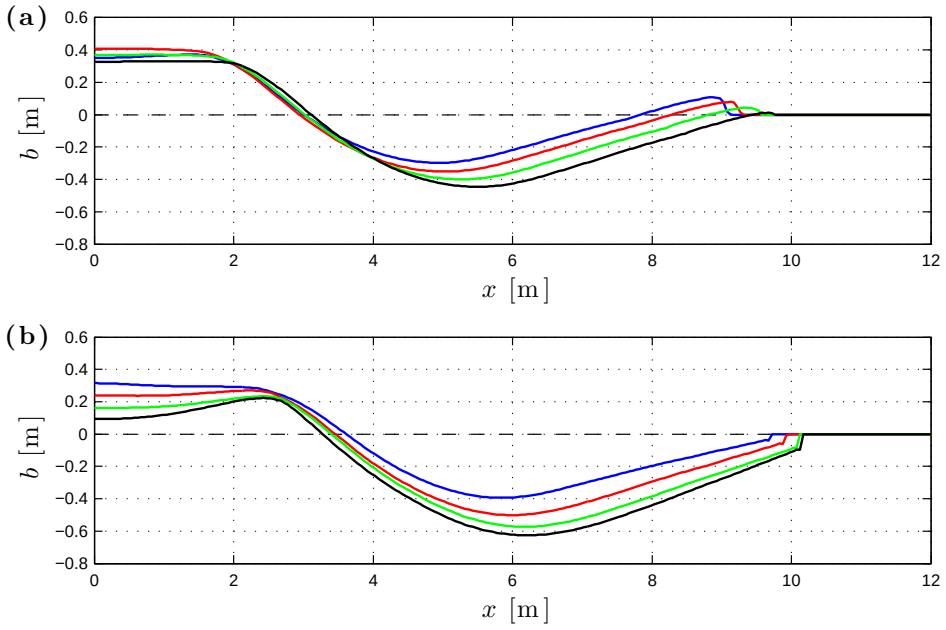

Figure 7.9: Mid-term permeable beach evolution with bed-load. Sensitivity of bed change (b) profiles to used resistance law. (a): Darcy law, with $k_{inf} = 0.013$ ms^{-1}. (b): Forchheimer law, with $a_{inf} = 81.2$ sm^{-1} and $b_{inf} = 3,587$ s^{2}m^{-2}. Dashed black line: no change line ($t = 0$ s). Solid lines: results at $t = 5,000$ s (blue), $t = 10,000$ s (red), $t = 15,000$ s (green) and $t = 20,000$ s (black).

Finally, variations in the sediment mobility parameter are considered, as it plays a predominant role in the bed change evolution rate. The results for a reduced A_{sed} value (i.e. 0.001 s^{2}m^{-1}) are shown in panel (a) of Fig. 7.10, confirming the scaling effect previously noted by Sriariyawat (2009), i.e. that

a reduced (increased) A_{sed} accelerates (slows down) the rate of bed change rather than affecting other aspects. The results for a higher A_{sed} value (i.e. 0.04 s^2m^{-1}) are not reported as the model crashed in this particular simulation. The reason for this is found in the collision of very thin backwash lens from a previous swash event with the uprush of the subsequent one, involving a sudden change in sign of the depth-averaged velocity and consequently in the sediment transport fluxes (recall the adopted Grass formula, Eq. (3.7)). This mechanism was well examined by Sriariyawat (2009) and therefore it is not discussed further here.

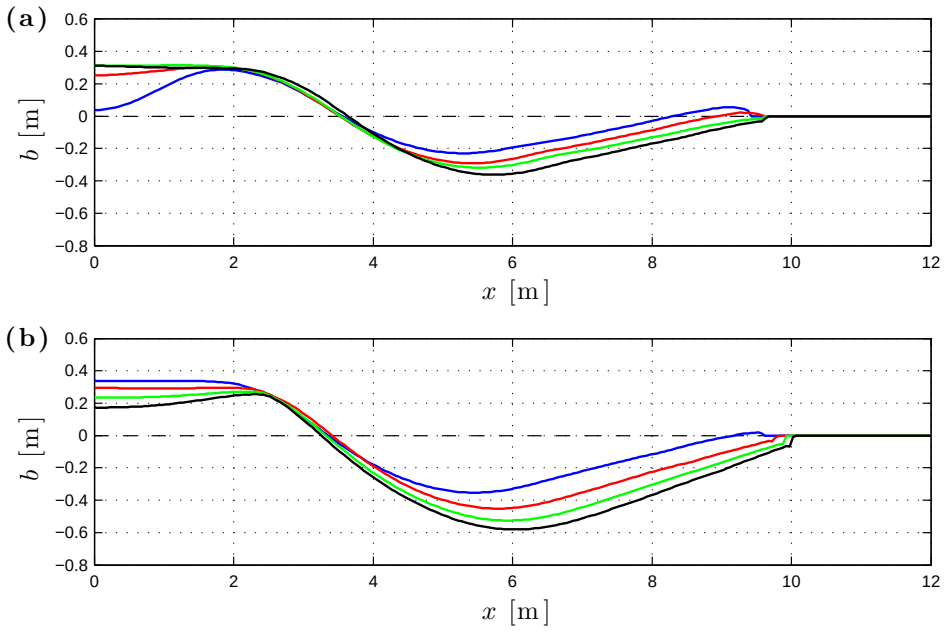

Figure 7.10: Mid-term permeable beach evolution with bed-load. Sensitivity of bed change (b) profiles to A_{sed}. (a): $A_{sed} = 0.001$ s^2m^{-1}. (b): $A_{sed} = 0.004$ s^2m^{-1} (default). Dashed black line: no change line ($t = 0$ s). Solid lines: results at $t = 5,000$ s (blue), $t = 10,000$ s (red), $t = 15,000$ s (green) and $t = 20,000$ s (black).

7.3 Mid-term beach evolution test with combined load

In this section, the beach evolution is studied considering the combined load transport. While the bed-load only test and related sensitivity analyses are carried out with conditions and settings which allow meaningful comparisons with previous work of Dodd et al. (2008) and Sriariyawat (2009), the present combined load one is designed using as guidance the field simulations of § 6.

The initial conditions are the same as those for the bed-load test (see Fig. 7.1), except that now the beach slope is 1:15 ($\approx \tan 4°$), which coincides with the approximate gradient for the upper beach at Le Truc Vert, as indicated by Blenkinsopp et al. (2011). This reduced slope value, with respect to the bed-load test one, may be more consistent with a real beach made of fine or medium sand where suspended sediment transport is more likely to occur. The domain length is now $L_x = 24$ m. The water is initially motionless and no pre-suspended sediment concentration is imposed. The incoming signal is a series of sinusoidal waves with period $T = 5$ s and height $H = 0.25$ m, as in the previous bed-load only test. The whole test duration is kept at $20,000$ s. Sensitivity to incoming wave characteristics is examined in § 7.3.3.

The hydrodynamic BCs of Kobayashi et al. (1987) are used for h and u at the seaward boundary. The extrapolation approach for z_b from Dodd et al. (2008) is maintained and it is applied to c as well. The downstream BCs are the shoreline ones (see § 4.3.3).

To estimate bottom friction, the Chézy approach is adopted (see § 3.2.1) instead of the BBL solver used for the single swash event simulations in § 6. The reason for this choice is that the BBL solver is currently unable to capture the effects of turbulence on the sediment transport, which is thought to play a

major role in a long series of swash-swash interactions. $f_c = 0.02$ is chosen as it is in good agreement with values estimated for a beach with analogies with Le Truc Vert one (see Puleo et al., 2014a; Inch et al., 2015).

As in § 6.3.2, $p_b = 0.35$, $\rho_w = 1,027$ kgm^{-3} and $s_{rel} = 2.580$. Additionally, $d_{50} = 4.0 \times 10^{-4}$ m, $\theta_{crb} = 0.036$ in the MPM formula and $\phi = 33°$ is assumed in the bed diffusion term.

Some attempts were made to consider the complete MPM formula, i.e. at including the critical Shields parameter, which represents the threshold for sediment movement, but the model often returned instabilities at the tip of the swash lens in some of the simulations performed for the sensitivity analyses and non-physical predictions (e.g. spurious negative water depth values or unrealistic sediment accumulation at the wet / dry front), which are deemed unacceptable.

Note that these issues are not experienced in the single swash simulations of § 6 and generally occurred after the generation of several hundreds of incoming waves. Nevertheless, the above-mentioned threshold is removed, following Zhu & Dodd (2015), who observed that the neglect of it is unlikely to have a significant impact on the swash zone morphodynamics (for discussion of this assumption, see § 7.3.1).

The entrainment rate for suspended load E is specified as in Eq. (5.13), adopting the Chézy approach, with the following parameters: $m_e = 0.002$ ms^{-1}, $u_{crs} = U_{f,crs}\,(f_c/2)^{-1/2}$ with $U_{f,crs} = 0.025$ ms^{-1} and $u_{rep} = \sqrt{g h_{rep}}$ ms^{-1} with $h_{rep} = 1$ m. Additionally, $w_s = 0.05$ ms^{-1}.

In the Darcy law, $k_{inf} = 0.001$ ms^{-1}, while the water table is set at the initial still water surface level (see again Fig. 7.1).

As in the bed-load test, $\Delta x = 0.05$ m and $CN = 0.80$. The applied flux limiter is Minmod and $h_{min} = 0.001$ m.

A summary of this test assumptions, BCs, physical parameters and numerical settings is provided in Tab. 7.3, which represent the default ones for the following combined load simulations.

Fig. 7.11 displays the (default) results for this test. The final bed change profile shows the development of three bars and, with respect to the initial slope, presents erosion landward and deposition seaward, while little morphodynamic change is apparent near the seaward boundary.

For this case (and later for those in § 7.3.3), the evolution of the swash zone extension is tracked by means of a simplified procedure. The shoreline position is recorded for an interval equal to $2\,T$ before of each time of interest (e.g. between $4,990$ s and $5,000$ s for $t = 5,000$ s with $T = 5$ s), this to be reasonably sure to capture at the least one whole single swash motion. Then the recorded minimum and maximum shoreline positions are assumed to be representative of the run-down and the run-up limits at the corresponding time of interest. In panel (a) of Fig. 7.11, the results show that the swash zone extensions are around 2 m long and that they move landward as the erosional profile advances onshore.

As for the bed-load only test, the sensitivity to numerical settings (i.e. to h_{min} and to the applied flux limiter) is examined, however corresponding results are not shown because they confirm the conclusions already drawn for the previous test. In particular, the results converge for $h_{min} \leq 0.001$ m and those obtained with the different limiters show good quantitative agreement.

In the next sections, firstly the sensitivity to the thresholds for sediment movement is discussed in § 7.3.1 for both bed- and suspended load transport modes. Secondly the sensitivity analyses to some physical parameters and to the incoming wave characteristics are presented in §§ 7.3.2 and 7.3.3 respectively.

Assumptions and BCs	
Friction	Chézy approach
Sediment transport	combined load (MPM without threshold)
Bed diffusion	included (formulation with b)
Infiltration	Darcy law
Upstream BCs	Kobayashi et al. (1987) and extrapolation
Downstream BCs	shoreline

Physical parameters and numerical settings	
Friction coefficient (f_c)	0.02
Bed porosity (p_b)	0.35
Angle of repose of sediment (ϕ)	33°
Median sediment grain diameter (d_{50})	4.0×10^{-4} m
Salted water density (ρ_w)	$1,027$ kgm^{-3}
Relative density of sediment (s_{rel})	2.580
Erosional rate parameter (m_e)	0.002 ms^{-1}
Critical friction velocity for suspended load ($U_{f,crs}$)	0.025 ms^{-1}
Representative scale for velocity (u_{rep})	$\sqrt{gh_{rep}}$ ms^{-1}
Representative scale for water depth (h_{rep})	1.00 m
Effective settling velocity (w_s)	0.05 ms^{-1}
Darcy hydraulic conductivity (k_{inf})	0.001 ms^{-1}
Domain length (L_x)	24 m
Spatial step size (Δx)	0.05 m
Courant Number (CN)	0.80
Minimum water depth parameter (h_{min})	0.001 m
Duration of the simulation	$20,000$ s

Table 7.3: Mid-term beach evolution with combined load. Assumptions, BCs, physical parameters and numerical settings.

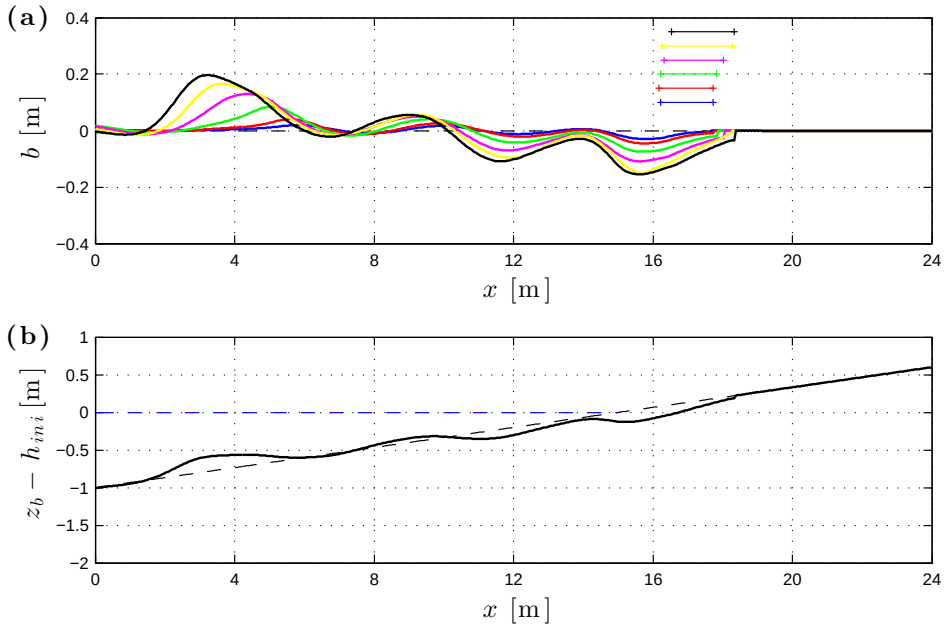

Figure 7.11: Mid-term beach evolution with combined load. (a): bed change (b) profiles and swash extensions at different times. Dashed black line: no change line ($t = 0$ s). Thick solid lines: results at $t = 1,000$ s (blue), $t = 2,000$ s (red), $t = 5,000$ s (green), $t = 10,000$ s (magenta), $t = 15,000$ s (yellow) and $t = 20,000$ s (black). Thin horizontal solid lines: swash extensions (colour legend as that for the b profiles). (b): final beach profile after $20,000$ s. Dashed black line: initial beach profile. Dashed blue line: initial water surface profile. Solid black line: present model results.

7.3.1 Sensitivity to thresholds for sediment movement

In this section, an analysis on the role of the thresholds for sediment movement for both bed- and suspended load is provided, aiming at assessing if the simplifying assumption of neglecting them (and in particular that in the MPM formula) is reasonable for this test or leads to significant differences in the final bed change profile.

About bed-load transport, the order of magnitude of a representative value for the Shields parameter (θ) is estimated to be compared with $\theta_{crb} = 0.036$, i.e. the critical one in the MPM formula. Thus, the Shields parameter, Eq. (3.9), is rewritten as follows, replacing τ_b with $\tau_{rep} = \rho_w f_c/2\, u_{rep}^2$, with $u_{rep} = \sqrt{g h_{rep}}$,

and including the required parameters from Tab. 7.3:

$$\theta = 791\, f_c\, h_{rep}. \tag{7.1}$$

Assuming f_c in the range 0.01–0.03 (see e.g. Puleo et al., 2014a) and the representative length scale in the interval 0.1–1 m (see Zhu & Dodd, 2015), θ is bounded between 0.79 and 24, with the smallest value obtained for $f_c = 0.01$. Therefore there is at least an order of magnitude between θ and θ_{crb} values, which may indicate that this threshold could play a minor role with the chosen settings.

The results considering the MPM formula with and without threshold and using $f_c = 0.01$ (the most demanding value for checking the assumption of negligible threshold) are presented in Fig. 7.12. Note that both suspended load and infiltration are removed to avoid possible masking effects. The results exhibit a very good qualitative and quantitative agreement, with the final profile without threshold showing more erosion than that with it in the upper beach, which is consistent with more sediment mobilisation. Therefore, it can be reasonably stated that the neglect of the threshold in the MPM formula is not expected to have a substantial effect on the mid-term morphological evolution, in the limits of the parameters chosen for this test.

The inclusion or exclusion of the equivalent threshold for the suspended load transport did not affect the model stability, therefore it is included in the modelling. However, it could be interesting to see if it plays an important role in morphodynamic evolution. It is possible to estimate an analogous critical Shields parameter for suspended transport (see Zhu & Dodd, 2015), which for this test is $\theta_{crs} = 0.1$. Note that θ_{crs} is an order of magnitude bigger than θ_{crb}.

The results for the combined load simulations including or excluding this threshold are presented in Fig. 7.13. $f_c = 0.02$ is used, as for $f_c = 0.01$ the morphological change is substantially reduced (see § 7.3.2) and possible

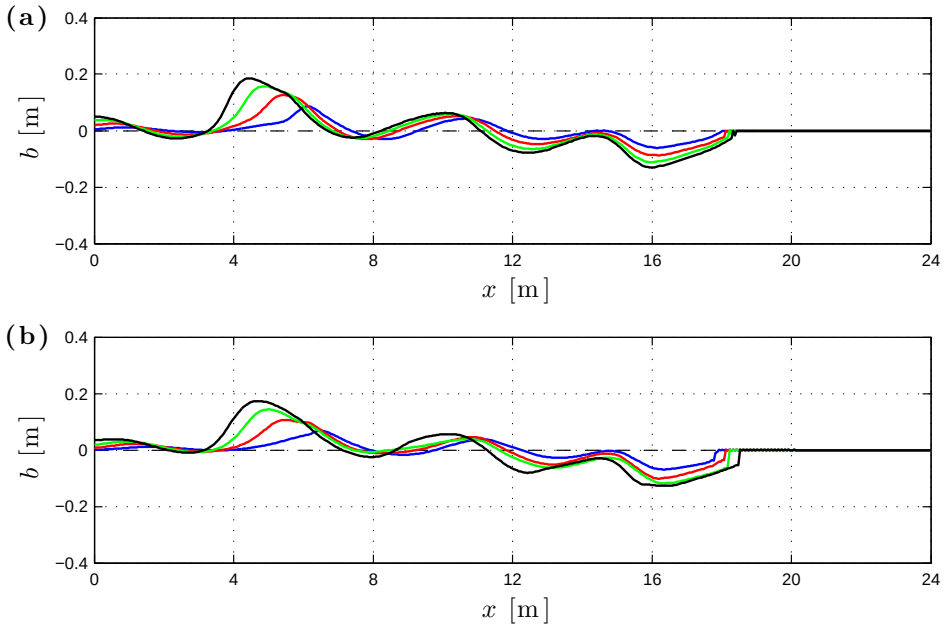

Figure 7.12: Mid-term beach evolution with combined load. Sensitivity of bed change (b) profiles to the threshold in the MPM formula. Suspended sediment transport and infiltration removed. $f_c = 0.01$. (a): with threshold. (b): without threshold. Dashed black line: no change line ($t = 0$ s). Solid lines: results at $t = 5,000$ s (blue), $t = 10,000$ s (red), $t = 15,000$ s (green) and $t = 20,000$ s (black).

differences could be less apparent. Infiltration is removed as previously done for the study of the threshold in the MPM formula. No significant discrepancy can be seen between the two final bed change profiles, with the shape of the three bars being nearly identical. This suggests that also the threshold for suspended sediment movement may play a minor role in this combined load test, however it is retained according to the more general formulation of the entrainment rate.

7.3.2 Sensitivity to physical parameters

In this section, the sensitivity analyses to f_c, m_e and k_{inf} are presented, these parameters being already identified as possible sources of uncertainties in the field-scale modelling (see § 6.6.1).

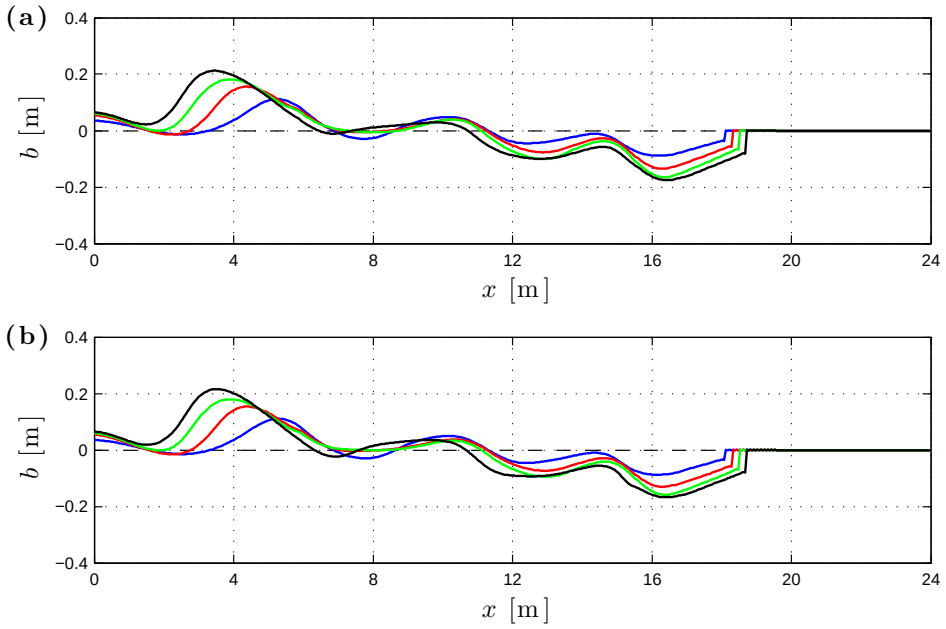

Figure 7.13: Mid-term beach evolution with combined load. Sensitivity of bed change (b) profiles to the threshold in the entrainment rate for suspended sediment transport. Infiltration removed. (a): with threshold. (b): without threshold. Dashed black line: no change line ($t = 0$ s). Solid lines: results at $t = 5{,}000$ s (blue), $t = 10{,}000$ s (red), $t = 15{,}000$ s (green) and $t = 20{,}000$ s (black).

Fig. 7.14 shows the results obtained by varying the friction coefficient in the range 0.01–0.03. As expected, a reduced f_c value decrease the morphodynamic impact of the incoming waves, even though three bars are still formed. Additionally, note that changes in landward extension of the erosional area in the upper beach are small in comparison to those shown in the bed-load only test (see Fig. 7.7). This is partly due to the smaller range of f_c values considered for this test with respect to that used for the previous one. However note that, while the Grass formula is independent of f_c, this parameter affects the MPM formula directly, yielding a reduction in sediment mobility for a decrease in the friction coefficient value. Therefore the comparison of the model response to variations in f_c between the bed- and combined load tests is not straightforward.

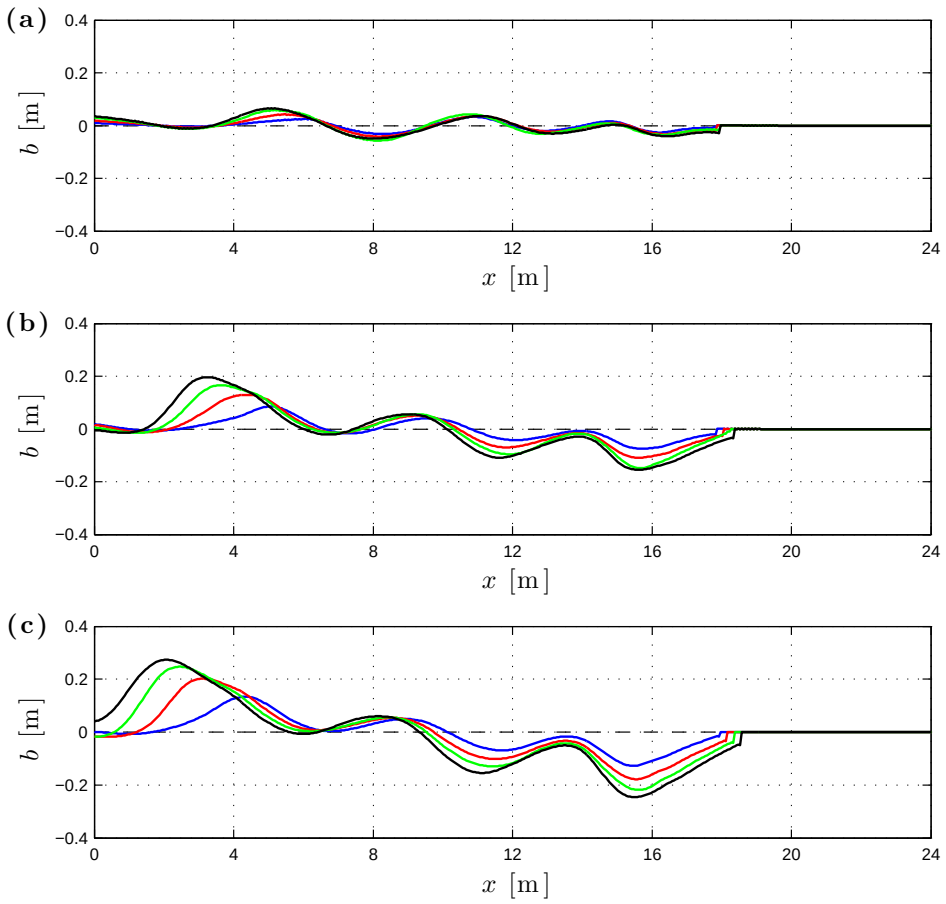

Figure 7.14: Mid-term beach evolution with combined load. Sensitivity of bed change (b) profiles to f_c. (a): $f_c = 0.01$. (b): $f_c = 0.02$ (default). (c): $f_c = 0.03$. Dashed black line: no change line ($t = 0$ s). Solid lines: results at $t = 5,000$ s (blue), $t = 10,000$ s (red), $t = 15,000$ s (green) and $t = 20,000$ s (black).

Fig. 7.15 displays the results of the simulations with different m_e values, i.e. halving and doubling the default one. Interestingly, the higher the m_e parameter, i.e. the efficiency in the suspended load entrainment, the lower is the erosion and the deposition in the upper and lower swash zone respectively. This is consistent with the existence of settling lag (noted by Pritchard & Hogg, 2005, in a single swash event), which tends to shift sediment from seaward to landward. However the morphodynamic pattern, i.e. the sequence of depositional and erosional areas, is not affected by variations in m_e, as previously

observed for the single swash field events (see § 6.6.1).

Note that no results for simulations excluding the suspended sediment transport are reported here, as it is believed that reducing m_e already highlights the nature of the bed change due to the bed-load transport, i.e. deposition and erosion in the lower and upper parts of the beach respectively.

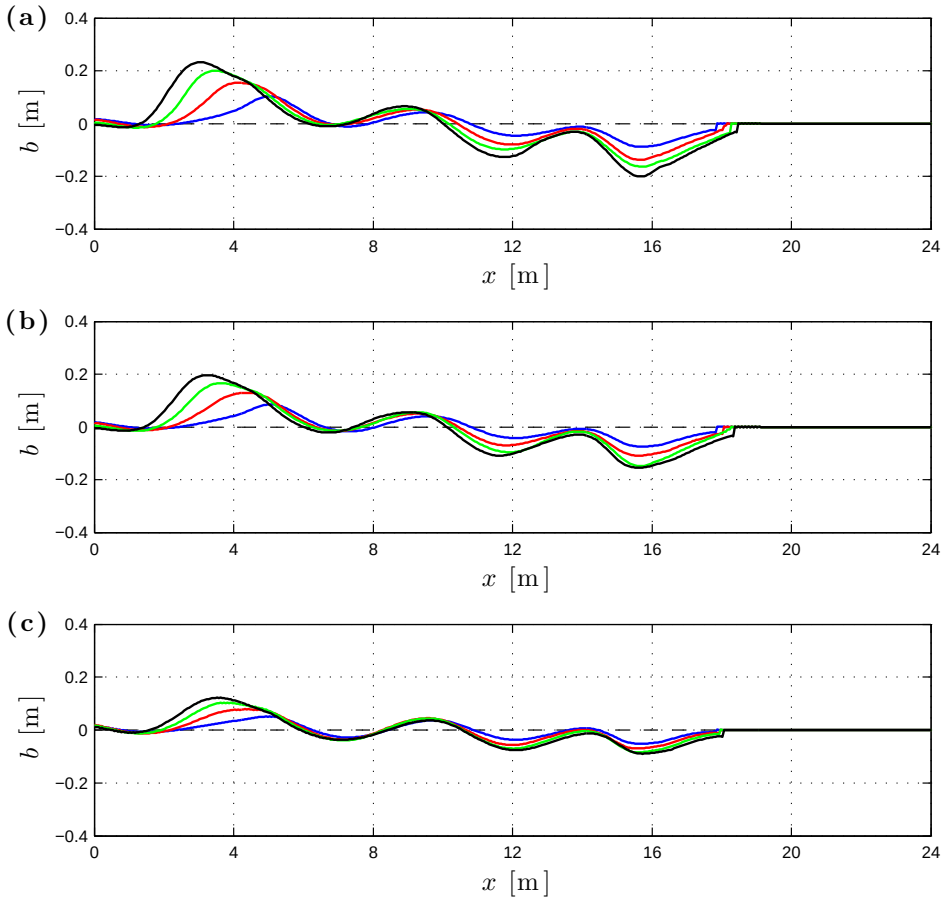

Figure 7.15: Mid-term beach evolution with combined load. Sensitivity of bed change (b) profiles to m_e. (a): $m_e = 0.001$ ms^{-1}. (b): $m_e = 0.002$ ms^{-1} (default). (c): $m_e = 0.004$ ms^{-1}. Dashed black line: no change line ($t = 0$ s). Solid lines: results at $t = 5,000$ s (blue), $t = 10,000$ s (red), $t = 15,000$ s (green) and $t = 20,000$ s (black).

Lastly, infiltration is accounted for in this combined load test, however it can be interesting to investigate the case of an impermeable beach. The results obtained removing infiltration are showed in Fig. 7.16. Small differences can

be seen in the bed change profile seaward of the initial shoreline, i.e. $x = 15$ m, while landward of it increased erosion is predicted excluding infiltration, even though no substantial quantitative deviation is apparent. Again, the present behaviour is consistent with the expected morphological response when swash asymmetry is enhanced (diminished) by inclusion (exclusion) of the infiltration effects (see Masselink & Li, 2001).

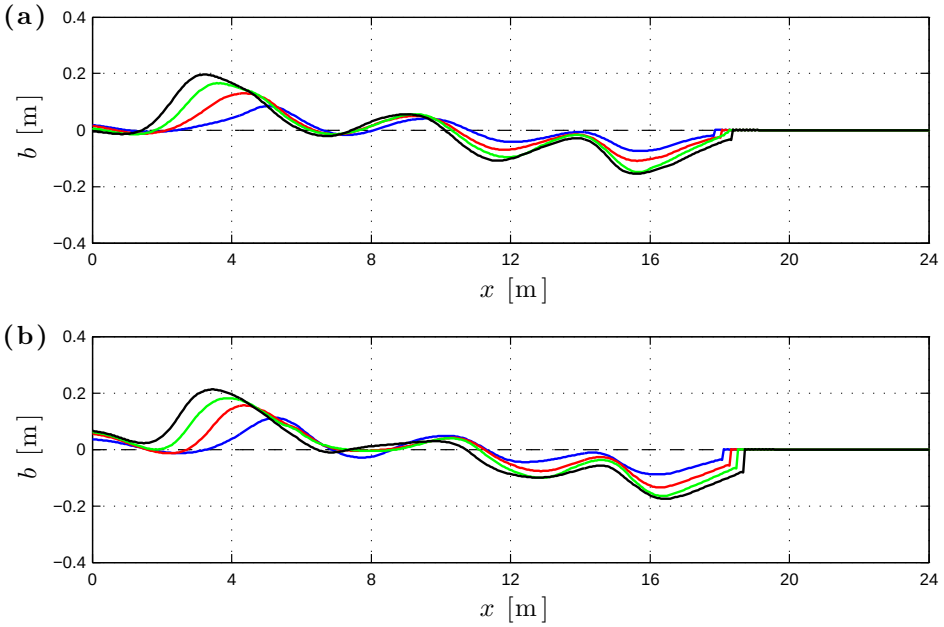

Figure 7.16: Mid-term beach evolution with combined load. Sensitivity of bed change (b) profiles to infiltration. (a): with infiltration (default). (b): without infiltration. Dashed black line: no change line ($t = 0$ s). Solid lines: results at $t = 5,000$ s (blue), $t = 10,000$ s (red), $t = 15,000$ s (green) and $t = 20,000$ s (black).

7.3.3 Sensitivity to incoming wave characteristics

In all the results for the combined load test showed so far (see Figs. 7.11–7.16), the mid-term evolution of the beach exhibits some common features, e.g. the development of three long-shore bars and generally deposition seaward and erosion landward. It can be interesting to understand if and how this pattern

is affected by variations in the characteristics of the incoming wave.

Sriariyawat (2009) compared his default results for incoming sinusoidal waves (with bed-load transport only) with those obtained for an incoming sawtooth ones, finding that the latter promote deposition (erosion) in the upper (lower) beach. However both incoming wave shapes (sinusoidal and sawtooth) yield the same qualitative morphological pattern, which consists of a long-shore bar, a trough and a swash berm (sometimes absent in the later stages of the simulation) from offshore to the shoreline.

Instead of modifying the shape of the incoming wave, this work considers the effect of different choices for the wave period T and height H, maintaining fixed the initial conditions and the other parameters and settings from Tab. 7.3. Recall that the default values are $T = 5$ s and $H = 0.25$ m. It is unrealistic to reduce T further, as this would lead to the breaking of the shallow water assumption, because of an excessively small corresponding wavelength L. Very small H values are expected to reduce significantly the morphodynamic wave action and thus to yield nearly inappreciable bed changes. On the other hand, substantially bigger ones could be inappropriate for the linear wave assumption included in the hydrodynamic BCs of Kobayashi et al. (1987) at the seaward boundary.

Therefore, two values for T bigger than the default one are chosen ($T = 7$ and 9 s) and H is varied around the default value ($H = 0.15$, 0.25 and 0.35 m). The results are displayed in Figs. 7.17 and 7.18 for the $T = 7$ s and the $T = 9$ s choices respectively.

In Fig. 7.17, the final bed change profiles show two long-shore bars only, while the overall morphodynamic response, i.e. deposition seaward and erosion landward, is analogous to that of the default simulation (see Fig. 7.11). The increase in H consistently leads to enhanced bed change, as a consequence of

more energetic wave conditions. Additionally, the more the upper beachface is eroded the more the most seaward long-shore bar extends towards the offshore boundary.

The estimated swash extensions do not vary substantially during the simulation. It is noted that they are roughly 3 m long and wider with increasing H. Comparing the results in panel (b) of Fig. 7.17 with the corresponding default ones in panel (a) of Fig. 7.11, the swash extensions for a given H are found to be consistently wider for bigger imposed T.

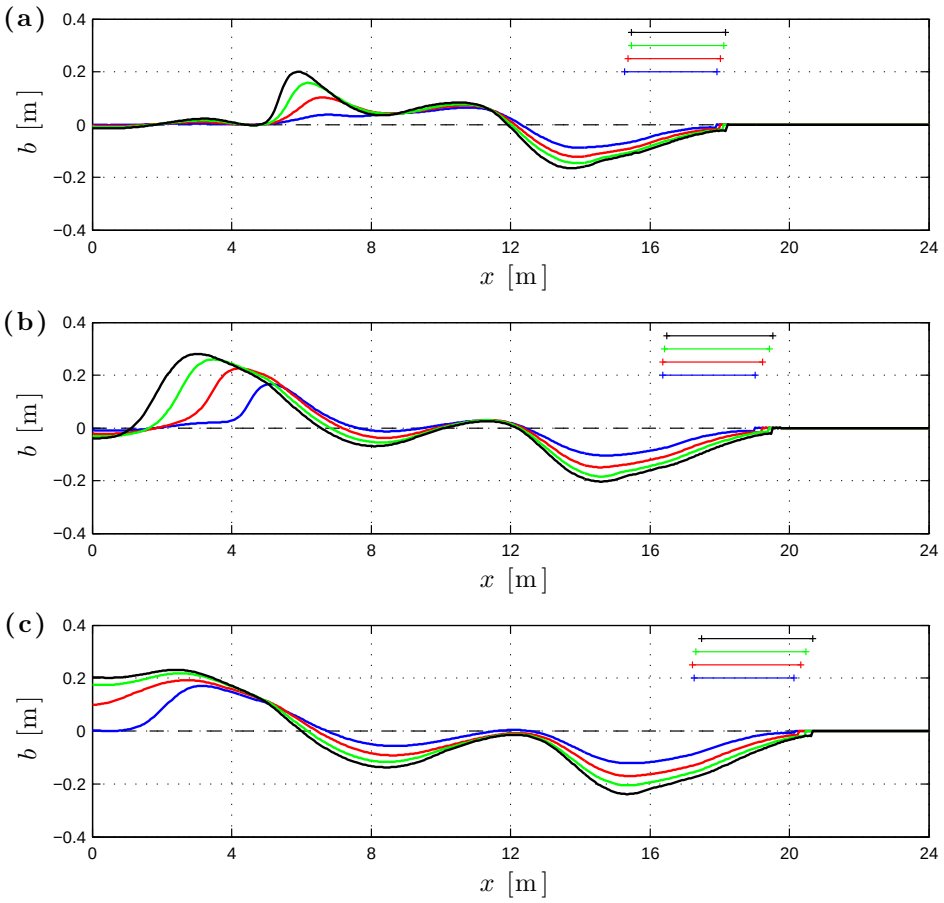

Figure 7.17: Mid-term beach evolution with combined load. Sensitivity of bed change (b) profiles and swash extensions to incoming wave characteristics. $T = 7$ s. (a): $H = 0.15$ m. (b): $H = 0.25$ m. (c): $H = 0.35$ m. Dashed black line: no change line ($t = 0$ s). Thick solid lines: results at $t = 5,000$ s (blue), $t = 10,000$ s (red), $t = 15,000$ s (green) and $t = 20,000$ s (black). Thin horizontal solid lines: swash extensions (colour legend as that for the b profiles).

The results using $T = 9$ s (see Fig. 7.18) show further differences with respect to the default ones, with only one long-shore bar developing. For the smallest H value (see panel (a)), erosion develops landward of the long-shore bar, which, as observed by Sriariyawat (2009), coincides with the location where wave breaking occurs, thus producing a marked influence on the final bed changes. For the mid H value (see panel (b)) a swash berm builds up in the upper beach, while the bar broadens until the seaward boundary. Lastly, the highest value for H exaggerates further the aforementioned bed change features (see panel (c)).

The estimated swash extensions with $T = 9$ s are bigger than with the other two values (see Figs. 7.11 and 7.17), roughly ranging from 4 m to 6 m as H increases. However note that again they do not vary substantially for a given case as the simulation progresses.

It is not straightforward to explain why the results for $T = 9$ s and $H = 0.25$ and 0.35 m exhibit a significant final swash berm, which is missing from all the other cases. This accretive effect in the upper beach can be tentatively attributed to the higher wave period and heights, which consequently yield a wider swash motion. Additionally, the more the flow extends landward of the initial shoreline, the more the infiltration becomes important because of more time and more pore space available for the percolating process. These aspects could have promoted the landward movement of the sediment.

Finally, it seems that a qualitative relationship could be established between the number of long-shore bars and the incoming wavelength, i.e. more bars when L is smaller, however it is not clear how to convert this in quantitative terms, if possible.

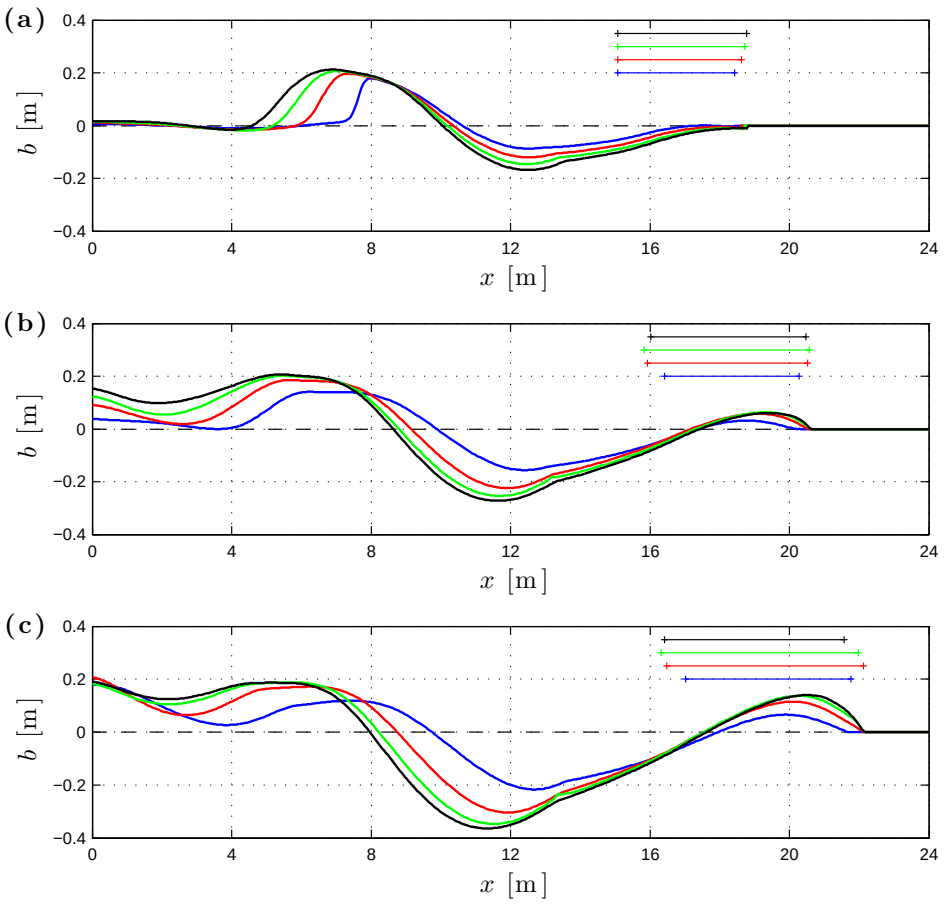

Figure 7.18: Mid-term beach evolution with combined load. Sensitivity of bed change (b) profiles and swash extensions to incoming wave characteristics. $T = 9$ s. (a): $H = 0.15$ m. (b): $H = 0.25$ m. (c): $H = 0.35$ m. Dashed black line: no change line ($t = 0$ s). Thick solid lines: results at $t = 5,000$ s (blue), $t = 10,000$ s (red), $t = 15,000$ s (green) and $t = 20,000$ s (black). Thin horizontal solid lines: swash extensions (colour legend as that for the b profiles).

7.4 Concluding remarks

This chapter deals with the analysis of the morphodynamic evolution of two beaches at the storm time-scale. Both bed- and combined load are considered, the former for comparison with reference cases while the latter for a novel investigation.

In the bed-load only test, the results compare very well with reference ones for both the impermeable (Dodd et al., 2008) and permeable (Sriariyawat,

2009) cases. The sensitivity analyses for the latter case substantially confirm the findings of Sriariyawat (2009), even though differences in simulations with the lowest f_c and k_{inf} values are observed. They are thought to be due to the implementation of the wetting restriction in the shoreline BCs (see § 4.3.3), which was not taken in account by Sriariyawat (2009). Simulations using the Darcy and the Forchheimer laws return quite different final bed change profiles, suggesting additional modelling care when higher infiltration rates are involved.

From the numerical viewpoint, the sensitivity to the minimum water depth parameter confirms the previous work of Sriariyawat (2009), showing convergence of the results for $h_{min} \leq 0.001$ m, while the sensitivity to the applied flux limiter is found not large enough to justify the substitution of the reliable and robust Minmod, widely used in previous literature.

The combined load test is designed using the field simulations of § 6 as guidance. The MPM formula is introduced, but it sometimes affected the model stability, because of the embedded threshold for sediment movement. Following Zhu & Dodd (2015), this threshold is removed (see supporting discussion in § 7.3.1) and the results for a specific case confirm that this assumption is not expected to have a significant impact on the mid-term morphodynamic evolution, in the limits of the parameters and settings chosen. The effect of neglecting the analogous threshold in the entrainment rate for the suspended load is considered as well. Despite the fact that this threshold is an order of magnitude bigger than that for bed-load, its impact on the mid-term beach evolution is found not to be substantial.

The sensitivity analysis to the friction coefficient shows increasing morphological change for higher f_c values, consistent with a higher sediment mobilisation. Increased efficiency in the entrainment rate for suspended load tends

to promote onshore transport, extending Pritchard & Hogg (2005) observation about single swash events to the case of multiple ones. Additionally, a simulation removing infiltration shows little difference with respect to the default one.

The morphodynamic response due to variations in the incoming wave period and height is also studied. The final bed change patterns differ from the default case one (three long-shore bars and generally erosion landward and deposition seaward) in the number of bars (which decreases with increasing wave period) and also qualitatively, sometimes with the formation of a swash berm. This final accretion in the upper part of the beach could have been promoted by a wider swash zone and increased infiltration caused by the higher incoming wave period and heights.

Finally, additional simulations using the fully-coupled approach (i.e. that of the present model) and a decoupled one are carried out to understand if the two of them converge to the same final results or substantial differences emerge. The corresponding results are provided in Appendix F, as, in order to make meaningful comparisons and because of the instabilities shown by the decoupled solver, some important features of the mid-term tests are removed (e.g. no bed diffusion, suspended load or infiltration are considered) and the duration of the simulation is significantly reduced. Notwithstanding these limitations, this comparison shows considerable differences in the bed change profiles predicted through the two above-mentioned approaches, confirming previous findings of Kelly & Dodd (2010) and Postacchini et al. (2012). Further study is warranted to understand better the causes of these discrepancies.

Chapter 8

Fully-coupled absorbing-generating seaward BCs

8.1 Introduction

This chapter presents a new technique for the open boundary treatment for the fully-coupled hydro-morphodynamical numerical solvers based on the NSWEs-Exner equation system. The new conditions, named REBCs, allow the generation of the incoming signals and the absorption of the reflected ones, considering the simultaneous evolution of the bed level at the seaward boundary. Approximations for linear waves in shallow water are employed and the updated values at the boundary are obtained through the solution of the Riemann Equations.

As noted in § 4.3, the chosen location for the seaward boundary often depends on computational cost constraints and on the extension of the area of interest but it can also be limited by the applicability of the equations (e.g. validity of the shallow water assumption) and for example by missing information about the bed level evolution therein.

Absorbing-generating BCs are available for the hydrodynamic only problem (e.g. Kobayashi et al., 1987; van Dongeren & Svendsen, 1997) and rely on the knowledge of the corresponding exact Riemann invariants. However, analogous morphodynamic ones for fully-coupled numerical solvers based on the NSWEs-Exner equation system were not formulated.

Therefore the REBCs are derived (see § 8.2) and then applied to some validation tests (see § 8.3), the solutions of which are computed using the TVD-MCC solver described in § 4.3.1. Note that part of this chapter is published in Incelli et al. (2015a), for the online version of which supplementary data (i.e. videos) are provided to enhance description and understanding of results.

The REBCs are for the frictionless case only. Additionally, no bed diffusion, suspended load or infiltration are considered. Furthermore, Incelli et al. (2015a) demonstrated that the new conditions do not suit simulations with significant bore heights because of increasing errors caused by the included linear approximations. Hence, the REBCs have not straightforward applicability to the previous tests presented in §§ 5 and 7. They are an interesting added value to this work and represent a topic of future research development.

8.2 Derivation of the REBCs

In this section, the REBCs are derived. The considered system of equations consists of the frictionless NSWEs (3.1) and (3.2) and of the Exner equation (3.6), rewritten in primitive form as follows:

$$\frac{\partial h}{\partial t} + u\frac{\partial h}{\partial x} + h\frac{\partial u}{\partial x} = 0, \tag{8.1}$$

$$\frac{\partial u}{\partial t} + u\frac{\partial u}{\partial x} + g\frac{\partial h}{\partial x} + g\frac{\partial z_b}{\partial x} = 0, \tag{8.2}$$

$$\frac{\partial z_b}{\partial t} + \xi\frac{\partial q_b}{\partial x} = 0. \tag{8.3}$$

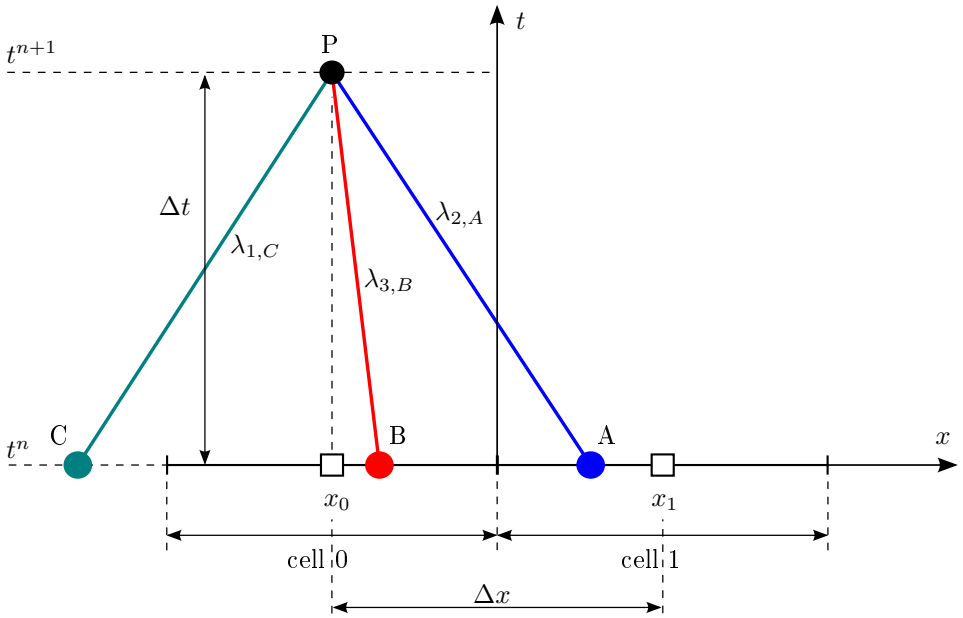

Figure 8.1: Sketch for the fully-coupled absorbing-generating seaward BCs. Empty squares on x axis indicate cell centres.

It is assumed that the flow at the seaward boundary is subcritical and that the approximations for linear waves in shallow water can be used therein, following previous work of Kobayashi et al. (1987). It is recalled that the seaward boundary is located at the left edge of cell 1, while the new conditions are imposed at cell 0, the centre of which is at $x = x_0$ as illustrated in Fig. 8.1.

At the seaward boundary, water depth and velocity, i.e. $h(x_0, t)$ and $u(x_0, t)$, can be computed as

$$h(x_0, t) = h_{ini} + z_b(x_0, 0) - z_b(x_0, t) + \eta_i(x_0, t) + \eta_r(x_0, t) \text{ and} \tag{8.4}$$

$$u(x_0, t) = u_i(x_0, t) + u_r(x_0, t), \tag{8.5}$$

with

$$u_i(x_0, t) \simeq \quad \eta_i(x_0, t)\sqrt{\frac{g}{h_{ini} - z_b(x_0, t)}} \text{ and} \tag{8.6}$$

$$u_r(x_0, t) \simeq -\eta_r(x_0, t)\sqrt{\frac{g}{h_{ini} - z_b(x_0, t)}}. \tag{8.7}$$

In Eqs. (8.4) and (8.5), h_{ini} is the still water depth at the seaward boundary

and η is the perturbation from the initial surface level, i.e. $h_{ini} + z_b(x_0, 0)$, due to the incident (η_i) and reflected (η_r) waves respectively. In particular, $\eta_i(x_0, t)$ is imposed (i.e. known), while $\eta_r(x_0, t)$ is unknown and they are related to $u_i(x_0, t)$ and $u_r(x_0, t)$ through Eqs. (8.6) and (8.7) respectively. Note that the initial bed level $z_b(x_0, 0)$ is set equal to 0 m and therefore omitted hereafter.

The new technique uses two of the three Riemann Equations associated to Eqs. (8.1)–(8.3) at the seaward boundary to determine two unknowns, $z_b(x_0, t)$ and $\eta_r(x_0, t)$, by means of Eqs. (8.4)–(8.7). The generic Riemann Equation (see Zhu, 2012, for the derivation) is written as

$$\Re_k = \frac{Dz_b}{Dt} + \frac{\lambda_k + \xi \frac{\partial q_b}{\partial h}}{\lambda_k - u} \frac{Dh}{Dt} + \frac{\lambda_k}{g} \frac{Du}{Dt} = 0, \tag{8.8}$$

where $\frac{D\cdot}{Dt}$ indicates the total (material) derivative and λ_k (for $k = 1, 2, 3$) are the eigenvalues of the Jacobian matrix associated to Eqs. (8.1)–(8.3). These eigenvalues are computed numerically (see e.g. Kelly & Dodd, 2009) as no analytical expression is available for the morphodynamic problem. Under the subcritical flow assumption, λ_1 is positive, λ_2 negative, while λ_3 can be positive or negative depending on the chosen formulation for q_b.

Note that Eq. (8.8) differs from the analogous one reported in Incelli et al. (2015a), i.e. Eq. (8) therein, as it includes the additional term $\xi \frac{\partial q_b}{\partial h}$ in the case of $q_b = q_b(h, u)$. The formulation proposed in the above-mentioned paper is suitable for $q_b = q_b(u)$, which is common for bed-load flux formulae (see Zhu & Dodd, 2013, among others). In this derivation Eq. (8.8) is considered, provided that the choice between the two different generic Riemann Equation does not affect the generality of the new technique.

With reference to Fig. 8.1, two consecutive time levels are involved, i.e. n and $n+1$. P is the centre of cell 0 at time t^{n+1}, where dependent variables (h, u and z_b) require updating. The needed $\lambda_{2,A}$ and $\lambda_{3,B}$ characteristics originate from points A and B (both to be located) at time t^n and pass through P

at time t^{n+1}. Therefore, only the Riemann Equations for $k = 2, 3$ are used to determine the two unknowns ($z_{b,P}$ and $\eta_{r,P}$). For the sake of clarity, the following notation is adopted: $z_{b,P} = z_b(P) = z_b(x = x_P, t = t_P = t^{n+1})$. Dependent variable values are available at time t^n at each cell centre. At a given time level, variable and eigenspeed values are assumed to vary smoothly in space so that linear interpolation between cells 0 and 1 gives reasonable accuracy.

The procedure starts by estimating x_A and x_B. Subsequently, values for h, u and z_b at these two points are computed. Although A and B spatial coordinates are unknown, the Courant Number condition ensures that $|\lambda_k|\Delta t < \Delta x$. Hence, the following iterative method is employed (described for one eigenspeed only because the other is analogous):

1. λ_2 eigenspeeds at centres of cells 0 and 1 are computed ($\lambda_{2,0}$ and $\lambda_{2,1}$) from dependent variables at time t^n;

2. initial guesses for x_A and $\lambda_{2,A}$ are made:

$$x_A = x_P + \frac{\Delta x}{2} \text{ and}$$
$$\lambda_{2,A} = \frac{\lambda_{2,0} + \lambda_{2,1}}{2};$$

3. a new estimate of x_A is computed using the additional relationship

$$x_{A,new} = x_P - \lambda_{2,A}\Delta t;$$

4. the relative error ϵ_A between $x_{A,new}$ and x_A, defined as

$$\epsilon_A = \frac{x_{A,new} - x_A}{x_A}, \tag{8.9}$$

is compared with a tolerance value ($tol = 10^{-2}$):

- if $\epsilon_A < tol$, then variable values ($h_A, u_A, z_{b,A}$) are computed by linear interpolation between those at cells 0 and 1;

- if $\epsilon_A > tol$, then a bisection method is undertaken: new x_A and $\lambda_{2,A}$ values are computed and the process goes back to point 3.

Note that if $\lambda_{3,B} > 0$, then values are extrapolated rather than interpolated from those at cell centres 0 and 1. The error related to the extrapolation is assumed negligible if $|\lambda_3| \ll |\lambda_1|, |\lambda_2|$. This is true, for example, when q_b is expressed by the Grass formula, i.e. Eq. (3.7), under the test conditions chosen by Incelli et al. (2015a). However, in general, the fact that $|\lambda_3|$ is small needs preliminary verification.

Once dependent variables at A and B are known, the Riemann Equations can be expressed as

$$(z_{b,P} - z_{b,A}) + \mu_{2,A}(h_P - h_A) + \omega_{2,A}(u_P - u_A) = 0 \text{ and} \tag{8.10}$$

$$(z_{b,P} - z_{b,B}) + \mu_{3,B}(h_P - h_B) + \omega_{3,B}(u_P - u_B) = 0, \tag{8.11}$$

where

$$\mu_{k,j} = \frac{\lambda_{k,j} + \xi \left.\frac{\partial q_b}{\partial h}\right|_j}{\lambda_{k,j} - u_j} \text{ and} \tag{8.12}$$

$$\omega_{k,j} = \frac{\lambda_{k,j}}{g}, \tag{8.13}$$

with $(k, j) = (2, A), (3, B)$. The aforementioned equations can be rearranged in this way:

$$z_{b,P} + \mu_{2,A} h_P + \omega_{2,A} u_P = \sigma_{2,A} \text{ and} \tag{8.14}$$

$$z_{b,P} + \mu_{3,B} h_P + \omega_{3,B} u_P = \sigma_{3,B}, \tag{8.15}$$

where

$$\sigma_{k,j} = \left(z_{b,j} + \mu_{k,j} h_j + \omega_{k,j} u_j\right), \text{ with } (k, j) = (2, A), (3, B).$$

It is convenient to subtract Eq. (8.15) from Eq. (8.14) to eliminate $z_{b,P}$, obtaining

$$\mu h_P + \omega u_P = \sigma, \tag{8.16}$$

with

$$\mu = \mu_{2,A} - \mu_{3,B} \ ,$$

$$\omega = \omega_{2,A} - \omega_{3,B} \ ,$$

$$\sigma = \sigma_{2,A} - \sigma_{3,B}.$$

Then Eqs. (8.4)–(8.7) are substituted into Eqs. (8.14) and (8.16):

$$z_{b,P} + \mu_{2,A}\left(h_{ini} - z_{b,P} + \eta_{i,P} + \eta_{r,P}\right) + \\ + \omega_{2,A}\sqrt{\frac{g}{h_{ini} - z_{b,P}}}\left(\eta_{i,P} - \eta_{r,P}\right) = \sigma_{2,A} \text{ and} \tag{8.17}$$

$$\mu\ \left(h_{ini} - z_{b,P} + \eta_{i,P} + \eta_{r,P}\right) + \\ + \omega\ \sqrt{\frac{g}{h_{ini} - z_{b,P}}}\left(\eta_{i,P} - \eta_{r,P}\right) = \sigma. \tag{8.18}$$

An auxiliary variable is defined as

$$\Omega = \sqrt{h_{ini} - z_{b,P}} > 0 \text{ by definition.} \tag{8.19}$$

Then $\eta_{r,P}$ is made explicit from Eq. (8.18):

$$\eta_{r,P} = \eta_{i,P} + \Omega\,\frac{\sigma - \mu\left(\Omega^2 + 2\eta_{i,P}\right)}{\Omega\mu - \sqrt{g}\omega} \tag{8.20}$$

and substituted into Eq. (8.17), obtaining a cubic equation in Ω:

$$\Omega^3 + a_2\Omega^2 + a_1\Omega + a_0 = 0, \tag{8.21}$$

where

$$a_2 = -\sqrt{g}\,\frac{\omega - \omega\mu_{2,A} + \mu\omega_{2,A}}{\mu}, \tag{8.22}$$

$$a_1 = -\,\frac{\mu h_{ini} - \mu\sigma_{2,A} + \sigma\mu_{2,A}}{\mu}, \tag{8.23}$$

$$a_0 = -\sqrt{g}\,\frac{\omega\sigma_{2,A} - \sigma\omega_{2,A} - \omega h_{ini} + 2\eta_{i,P}\left(\mu\omega_{2,A} - \omega\mu_{2,A}\right)}{\mu}. \tag{8.24}$$

Eq. (8.21) is solved through the Cardano formula (see Abramowitz & Stegun, 1972, and Appendix B for more details about the cubic equation solution);

when there are three real roots, the one that yields the closest value of $z_{b,P}$ to the previous one at time t^n is used as the updated bed level. At this point, $\eta_{r,P}$ is computed from Eq. (8.20) and the dependent variables at the seaward boundary cell are updated by means of Eqs. (8.4) and (8.5).

In order to refine the obtained values, a further iterative procedure is introduced. New eigenspeed values $\lambda_{k,P}$ are computed from h_P, u_P and $z_{b,P}$, and then averaged with the previously estimated ones at A and B:

$$\lambda_{2,AP} = \frac{\lambda_{2,A} + \lambda_{2,P}}{2} \text{ and}$$
$$\lambda_{3,BP} = \frac{\lambda_{3,B} + \lambda_{3,P}}{2}.$$

These averages are used to update coefficients defined by Eqs. (8.12) and (8.13), together with the following ones:

$$u_{jP} = \frac{u_j + u_P}{2} \text{ and}$$
$$\left.\frac{\partial q_b}{\partial h}\right|_{jP} = \frac{\left.\frac{\partial q_b}{\partial h}\right|_j + \left.\frac{\partial q_b}{\partial h}\right|_P}{2},$$

with $j = A, B$. Hence, Riemann Equations (8.10) and (8.11) are solved again and new values are available for the dependent variable at P. This iteration can be repeated until subsequent values of h_P, u_P and $z_{b,P}$ agree to a chosen degree of accuracy. In particular, it is convenient to define a relative error on h_P as

$$\epsilon_h = \frac{h_{P,new} - h_{P,old}}{h_{P,old}}, \tag{8.25}$$

with *new* and *old* labelling the last and the second last computed values respectively. The procedure is then terminated when $|\epsilon_h| < 10^{-12}$.

8.3 Validation of the REBCs

Seaward BCs are often validated through tests of reflection of sinusoidal waves (e.g. Wei et al., 1999) but, while analytical solutions are available for the fixed bed case, none exists for wave reflection on mobile bed in the previous literature. However an exact solution is provided by the Rankine-Hugoniot conditions for moving discontinuities, i.e. uniform bores (see Kelly & Dodd, 2010, among others, and Appendix D). Hence the proposed validation of the REBCs comprises a test involving monochromatic waves (see § 8.3.1) and a test for uniform bores (see § 8.3.2).

The wave test consists of different cases. The first case is the full reflection of a single monochromatic wave on mobile bed, aiming at quantifying the capability of the REBCs to allow reflected signals to exit the domain. The second involves a monochromatic wave train on mobile bed with the purpose of checking whether the evolution of the bed is affected by the REBCs or not. The third presents a monochromatic wave train on virtually-fixed / fixed bed, looking for convergence of the REBCs to hydrodynamic only ones when the sediment mobility tends to zero.

Lastly, the test for the reflection of a uniform bore on a mobile bed is studied. This is very demanding for the REBCs, as in shocks the water velocity departs from the linear approximations adopted in the new BCs, namely Eqs. (8.6) and (8.7). It is thus a useful test to assess the robustness of the REBCs.

All simulations are carried out excluding bottom friction in order to prevent its effects from masking potential spurious oscillation introduced by the REBCs. Additionally, to avoid unnecessary complication and uncertainties, the bed-load transport is modelled using the Grass formula. Therefore the derivation presented in § 8.2 reverts back to that originally included in Incelli

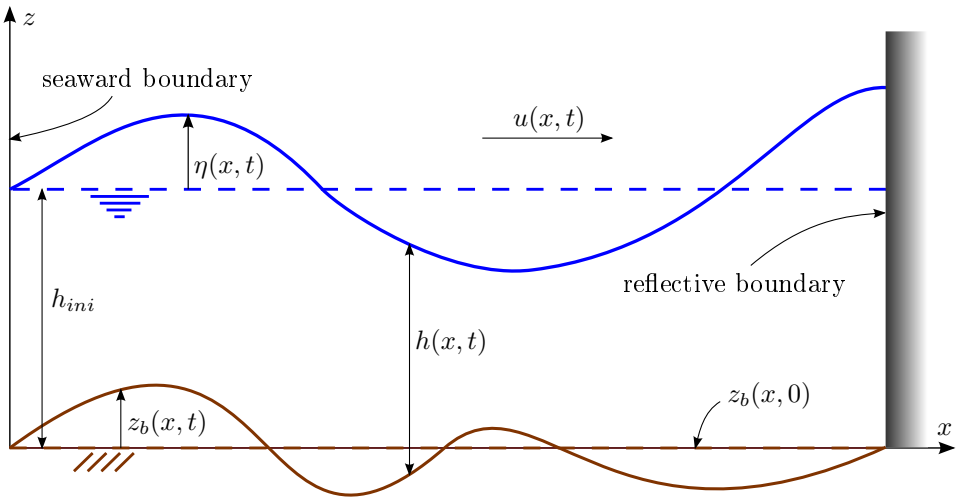

Figure 8.2: Monochromatic wave test. Sketch of initial conditions, involved variables and generic evolution profiles for the water depth (h) and the bed level (z_b) in the case of a mobile bed. Dashed lines: initial conditions for h and z_b. Solid lines: generic evolution profiles for h and z_b.

et al. (2015a).

Finally, the numerical solutions are computed through the TVD-MCC scheme described in § 4.3.1, excluding the redundant physics with respect of that considered in the REBCs (i.e. bottom friction, suspended load, bed diffusion and infiltration) and applying Minmod as default.

8.3.1 Monochromatic wave test

This test considers a single monochromatic wave or a monochromatic wave train entering an initially flat bottomed channel with uniform still water depth h_{ini}. Fig. 8.2 displays the initial conditions and the variables involved in this test, along with the generic evolution profiles for the water depth and the bed level in the case of a mobile bed.

The input signal is a monochromatic wave of height H, period T and wavelength L. The different cases are always carried out within the shallow water limit, i.e. $h_{ini}/L < 1/20$ (Svendsen, 2005). Furthermore, less steep waves

are tested to limit their steepening caused by the adoption of the NSWEs, so that wave breaking is avoided. Breaking waves (bores) are considered in § 8.3.2.

For the mobile and the virtually-fixed bed cases, $A_{sed} = 0.004$ s^{2}m^{-1} and $A_{sed} = 10^{-8}$ s^{2}m^{-1} respectively, while $p_b = 0.40$, following Kelly & Dodd (2009) and Briganti et al. (2012a).

At upstream (left) boundary the REBCs are used, while at the downstream (right) one these fully reflective conditions are applied:

$$h^n_{M+1} = \quad h^n_M, \tag{8.26}$$

$$u^n_{M+1} = -u^n_M, \tag{8.27}$$

$$z^n_{b,M+1} = \quad z^n_{b,M}. \tag{8.28}$$

Finally, $\Delta x = 0.10$ m and $CN = 0.90$.

Single monochromatic wave on mobile bed

The case with a single monochromatic wave is performed using the parameters and the settings shown in Tab. 8.1. The aim of this case is to provide a quantification of the error in absorption produced by the application of the REBCs and to understand if and how it varies with the ratios h_{ini}/L and H/L, i.e. wavelength parameter and wave steepness.

Their variation is obtained by fixing L and changing values of h_{ini} and H. The values for h_{ini} and H are selected to let the parameters h_{ini}/L and H/L span an order of magnitude. Firstly, four different values for h_{ini} are chosen, corresponding to four different incoming wave periods T for fixed L. Periods are computed through the dispersion relationship for linear waves in shallow water (see Svendsen, 2005). Secondly, three values of H are adopted (see Tab. 8.1).

In this case the domain is long enough so that the generation of the incoming signal at the seaward boundary ceases before the absorption of the reflected

Physical parameters and numerical settings	
Sediment mobility parameter (A_{sed})	0.004 s^2m^{-1}
Bed porosity (p_b)	0.40
Initial still water depth (h_{ini})	0.50 / 1.00 / 2.00 / 5.00 m
Incoming wave period (T)	45.16 / 31.93 / 22.58 / 14.28 s
Incoming wave length (L)	100.00 m
Incoming wave height (H)	0.02 / 0.05 / 0.10 m
Domain length (L_x)	100.00 m
Spatial step size (Δx)	0.10 m
Courant Number (CN)	0.90
Duration of the simulations	$> 4T$ s

Table 8.1: Single monochromatic wave on mobile bed. Physical parameters and numerical settings. '/' separates alternative values used in the different simulations.

wave begins. Three snapshots for one of the performed simulations (see also Video 1 available for the online version of Incelli et al., 2015a) are provided in Fig. 8.3 to illustrate the typical evolution of the variables. The final bed profile shows respectively one erosional and one depositional area moving away from the right boundary. If a single wave with a leading trough is simulated instead, the order of the areas is reversed, as shown in Fig. 8.4.

Any wave that enters the domain should eventually exit from the seaward boundary, leaving a quiescent flow state behind (see panels (c) of Figs. 8.3 and 8.4). From the time history of $\eta_{r,P}$ it is possible to identify the time level after which its value falls below a defined threshold, so that the reflected wave can be assumed to be completely passed through the seaward boundary. Here the threshold is set at $1/1,000$ of the maximum absolute value of $\eta_{i,P}$, i.e. $H/2$. Then, maximum and minimum values for surface level perturbation and velocity in the whole domain are recorded after the absorption terminated.

The following non-dimensional estimates of (local) error are defined:

$$\epsilon_\eta = \frac{\eta_m}{H/2} \text{ and} \tag{8.29}$$

$$\epsilon_u = \frac{u_m}{u_{i,max}}, \tag{8.30}$$

where η_m and u_m refer to the above-mentioned maximum (or minimum) values, detected at a certain cell m, while $u_{i,max}$ is the maximum velocity of the particular incoming wave of height H. In panels (a) and (b) of Fig. 8.5 it is apparent that absolute values for minimum ϵ_η and ϵ_u decrease as the wavelength parameter increases and rise with incoming wave steepness. The maximum values show the same behaviour but are always so small that this cannot be seen at Fig. 8.5 scale. Local errors for the simulation with $h_{ini}/L = 0.005$ and $H = 0.10$ m are included in panels (a) and (b) of Fig. 8.5 for completeness, even though in this simulation the sinusoidal wave clearly broke, generating a bore (not showed here) and deteriorating the performance of the REBCs. This is the only simulation in which breaking occurred. In all remaining simulations the local errors are small and within the 1% threshold.

Panel (c) of Fig. 8.5 shows the root mean squared errors (RMSE) for the surface level perturbation and the water velocity, computed throughout the domain after the absorption terminated. These are defined as

$$\text{RMSE}(q) = \left(\frac{1}{M} \sum_{m=1}^{M} (q_m - \tilde{q})^2 \right)^{1/2}, \tag{8.31}$$

where q indicates a generic quantity (η or u here), $\tilde{q}$ is the corresponding expected value (which is zero for both η or u in this case). These RMSE results confirm that errors decrease as h_{ini}/L increases and rise with H values. Moreover, the errors remain at least two orders of magnitude smaller than the respective maximum incoming signal, indicating that the REBCs are effective.

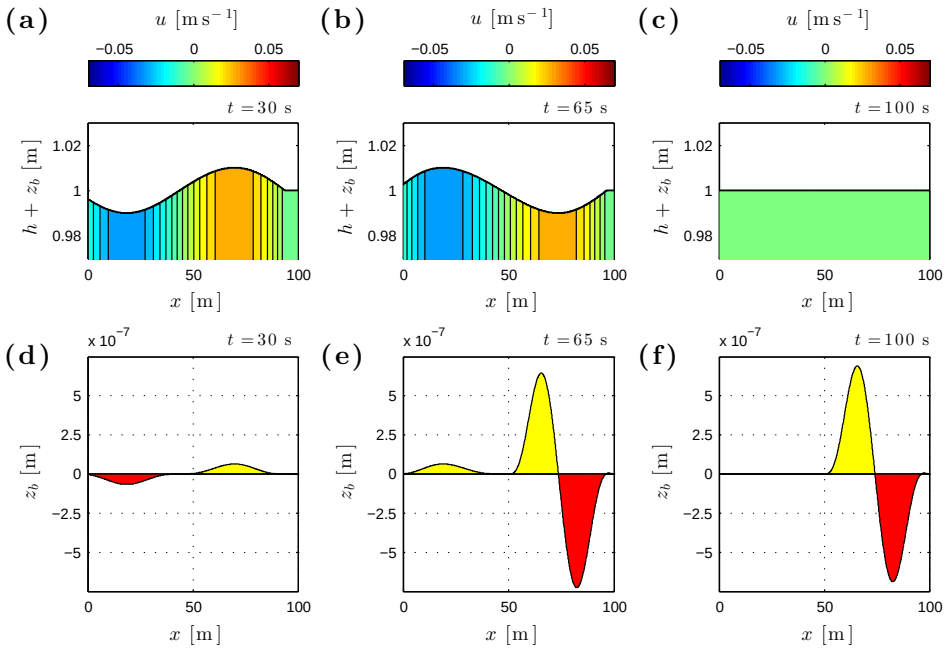

Figure 8.3: Single monochromatic wave on mobile bed. Incoming wave with leading crest. Snapshots at three different times, namely at $t = 30$ s (left column, (a) and (d)), $t = 65$ s (mid column, (b) and (e)) and $t = 100$ s (right column, (c) and (f)). $h_{ini} = 1.00$ m, $T = 31.93$ s and $H = 0.02$ m. (a)–(c): surface level ($h + z_b$) profiles with water velocity (u) contours every 0.005 ms^{-1} .(d)–(f): bed level (z_b) profiles, with depositional and erosional areas filled in yellow and red respectively.

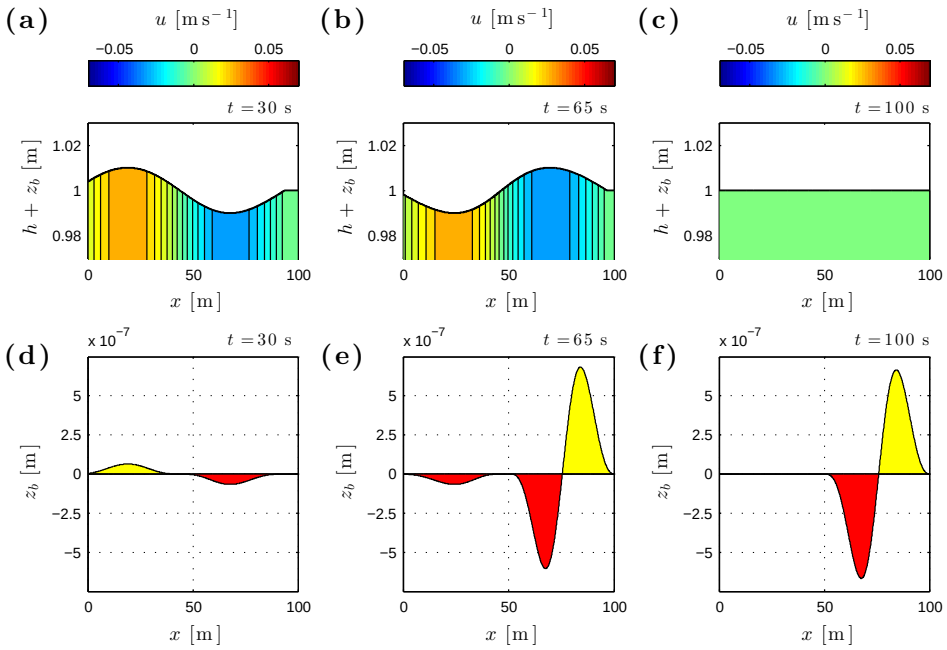

Figure 8.4: Single monochromatic wave on mobile bed. Incoming wave with leading trough. Snapshots at three different times, namely at $t = 30$ s (left column, (a) and (d)), $t = 65$ s (mid column, (b) and (e)) and $t = 100$ s (right column, (c) and (f)). $h_{ini} = 1.00$ m, $T = 31.93$ s and $H = 0.02$ m. (a)–(c): surface level ($h + z_b$) profiles with water velocity (u) contours every 0.005 ms^{-1}. (d)–(f): bed level (z_b) profiles, with depositional and erosional areas filled in yellow and red respectively.

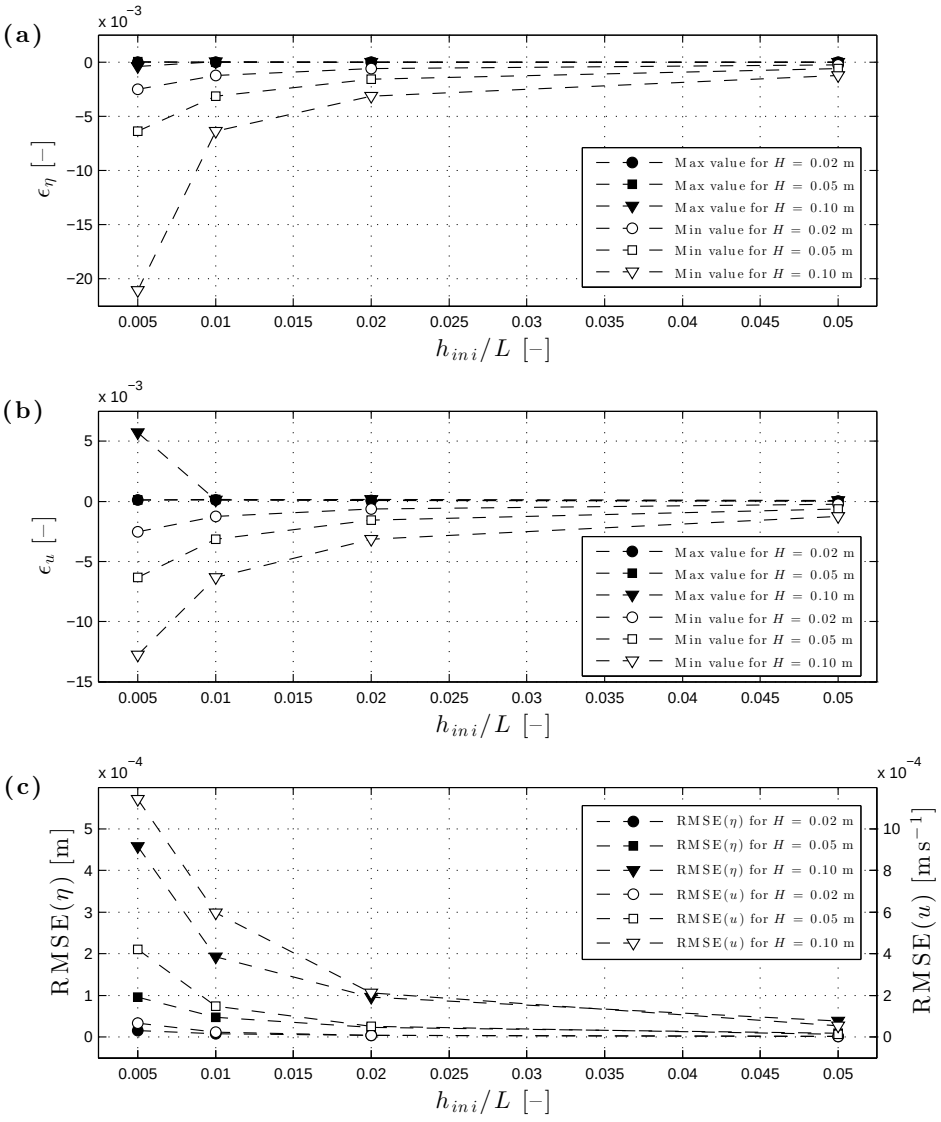

Figure 8.5: Single monochromatic wave on mobile bed. Error analysis with respect to h_{ini}/L for given H values. (a): maximum and minimum estimates of local error for surface level perturbations (ϵ_η). (b): maximum and minimum estimates of local error for velocity (ϵ_u). (c): root mean squared errors for surface level perturbation (RMSE(η)) and velocity (RMSE(u)).

Monochromatic wave train on mobile bed

This case is carried out with the parameters and the settings summarised in Tab. 8.2, which shows the two considered values for h_{ini}, namely 0.50 m and 1.00 m, corresponding to wavelengths L of 100.00 m and 141.42 m respectively. The domain length is chosen in order to be long enough to contain at least one wavelength.

Physical parameters and numerical settings	
Sediment mobility parameter (A_{sed})	0.004 s^2m^{-1}
Bed porosity (p_b)	0.40
Initial still water depth (h_{ini})	0.50 / 1.00 m
Incoming wave period (T)	45.16 s
Incoming wave length (L)	100.00 / 141.42 m
Incoming wave height (H)	0.02 m
Domain length (L_x)	200.00 m
Spatial step size (Δx)	0.10 m
Courant Number (CN)	0.90
Duration of the simulation	200,000 s

Table 8.2: Monochromatic wave train on mobile bed. Physical parameters and numerical settings. '/' separates alternative values used in the different simulations.

Figs. 8.6 and 8.7 display surface level, velocity and bed level time stacks for the last $1,000$ s of the simulations with $h_{ini} = 0.50$ m and $h_{ini} = 1.00$ m respectively (see also Videos 2 and 3 available for the online version of Incelli et al., 2015a, for a dynamic description of flow and bed evolution). The monochromatic wave train generates a nonlinear standing water wave for the flow (panels (a) and (b)) and a corresponding pattern in the bed profile (panels (c)). Surface level and velocity contours highlight the effects of nonlinearity, i.e. the wave steepening, which is exacerbated when h_{ini} is smaller. Those

of the bed level exhibit a remarkable stability in time of the solution for the bed profile. The bedforms develop and remain almost stationary with small oscillations, consistently with the nature of the hydrodynamic field.

Panels (a) and (c) of Fig. 8.8 present the final bed level profiles for both simulations, better showing the bottom pattern, which comprises a sequence of deposition-erosion-deposition areas and two zero-bed-change points every half wavelength. This pattern is not altered by the location of the seaward boundary, even when the latter is set at a non-integer multiple of L, indicating that the REBCs act effectively as a transparent boundary.

In contrast with the linear theory, the nonlinearity of the waves causes oscillation of the nodal points and asymmetry in the deposition / erosion pattern. The more the wave steepens, that is in the direction of decreasing x, the more the velocity nodes oscillate and the bed profile is affected, showing a small accretion between consecutive depositional areas (for example see panel (a) of Fig. 8.8). However, drawing back attention to the boundary condition validation, it is important to remark that no significant spurious oscillation is generated or propagates through the bed level profiles, as previously shown by the bed level contours being substantially parallel to the time axis (see Figs. 8.6 and 8.7).

Panels (b) and (d) of Fig. 8.8 present the amplitudes (Λ) of the first two harmonics of the surface level standing wave for both simulations. The depositional areas occur at both sides of each wave antinode position while the erosional trough is apparent where wave nodes are located. It is very interesting to note analogies with the experimental results in Fig. 4, panel (e), at page 697 of Landry et al. (2007), showing the final profile of a fine sand bed which underwent standing wave action for 4.0 days. The bottom evolution pattern obtained in this case qualitatively agrees with that of the aforementioned

panel, even though ripples are not modelled here. Additionally, Landry et al. (2007) explicitly mentioned vertical water velocities and suspended sediment transport, which are not included in these simulations.

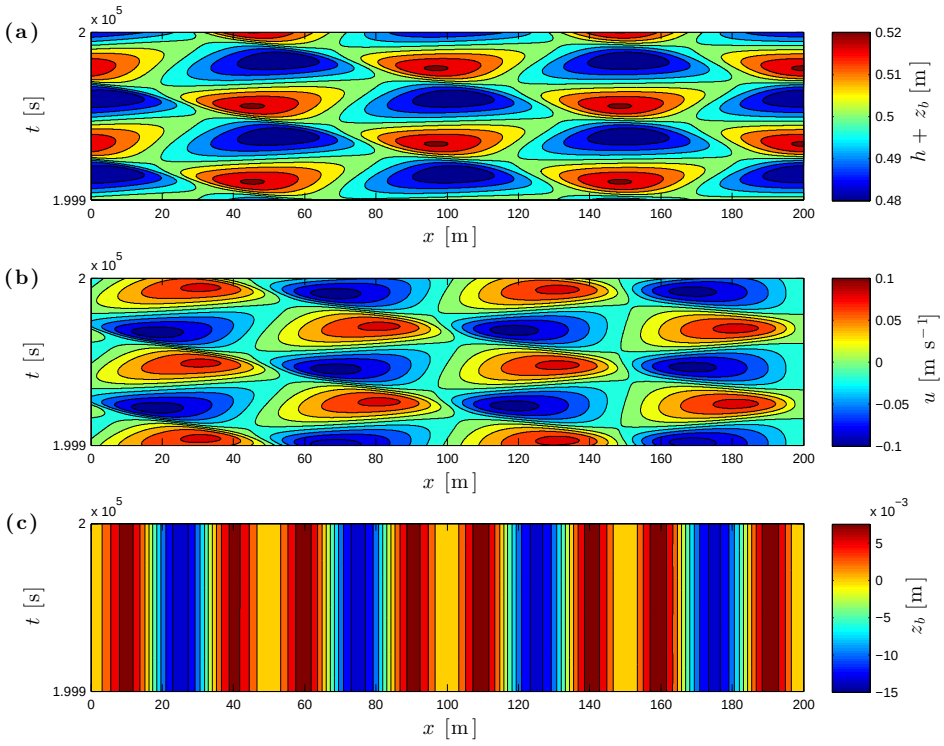

Figure 8.6: Monochromatic wave train on mobile bed. Time stacks. $h_{ini} = 0.50$ m, $T = 45.16$ s and $H = 0.02$ m. (a): surface level ($h + z_b$), with contours every 0.005 m. (b): velocity (u), with contours every 0.02 ms^{-1}. (c): bed level (z_b), with contours every 2.5×10^{-3} m.

Monochromatic wave train on virtually-fixed / fixed bed

This case is performed with $h_{ini} = 0.50$ m, which corresponds to $L = 100.00$ m. For the virtually-fixed bed simulation $A_{sed} = 10^{-8}$ s^{2}m^{-1}, while the simulation on fixed bed is obtained by running the solver for the NSWEs only, i.e. Eqs. (3.1) and (3.2), and applying the hydrodynamic BCs of Kobayashi et al. (1987) at the seaward boundary. The scope is to check if, when A_{sed} is very small, the results obtained with the REBCs converge to those for the

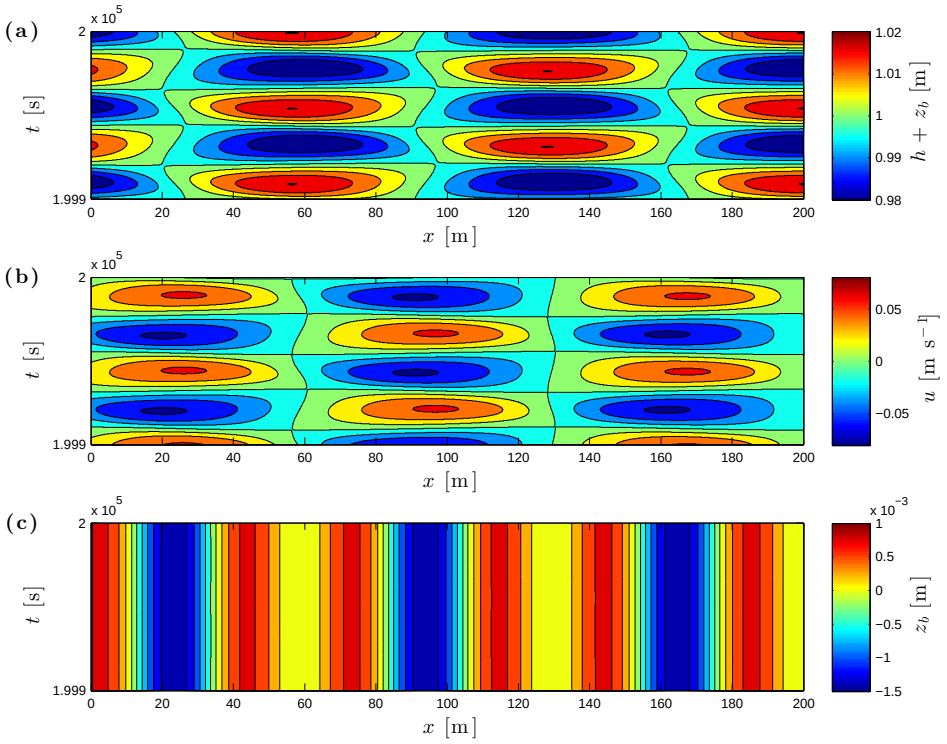

Figure 8.7: Monochromatic wave train on mobile bed. Time stacks. $h_{ini} = 1.00$ m, $T = 45.16$ s and $H = 0.02$ m. (a): surface level ($h + z_b$), with contours every 0.005 m. (b): velocity (u), with contours every 0.02 ms^{-1}. (c): bed level (z_b), with contours every 2.5×10^{-4} m.

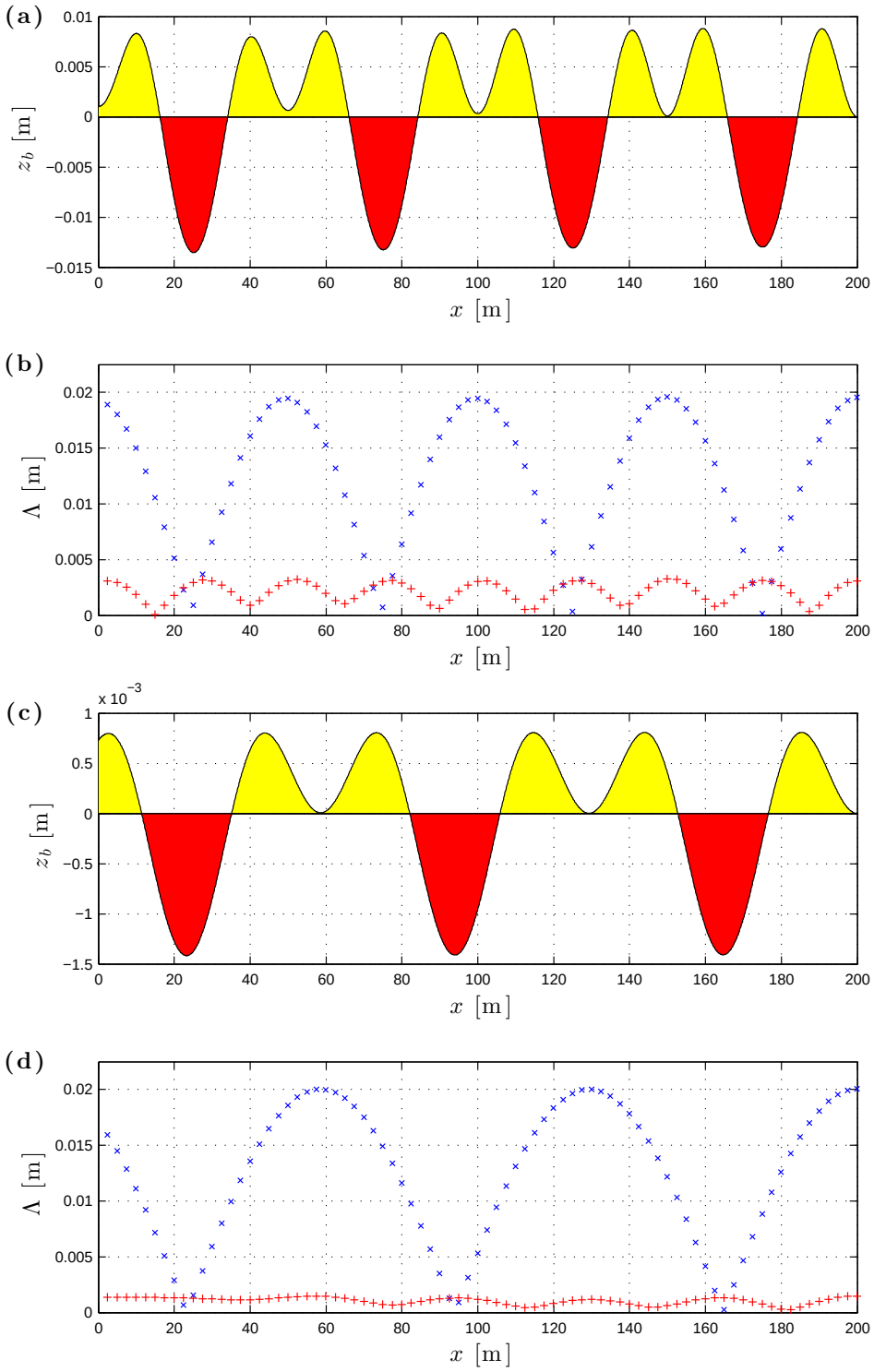

Figure 8.8: Monochromatic wave train on mobile bed. $T = 45.16$ s and $H = 0.02$ m. (a) and (b): $h_{ini} = 0.50$ m. (c) and (d): $h_{ini} = 1.00$ m. (a) and (c): final bed level (z_b) profile at $t = 200,000$ s, with depositional and erosional areas filled in yellow and red respectively. (b) and (d): amplitudes (Λ) of the first two harmonics of the surface level standing wave.

hydrodynamic only case. The used physical parameters and numerical settings are summarised in Tab. 8.3, where A_{sed} and p_b values are valid for the virtually-fixed bed simulation only.

Physical parameters and numerical settings	
Sediment mobility parameter (A_{sed})	10^{-8} s^{2}m^{-1}
Bed porosity (p_b)	0.40
Initial still water depth (h_{ini})	0.50 m
Incoming wave period (T)	45.16 s
Incoming wave length (L)	100.00 m
Incoming wave height (H)	0.02 m
Domain length (L_x)	200.00 m
Spatial step size (Δx)	0.10 m
Courant Number (CN)	0.90
Duration of the simulation	1,000 s

Table 8.3: Monochromatic wave train on virtually-fixed and fixed bed. Physical parameters and numerical settings. A_{sed} and p_b values are valid for the virtually-fixed bed simulation only.

Fig. 8.9 presents surface level time stacks for the virtually-fixed and fixed bed simulations. In particular, panel (a) shows the results obtained using the REBCs with a virtually-fixed bed; panel (b) displays the results achieved using the hydrodynamic BCs with a fixed bed; panel (c) shows the results (courtesy of Dr B. Tatlock) obtained again with the hydrodynamic BCs and a fixed bed but employing a different hydrodynamic solver, namely the finite volume solver of Briganti & Dodd (2009), based on the WAF method (Toro, 2001). Fig. 8.9 displays excellent consistency of the above-mentioned results, with differences in surface level values of the order of 10^{-4} m among the three simulations. This figure shows that the (morphodynamic) virtually-fixed bed results converge to the (hydrodynamic) fixed bed ones and indicates that in

this limit the REBCs converge to the hydrodynamic only BCs. Moreover, the TVD-MCC solution for the fixed bed case is confirmed by that obtained using the WAF solver. In the light of this, it can be stated that the result features, for instance the wave steepening and the node oscillations, are not introduced by the REBCs or scheme-specific (i.e. due to a potential misbehaviour of the TVD-MCC scheme).

8.3.2 Morphodynamic bore test

This test involves the reflection of a uniform bore using the parameters and the settings shown in Tab. 8.4. The domain consists of an initially flat bottomed channel, which is 10.00 m long and with an erodible bed. $h_{ini} = 1.00$ m, while the default value for the incoming bore height is 0.20 m. As previously for the wave test on mobile bed, $A_{sed} = 0.004$ s^{2}m^{-1} and $p_b = 0.40$. The BCs are the REBCs on the left of the domain and the reflective ones on the right, i.e. Eqs. (8.26)–(8.28). Finally, $\Delta x = 0.01$ m and $CN = 0.80$.

Physical parameters and numerical settings	
Sediment mobility parameter (A_{sed})	0.004 s^{2}m^{-1}
Bed porosity (p_b)	0.40
Still water depth (h_{ini})	1.00 m
Incoming bore height (H)	0.05 / 0.10 / 0.20 / 0.40 / 0.60 / 0.80 / 1.00 m
Domain length (L_x)	10.00 m
Spatial step size (Δx)	0.01 m
Courant Number (CN)	0.80
Duration of the simulation	10 s

Table 8.4: Morphodynamic bore test. Physical parameters and numerical settings. '/' separates alternative values used in the different simulations.

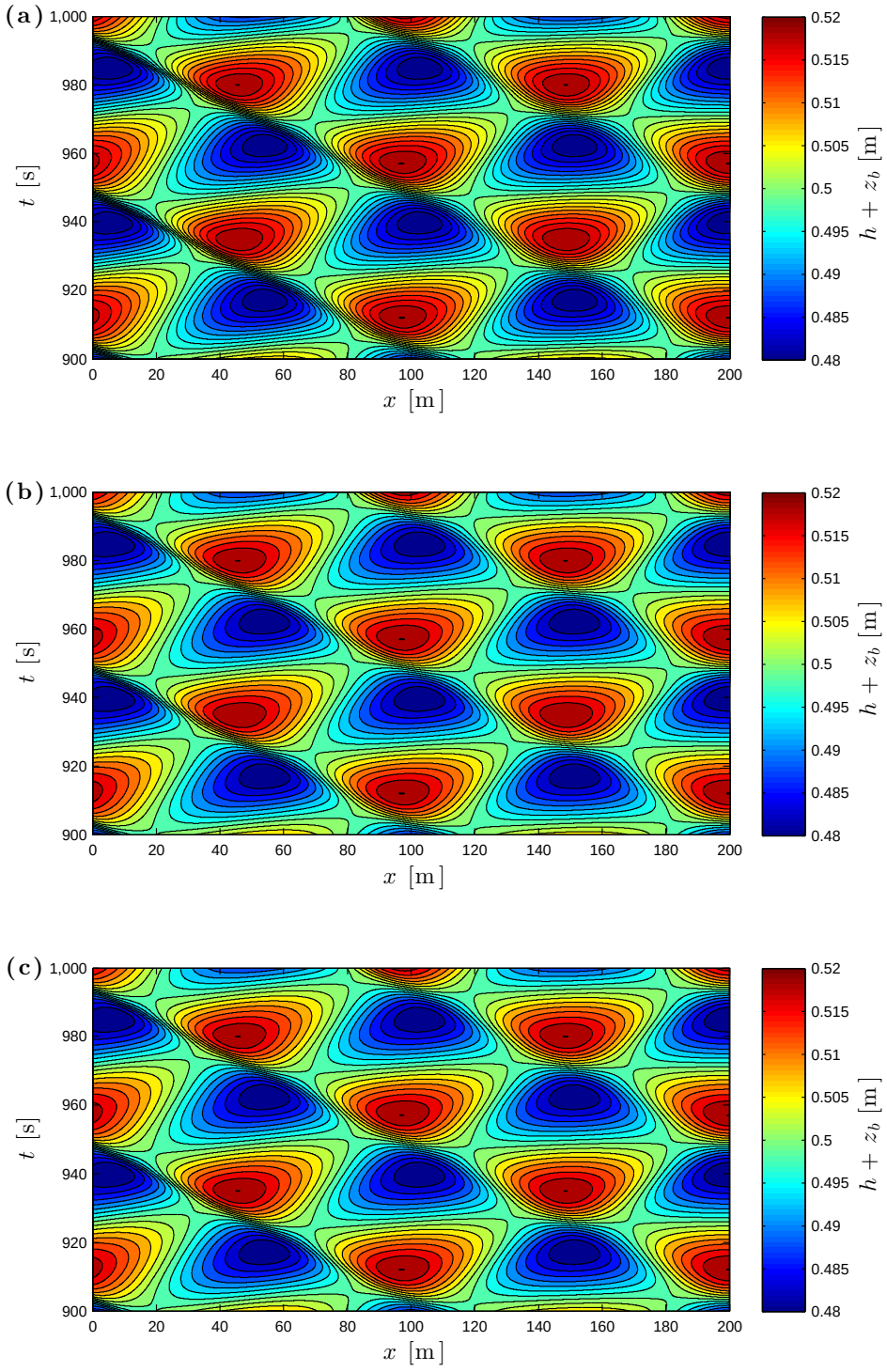

Figure 8.9: Monochromatic wave train on virtually-fixed / fixed bed. Time stacks for surface level ($h+z_b$), with contours every 0.002 m. $h_{ini} = 0.50$ m, $T = 45.16$ s and $H = 0.02$ m. (a): REBCs, virtually-fixed bed and TVD-MCC scheme. (b): hydrodynamic BCs, fixed bed and TVD-MCC scheme. (c): hydrodynamic BCs, fixed bed and WAF solver.

As mentioned in § 8.3, the exact solutions are provided by the Rankine-Hugoniot conditions. The following three distinct phases are expected to be reproduced in the simulation:

1. an incoming bore advancing rightward with the following left side values:

$$h = 1.200 \text{ m}, \tag{8.32}$$

$$u = 0.600 \text{ ms}^{-1}, \tag{8.33}$$

$$z_b = 4.003 \times 10^{-4} \text{ m}; \tag{8.34}$$

2. a reflected bore advancing leftward with the following right side values:

$$h = 1.418 \text{ m}, \tag{8.35}$$

$$u = 0.000 \text{ ms}^{-1}, \tag{8.36}$$

$$z_b = 8.373 \times 10^{-4} \text{ m}; \tag{8.37}$$

3. a restored quiescent flow state where dependent variables assume the right side values of point 2 throughout the domain.

Fig. 8.10 provides three snapshots of the simulation, with each column of panels representing one of the aforementioned phases, to describe the physical evolution (see also Video 4 available for the online version of Incelli et al., 2015a). It is apparent that when the reflected bore reaches the seaward domain, it is not fully absorbed and partly propagates back into the domain (see panel (c) of Fig. 8.10). To provide a quantification of the absorption defect, the (negative) water velocity value retained in the domain is 6.83% of the incoming one, i.e. of the value in Eq. (8.33).

It is known that the approximations for linear waves in shallow water included in the REBCs, namely Eqs. (8.6) and (8.7), do not suit the bore modelling, as they produce non-negligible errors in the water velocity estimates. For

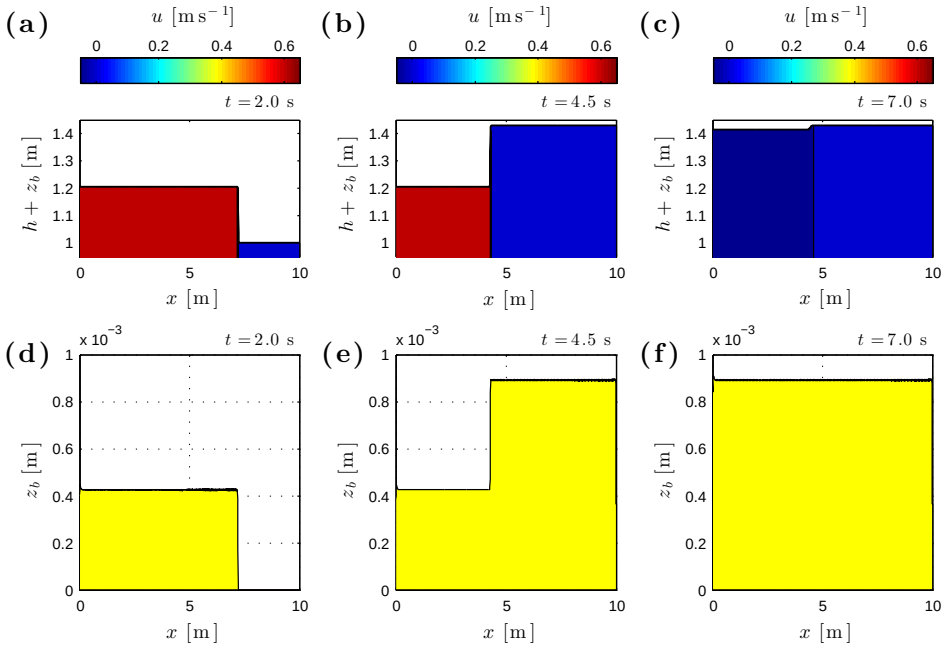

Figure 8.10: Morphodynamic bore. Snapshots at three different times, namely at $t = 2.0$ s (left column, (a) and (d)), $t = 4.5$ s (mid column, (b) and (e)) and $t = 7.0$ s (right column, (c) and (f)). $h_{ini} = 1.00$ m and $H = 0.20$ m. (a)–(c): surface level ($h + z_b$) profiles with water velocity (u) contours. (d)–(f): bed level (z_b) profiles.

example, the incoming bore velocity using Eq. (8.6) is 0.628 ms^{-1}, introducing an absolute error of 0.028 ms^{-1} and a relative one of 4.58% with respect to the exact one, i.e. the value in Eq. (8.33).

Therefore a range of bores of different heights (see Tab. 8.4) is simulated to analyse the performance of the REBCs with respect to the relative incoming bore heights (H/h_{ini}). Two types of error are studied and the corresponding results reported in Fig. 8.11. Firstly, ϵ_a is a quantification of the error related to the adoption of approximations for linear waves in shallow water. It is defined as the relative error of the approximate incoming bore velocity with respect to the exact one:

$$\epsilon_a = \frac{u_{i,approx} - u_{i,exact}}{u_{i,exact}}. \tag{8.38}$$

Secondly, ϵ_d is an estimate of the absorption defect. It is calculated as the

ratio between the minimum (as it is negative) water velocity value retained in the domain (after the reflected bore reached the seaward boundary) and the incoming bore exact one:

$$\epsilon_d = \frac{u_{retained}}{u_{i,exact}}. \tag{8.39}$$

Fig. 8.11 shows that ϵ_a is roughly half of the corresponding $|\epsilon_d|$ and that both errors consistently tend to zero with decreasing H/h_{ini}, i.e. for smaller incoming bores.

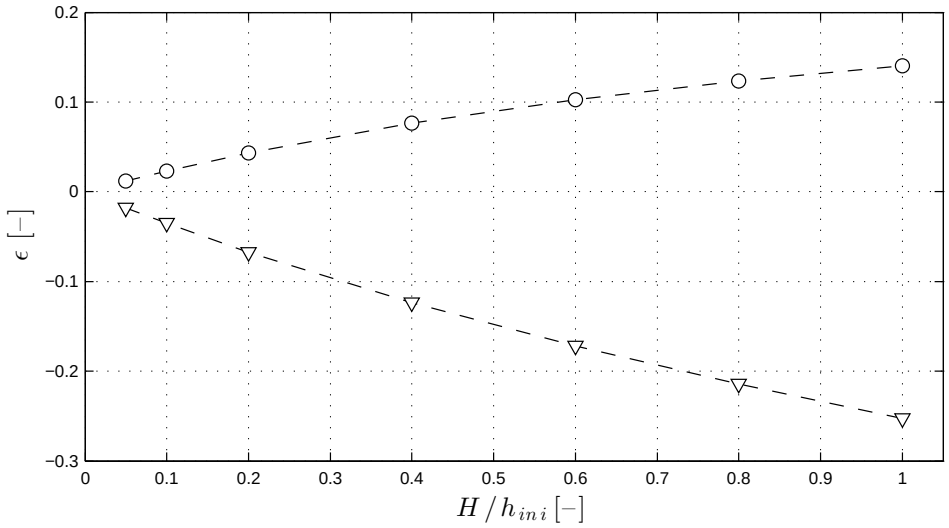

Figure 8.11: Morphodynamic bore. Error analysis with respect to H/h_{ini}. Dashed lines: error related to the adoption of the approximations for linear waves in shallow water (ϵ_a, empty circles) and that related to the absorption defect (ϵ_d, empty triangles).

In particular, for $H = 0.05$ m, $\epsilon_a \approx 1.00\%$ and the new exact solutions are provided for convenience below:

1. for the incoming bore left side (advancing rightward):

$$h = 1.050 \text{ m}, \tag{8.40}$$

$$u = 0.155 \text{ ms}^{-1}, \tag{8.41}$$

$$z_b = 7.599 \times 10^{-6} \text{ m}; \tag{8.42}$$

2. for the reflected bore right side (advancing leftward):

$$h = 1.101 \text{ m}, \tag{8.43}$$

$$u = 0.000 \text{ ms}^{-1}, \tag{8.44}$$

$$z_b = 1.538 \times 10^{-5} \text{ m}. \tag{8.45}$$

Fig. 8.12 shows the profiles of surface level, velocity and bed level in the proximity of the seaward boundary at three different times around time of reflected bore arrival therein. The REBCs give reasonably good results for $H = 0.05$ m and this is confirmed by the fact that ϵ_d falls from 6.83% of the previous case (with $H = 0.20$ m) to 1.82% of the present one.

Further simulations (not shown) demonstrated that reducing the Courant Number or increasing the spatial resolution (i.e. adopting a smaller Δx) do not improve the results. Moreover, even switching from the adopted flux limiter (i.e. Minmod) to Superbee or van Leer do not yield significant changes. In addition to this, cases for a morphodynamic bore on virtually-fixed bed were studied and substantially the same amount of ϵ_d for each bore previously simulated on mobile bed is obtained. This confirms that the absorption defect is more closely related to the adoption of the approximations for linear waves than to the morphodynamic problem.

Although the focus of this chapter is on the seaward boundary, the results (see Fig. 8.13) show a numerical error in the bed profile at the reflective boundary, i.e. after the reflection of the incoming bore the bed does not reach the right final value but remains considerably lower therein. Note that, apart from validation purposes, flow reflection against impermeable walls, which are the real counterpart of numerical reflective boundaries, is unlikely to be modelled through the one-dimensional NSWEs, as they cannot capture the expected strong three-dimensional aspects of the fluid impact, thus excluding this issue from potential engineering-related applications. Nevertheless, the latter

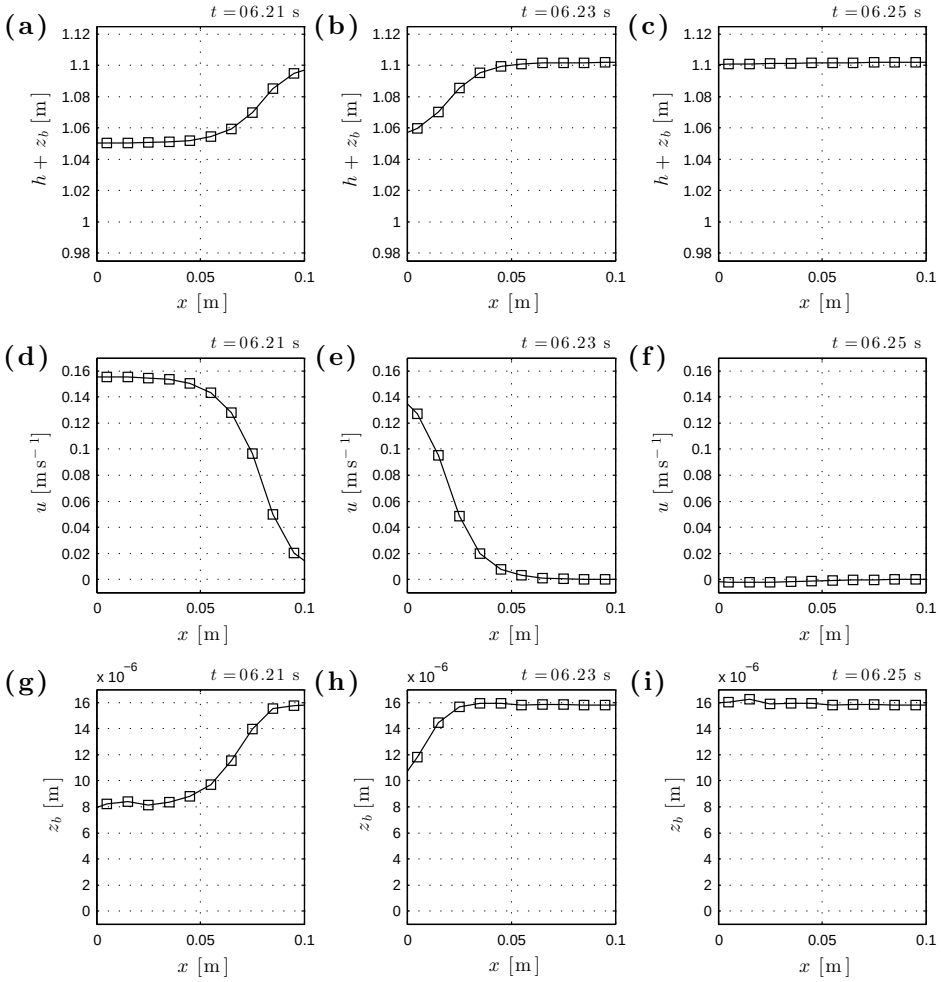

Figure 8.12: Morphodynamic bore. Profiles in the proximity of the seaward boundary at three different times around the time of reflected bore arrival therein, namely at $t = 6.21$ s (left column, (a),(d) and (g)), $t = 6.23$ s (mid column, (b),(e) and (h)) and $t = 6.25$ s (right column, (c),(f) and (i)). $h_{ini} = 1.00$ m and $H = 0.05$ m. (a)–(c): surface level ($h + z_b$). (d)–(f): velocity (u). (g)–(i): bed level (z_b). Empty squares indicate computed values at cell centres.

error represents an interesting theoretical challenge and therefore it was studied in detail, but unfortunately not solved. Outcomes and observations of the undertaken analysis are summarised in Appendix G.

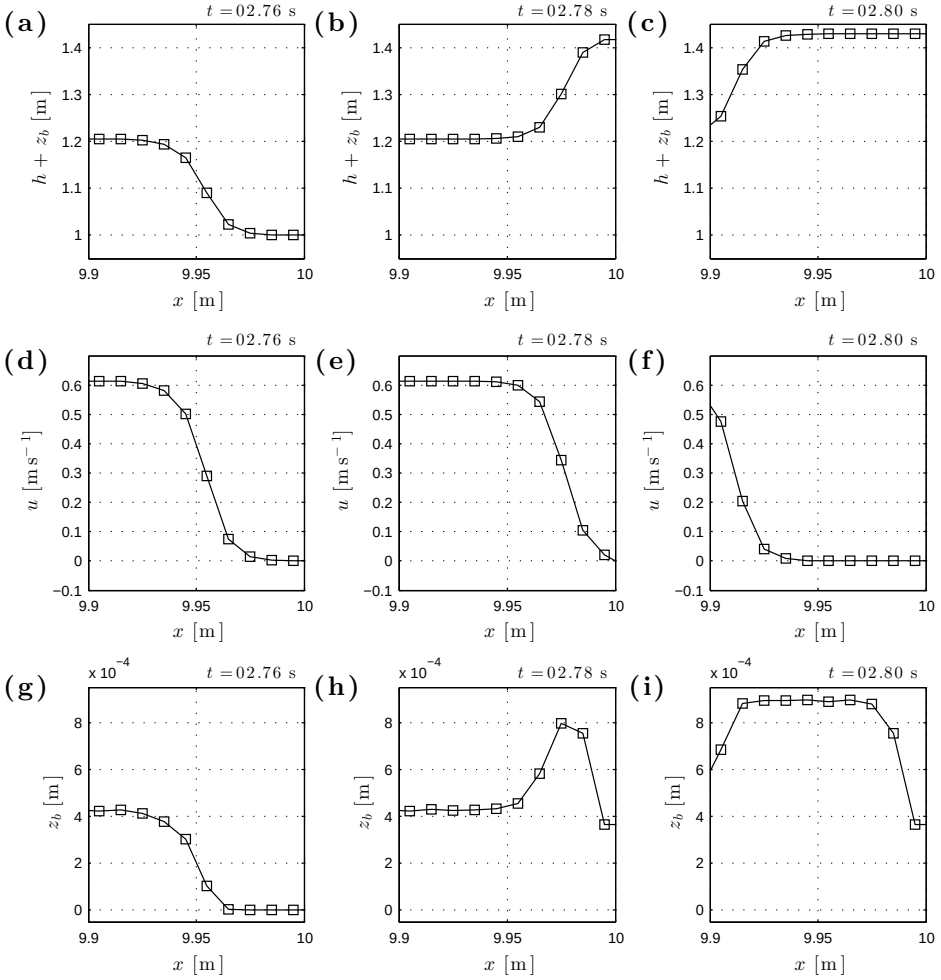

Figure 8.13: Morphodynamic bore. Profiles in the proximity of the reflective boundary at three different times around the time of incoming bore reflection therein, namely at $t = 2.76$ s (left column, (a),(d) and (g)), $t = 2.78$ s (mid column, (b),(e) and (h)) and $t = 2.80$ s (right column, (c),(f) and (i)). $h_{ini} = 1.0$ m and $H = 0.20$ m. (a)–(c): surface level ($h + z_b$). (d)–(f): velocity (u). (g)–(i): bed level (z_b). Empty squares indicate computed values at cell centres.

8.4 Concluding remarks

The REBCs are new BCs for fully-coupled hydro-morphodynamical numerical solvers based on the NSWEs-Exner equation system. They are applied to the open seaward boundary, where both the incoming and the reflected signals are accounted for. They consist of the solution of the Riemann Equations at this boundary using the approximations for linear waves in shallow water.

The REBCs are validated against tests involving monochromatic waves and morphodynamic bores. Quantified local (max and min) and global (RMSE) errors for the reflection of a single monochromatic wave are found to decrease with reducing incoming wave steepness and with increasing wavelength parameter. In all the simulations, except that where breaking occurred, errors are within the 1% threshold, giving evidence of the effectiveness of the REBCs.

The REBCs do not alter flow and bed level patterns generated by nonlinear standing waves on mobile bed, even when the seaward boundary is located at a non-integer multiple of the incoming wavelength. Additionally, the results with the REBCs on virtually-fixed bed consistently converge to those using the hydrodynamic only BCs on fixed bed.

Finally, notwithstanding the limitations due to the approximations for linear waves in shallow water embedded in the new technique, the REBCs perform reasonably well even in the demanding morphodynamic bore test.

Chapter 9

Conclusions and recommendations

9.1 Conclusions

This research work has aimed at using a fully-coupled hydro-morphodynamical numerical solver to study the beachface evolution caused by multiple swash events at the storm time-scale.

The employed model originates from that of Briganti et al. (2012a), who considered a NSWEs-Exner equation system with bed-load only. Following Briganti et al. (2011, 2012b), both the Chézy approach and the momentum integral method for the BBL description are used to estimate the bottom friction. Additionally, the suspended sediment transport mode is now included through a further equation, following Zhu (2012). Moreover a bed diffusion mechanism to allow the sediment to move downslope is added to the mathematical formulation (see Dodd et al., 2008). Finally, infiltration is considered through a simple approach, which can use both the Darcy and the Forchheimer resistance laws.

The original TVD-MCC scheme of Briganti et al. (2012a) is modified, including the aforementioned additional physics (see § 4.3.1). The infiltration

computation is implemented at the end of each time step, following Dodd et al. (2008), as this approach proved to be far more robust than including it into the TVD-MCC scheme. Different shoreline BCs from those used by Briganti et al. (2012a) are applied, because the latter were found not to be sediment conservative. This issue, while negligible in short simulations, is deemed to be unacceptable for mid-term ones. The new treatment for the wet / dry front follows the work of Hubbard & Dodd (2002) and includes a wetting restriction which helps to prevent the occurrence of spurious numerical oscillations.

Several validation tests are presented in order to assess the model performance against analytical and benchmark solutions from literature. The model provides enhanced results in both the fluvial dune and dam break tests with respect to those shown by Briganti et al. (2012a).

In the uniform bore test with bed-load only, the present results confirm those obtained with the previous version of the model (see Zhu et al., 2012), even though the minimum depth parameter needs to be reduced to 10^{-4} m, this probably because of the different applied shoreline BCs. Comparison with the MOC solution for the case with combined load reveals an overall good agreement; however maximum run-up is underestimated. A better prediction can be achieved providing that a considerably higher computational cost is accounted for.

The single swash on fixed slope experiments are reproduced for both the impermeable and the permeable beach cases. In the former, the present results are improved on those of the WAF solver of Briganti et al. (2011), especially in the later backwash phase. This is believed partly due to the choice of extending the numerical domain to the whole rig. In the latter, the uprush phase is very well predicted if the Forchheimer resistence law is applied, consistent with the sediment being a coarse sand. Notwithstanding a faster backwash than that

measured, because of an excess of infiltration in the simulation, the overall performance is thought to be reasonable, considered the simplified approach adopted for the infiltration modelling.

The flux limiter choice does not significantly affect the solutions in both the dam break and single swash on fixed slope tests, but Superbee and van Leer show to improve Minmod results in the very long simulation with the submerged dune. Even though Superbee and van Leer return more noise in the bed change evolution in the uniform bore test, the sensitivity to the applied flux limiter is examined in the mid-term simulations as well.

Modelling of real single swash events is also carried out. Although the maximum inundations are smaller than those recorded, the numerical results compare quite well with the field data in terms of hydrodynamics, thus confirming that one-dimensional, depth-averaged description of the swash is reasonable. The final predicted bed changes show the correct order of magnitude but are generally underestimated, in terms of both deposition and erosion, and the predicted pattern is not always observed in the data. The sensitivity analyses indicate that this discrepancy is not primarily due to inaccurate estimation of parameters (e.g. m_e, k_{inf} and k_b), but more probably to initial (spatially-varying and unknown) distributions of pre-suspended sediment concentration and velocity. This demonstrates that difficulties and uncertainties in the field measurements can remarkably affect the predictions of numerical solvers, even though a relatively simple physical description is implemented, as in the present model.

The morphodynamic evolutions of two beaches at the storm time-scale are studied, the first considering bed-load only (for a consistent comparison with previous literature) and the second simulating combined load. In the bed-load only test, the results compare very well with the reference ones for both the

impermeable and the permeable cases, provided by Dodd et al. (2008) and Sriariyawat (2009) respectively. In general, the sensitivity analyses for the latter case substantially confirm previous findings, however significant differences in the simulations with the lowest f_c and k_{inf} values are observed, with the wetting restriction thought to have an influence on this. The simulations using the Darcy and the Forchheimer laws return quite different final bed change profiles, suggesting additional modelling care when higher infiltration rates are involved. From the numerical viewpoint, the sensitivity to the applied flux limiter is found not large enough to justify the substitution of the reliable and robust Minmod.

In the combined load test, the MPM formula is introduced, but it sometimes affected the model stability because of the threshold for sediment movement. This suggests that the implementation of complex sediment transport formulae could reduce the numerical robustness of the present model, thus limiting somehow its flexibility. However, following Zhu & Dodd (2015) the above-mentioned threshold is removed, as this assumption is not expected to have a significant impact on the morphodynamic evolution, in the limits of the parameters and settings chosen (see discussion in § 7.3.1). Besides, the effect of neglecting the analogous threshold for the suspended load is found not to be substantial for the mid-term beach evolution, despite the fact that this threshold is an order of magnitude bigger than that for bed-load. The sensitivity analyses show that a higher friction coefficient produces higher sediment mobilisation and thus more morphological change, while increased efficiency in the entrainment rate for suspended load tends to promote onshore transport. Changes in the morphodynamic response due to variations in the incoming wave period and height are considered as well. The final bed change patterns differ from the default case one (three long-shore bars and generally erosion

landward and deposition seaward) in the number of formed bars (which decreases with increasing wave period) and also qualitatively, sometimes with the formation of a relatively high swash berm. This accretion in the upper part of the beach could have been promoted by a wider swash zone and by increased infiltration due to the higher incoming wave period and heights.

Beside this main work-stream, new BCs for fully-coupled hydro-morphodynamical numerical solvers which adopt the NSWEs-Exner equation system are derived. In this work the derivation is for a more general case than that presented by Incelli et al. (2015a), considering $q_b = q_b(h, u)$ instead of $q_b = q_b(u)$ only. The REBCs apply to the open seaward boundary, where both the incoming and the reflected signals are accounted for, and consist of the solution of the Riemann Equations therein using the approximations for linear waves in shallow water. Error estimates for the reflection of a single monochromatic wave are found to be small and to decrease with reducing incoming wave steepness and with increasing wavelength parameter. The REBCs do not alter flow and bed level patterns generated by nonlinear standing waves on mobile bed and results applying the REBCs to a virtually-fixed bed simulation consistently converge to those using the hydrodynamic only BCs in a fixed bed one. Finally, notwithstanding the limitations due to the use of approximations for linear waves in shallow water, the REBCs perform reasonably well even in the demanding morphodynamic bore test.

9.2 Recommendations

Several aspects can be regarded as important topics for future research about the further development of the present model and, more generally, in the study of swash zone morphodynamics.

Firstly, it is noted that the considered sediment flux formulations, i.e. the

Grass and the MPM formulae, are both independent of the water depth. This is likely to lead to excessive sediment transport prediction in very shallow water, which in turn can generate numerical issues in the vicinity of the shoreline or in the case of a multiple swash event involving numerous wave collisions. Some numerical investigations were carried out for example by Briganti et al. (2012a) and Zhu & Dodd (2013) introducing a linear dependence on h into the original Grass formula. However experimental evidence would be important to provide broader support to this approach. Additionally, as noted in § 2, bore- and bed-generated turbulence in the uprush and backwash phases respectively can be a key aspect towards the improvement of the morphodynamic prediction. Turbulence effects could be included directly in the sediment flux formula or as a modification of the friction estimated through the BBL solver.

Secondly, on coarser sediment beaches the subsurface flow is expected to play a crucial role. Hence the development of a solver coupling not only hydro- and morphodynamics but also both the surface and the subsurface flows would be beneficial. This would also include the modelling of exfiltration and groundwater motion, which were considered for the hydrodynamic only problem by Steenhauer et al. (2012a). They also modelled the evolution of pore-air pressure, which was found to significantly affect the subsurface processes. Beside this, recall that very recently gravel beach evolution was successfully predicted using a decoupled solver (see McCall et al., 2015).

Thirdly, both the seaward and the shoreline BCs would require further study. The REBCs are the possible first example of a family of approximate conditions for fully-coupled solvers. Introduction of additional physics, such as bottom friction, bed diffusion and suspended sediment transport, should be considered, even though the further validation could not be achievable through numerical simulations but by means of experiments only. The shoreline BCs

used in this work proved to be robust, as they permit the simulations of both idealised and real events. An approach for the shoreline boundary treatment like that adopted in the MOC solver of Zhu (2012), i.e. based on the extrapolation of values at the wet / dry front, is thought to be not suitable for this TVD-MCC solver, which aims at a possible future engineering use. Further theoretical study on the morphodynamic wet / dry problem, following the work of Zhu (2012), would be of paramount importance to develop improved, and possibly exact, shoreline BCs.

Fourthly, it would be envisaged to connect the present swash zone model with a surf zone one or to alter the hydrodynamic formulation to include the dispersion required for a correct wave modelling further seaward. This would allow the simulation of the available laboratory experiments from literature, which usually locate the flow field measurements in the surf zone.

Finally, the depth-averaged approach proved to be in good agreement with real swash measurements, increasing confidence in this choice with respect to the depth-resolving one, which is adopted in more complicated and computationally expensive solvers. Besides, it would be useful to extend the present implementation to two dimensions on the horizontal plane, thus making possible the study of alongshore variability and more complex coastal processes.

Appendix A

Equations for the momentum integral method for the BBL

The BBL solver assumes a logarithmic law profile for the horizontal velocity $U(x, z, t)$ within the BBL, with z being an upward-directed vertical axis with origin at the local instantaneous bed level. This law links U to the friction velocity $U_f = \sqrt{|\tau_b|/\rho_w}$ and is

$$U(x, z, t) = \frac{U_f}{k_{vk}} \ln\left(\frac{z}{z_0}\right), \tag{A.1}$$

where $k_{vk} = 0.41$ is the von Karman constant and z_0 is the height at which U is assumed to be zero. Following Nikuradse (1932), $z_0 \simeq k_b/30$, with k_b being the bed roughness, which is usually estimated as a function of the sediment grain size at various percentiles (see van Rijn, 1982, among many others).

Note that because of the definition of U_f and of Eq. (A.1), the BBL solver works with positive velocity only. In other words, the development of the BBL is independent of the direction of the flow, which is physically reasonable. The sign of the bed shear stress to be considered in Eq. (3.3) is then applied keeping in mind that it is a resisting action to the flow motion.

Following Fredsøe & Deigaard (1992), the momentum equation for the BBL

is integrated throughout its thickness δ, i.e. for $z_0 < z < z_0 + \delta$. At $z = z_0 + \delta$ it is assumed that $U = U_0$, where U_0 is the velocity above the BBL, or free stream velocity. A non-dimensional parameter Z is defined as

$$Z = \frac{U_0}{U_f} k_{vk} = \ln\left(\frac{\delta + z_0}{z_0}\right), \tag{A.2}$$

and its time derivative is

$$\frac{dZ}{dt} = \frac{Z}{U_0}\frac{dU_0}{dt} - \frac{Z}{U_f}\frac{dU_f}{dt}. \tag{A.3}$$

Then Eqs. (A.2) and (A.3) are substituted in the integrated momentum equation for the BBL (see Fredsøe & Deigaard, 1992) and the following ordinary differential equation in Z is obtained:

$$\frac{dZ}{dt} = \left[\frac{k_{vk}^2 U_0}{z_0} - Z\left(e^Z - Z - 1\right)\frac{1}{U_0}\frac{dU_0}{dt}\right] / \left[e^Z\left(Z - 1\right) + 1\right]. \tag{A.4}$$

Eq. (A.4) can be solved, in this model using a Runge-Kutta 4^{th} order explicit scheme, once U_0 and its time derivative are known. The free stream velocity value is back-calculated from the depth-averaged one (u), following the approach proposed by Clarke et al. (2004):

- if $h \geq \delta + z_0$, then

$$U_0 = \frac{u(h - z_0)\ln\left((\delta + z_0)/z_0\right)}{h\ln\left((\delta + z_0)/z_0\right) - \delta}, \tag{A.5}$$

- otherwise if $h < \delta + z_0$, then

$$U_0 = \frac{u(h - z_0)\ln\left(h/z_0\right)}{h\ln\left(h/z_0\right) - (h - z_0)}. \tag{A.6}$$

Appendix B

Infiltration equation solutions for the initial integration step

Following Packwood (1983) and Dodd et al. (2008), a particular solution of Eq. (3.19) is available under the assumptions of linear variation in time of h and ζ during the initial integration step. This solution is[1]

$$\zeta = \frac{1}{2}\frac{k_{inf}}{p_b}\left[1 + \left(1 + \frac{4\,p_b\,h}{k_{inf}\,\Delta t}\right)^{1/2}\right]\Delta t, \tag{B.1}$$

where ζ is the infiltration depth value at the end of the first time step Δt.

Under the same assumptions for h and ζ, it is possible to derive an analogous solution for Eq. (3.21) as well. In particular, imposing

$$h = \gamma_h \Delta t \text{ and} \tag{B.2}$$

$$\zeta = \gamma_\zeta \Delta t, \tag{B.3}$$

the following cubic equation in γ_ζ is obtained:

$$\gamma_\zeta^3 + a_2\gamma_\zeta^2 + a_1\gamma_\zeta + a_0 = 0, \tag{B.4}$$

[1] There appear to be two different misprints in Packwood (1983) and Dodd et al. (2008), in which, respectively, the equivalent of Eq. (B.1) is missing of the 1/2 multiplying factor and of the 1/2 exponent at the right-hand side.

with

$$a_2 = \frac{a_{inf}}{b_{inf}\, p_b}, \tag{B.5}$$

$$a_1 = -\frac{1}{b_{inf}\, p_b^2}, \tag{B.6}$$

$$a_0 = -\frac{\gamma_h}{b_{inf}\, p_b^2}. \tag{B.7}$$

Applying the Cardano formula for the solution of the cubic equation (see Abramowitz & Stegun, 1972, among others), the parameters Q_{par} and R_{par} and the discriminant D_{par} are defined as follows:

$$Q_{par} = \frac{1}{9}\left(3a_1 - a_2^2\right), \tag{B.8}$$

$$R_{par} = \frac{1}{54}\left(9a_2a_1 - 27a_0 - 2a_2^3\right), \tag{B.9}$$

$$D_{par} = Q_{par}^3 + R_{par}^2. \tag{B.10}$$

Then if

- $D_{par} > 0$, then one root is real and two are complex. In particular, the only real root is given by

$$\gamma_\zeta = \left(R_{par} + \sqrt{D_{par}}\right)^{1/3} + \left(R_{par} - \sqrt{D_{par}}\right)^{1/3} - \frac{a_2}{3}; \tag{B.11}$$

- $D_{par} = 0$, then all roots are real and two are equal:

$$\gamma_{\zeta,1} = 2\sqrt{-Q_{par}} - \frac{a_2}{3} \text{ and} \tag{B.12}$$

$$\gamma_{\zeta,2} = \gamma_{\zeta,3} = -\sqrt{-Q_{par}} - \frac{a_2}{3}; \tag{B.13}$$

- $D_{par} < 0$, then all roots are real and unequal. They are

$$\gamma_{\zeta,1} = 2\sqrt{-Q_{par}}\,\cos\left(\frac{\theta_{par}}{3}\right) - \frac{a_2}{3}, \tag{B.14}$$

$$\gamma_{\zeta,2} = 2\sqrt{-Q_{par}}\,\cos\left(\frac{\theta_{par}+2\pi}{3}\right) - \frac{a_2}{3}, \tag{B.15}$$

$$\gamma_{\zeta,3} = 2\sqrt{-Q_{par}}\,\cos\left(\frac{\theta_{par}+4\pi}{3}\right) - \frac{a_2}{3}, \tag{B.16}$$

where

$$\theta_{par} = \cos^{-1}\left(\frac{R_{par}}{\sqrt{-Q_{par}^3}}\right). \tag{B.17}$$

For Eq. (B.4), Eq. (B.10) is equivalent to

$$D_{par} = \frac{3\left(3\,\gamma_h\,p_b\,b_{inf} - a_{inf}\right)^2 - 4\left(b_{inf} + a_{inf}^2 + \gamma_h\,p_b\,a_{inf}^3\right)}{108\,b_{inf}^4\,p_b^6} \tag{B.18}$$

and its sign depends on the infiltration properties of the sediment, through a_{inf} and b_{inf}, on the bed porosity p_b and on the ratio between pressure head and time step $\gamma_h = h/\Delta t$, which is a simulation-dependent numerical value.

Therefore, the sign of D_{par} cannot be predicted in advance. However, in all the simulations performed in the present work it is always found $D_{par} > 0$, hence the only real root given by Eq. (B.11) is used to compute the infiltration depth after the first integration step, i.e. $\zeta = \gamma_\zeta \Delta t$.

Appendix C

Dam break test benchmarks

For the dam break test on virtually-fixed bed, the reference analytical solution is the Ritter one (see Dressler, 1952; Brocchini et al., 2001, among others):

$$h(x,t) = \frac{1}{9\,g}\left(2\sqrt{g\,h_{rsv}} - \frac{x}{t}\right)^2 \text{ and} \tag{C.1}$$

$$u(x,t) = \frac{2}{3}\left(\sqrt{g\,h_{rsv}} + \frac{x}{t}\right) \tag{C.2}$$

which are defined in the interval $-t\sqrt{g\,h_{rsv}} < x < 2\,t\sqrt{g\,h_{rsv}}$. Note that the Ritter solution is for a rigid (i.e. fixed) bed, therefore $z_b(x,t) = z_b(x,0)$.

About the dam break test on mobile bed case, the reference solution is provided by a Riemann wave solver, which is implemented in a separated code following the approach described by Kelly & Dodd (2009). This solver, which relies on available qualitative knowledge of the wave structure of the solution for a dam break problem on a mobile bed (see Fraccarollo & Capart, 2002), is briefly outlined below.

Under the assumptions for the dam break test, System (4.1) is rewritten in terms of primitive variables and in linearised form:

$$\frac{\partial \mathbf{w}}{\partial t} + \mathbf{J}(\mathbf{w})\frac{\partial \mathbf{w}}{\partial x} = \mathbf{0}, \tag{C.3}$$

where

$$\mathbf{w} = [h, u, z_b]^T \tag{C.4}$$

and

$$\mathbf{J}(\mathbf{w}) = \begin{bmatrix} u & h & 0 \\ g & u & g \\ 0 & \xi\frac{\partial q_b}{\partial u} & 0 \end{bmatrix}, \tag{C.5}$$

with

$$\xi\frac{\partial q_b}{\partial u} = \xi\frac{\partial}{\partial u}\left(A_{sed}\, u^3\right) = \xi\, 3A_{sed}\, u^2. \tag{C.6}$$

Then, the generalised Riemann invariants of System (C.3) are used to obtain the following equations for the velocity and the bed level:

$$u_{j+1} = u_j + \frac{\lambda_{k,j} - u_j}{h_j}(h_{j+1} - h_j) \text{ and} \tag{C.7}$$

$$z_{b,j+1} = z_{b,j} + \frac{\xi\, 3A_{sed}\, u_j^2(\lambda_{k,j} - u_j)}{\lambda_{k,j} h_j}(h_{j+1} - h_j), \tag{C.8}$$

where, limited to this appendix only, the subscripts j and $j+1$ refer to the values on the previous and the current characteristics respectively, with $\lambda_{k,j}$ being the k-th eigenvalue of the Jacobian, i.e. Eq. (C.5), on the previous characteristic j.

The integration of Eqs. (C.7) and (C.8) is performed along a constant time line, beginning from the initial left constant state (see Fig. 5.3) through a first rarefaction fan until the central constant state and then through a second rarefaction fan until the vanishing water depth at the tip (a minimum water depth value has to be set) and the final bed shock.

The computation implies an iterative procedure until the desired level of accuracy because some first guesses are required. The conservation of sediment is chosen as final refinement criterion following Kelly & Dodd (2009).

Appendix D

Morphodynamic shock conditions

The morphodynamic shock conditions are recalled for both the bed- and the combined load cases. They are obtained from the integral form of the Rankine-Hugoniot jump conditions.

While the morphodynamic shock conditions for the bed-load problem were presented by Kelly & Dodd (2010), their extension to the combined load case was shown in Zhu & Dodd (2015). Their complete derivation is available in Zhu (2012).

With reference to Fig. D.1, two generic constant states are considered, the left (Lt) and right (Rt) ones, separated by a discontinuity, or shock, moving with speed V_{shock}.

For the bed-load only case, the morphodynamic shock conditions are

$$h_{Rt}u_{Rt} - h_{Lt}u_{Lt} - (h_{Rt} - h_{Lt})\,V_{shock} = 0, \tag{D.1}$$

$$(h_{Rt}u_{Rt} - h_{Lt}u_{Lt})\,V_{shock} - \left(h_{Rt}u_{Rt}^2 + \frac{gh_{Rt}^2}{2} - h_{Lt}u_{Lt}^2 - \frac{gh_{Lt}^2}{2}\right) + \\ - \frac{g}{2}\,(z_{b,Rt} - z_{b,Lt})\,(h_{Rt} + h_{Lt}) = 0, \tag{D.2}$$

$$(z_{b,Rt} - z_{b,Lt})\,V_{shock} - \xi\,(q_{b,Rt} - q_{b,Lt}) = 0. \tag{D.3}$$

For the combined load case, those expressed by Eqs. (D.1)–(D.3) remain

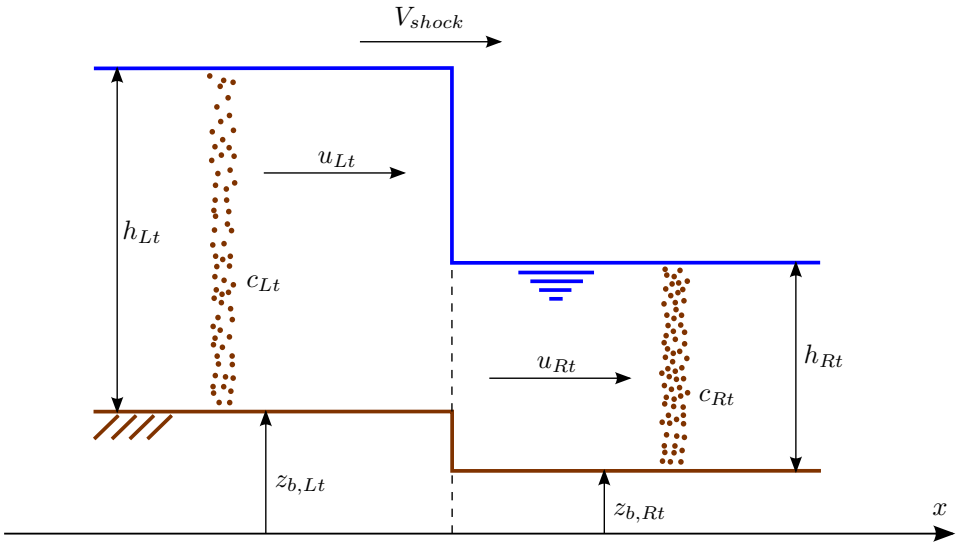

Figure D.1: Sketch for the morphodynamic shock conditions.

unchanged, while the additional shock condition for the suspended sediment equation is

$$(h_{Rt}c_{Rt} - h_{Lt}c_{Lt})\,V_{shock} - (h_{Rt}u_{Rt}c_{Rt} - h_{Lt}u_{Lt}c_{Lt}) = 0. \tag{D.4}$$

Appendix E

Friction coefficient estimate for the representative bottom shear stress in field-scale events

The friction coefficient value (f_c) in the representative bottom shear stress (τ_{rep}) should be typical of the generic swash event. Note that the literature conflicts about the possibility of a single value for the whole swash motion (i.e. for both the uprush and the backwash phases) and about its quantification as well.

With respect to the first point, Conley & Griffin (2004) and Masselink et al. (2005) suggested that the friction coefficient during uprush should be greater than during backwash. However, very recent studies (e.g. Puleo et al., 2014a) found no significant difference in mean friction coefficient values between the two phases.

About the second aspect, Kikkert et al. (2012) found $f_c \approx 0.01$ in their laboratory experiments for bore-driven swash flows on an impermeable rough slope with coarse sand. However, Inch et al. (2015) estimated a friction coeffi-

cient of approximately 0.02 for a beach with analogies with Le Truc Vert one (i.e. a macrotidal dissipative beach, with $d_{50} = 3.3 \times 10^{-4}$ m). Moreover, Masselink et al. (2009) used $f_c = 0.03$ for their model predictions on net sediment transport and bed change, but they found important limitations in their results and poor agreement with field measurements (collected at Le Truc Vert).

Hence, to find a suitable f_c value for τ_{rep}, some preliminary simulations of the selected events are carried out adopting the Chézy approach instead of the BBL solver (see § 3.2.1). The tested values of f_c are 0.005, 0.01, 0.015 and 0.02. No value higher than 0.02 is considered, as the simulation for Event 3 crashed in this case, and therefore also this value is excluded.

Comparisons of the results of these preliminary simulations with the field data are presented in terms of surface level time series in Figs. E.1, E.2 and E.2 for Events 1, 3 and 5 respectively, and of final bed change profiles in Fig. E.4. For each event, the hydrodynamic evolution is not significantly affected by the f_c choice, apart in the upper swash zone, where the smallest f_c value allows a better performance, consistently reducing the maximum run-up underprediction (common to all these simulations). From the morphodynamic viewpoint, it is not immediate to assess which f_c choice yields the overall best results, which show generally an underestimation of the final bed change.

Considering realistic values from previous literature and these, although not conclusive, preliminary results, $f_c = 0.01$ is chosen. This value is thought to reasonably represent at least the correct order of magnitude for the friction coefficient in the single swash events as those considered in § 6.

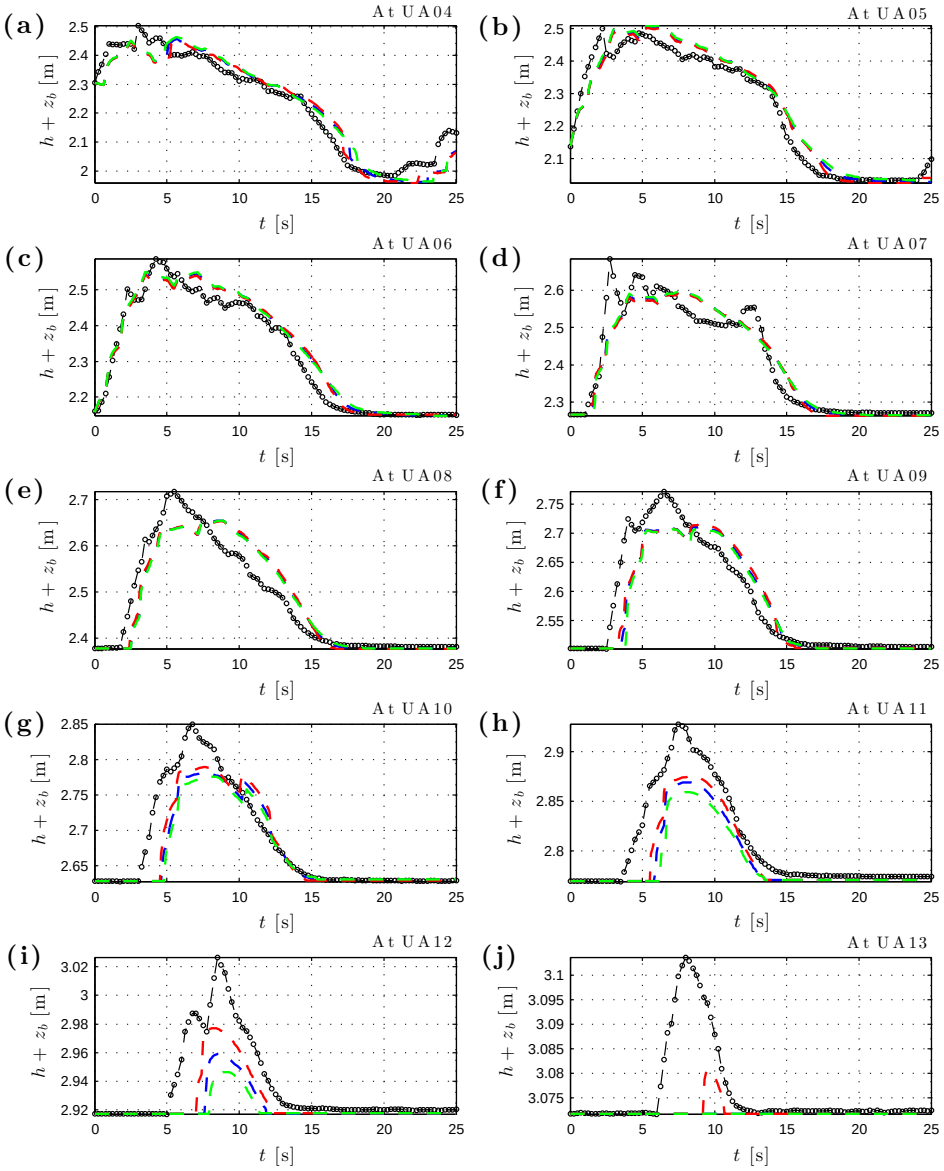

Figure E.1: Event 1. Preliminary simulations with the Chézy approach for f_c estimate in τ_{rep}. Comparison of surface level ($h + z_b$) time series at UA locations. Dashed black line with circles: data. Dashed lines: computed results with $f_c = 0.005$ (red), $f_c = 0.01$ (blue) and $f_c = 0.015$ (green) respectively.

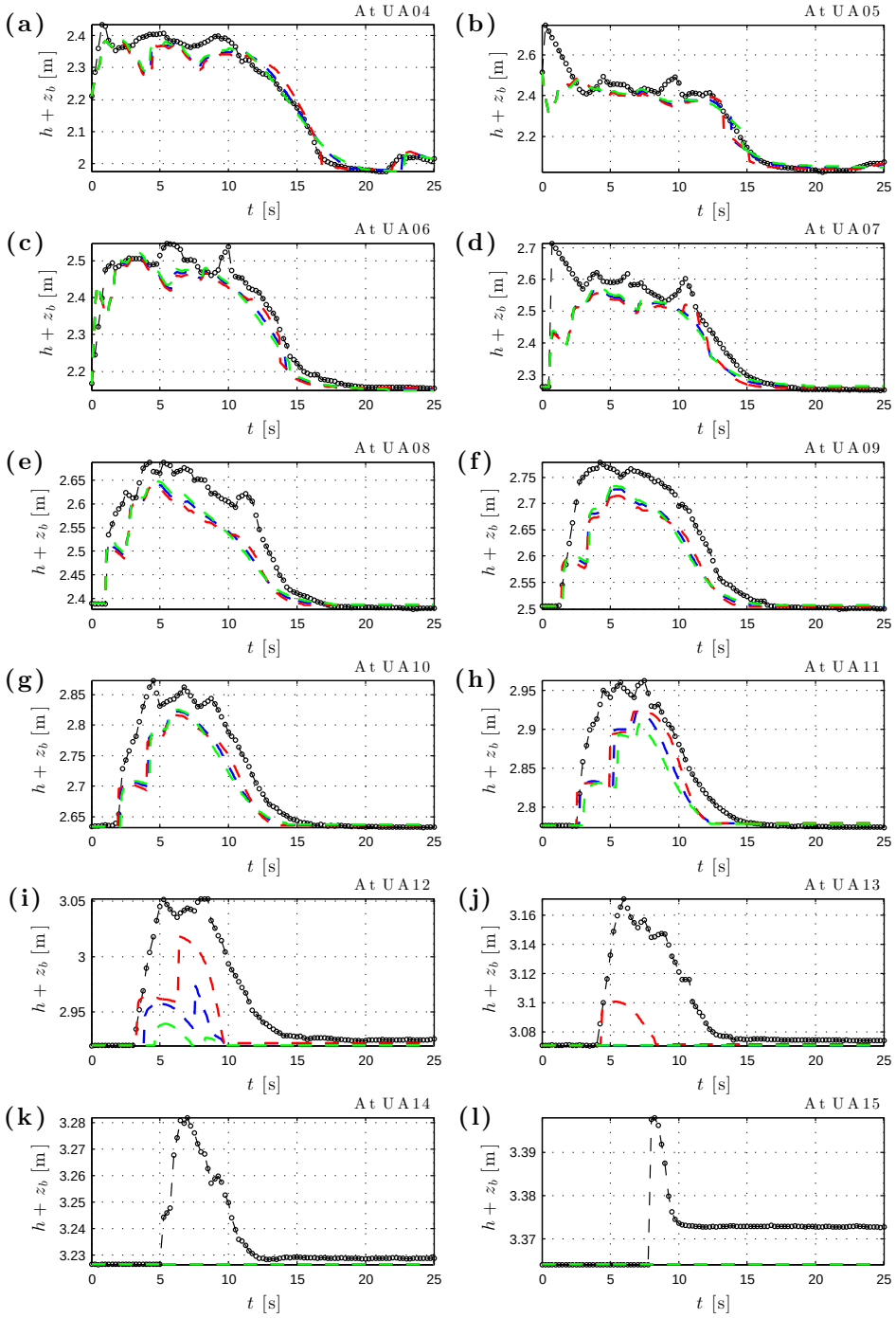

Figure E.2: Event 3. Preliminary simulations with the Chézy approach for f_c estimate in τ_{rep}. Comparison of surface level ($h + z_b$) time series at UA locations. Dashed black line with circles: data. Dashed lines: computed results with $f_c = 0.005$ (red), $f_c = 0.01$ (blue) and $f_c = 0.015$ (green) respectively.

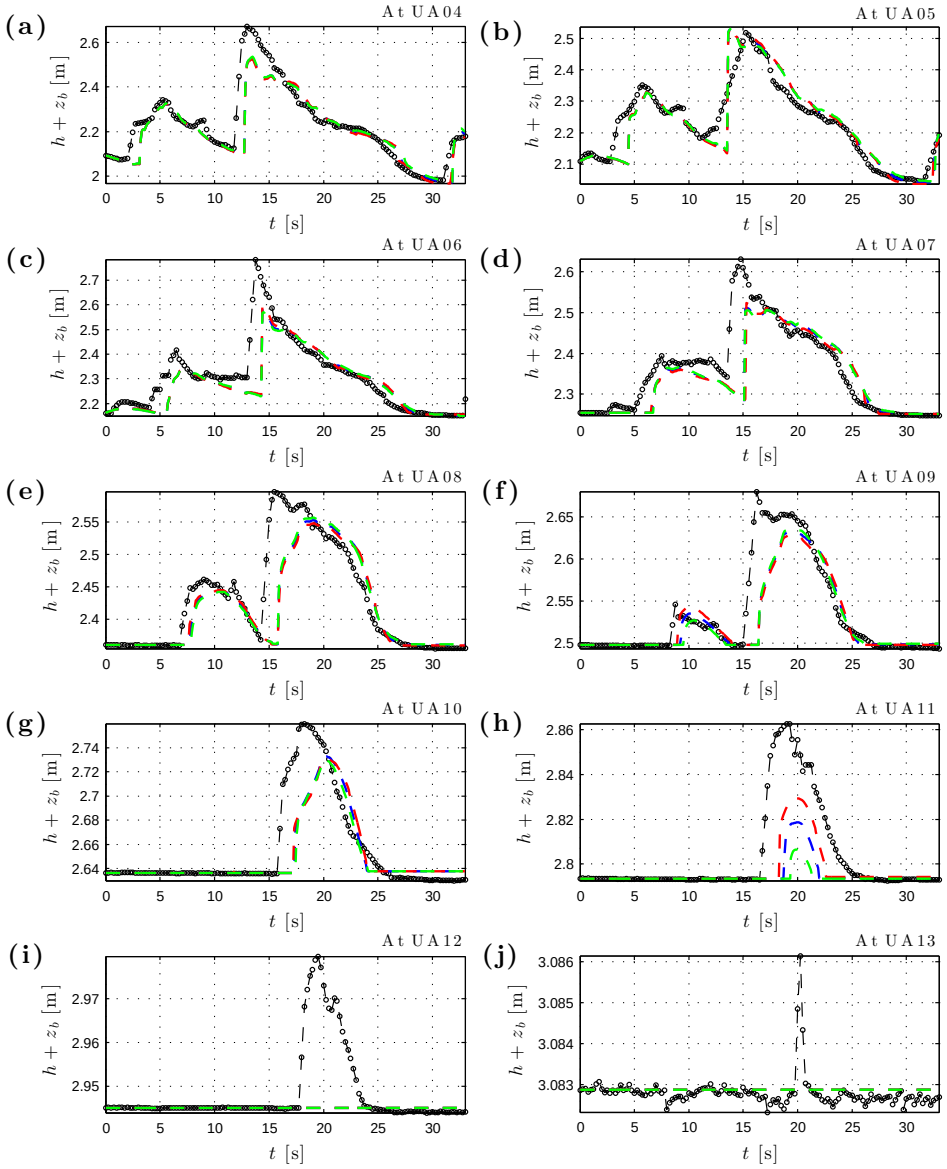

Figure E.3: Event 5. Preliminary simulations with the Chézy approach for f_c estimate in τ_{rep}. Comparison of surface level ($h + z_b$) time series at UA locations. Dashed black line with circles: data. Dashed lines: computed results with $f_c = 0.005$ (red), $f_c = 0.01$ (blue) and $f_c = 0.015$ (green) respectively.

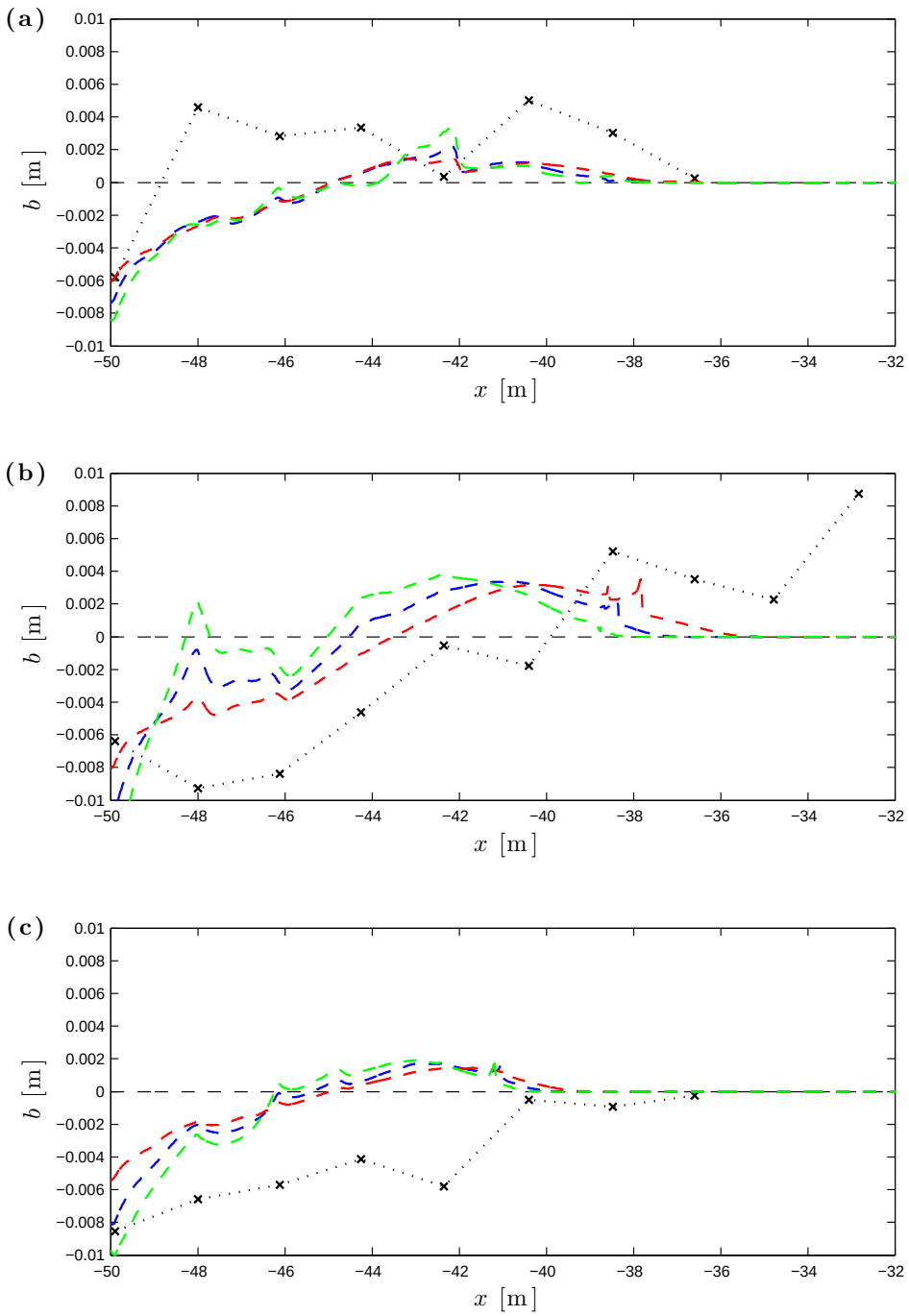

Figure E.4: All events. Preliminary simulations with the Chézy approach for f_c estimate in τ_{rep}. Comparison of final bed change (b) profiles. (a): Event 1. (b): Event 3. (c): Event 5. Dotted black line with crosses: data at UA locations. Dashed black line: no change line. Other dashed lines: computed results with $f_c = 0.005$ (red), $f_c = 0.01$ (blue) and $f_c = 0.015$ (green) respectively.

Appendix F

Comparison of fully-coupled and decoupled simulations

In this appendix a comparison of results using the fully-coupled approach (i.e. that of the present model, which solves simultaneously flow and bed evolution equations) and a decoupled one (i.e. one that solves hydrodynamics and morphodynamics separately, one after the other) is presented.

In particular, the decoupled approach consists of a TVD-MCC scheme for the flow modelling (see Garcia-Navarro et al., 1992) and of a Runge-Kutta 2^{nd} order one (called also Heun method) for the bed update. Note that, for instance, a Runge-Kutta 4^{th} order method could be employed, but its accuracy is deemed excessive with respect to that of the TVD-MCC scheme used for the hydrodynamic part, which is second order at most.

In this comparison, the initial conditions, the parameters and the settings for the bed-only test (see § 7.2.2) are used, except that infiltration and bed diffusion are removed. Furthermore, with reference to Tab. 7.2, the Courant Number and the duration of the simulation are reduced to 0.50 and $1,000$ s respectively (explanation for this is provided later).

The choice of not modelling infiltration and suspended load stems from the requirement to avoid unnecessary complications for a better understanding of the outcomes. Moreover, bed diffusion is not included, as the Runge-Kutta method is for the integration of ordinary differential equations and the bed diffusion source term, i.e. Eq. (3.28), contains some spatial derivatives of z_b.

Fig. F.1 shows the results for the aforementioned comparison. While the location and the amount of the erosion in the upper beach appear to be in very good agreement, the stoss (seaward) side front of the long-shore bar and the maximum erosion at the trough display significant mismatches between the two approaches. In particular, the results with the fully-coupled solver return a long-shore bar which advances seaward more quickly and more erosion in the mid part of the beach (showing also the formation of a bed step around $x = 6$ m at $t = 1,000$ s, see panel (d)) than those with the decoupled one.

The decoupled approach proved to be far less robust than the fully-coupled one, requiring the above-mentioned reduction of CN. Additionally, the results are presented until $t = 1,000$ s as soon after this time, when the long-shore bar reached the seaward boundary in the decoupled simulation, the solver crashed. Other simulations with a smaller Δx (until as small as 0.01 m) were carried out, but corresponding results are not shown as errors at the tip of the swash lens occurred later (around $t = 3,000$ s).

These results, although limited by model simplifications (e.g. neither bed diffusion nor suspended load are considered) and restricted to a particular case, confirm previous findings of Kelly & Dodd (2010) and Postacchini et al. (2012) for a single swash event. They observed, respectively, significant differences in the morphodynamic evolution predicted through the aforementioned two approaches and a poorer performance with the decoupled approach than that of their weakly-coupled solver.

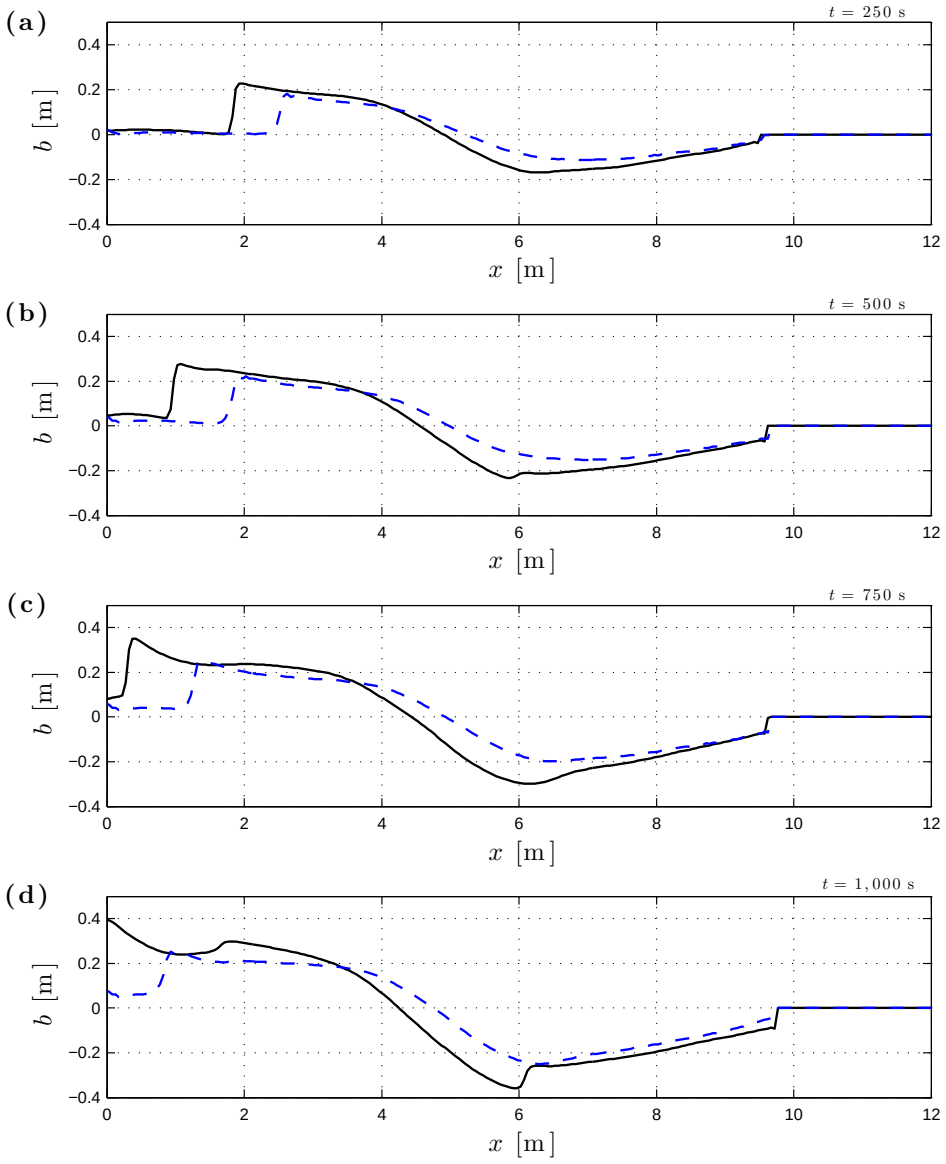

Figure F.1: Fully-coupled and decoupled simulations. Comparison of bed change (b) profiles at different times. (a): $t = 250$ s; (b): $t = 500$ s; (c): $t = 750$ s; (d): $t = 1,000$ s. Solid black line: results with the fully-coupled approach. Dashed blue line: results with the decoupled approach.

Appendix G

Open problem at reflective boundary

In the morphodynamic bore test (see § 8.3.2), it is observed that at the last two cells next to the reflective boundary the bed level profile does not reach the final correct value while the free surface returns to be flat, consistently with quiescent water (see Fig. 8.13).

This error was studied further through a number of additional simulations (not shown). Firstly, suspecting of the predictor-corrector procedure of the TVD-MCC scheme, the test was repeated applying the well-known Lax-Wendroff one (see Hudson, 2001, among others) to the last cell of the domain. However, the results are very similar to those of Fig. 8.13. Secondly the space resolution was increased and / or the Courant Number reduced, but the results do not improve. Thirdly, not only Minmod, but also Superbee and van Leer were employed. The results show a limited dependence of the solution on the particular flux limiter but none of them fix the error.

No other result for the reflection of a bore over a mobile bed with NSWEs-Exner equation solvers is available in literature. However, this issue shows

strong analogies with a numerical error reported in gas dynamics simulations using shock-capturing schemes, known as overheating (see Donat & Marquina, 1996). It was observed in a wide range of methods, both Eulerian and Lagrangian (see Zaide & Roe, 2012), and it seems to be still an open problem in that research field (Liou, 2012).

There are some points of interest about this numerical error. Firstly, the last cell inside the domain and the boundary one have opposite but same absolute value velocities at any time. This means that a sonic point for the bed level eigenspeed is always located at the reflective boundary and this is consistent with what experienced in gas dynamics (see Toro, 1999).

Secondly, the TVD-MCC scheme cannot resolve a sharp theoretical discontinuity, hence the morphodynamic bore is represented as a smeared transition. Some researchers in the gas dynamics field (e.g. Menikoff, 1994) argued that this artificial shock width causes the mismatch.

Thirdly, the error could be related to the nonlinearity of the Exner equation and to that of the whole system (see Zaide, 2012).

About this last point, two additional simulations (not shown) were carried out adopting a linear and a quadratic relationship in u for q_b, instead of the standard cubic one, Eq. (3.7). Interestingly, the error disappears with the linear formula, while persists with the quadratic one. Note that no sonic point occurs at the reflective boundary using the quadratic formula, therefore it does not cause the error. However, the smearing of the bore is apparent even with the linear formula and this means that the artificial bore width does not produce the mismatch by itself.

To summarise, this error appears to be first of all related to the nonlinearity of the Exner equation and subsequently probably affected by the bore smearing, while it seems independent of the occurrence of the sonic point.

Bibliography

van der A, D. A., O'Donoghue, T., & Ribberink, J. S. (2010). Measurements of sheet flow transport in acceleration-skewed oscillatory flow and comparison with practical formulations. *Coastal Engineering*, *57*, 331–342. DOI: `http://dx.doi.org/10.1016/j.coastaleng.2009.11.006`.

Abramowitz, M., & Stegun, I. A. (Eds.) (1972). *Handbook of mathematical functions: with formulas, graphs, and mathematical tables*. Volume 55 of *National Bureau of Standards Applied Mathematics Series*. New York: Dover Publications.

Alsina, J. M., Caceres, I., Brocchini, M., & Baldock, T. E. (2012). An experimental study on sediment transport and bed evolution under different swash zone morphological conditions. *Coastal Engineering*, *68*, 31–43. DOI: `http://dx.doi.org/10.1016/j.coastaleng.2012.04.008`.

Antuono, M., Soldini, L., & Brocchini, M. (2012). On the role of the Chezy frictional term near the shoreline. *Theoretical and Computational Fluid Dynamics*, *26*, 105–116. DOI: `http://dx.doi.org/10.1007/s00162-010-0220-8`.

Baldock, T. E., Holmes, P., & Horn, D. P. (1997). Low frequency swash motion induced by wave grouping. *Coastal Engineering*, *32*, 197–222. DOI: `http://dx.doi.org/10.1016/S0378-3839(97)81750-4`.

Blenkinsopp, C. E., Turner, I. L., Masselink, G., & Russell, P. E. (2011). Swash

zone sediment fluxes: Field observations. *Coastal Engineering*, *58*, 28–44. DOI: http://dx.doi.org/10.1016/j.coastaleng.2010.08.002.

Briganti, R., & Dodd, N. (2009). Shoreline motion in nonlinear shallow water coastal models. *Coastal Engineering*, *56*, 495–505. DOI: http://dx.doi.org/10.1016/j.coastaleng.2008.10.008.

Briganti, R., Dodd, N., Kelly, D. M., & Pokrajac, D. (2012a). An efficient and flexible solver for the simulation of the morphodynamics of fast evolving flows on coarse sediment beaches. *International Journal for Numerical Methods in Fluids*, *69*, 859–877. DOI: http://dx.doi.org/10.1002/fld.2618.

Briganti, R., Dodd, N., Pokrajac, D., & O'Donoghue, T. (2011). Non linear shallow water modelling of bore-driven swash: Description of the bottom boundary layer. *Coastal Engineering*, *58*, 463–477. DOI: http://dx.doi.org/10.1016/j.coastaleng.2011.01.004.

Briganti, R., Dodd, N., Pokrajac, D., & O'Donoghue, T. (2012b). Numerical and experimental description of the flow, boundary layer and bed evolution in bore-driven swash on a coarse sediment beach. In P. Lynett, & J. McKee Smith (Eds.), *Proceedings of 33rd International Conference on Coastal Engineering, Santander, Spain, 2012* (pp. currents–33). Coastal Engineering Research Council Volume 33. DOI: http://dx.doi.org/10.9753/icce.v33.currents.33.

Brocchini, M., & Baldock, T. E. (2008). Recent advances in modeling swash zone dynamics: Influence of surf-swash interaction on nearshore hydrodynamics and morphodynamics. *Reviews of Geophysics*, *46*, 1–21. DOI: http://dx.doi.org/10.1029/2006RG000215.

Brocchini, M., Bernetti, R., Mancinelli, A., & Albertini, G. (2001). An efficient

solver for nearshore flows based on the waf method. *Coastal Engineering*, *43*, 105–129. DOI: http://dx.doi.org/10.1016/S0378-3839(01)00009-6.

Brocchini, M., & Dodd, N. (2008). Nonlinear shallow water equation modeling for coastal engineering. *Journal of Waterway, Port, Coastal and Ocean Engineering*, *134*, 104–120. DOI: http://dx.doi.org/10.1061/(ASCE)0733-950X(2008)134:2(104).

Burcharth, H. F., & Andersen, O. H. (1995). On the one-dimensional steady and unsteady porous flow equations. *Coastal Engineering*, *24*, 233–257. DOI: http://dx.doi.org/10.1016/0378-3839(94)00025-S.

Butt, T., Russell, P., Puleo, J., & Masselink, G. (2005). The application of Bagnold-type sediment transport models in the swash zone. *Journal of Coastal Research*, *21*, 887–895. DOI: http://dx.doi.org/10.2112/04-0210.1.

Caceres, I., & Alsina, J. M. (2012). A detailed, event-by-event analysis of suspended sediment concentration in the swash zone. *Continental Shelf Research*, *41*, 61–76. DOI: http://dx.doi.org/10.1016/j.csr.2012.04.004.

Castro Diaz, M. J., Fernandez-Nieto, E. D., & Ferreiro, A. M. (2008). Sediment transport models in shallow water equations and numerical approach by high order finite volume methods. *Computers & Fluids*, *37*, 299–316. DOI: http://dx.doi.org/10.1016/j.compfluid.2007.07.017.

Clarke, S., Dodd, N., & Damgaard, J. (2004). Modeling flow in and above a porous beach. *Journal of Waterway, Port, Coastal and Ocean Engineering*, *130*, 223–233. DOI: http://dx.doi.org/10.1061/(ASCE)0733-950X(2004)130:5(223).

Conley, D. C., & Griffin, J. G. (2004). Direct measurements of bed stress under swash in the field. *Journal of Geophysical Research: Oceans (1978–2012)*, *109*, 1–12. DOI: http://dx.doi.org/10.1029/2003JC001899.

Dodd, N., Stoker, A. M., Calvete, D., & Sriariyawat, A. (2008). On beach cusp formation. *Journal of Fluid Mechanics*, *597*, 145–169. DOI: http://dx.doi.org/10.1017/S002211200700972X.

Donat, R., & Marquina, A. (1996). Capturing shock reflections: an improved flux formula. *Journal of Computational Physics*, *125*, 42–58. DOI: http://dx.doi.org/10.1006/jcph.1996.0078.

van Dongeren, A. R., & Svendsen, I. A. (1997). Absorbing-generating boundary condition for shallow water models. *Journal of Waterway, Port, Coastal and Ocean Engineering*, *123*, 303–313. DOI: http://dx.doi.org/10.1061/(ASCE)0733-950X(1997)123:6(303).

Dressler, R. F. (1952). Hydraulic resistance effect upon the dam-break functions. *Journal of Research of the National Bureau of Standards*, *49*, 217–225. URL: http://nvlpubs.nist.gov/nistpubs/jres/049/3/V49.N03.A08.pdf.

Elfrink, B., & Baldock, T. (2002). Hydrodynamics and sediment transport in the swash zone: a review and perspectives. *Coastal Engineering*, *45*, 149–167. DOI: http://dx.doi.org/10.1016/S0378-3839(02)00032-7.

Erikson, L., Larson, M., & Hanson, H. (2005). Prediction of swash motion and run-up including the effects of swash interaction. *Coastal Engineering*, *52*, 285–302. DOI: http://dx.doi.org/10.1016/j.coastaleng.2004.12.001.

Falques, A., Montoto, A., & Iranzo, V. (1996). Bed-flow instability of the longshore current. *Continental Shelf Research*, *16*, 1927–1964. DOI: http://dx.doi.org/10.1016/0278-4343(96)00031-3.

Fraccarollo, L., & Capart, H. (2002). Riemann wave description of erosional dam-break flows. *Journal of Fluid Mechanics*, *461*, 183–228. DOI: http://dx.doi.org/10.1017/S0022112002008455.

Fredsøe, J., & Deigaard, R. (1992). *Mechanics of coastal sediment transport*. Volume 3 of *Advanced Series on Ocean Engineering*. Singapore: World Scientific Publishing.

Garcia-Navarro, P., Alcrudo, F., & Saviron, J. M. (1992). 1-D open-channel flow simulation using TVD-McCormack scheme. *Journal of Hydraulic Engineering*, *118*, 1359–1372. DOI: http://dx.doi.org/10.1061/(ASCE)0733-9429(1992)118:10(1359).

Garnier, R. (2006). *Nonlinear modelling of surf zone morphodynamical instabilities*. Ph.D. thesis. Universitat Politècnica de Catalunya.

Garnier, R., Calvete, D., Falques, A., & Dodd, N. (2008). Modelling the formation and the long-term behavior of rip channel systems from the deformation of a longshore bar. *Journal of Geophysical Research*, *113*, 1–18. DOI: http://dx.doi.org/10.1029/2007JC004632.

Harten, A., & Hyman, J. M. (1983). Self adjusting grid methods for one-dimensional hyperbolic conservation laws. *Journal of Computational Physics*, *50*, 235–269. DOI: http://dx.doi.org/10.1016/0021-9991(83)90066-9.

Hibberd, S., & Peregrine, D. (1979). Surf and run-up on a beach: a uniform

bore. *Journal of Fluid Mechanics*, *96*, 323–346. DOI: http://dx.doi.org/10.1017/S002211207900149X.

Hubbard, M. E., & Dodd, N. (2002). A 2D numerical model of wave run-up and overtopping. *Coastal Engineering*, *47*, 1–26. DOI: http://dx.doi.org/10.1016/S0378-3839(02)00094-7.

Hudson, J. (2001). *Numerical techniques for morphodynamical modelling*. Ph.D. thesis. University of Reading.

Hudson, J., & Sweby, P. K. (2003). Formulations for numerically approximating hyperbolic systems governing sediment transport. *Journal of Scientific Computing*, *19*, 225–252. DOI: http://dx.doi.org/10.1023/A:1025304008907.

Hughes, M. G., Masselink, G., & Brander, R. W. (1997). Flow velocity and sediment transport in the swash zone of a steep beach. *Marine Geology*, *138*, 91–103. DOI: http://dx.doi.org/10.1016/S0025-3227(97)00014-5.

Incelli, G., Briganti, R., & Dodd, N. (2015a). Absorbing–generating seaward boundary conditions for fully-coupled hydro-morphodynamical solvers. *Coastal Engineering*, *99*, 96–108. DOI: http://dx.doi.org/10.1016/j.coastaleng.2015.02.002.

Incelli, G., Dodd, N., Blenkinsopp, C. E., Zhu, F., & Briganti, R. (2015b). Morphodynamical Modelling of Field-Scale Swash Events. *Coastal Engineering*, *accepted manuscript for 'Special Issue: Swash-zone Processes'*. DOI: http://dx.doi.org/10.1016/j.coastaleng.2015.09.006.

Inch, K., Masselink, G., Puleo, J. A., Russell, P., & Conley, D. C. (2015). Vertical structure of near-bed cross-shore flow velocities in the swash zone

of a dissipative beach. *Continental Shelf Research*, *101*, 98–108. DOI: http://dx.doi.org/10.1016/j.csr.2015.04.006.

Kelly, D. M. (2009). *Bore-driven swash on a mobile beach*. Ph.D. thesis. The University of Nottingham.

Kelly, D. M., & Dodd, N. (2009). Floating grid characteristics method for unsteady flow over a mobile bed. *Computers & Fluids*, *38*, 899–909. DOI: http://dx.doi.org/10.1016/j.compfluid.2008.09.011.

Kelly, D. M., & Dodd, N. (2010). Beach-face evolution in the swash zone. *Journal of Fluid Mechanics*, *661*, 316–340. DOI: http://dx.doi.org/10.1017/S0022112010002983.

Kermani, M. J., & Plett, E. G. (2001). Modified entropy correction formula for the Roe scheme. In *Proceedings of 39th AIAA Aerospace Sciences Meeting & Exhibit, Reno, Nevada, USA, 2001*. American Institute of Aeronautics and Astronautics. URL: http://me.aut.ac.ir/mkermani/pdf-files/conferences/aiaa2001-0083.pdf.

Kikkert, G. A., O'Donoghue, T., Pokrajac, D., & Dodd, N. (2012). Experimental study of bore-driven swash hydrodynamics on impermeable rough slopes. *Coastal Engineering*, *60*, 149–166. DOI: http://dx.doi.org/10.1016/j.coastaleng.2011.09.006.

Kikkert, G. A., Pokrajac, D., O'Donoghue, T., & Steenhauer, K. (2013). Experimental study of bore-driven swash hydrodynamics on permeable rough slopes. *Coastal Engineering*, *79*, 42–56. DOI: http://dx.doi.org/10.1016/j.coastaleng.2013.04.008.

Kikkert, G. A., & Steenhauer, K. (2008). Experimental Study of Swash Zone.

Hydrodynamics and Sediment Transport. Phase 2: Permeable, Fixed Slopes. Unpublished report.

Kim, D.-H. (2015). H2D morphodynamic model considering wave, current and sediment interaction. *Coastal Engineering*, *95*, 20–34. DOI: http://dx.doi.org/10.1016/j.coastaleng.2014.09.006.

Kobayashi, N., & Johnson, B. D. (2001). Sand suspension, storage, advection, and settling in surf and swash zones. *Journal of Geophysical Research*, *106*, 9363–9376. DOI: http://dx.doi.org/10.1029/2000JC000557.

Kobayashi, N., Otta, A. K., & Roy, I. (1987). Wave reflection and run-up on rough slopes. *Journal of Waterway, Port, Coastal and Ocean Engineering*, *113*, 282–298. DOI: http://dx.doi.org/10.1061/(ASCE)0733-950X(1987)113:3(282).

Lanckriet, T., & Puleo, J. A. (2015). A semianalytical model for sheet flow layer thickness with application to the swash zone. *Journal of Geophysical Research: Oceans*, *120*, 1333–1352. DOI: http://dx.doi.org/10.1002/2014JC010378.

Lanckriet, T., Puleo, J. A., Masselink, G., Turner, I. L., Conley, D., Blenkinsopp, C., & Russell, P. (2014). A Comprehensive Field Study of Swash-Zone Processes, II: Sheet Flow Sediment Concentrations During Quasi-Steady Backwash. *Journal of Waterway, Port, Coastal and Ocean Engineering*, *140*, 29–43. DOI: http://dx.doi.org/10.1061/(ASCE)WW.1943-5460.0000209.

Landry, B. J., Hancock, M. J., & Mei, C. C. (2007). Note on sediment sorting in a sandy bed under standing water waves. *Coastal Engineering*, *54* , 694–699. DOI: http://dx.doi.org/10.1016/j.coastaleng.2007.02.003.

Liou, M.-S. (2012). Unresolved Problems by Shock Capturing: Taming the Overheating Problem. In *Proceedings of 7th International Conference on Computational Fluid Dynamics, Big Island, Hawaii, USA, 2012*. URL: http://ntrs.nasa.gov/archive/nasa/casi.ntrs.nasa.gov/20130000503.pdf.

Masselink, G., Evans, D., Hughes, M. G., & Russell, P. (2005). Suspended sediment transport in the swash zone of a dissipative beach. *Marine Geology*, *216*, 169–189. DOI: http://dx.doi.org/10.1016/j.margeo.2005.02.017.

Masselink, G., & Hughes, M. (1998). Field investigation of sediment transport in the swash zone. *Continental Shelf Research*, *18*, 1179–1199. DOI: http://dx.doi.org/10.1016/S0278-4343(98)00027-2.

Masselink, G., & Hughes, M. G. (2003). *Introduction to coastal processes & geomorphology*. London: Hodder Arnold.

Masselink, G., & Li, L. (2001). The role of swash infiltration in determining the beachface gradient: a numerical study. *Marine Geology*, *176*, 139–156. DOI: http://dx.doi.org/10.1016/S0025-3227(01)00161-X.

Masselink, G., & Puleo, J. A. (2006). Swash-zone morphodynamics. *Continental Shelf Research*, *26*, 661–680. DOI: http://dx.doi.org/10.1016/j.csr.2006.01.015.

Masselink, G., & Russell, P. (2006). Flow velocities, sediment transport and morphological change in the swash zone of two contrasting beaches. *Marine Geology*, *227*, 227–240. DOI: http://dx.doi.org/10.1016/j.margeo.2005.11.005.

Masselink, G., Russell, P., Turner, I., & Blenkinsopp, C. (2009). Net sediment transport and morphological change in the swash zone of a high-energy sandy beach from swash event to tidal cycle time scales. *Marine Geology*, *267*, 18–35. DOI: http://dx.doi.org/10.1016/j.margeo.2009.09.003.

McCall, R. T., Masselink, G., Poate, T. G., Roelvink, J. A., & Almeida, L. P. (2015). Modelling the morphodynamics of gravel beaches during storms with XBeach-G. *Coastal Engineering*, *103*, 52–66. DOI: http://dx.doi.org/10.1016/j.coastaleng.2015.06.002.

Menikoff, R. (1994). Errors when shock waves interact due to numerical shock width. *Journal on Scientific Computing*, *15*, 1227–1242. DOI: http://dx.doi.org/10.1137/0915075.

Nielsen, P. (2002). Shear stress and sediment transport calculations for swash zone modelling. *Coastal Engineering*, *45*, 53–60. DOI: http://dx.doi.org/10.1016/S0378-3839(01)00036-9.

Nikuradse, J. (1932). Gesetzmässigkeiten der turbulenten strömung in glatten rohren. *Ver. Dtsch. Ing. Forschungsheft*, (p. 356).

Packwood, A. R. (1983). The influence of beach porosity on wave uprush and backwash. *Coastal Engineering*, *7*, 29–40. DOI: http://dx.doi.org/10.1016/0378-3839(83)90025-X.

Packwood, A. R., & Peregrine, D. H. (1980). The propagation of solitary waves and bores over a porous bed. *Coastal Engineering*, *3*, 221–242. DOI: http://dx.doi.org/10.1016/0378-3839(79)90022-X.

Peregrine, D. H., & Williams, S. M. (2001). Swash overtopping a truncated plane beach. *Journal of Fluid Mechanics*, *440*, 391–399. DOI: http://dx.doi.org/10.1017/S002211200100492X.

Pintado-Patiño, J. C., Torres-Freyermuth, A., Puleo, J. A., & Pokrajac, D. (2015). On the role of infiltration and exfiltration in swash zone boundary layer dynamics. *Journal of Geophysical Research: Oceans*, *120*, 6329–6350. DOI: http://dx.doi.org/10.1002/2015JC010806.

Postacchini, M., Brocchini, M., Mancinelli, A., & Landon, M. (2012). A multi-purpose, intra-wave, shallow water hydro-morphodynamic solver. *Advances in Water Resources*, *38*, 13–26. DOI: http://dx.doi.org/10.1016/j.advwatres.2011.12.003.

Postacchini, M., Othman, I. K., Brocchini, M., & Baldock, T. E. (2014). Sediment transport and morphodynamics generated by a dam-break swash uprush: Coupled vs uncoupled modeling. *Coastal Engineering*, *89*, 99–105. DOI: http://dx.doi.org/10.1016/j.coastaleng.2014.04.003.

Pritchard, D. (2009). Sediment transport under a swash event: the effect of boundary conditions. *Coastal Engineering*, *56*, 970–981. DOI: http://dx.doi.org/10.1016/j.coastaleng.2009.06.004.

Pritchard, D., Guard, P. A., & Baldock, T. E. (2008). An analytical model for bore-driven run-up. *Journal of Fluid Mechanics*, *610*, 183–193. DOI: http://dx.doi.org/10.1017/S0022112008002644.

Pritchard, D., & Hogg, A. J. (2005). On the transport of suspended sediment by a swash event on a plane beach. *Coastal Engineering*, *52*, 1–23. DOI: http://dx.doi.org/10.1016/j.coastaleng.2004.08.002.

Puleo, J. A., Beach, R. A., Holman, R. A., & Allen, J. S. (2000). Swash zone sediment suspension and transport and the importance of bore-generated turbulence. *Journal of Geophysical Research: Oceans (1978–2012)*, *105*, 17021–17044. DOI: http://dx.doi.org/10.1029/2000JC900024.

Puleo, J. A., Blenkinsopp, C., Conley, D., Masselink, G., Turner, I. L., Russell, P., Buscombe, D., Howe, D., Lanckriet, T., McCall, R., & Poate, T. (2014a). A Comprehensive Field Study of Swash-Zone Processes, I: Experimental Design with Examples of Hydrodynamic and Sediment Transport Measurements. *Journal of Waterway, Port, Coastal and Ocean Engineering*, *140*, 14–28. DOI: http://dx.doi.org/10.1061/(ASCE)WW.1943-5460.0000210.

Puleo, J. A., Farhadzadeh, A., & Kobayashi, N. (2007). Numerical simulation of swash zone fluid accelerations. *Journal of Geophysical Research: Oceans (1978–2012)*, *112*, 1–16. DOI: http://dx.doi.org/10.1029/2006JC004084.

Puleo, J. A., Holland, K. T., Plant, N. G., Slinn, D. N., & Hanes, D. M. (2003). Fluid acceleration effects on suspended sediment transport in the swash zone. *Journal of Geophysical Research: Oceans (1978–2012)*, *108*, 1–12. DOI: http://dx.doi.org/10.1029/2003JC001943.

Puleo, J. A., Lanckriet, T., & Blenkinsopp, C. (2014b). Bed level fluctuations in the inner surf and swash zone of a dissipative beach. *Marine Geology*, *349*, 99–112. DOI: http://dx.doi.org/10.1016/j.margeo.2014.01.006.

Reniers, A. J. H. M., Gallagher, E. L., MacMahan, J. H., Brown, J. A., Rooijen, A. A., van Thiel de Vries, J. S. M., & van Prooijen, B. C. (2013). Observations and modeling of steep-beach grain-size variability. *Journal of Geophysical Research: Oceans*, *118*, 577–591. DOI: http://dx.doi.org/10.1029/2012JC008073.

Reniers, A. J. H. M., Roelvink, J. A., & Thornton, E. B. (2004). Morphodynamic modeling of an embayed beach under wave group forcing. *Journal of Geophysical Research: Oceans (1978–2012)*, *109*, 1–22. DOI: http://dx.doi.org/10.1029/2002JC001586.

van Rijn, L. C. (1982). Equivalent roughness of alluvial bed. *Journal of Hydraulic Engineering*, *108*, 1215–1218. URL: http://www.leovanrijn-sediment.com/papers/P1-1982a.pdf.

van Rijn, L. C. (1984). Sediment transport, Part II: Suspended load transport. *Journal of Hydraulic Engineering*, *110*, 1613–1641. DOI: http://dx.doi.org/10.1061/(ASCE)0733-9429(1984)110:11(1613).

van Rijn, L. C. (2007a). Unified view of sediment transport by currents and waves. I: Initiation of motion, bed roughness, and bed-load transport. *Journal of Hydraulic Engineering*, *133*, 649–667. DOI: http://dx.doi.org/10.1061/(ASCE)0733-9429(2007)133:6(649).

van Rijn, L. C. (2007b). Unified view of sediment transport by currents and waves. II: Suspended transport. *Journal of Hydraulic Engineering*, *133*, 668–689. DOI: http://dx.doi.org/10.1061/(ASCE)0733-9429(2007)133:6(668).

Roelvink, D., Reniers, A., van Dongeren, A. P., van Thiel de Vries, J., McCall, R., & Lescinski, J. (2009). Modelling storm impacts on beaches, dunes and barrier islands. *Coastal Engineering*, *56*, 1133–1152. DOI: http://dx.doi.org/10.1016/j.coastaleng.2009.08.006.

van Rooijen, A., Reniers, A., van Thiel de Vries, J., Blenkinsopp, C., & McCall, R. (2012). Modeling swash zone sediment transport at Truc Vert Beach. In P. Lynett, & J. McKee Smith (Eds.), *Proceedings of 33rd International Conference on Coastal Engineering, Santander, Spain, 2012* (pp. sediment–105). Coastal Engineering Research Council Volume 33. DOI: http://dx.doi.org/10.9753/icce.v33.sediment.105.

Senechal, N., & Ardhuin, F. (2008). ECORS Truc Vert'08: a multi-institutional

international nearshore field experiment. In *AGU Fall Meeting Abstracts* (pp. B–02). URL: http://adsabs.harvard.edu/abs/2008AGUFMOS12B..02S.

Shen, M. C., & Meyer, R. E. (1963). Climb of a bore on a beach. Part 3. Run-up. *Journal of Fluid Mechanics*, *16*, 113–125. DOI: http://dx.doi.org/10.1017/S0022112063000628.

Sriariyawat, A. (2009). *Formation and evolution of beach cusps*. Ph.D. thesis. The University of Nottingham.

Steenhauer, K., Pokrajac, D., & O'Donoghue, T. (2012a). Implementation of ADER scheme for a bore on an unsaturated permeable slope. *International Journal for Numerical Methods in Fluids*, *70*, 682–702. DOI: http://dx.doi.org/10.1002/fld.2706.

Steenhauer, K., Pokrajac, D., & O'Donoghue, T. (2012b). Numerical model of swash motion and air entrapment within coarse-grained beaches. *Coastal Engineering*, *64*, 113–126. DOI: http://dx.doi.org/10.1016/j.coastaleng.2012.01.004.

Steenhauer, K., Pokrajac, D., O'Donoghue, T., & Kikkert, G. A. (2011). Subsurface processes generated by bore-driven swash on coarse-grained beaches. *Journal of Geophysical Research: Oceans (1978–2012)*, *116*, 1–17. DOI: http://dx.doi.org/10.1029/2010JC006789.

Svendsen, I. A. (2005). *Introduction to nearshore hydrodynamics*. Volume 24 of *Advanced Series on Ocean Engineering*. Singapore: World Scientific Publishing.

Sweby, P. K. (1984). High resolution schemes using flux limiters for hyper-

bolic conservation laws. *Journal on Numerical Analysis*, *21*, 995–1011. DOI: http://dx.doi.org/10.1137/0721062.

Toro, E. F. (1999). *Riemann solvers and numerical methods for fluid dynamics*. Volume 16 (2nd ed.). Berlin: Springer-Verlag.

Toro, E. F. (2001). *Shock-capturing methods for free-surface shallow fluids*. Chichester: John Wiley & Sons.

Turner, I. L., Russell, P. E., & Butt, T. (2008). Measurement of wave-by-wave bed-levels in the swash zone. *Coastal Engineering*, *55*, 1237–1242. DOI: http://dx.doi.org/10.1016/j.coastaleng.2008.09.009.

Wei, G., Kirby, J. T., & Sinha, A. (1999). Generation of waves in Boussinesq models using a source function method. *Coastal Engineering*, *36*, 271–299. DOI: http://dx.doi.org/10.1016/S0378-3839(99)00009-5.

Wilson, K. C. (1989). Mobile-bed friction at high shear stress. *Journal of Hydraulic Engineering*, *115*, 825–830. DOI: http://dx.doi.org/10.1061/(ASCE)0733-9429(1989)115:6(825).

Xiao, H., Young, Y. L., & Prevost, J. H. (2010). Hydro-and morpho-dynamic modeling of breaking solitary waves over a fine sand beach. Part II: Numerical simulation. *Marine Geology*, *269*, 119–131. DOI: http://dx.doi.org/10.1016/j.margeo.2009.12.008.

Young, Y. L., Xiao, H., & Maddux, T. (2010). Hydro-and morpho-dynamic modeling of breaking solitary waves over a fine sand beach. Part I: Experimental study. *Marine Geology*, *269*, 107–118. DOI: http://dx.doi.org/10.1016/j.margeo.2009.12.009.

Zaide, D. W., & Roe, P. L. (2012). Flux Functions for Reducing Numerical Shockwave Anomalies. In *Proceedings of 7th International Conference on Computational Fluid Dynamics, Big Island, Hawaii, USA, 2012*. URL: http://www.iccfd.org/iccfd7/assets/pdf/papers/ICCFD7-2205_paper.pdf.

Zaide, D. W.-M. (2012). *Numerical Shockwave Anomalies*. Ph.D. thesis. The University of Michigan.

van der Zanden, J., Alsina, J. M., Caceres, I., Buijsrogge, R. H., & Ribberink, J. S. (2015). Bed level motions and sheet flow processes in the swash zone: Observations with a new conductivity-based concentration measuring technique (CCM+). *Coastal Engineering*, *105*, 47–65. DOI: http://dx.doi.org/10.1016/j.coastaleng.2015.08.009.

Zhu, F. (2012). *1D morphodynamical modelling of swash zone beachface evolution*. Ph.D. thesis. The University of Nottingham.

Zhu, F., & Dodd, N. (2013). Net beach change in the swash zone: A numerical investigation. *Advances in Water Resources*, *53*, 12–22. DOI: http://dx.doi.org/10.1016/j.advwatres.2012.10.002.

Zhu, F., & Dodd, N. (2015). The morphodynamics of a swash event on an erodible beach. *Journal of Fluid Mechanics*, *762*, 110–140. DOI: http://dx.doi.org/10.1017/jfm.2014.610.

Zhu, F., Dodd, N., & Briganti, R. (2012). Impact of a uniform bore on an erodible beach. *Coastal Engineering*, *60*, 326–333. DOI: http://dx.doi.org/10.1016/j.coastaleng.2011.08.006.